U.PORTO
FEUP FACULDADE DE ENGENHARIA
UNIVERSIDADE DO PORTO

Sorption-Enhanced Steam Reforming of Ethanol for Hydrogen Production

A Dissertation presented to the

UNIVERSITY OF PORTO

for the degree of Doctor in

Chemical and Biological Engineering

by

YIJIANG WU (吴一江)

Supervisor: Prof. Dr. Eng. Alirio E. Rodrigues

Co-advisor: Dr. Eng. Adelino F. Cunha

Associated Laboratory LSRE-LCM

Department of Chemical Engineering

Faculty of Engineering

University of Porto

July, 2014

Abstract

Concerns over environment and fossil fuel depletion led to the concept of "hydrogen economy", where hydrogen is used as energy carrier. Nowadays, hydrogen is mostly produced from natural gas. As alternative, ethanol is one of the ideal resources for hydrogen production, since it can be obtained from renewable biomass. The essence is that this process is carbon neutral. Moreover, the combination of steam reforming with *in situ* carbon dioxide adsorption during ethanol conversion enhances the reaction above the thermodynamic equilibrium to produce more hydrogen. As a result, sorption enhanced steam reforming for hydrogen production has been investigated in this thesis.

The objective of this work is to develop suitable catalytic/sorbent systems for high purity hydrogen production by sorption-enhanced steam reforming of ethanol (SE-SRE), applying different operating conditions and cyclic operations to improve the performance of the process.

First, a preliminary experimental study on SE-SRE with commercial materials has been carried out. Theoretical studies consist of the thermodynamic analysis of the SE-SRE system with different sorbent materials. A kinetic investigation on a commercial nickel-based catalyst can also be found. Furthermore, homemade hybrid materials with nickel and copper as active phases and hydrotalcite sorbent as support have been prepared and tested for SE-SRE. On the other hand, the adsorption capacity of the hydrotalcite sorbent could be improved by impregnating a potassium promoter with potassium nitrate as the alkali precursor. Finally, a multifunctional material with potassium promoted hydrotalcite sorbent as support, and a nickel-copper alloy as active phase has been developed.

The process study has been carried out to develop a continuous hydrogen production operation from SE-SRE. For this purpose, homogeneously packed columns with two sub-sections have been simulated, and a four-step pressure swing cyclic process has been used to achieve a continuous operation, where hydrogen with high purity can be produced continuously. Finally, adsorptive reactors with a two-dimensional mathematical model have been developed in the simulation of a pressure swing process with a seven-step cycle scheme. A parametric study has also been carried out to improve the performance of cyclic operation process.

Resumo

As preocupações com o meio ambiente e a escassez de fontes fósseis resultaram no conceito da economia do hidrogénio, onde hidrogénio é reconhecido como vector energético universal. Hoje em dia o hidrogénio é produzido maioritariamente a partir de gás natural. Como alternativa o etanol pode ser considerado uma fonte ideal para a produção de hidrogénio devido à sua obtenção a portei de biomassa renovável etanol. A essência deste processo é que ele é neutro na utilização do carbono. Podemos também admitir que a combinação da reforma por vapor de água *in situ* com a captura de dióxido de carbono por adsorção durante a conversão do etanol acelera a reacção, conseguindo assim, em teoria, aproximarmo-nos do equilíbrio termodinâmico. Concluindo, a reforma de etanol por vapor de água com sorção de dióxido de carbono para a produção de hidrogénio foi estudada na presente tese de doutoramento.

O objetivo deste trabalho foi desenvolver um sistema híbrido de catalisador com adsorvente para a produção de hidrogénio puro com sorção de dióxido de carbono para a reforma de etanol com vapor de água (SE-SRE), usando diferentes adsorventes e matérias com propriedades catalíticas, aplicando condições operatórias diversas e operações cíclicas para melhorar o desempenho do processo.

Foi elaborado um estudo experimental preliminar para a SE-SRE com materiais comerciais. Os estudos teóricos consistem na análise termodinâmica do sistema da SE-SRE com diferentes absorventes, e a investigação da cinética num catalisador de níquel comercial. Além disso, materiais híbridos caseiros com níquel e cobre como fases activas, e adsorvente à base da hidrotalcite usado como suporte, foram preparados e testados para a SE-SRE. A capacidade de adsorção do adsorvente à base da hidrotalcite foi também melhorada através da impregnação do promotor de potássio, com nitrato de potássio como precursor alcalino. Por último foi desenvolvido um material multifuncional com potássio como promotor, hidrotalcite como adsorvente e suporte, e uma liga de níquel-cobre como fase activa.

Finalmente, o estudo do processo foi realizado para desenvolver uma operação de produção de hidrogénio a partir da SE-SRE em contínuo. Para este fim, as colunas empacotadas homogéneamente com duas sub-secções foram simulados, e um processo cíclico de quatro etapas com modulação de pressão foi usado para conseguir uma operação contínua, em que o hidrogénio de elevado grau de pureza pode ser produzido. Reactores de adsorção com o modelo matemático bidimensional também

foram desenvolvidos na simulação de um processo de modulação de pressão com um sistema de ciclo de sete passos. Um estudo paramétrico também foi realizado para melhorar o desempenho do processo de funcionamento cíclico.

摘要

“氢经济”是为解决使用化石燃料引起的环境污染及能源危机而提出的一种解决方案。目前，天然气是主要的氢气生产原料。乙醇可从大量可再生生物质中获得，生产和使用过程能实现碳平衡，是一种很好的替代来源。与此同时，在常规乙醇蒸汽重整过程中加入二氧化碳吸附剂可使反应热力学平衡偏向产物端，生产更多氢气产品。因此，本论文的研究课题便是二氧化碳吸附强化乙醇重整制氢工艺。

在实验研究阶段，首先采用了商业催化剂及吸附剂材料对吸附强化乙醇重整反应的可行性进行验证。此外，通过热力学计算分析了不同高温吸附材料在反应体系中的表现并对商业镍催化剂建立了重整反应动力学模型。接着，本研究中还制备合成了一系列以镍和铜为活性催化金属，水滑石吸附剂为载体的复合材料并将其用于吸附强化反应。另一方面，利用硝酸钾为碱金属钾助剂的来源可以合成具有更高二氧化碳吸附能力的水滑石材料。最后，在材料研究方面开发合成了利用镍铜合金为活性催化金属，包含钾助剂的水滑石为载体的复合材料以用于生产高纯氢气的吸附强化反应过程。

为实现连续的高纯氢气生产，本论文针对吸附强化乙醇重整制氢反应展开了系统过程研究。首先建立了包含有两个分段的反应床层的数学模型，并利用该模型模拟了变压循环连续生产操作，模拟的结果表明高纯度氢气可通过强化乙醇重整反应获得。最后一部分，建立了包含轴向与径向的二维吸附反应器数学模型，利用四个反应器建立了包含七个操作步骤的变压连续操作过程生产高纯度氢气，并通过改变不同操作参数优化反应过程。

Acknowledgements

First of all, I would like to express my sincere gratitude to my supervisor, Prof. Alirio E. Rodrigues, for his intellectual supervision, continuous support, and encouragement which make this thesis possible. Besides, I am also willing to dedicate my appreciation to my co-advisor, Dr. Adelino F. Cunha, thanks to his valuable advices on the scientific research and kind help that I was able to learn all laboratory instruments, start experimental tests and become productive within a short period of time.

I also wish to thank all the LSRE group members for their great helps throughout my PhD study period. I would like to express my appreciation to Departamento de Engenharia Qu ́mica, Faculdade de Engenharia, Universidade do Porto, for all supports and facilities that have been given. In addition, I want to express my great appreciation to Prof. Jian-Guo Yu and Prof. Ping Li from the East China University of Science & Technology for their longtime assistances since I was a postgraduate student in China.

I want to thank all my family members, especially my wife Qian Zhang, whose love and encouragements help me through all the difficulties during these years.

Finally, I would like to acknowledge the doctoral grant from China Scholarship Council, number 2010674011. This research is co-financed by QREN, ON2 and FEDER, project NORTE-07-0124-FEDER-6 0000007.

Table of Contents

List of Tables

List of Figures

1. Introduction

1.1 Energy Demand and Environmental Impacts

Along with the development of economy, the demand for energy has increased dramatically. International Energy Outlook (IEO) analysis in 2013 [1] indicates a continuous world energy demand growth during the first half of this century, as shown in Figure 1-1. The world energy consumption is expected to expand from 553 quadrillion kJ in 2010 to 664 quadrillion kJ in 2020 and then to 865 quadrillion kJ in 2040 (an increase of 56% within three decades). Additionally, a large proportion of energy consumption grows up in developing countries outside the Organization for Economic Cooperation and Development (OECD), where the energy demands are driven by a robust long-term economic growth [2].

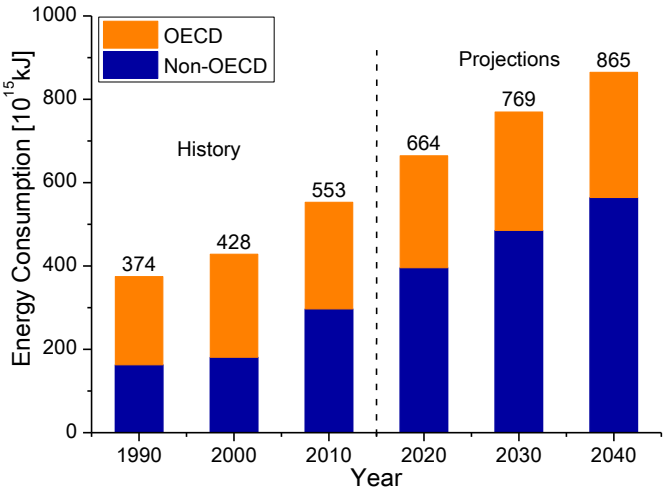

Figure 1-1 World energy consumption [1].

Nowadays, over 80 % of the energy consumption relies on fossil fuels such as oil, natural gas and coal, as depicted in Figure 1-2. According to the IEO [1], these nonrenewable energy sources will dominate the energy system in the first half of the 21st century. However, the use of fossil fuels for energy production leads to numerous environmental impacts. The release of greenhouse gases such as carbon dioxide and methane becomes the main concern for global warming up, while the emission of nitrogen oxides and sulfur-oxygen species contributes to acid rain. Consequently, finding alternative ways to meet the energy demands and solving the ecological

impacts at the same time is a major challenge for researchers nowadays. Recently, the "hydrogen economy" [3], which is considered as a promising solution has attracted worldwide interest.

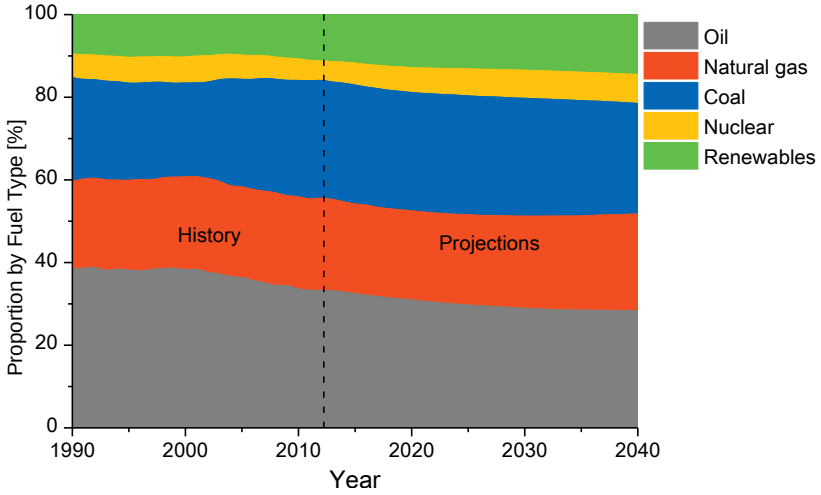

Figure 1-2 World energy consumption by forms of fuel [1].

1.2 Hydrogen Economy

The "hydrogen economy", which was proposed by Lawrence W. Jones in 1970 [4], is a system where hydrogen is used as universal energy carrier instead of using fossil fuels for the current hydrocarbon economy. As a clean energy carrier, hydrogen can offer many advantages for a sustainable future development. Hydrogen, as an universal fuel [5], can be produced from a wide range of feedstocks [6] including natural gas, heavy oil, light oil and coal. Supply infrastructures can be developed according to the feedstocks available in local regions [3]. Hydrogen can also be produced from renewable fuels or biomass, such as bio-ethanol. The contribution to net-zero carbon dioxide emissions [7] and long term a sustainable production [3] are the major advantages. In addition, the use of hydrogen is environmentally friendly, because little or no polluting emissions can be generated from the combustion of hydrogen. Hydrogen is especially applicable as fuel for fuel cells, which have higher energy utilization efficiencies than conventional combustion engines [8].

A variety of hydrogen production technologies are available and can be classified

into the following categories:

- Thermochemical, including coal gasification [9], hydrocarbons reforming [10], catalytic cracking [11], etc.;
- Electrochemical, including water electrolysis [12], water vapor electrolysis [13], chlor-alkali process [14], etc.;
- Photochemical [15] or photocatalytic [16] water cleavage;
- Biological technology, including photobiological production [17], organic fermentation [18], etc.

The thermochemical method [10] includes the catalytic steam reforming, partial oxidation and auto-thermal reforming of a variety of gaseous and liquid fuels such as hydrocarbons, methanol, ethanol and carbohydrates. In addition, gasification and pyrolysis processes [19] are used when the feedstocks are solids such as coal, wood and other biomass derivatives. On the other hand, hydrogen production from water by using electricity is a very typical electrochemical method to obtain high purity hydrogen. Other technologies, such as photobiological [20] or photocatalytic [16] methods produce hydrogen from water using the photosynthetic activity of microorganisms or catalysts are still in laboratory research stage.

Current commercial processes for hydrogen production largely (more than 50 % in the world) depend on natural gas as source for hydrogen and the source of energy for the production process. Most of these production processes employ the reforming technology [10, 21, 22]. Depending on the feed composition and type of the reactor employed, at least three different methodologies are employed for the industrial production of hydrogen from methane, steam methane reforming (SMR), partial oxidation (PROX) and auto thermal reforming (ATR)/oxidative steam reforming (OSR) [10, 21-23], as shown in Figure 1-3.

In the SMR process, a mixture of methane and steam reacts over the catalyst bed to produce carbon monoxide and hydrogen, known as the syngas product. The reaction is highly endothermic and requires external heat supply. On the other hand, methane and oxygen are used as reactants in the PROX process. In this process, a part of

methane is first combusted over the catalyst bed to produce carbon dioxide and water, and then subsequently reacts with the remaining methane to produce carbon monoxide and hydrogen [23]. PROX is a highly exothermic process and no external heat supply is required. The ATR process is a combination of SMR and PROX. In this process, a mixture of methane, steam and oxygen is feed into a combustion zone first, where a part of methane is converted to generate a mixture of carbon monoxide and water. At the same time, the heat generated in the combustion zone can be used for the endothermic catalytic steam reforming reaction to produce hydrogen. In some cases [24], the combustion and the catalyst bed sections are integrated into one section.

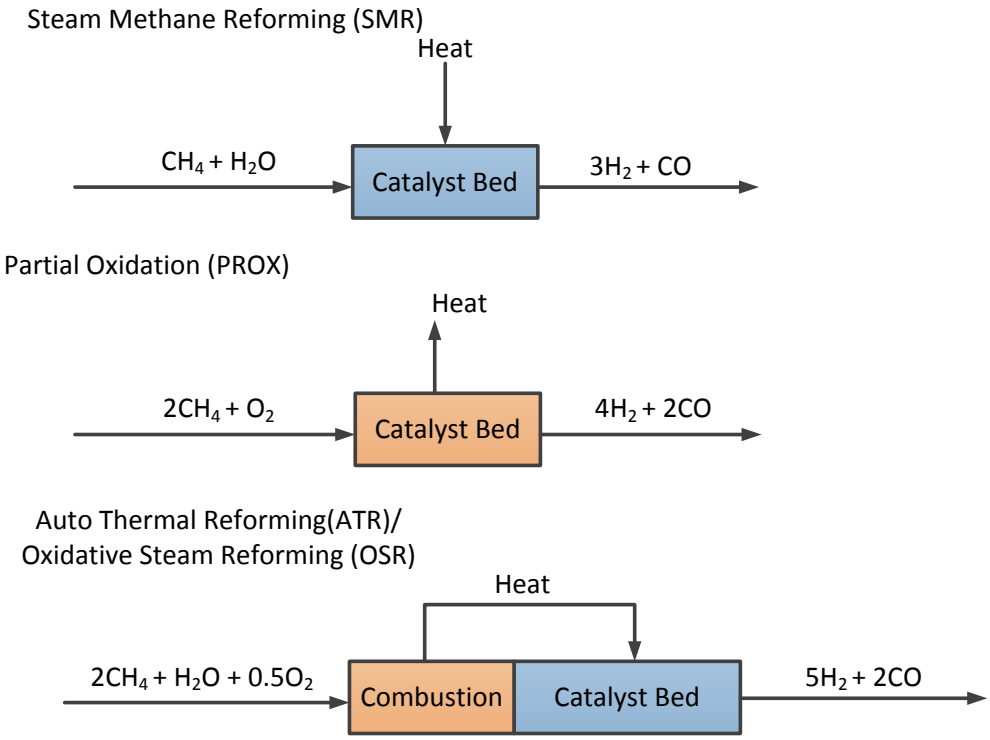

Figure 1-3 Different methodologies for hydrogen production from methane.

However, all these reforming methods produce hydrogen from non-renewable sources, resulting in additional carbon dioxide emissions and fossil fuel depletion. From the viewpoint of sustainable development, the use of methane as the feedstock cannot meet the requirement. Therefore, it is necessary to employ alternative source for hydrogen production which is renewable and eco-friendly.

1.3 Ethanol as Hydrogen Source

Ethanol is regarded as one possible solution to minimize global climatic changes as well as energy security [25]. Most ethanol is currently produced by fermentation of sugars derived from various biomass resources such as corn, sugarcane, lignocellulose, etc. However, ethanol produced from grains such as corn may lead to increasing food prices, due to the limited arable land for agriculture production [26].

On the other hand, lignocellulose is the most abundant biomass in the world which consists of three major components: cellulose (38-50 %), hemicellulose (23-32 %) and lignin (15-30 %) [27]. The use of lignocellulose as ethanol source can not only increase the availability of feedstock for ethanol production, but also considerably reduce the land need and environmental concern, which has been considered as a potential source for low-cost ethanol production [28]. As a result, there is an increasing interest in producing ethanol from lignocellulose [29].

However, the crude ethanol obtained from the fermentation process needs to be distilled before used as ethanol fuel. A large amount of energy is required for the distillation towers to produce water-free ethanol, while most of the power source comes from fossil-derived fuels. It is an energy intensive process which may contribute more than half of the total production costs of ethanol fuel [30]. According to the estimations of the U.S. Department of Agriculture [31], the ratio of energy output to energy input in the corn-based ethanol production is no more than 1.34, which means the overall energy efficiency of the production process is only around 25 %. However, the cost intensive distillation process can be avoided if the crude bio-ethanol is directly converted into hydrogen by catalytic reforming.

The use of ethanol-derived hydrogen for power generation through fuel cells suggests that the overall process completes in a closed carbon cycle, avoiding net carbon dioxide emission into the atmosphere [32], as shown in Figure 1-4.

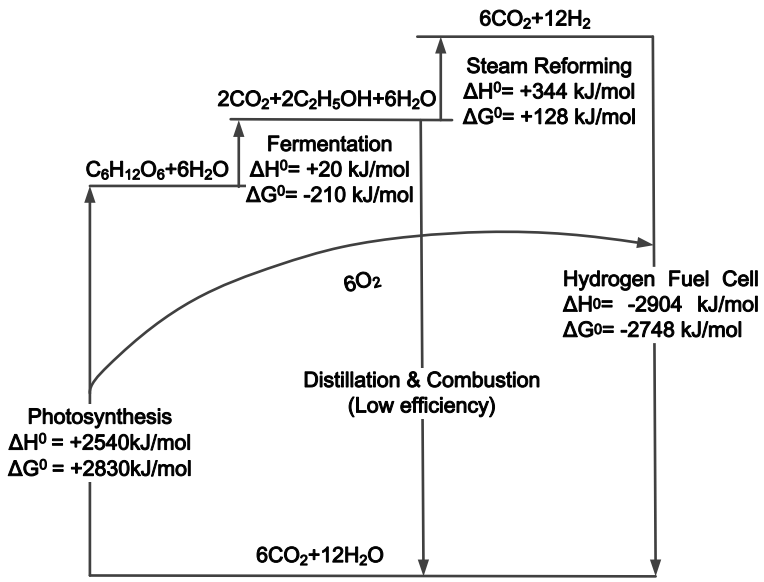

Figure 1-4 Carbon cycle for energy production based on bio-ethanol reforming, modified from Deluga et al. [32].

First, fermentable sugars (glucose, as an example) can be produced by hydrolysis of the lignocellulose material [27, 33], which is formed from photosynthesis of carbon dioxide and water, 6 moles of oxygen will be released during this process. Then, the fermentation process converts the sugar into 2 moles of ethanol and 2 moles of carbon dioxide using a small amount of energy. Steam reforming of these 2 moles of ethanol with 6 moles of water produces 12 moles of hydrogen and 4 additional moles of carbon dioxide.

The hydrogen produced can be employed in a proton exchange membrane fuel cell (PEMFC) to generate electricity, which has very high energy efficiency [34]. It is estimated that the overall energy efficiency can reach 50 % [32], which is much higher than using ethanol as fuel for combustion engines. Besides, the hydrogen produced can also be used for ammonia synthesis, methanol synthesis, petroleum refining and other hydrogenation processes.

As a result, research efforts on hydrogen production from ethanol have increased dramatically in recent years [35-42].

1.4 Steam Reforming of Ethanol

In principle, the reforming methodologies available for hydrogen production from light hydrocarbon can also be employed for ethanol as feedstock. However, some modifications are required. For instance, the additional combustion zone is not required in ATR of ethanol, since the reaction temperature for ethanol reforming is relatively lower than that required for methane reforming, as illustrated in Figure 1-5.

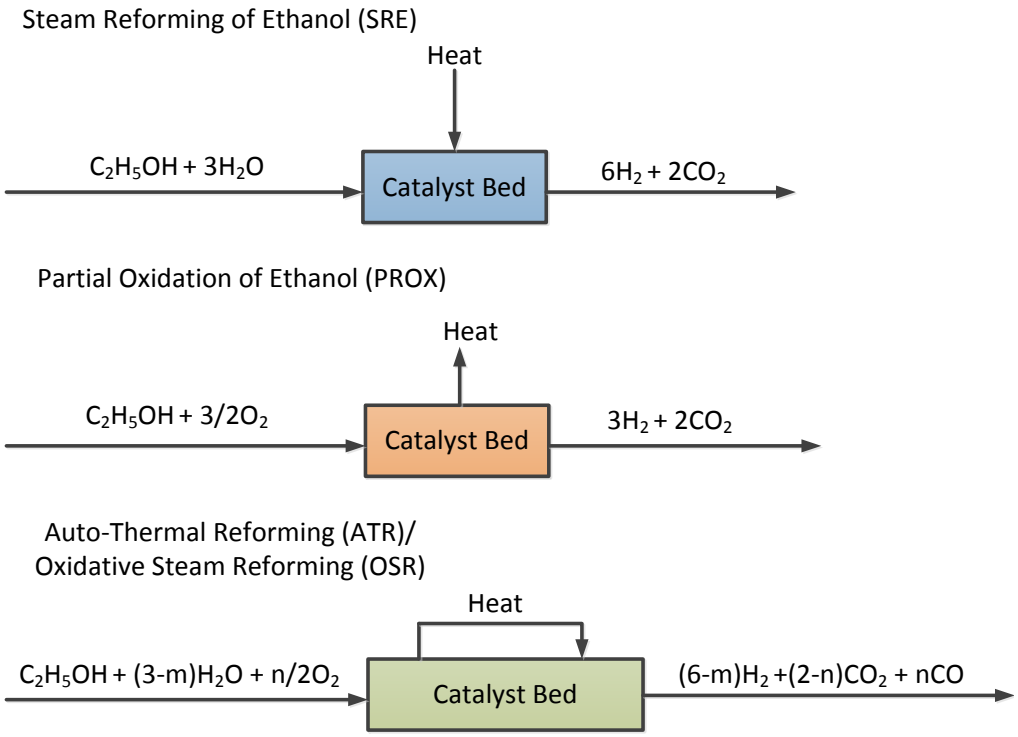

Figure 1-5 Different reforming methodologies for hydrogen based on ethanol as feedstock.

On one hand, PROX process is exothermic and an external heat supply is not required. However, only 3 moles of hydrogen are produced from each mole of ethanol converted in the PROX process. The theoretical amount of hydrogen produced from ethanol via PROX would only be half of that obtained from SRE process. As a result, PROX process is unlikely to be employed for hydrogen production [43].

On the other hand, a mixture of ethanol, steam and air/oxygen with an appropriate ethanol/water/oxygen ratio can be used as feed in the ATR process [32, 44]. The amount of air/oxygen depends on the reaction temperature required to achieve a condition of thermal balance. This process is also known as the oxidative steam

reforming (OSR) process [45-47], sometimes referred as catalytic partial oxidation (CPOX) by Verykios et al. [48] and Salge et al. [49] with a mixture of ethanol, water and oxygen reacting over structured noble metal based catalysts.

The ATR/OSR hydrogen production process from ethanol, as shown in equation (1.1), combines steam reforming and partial oxidation to overcome some obstacles of steam reforming (SR) and partial oxidation reactions (PROX) [32, 45-47].

$$C_2H_5OH(g) + 2.28H_2O(g) + 0.36O_2(g) \rightarrow 5.25H_2(g) + 2CO_2(g) \quad (1.1)$$

The process produces significantly more hydrogen than PROX, theoretically 5 moles of hydrogen will be obtained per mole of ethanol converted, and the process can become thermally neutral by adjusting the ethanol/water/oxygen(air) molar ratios [48], so that external heat supply is not required.

However, the ATR process also has its own drawbacks; an expensive and complex oxygen separation unit is always required in order to feed pure oxygen into the reactor, or using a similar equipment to separate the product gas diluted in nitrogen when air is used in the feed [5]. The highly exothermic reaction may also cause hotspots in the catalyst bed, leading to catalyst sintering and deactivation. Finally, this process produces less amount of hydrogen from each mole of ethanol converted than steam reforming process, making the ATR process less attractive.

Among the three different reforming processes discussed above, theoretically the SRE process can generate the highest hydrogen yield, 6 moles hydrogen can be obtained per mole of ethanol converted, as shown in equation (1.2):

$$C_2H_5OH(g) + 3H_2O(g) \leftrightarrow 6H_2(g) + 2CO_2(g) \quad (1.2)$$

This makes the SRE more attractive in terms of power generation via hydrogen fuel cells. It is estimated that around 12828 kJ net energy output can be obtained from 1 liter of ethanol via SRE, which is about 3 times higher than the energy output obtained when ethanol is used as a fuel for the internal combustion engine [50]. It is now clear that SRE is the preferred process in terms of hydrogen production. However, it is a highly endothermic process and an external heat supply is required.

The SRE process involves several reactions over the catalytic system, which is

highly endothermic and usually performed at relatively high temperatures in the range from 573 to 1073 K.

Most of the experimental investigations were performed with a stoichiometric steam-to-ethanol molar ratio ($R_{S/E}$) of 3 in the feed. However, higher $R_{S/E}$, even up to 20 can also be used [51], due to the fact that crude ethanol which contains 14 vol. % of ethanol has this molar ratio. It is worth to note that, higher $R_{S/E}$ in the feed can suppress the formation of carbon monoxide and carbon deposition, which are poisons for fuel cells and SRE catalysts, respectively. Besides, bio-ethanol is a slightly brown liquid mainly consist of ethanol and water with residual amounts of *n*-propanol (~ 0.4 vol. %), methanol (~ 1 vol. %), acetaldehyde (~ 0.4 vol. %), acetone (< 0.1 vol. %), etc. [52]. The impact of impurities from bio-ethanol on hydrogen production performance from SRE has been investigated by Le Valant et al. [53] with a $R_{S/E}$ = 4. They found that the addition of acetaldehyde and methanol can improve the hydrogen production without changing the product selectivity, while butanol, ethylether and ethyl acetate compounds have a strong deactivation effect [54]. In order to suppress the coke formation, the acidic sites of the support, which is responsible for olefin formation at the origin of coke production, can be decreased by addition of rare earth elements [55]. On the other hand, thermodynamic analyses have shown that the carbon deposition can be eliminated with a $R_{S/E}$ higher than 4 [56].

SRE is an endothermic reaction that means higher temperatures favor hydrogen yielding. However, the equilibrium limitation of the WGS reaction inhibits the production of high purity hydrogen (absence of carbon monoxide). Therefore, the hydrogen-rich product must be purified by cost intensive separation units before used in fuel cells [5], making the process economically unattractive. To overcome these drawbacks, sorption enhanced reaction process can be used as a promising solution.

1.5 Sorption-Enhanced Reaction Process

Most of the chemical reactions are limited by equilibrium between reactants and products. As a result, it is necessary to introduce separation processes to separate the

equilibrium mixtures and to recycle the unconverted reactants. The number of the separation steps is mainly dependent on the number of products produced, number of the solvents used and reactants that have not been converted. The more separation steps used, the more operation procedures and energy input are required.

In order to reduce the costs of separation processes, the integration of reaction unit(s) and separation unit(s) into one [57] is derived. In this integrated unit, the product compound(s) is continuously being separated from the reaction zone. The major characteristic of an integrated reaction and separation unit is the existence of at least two phases, a reaction phase and a transport phase [58]. In the case of hydrogen production via steam reforming, a selective solid adsorbent is used to adsorb carbon dioxide from the product gas phase, this integrated process is commonly referred as sorption-enhanced reaction process (SERP) [59].

The concept of SERP [60] is based on Le Chatelier's principle: when one of the products is removed, the equilibrium can be shifted towards the formation of more products. Therefore, if the carbon dioxide can be selectively removed from the product gas phase by an appropriated solid sorbent, the normal equilibrium limit of equation (1.2) can be displaced and a complete conversion can be closely approached [61]. According to Mayorga et al. [62], SERP has several potential advantages including:

- Replacement of high-temperatures (973-1273 K) required in the reforming reactor;
- Simplification of the hydrogen purification section due to higher hydrogen purity and lower concentrations of CO_x compositions;
- Suppression of carbon deposition in the reactor;
- Lower investment costs due to a reduced number of operating units.

To date, extensive research has been done on the SERP of hydrogen production from methane, but only few studies have been done on the sorption-enhanced steam reforming of ethanol (SE-SRE). Therefore, some part of the knowledge gained and concepts used in the sorption-enhanced steam methane reforming (SE-SMR) process

are useful for hydrogen production from ethanol. SE-SMR process has been investigated experimentally and theoretically. SE-SMR simulations and optimization were first reported at LSRE by Xiu et al [63-65]. Subsequently, the SMR kinetics of the nickel-based catalysts [66, 67] and the adsorption performance of modified carbon dioxide sorbents [68] were studied, and used to investigate SE-SMR for hydrogen production by Oliveira [69].

In previous studies, a hybrid system containing a steam reforming catalyst and carbon dioxide adsorbent mixture was developed. One typical example of this hybrid system used for SE-SRE can be found in Figure 1-6.

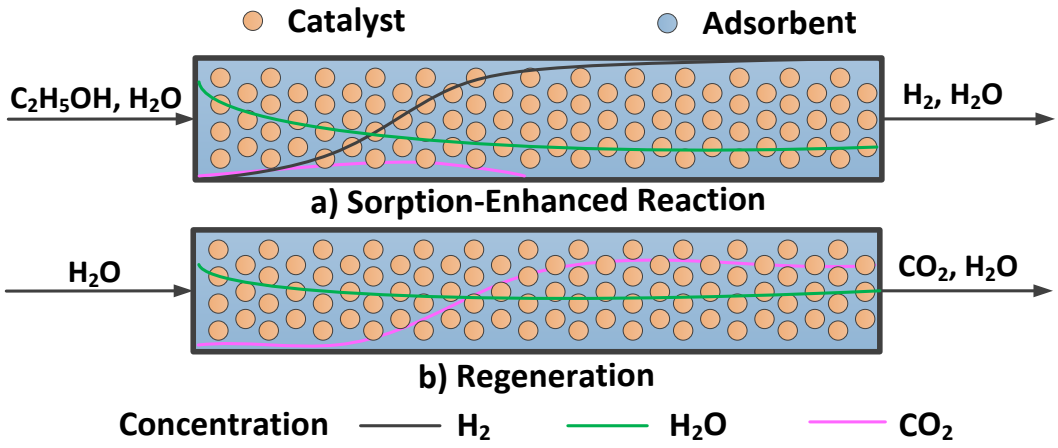

Figure 1-6 The hybrid system for sorption-enhanced steam reforming of ethanol.

On the upward side of Figure 1-6, SERP is carried out where the catalyst and the sorbent are arranged in a random mixing pattern system. Theoretically, only hydrogen and excess steam will be obtained from the outgoing stream before the carbon dioxide adsorbent is saturated. Note that SERP requires the periodical regeneration of the sorbent when it is saturated with carbon dioxide, as shown in Figure 1-6. The most common regeneration techniques are pressure swing, purge, temperature swing and the hybrid methods [59].

Temperature swing regeneration is carried out by increasing the temperature of the sorbent material, consequently decreasing the sorption capacity of the material and releasing the adsorbed carbon dioxide. The main drawback of this technology is an extended period of time required to cool down the sorbent. On the other hand,

pressure swing desorption can be carried out by decreasing the partial pressure of carbon dioxide in the gas phase, which can be completed in a few minutes.

The concept of SERP is not new, according to Harrison [59], the first report of SMR in the presence of a calcium-based sorbent was published in 1868 [70]. Up to date, most of the SERP researches have focused on the use of methane (natural gas) as feedstock, known as sorption-enhanced steam methane reforming (SE-SMR) [59, 71-75], sorption-enhanced water-gas-shift (SE-WGS) [76] process with carbon monoxide as feedstock and sorption-enhanced steam glycerol reforming [77-80]. In addition, several projects such as ZEG Power (Zero Emission Gas Power) [81] in Norway and SE-WGS process by Energy Research Centre of the Netherlands have reached pilot stages.

1.5.1 Sorption-Enhanced Steam Methane Reforming

There are already many publications available on SE-SMR process that can be found from some recent reviews [59, 71-75, 82]. Primary efforts were devoted to the development of high temperature carbon dioxide sorbents and multi-cycle operation performance of the catalyst-sorbent materials. Calcium-based sorbents and potassium promoted hydrotalcite (K-HTlc) sorbents have received more attention than lithium-based sorbents due to the relatively low adsorption rate and high cost of lithium-based materials [83], even though they are found to have excellent multi-cycle stability.

Calcium-based sorbents are employed in most of the SE-SMR studies. Johnsen et al. [84] carried out the experimental study with dolomite as the carbon dioxide sorbent in a bubbling fluidized-bed reactor. The operating temperature and pressure are 873 K and 1 atm, respectively. The product gas with a hydrogen concentration over 98 mol % could be obtained. Wu et al. [85] performed a SE-SMR process using calcium hydroxide as the carbon dioxide adsorbent. A 94 mol % hydrogen-rich gas was achieved, which is approximately equal to 96 % of the theoretical equilibrium limit, and much higher than the equilibrium concentration of 67.5 mol % without carbon

dioxide sorption under the same conditions at 773 K, 0.2 MPa pressure and a $R_{S/C}$ of 6. In addition, the residual mole fraction of carbon dioxide was less than 0.001. Chanburanasiri et al. [86] performed SE-SMR tests using Ni/CaO multifunctional material with a nickel metal content of 12.5 wt. % as the catalyst and carbon dioxide sorbent, a high hydrogen concentration (80 mol %) was obtained at atmospheric pressure with a $R_{S/C}$ of 3 and 873 K. In addition, Broda et al. [87] performed SE-SMR with Ni-Htlc derived catalyst and two different CaO-based sorbents, Ca-based pellets and Rheinkalk limestone. They found that high-purity hydrogen (99 %) can be obtained at 823 K and $R_{S/C}$ = 4, and the pellets showed better performance during the cyclic operation due to the stable nanostructured morphology.

On the other hand, Oliveira et al. [69] conducted sorption-enhanced experiments using a potassium promoted hydrotalcite as the carbon dioxide sorbent. It was found that during cyclic SE-SMR experiments, methane conversion and hydrogen purity was 43 % and 25 %, receptively, which is better than for a normal SMR reactor. Additionally, a mathematical model for this process was proposed and tested. It was found that this model was able to describe the SE-SMR experiments without any fitting parameters.

However, the performance of the SE-SMR process can be affected by several operating parameters, design parameters as well as physical and chemical parameters, while effects of these parameters are always coupled. As a result, it would be almost impossible to achieve the ideal conditions of SE-SMR process just by experimental tests alone. Modeling and simulation can significantly improve the performance of SE-SMR systems.

Different operating conditions were tested by Xiu et al. [63-65] to achieve high hydrogen purities and low carbon monoxide concentrations in the effluent stream from SE-SMR. The simulations performed by Xiu et al [63] show that a hydrogen purity of 86.8 mol % together with 587 ppm of carbon dioxide and 50 ppm carbon monoxide can be achieved. Xiu et al. [88] also applied a subsection-controlling strategy to design the SE-SMR reactor. The product gas had a concentration of

hydrogen over 85 mol %, together with a carbon monoxide concentration below 30 ppm and a carbon dioxide concentration below 300 ppm.

Ochoa-Fernandez et al. [89] studied SE-SMR with lithium zirconate as sorbent. A kinetic equation for the sorbent material, with carbon dioxide partial pressure and temperature as parameters, has been developed. Afterwards, the hydrogen production process by SE-SMR was simulated in a fixed-bed reactor, where a Ni catalyst derived from a hydrotalcite-like precursor has been employed as the steam reforming catalyst. Simulation results show that the product gas with a hydrogen purity more than 95 mol %, and the concentration of carbon monoxide less than 0.2 mol % can be produced in a single step.

Lee et al. [90, 91] simulated two different SE-SMR systems with in a fixed-bed reactor and in a moving-bed reactor, respectively. In the moving-bed reactor, the nickel-based reforming catalyst and calcium oxide based carbon dioxide sorbent pellets are moved simultaneously with gaseous reactants. Effects of operating parameters such as the temperature, pressure and $R_{S/C}$ on SE-SMR systems have been investigated. In the fixed-bed reactor, at 923 K, a $R_{S/C}$ 7 in the feed and a pressure higher than 100 bar, a product gas with less than 50 ppm of carbon monoxide can be obtained during the pre-breakthrough stage. In the moving-bed reactor, by using the optimal feed rates of 1.0 $kg \cdot h^{-1}$ of calcium oxide and 22.4 $NL \cdot h^{-1}$ of methane at 973 K with a $R_{S/C}$ of 3, the purity of hydrogen can reach 94.0 mol % with 2.5 mol % of carbon monoxide in the gas phase.

1.5.2 Sorption-Enhanced Steam Reforming of Ethanol

To date, most of the SERP researches are focused on the use of methane (natural gas) as feedstock, while only a small number of experimental studies have been carried out on sorption-enhanced steam reforming of ethanol (SE-SRE).

Among these studies, calcium oxide-based materials have been widely used as the carbon dioxide sorbents. Lysikov et al. [92] compared different feedstocks for hydrogen production via SERP over a mixture of a commercial nickel-based catalyst

and calcium oxide sorbent. It was found that ethanol exhibits the best performance among all the feedstocks studied, a 98 vol. % purity of hydrogen-rich gas, with impurities of carbon monoxide and carbon dioxide less than 20 ppm, was obtained. With ethanol as feedstock, He et al. [61] carried out SERP over a mixture of Co−Ni catalyst derived from hydrotalcite-like compounds (HTlc) and calcined dolomite as carbon dioxide sorbent. A good performance was observed at 823 K and the product gas contains 99 mol % hydrogen with only 0.1 mol % of carbon monoxide. Besides, a study on SE-SRE with Ni- and Co-incorporated MCM-41 catalysts, with calcium oxide as carbon dioxide sorbent, has been performed by Gunduz and Dogu [93], where the yield of hydrogen can reach 94 % (dry basis) at 873 K with a $R_{S/E}$ of 3.2 in the feed.

On the other hand, other high temperature carbon dioxide sorbents such as lithium-based materials and HTlc materials can also be used. Iwasaki et al. [94] performed SE-SRE reaction with lithium silicate as carbon dioxide sorbent over 1 wt. % Rh/CeO_2 catalyst. A product gas with hydrogen purity 96 mol % was obtained at 823 K, atmospheric pressure and steam-to-ethanol molar ratio of 3 in the feed. In addition, Essaki et al. [95] reported that the concentration of hydrogen can reach 99 mol % along with carbon monoxide below 0.12 mol % by SE-SRE over a commercial nickel-based catalyst, with lithium silicate as sorbent at similar conditions. Besides, a commercial nickel-based catalyst with an HTlc sorbent was employed by Cunha et al. [96] as a hybrid system in a multilayered pattern arrangement. The results of SE-SRE at 673 K with a $R_{S/E}$ of 10 in the feed showed that pure hydrogen was produced in the first 10 min of reaction.

Finally, hybrid materials [97, 98] with Cu or Ni as the active metal phase and HTlc sorbent as the support have also been employed for SE-SRE. These materials were found to have good catalytic performance to produce hydrogen from SE-SRE due to their relatively high surface areas and small crystal sizes.

1.6 Materials for Sorption-Enhanced Steam Reforming of Ethanol

As demonstrated in recent reviews [35-42], hydrogen production from ethanol has been extensively studied over the past two decades. Many efforts have been devoted to the development of catalysts for SRE process. On the other hand, a successful SE-SRE process requires promising high temperature carbon dioxide sorbents; these materials have also been extensively investigated in recent years.

1.6.1 Catalysts for Steam Reforming of Ethanol

The performance of catalytic materials depends on several factors such as the role of the active phases and supports on the reaction network, the precursors used, the method adopted for catalyst preparation as well as the presence of promoters.

Various catalytic systems such as single active metal, mixed active metals with single oxide support, mixed oxide supports and other novel support materials such as activated carbon have been used [39, 40, 42, 99]. According to the type of the active metals employed in these studies, catalytic systems can be generally classified into three categories:

- Supported noble metal based catalysts;
- Supported non-noble metal based catalysts;
- Bi-metallic/alloy catalysts.

The supported noble metal catalysts using Rh, Ru, Pd, Pt, Re, Au and Ir as active phase [99-107] have been extensively investigated for SRE; these catalysts are recognized as very active within a wide range of temperatures (623 ~ 1073 K) and space velocities (5000 ~ 300000 h^{-1}). The excellent catalytic performance of noble metal catalysts might be related with their excellent capability in C-C and C-O bond cleavage [99, 108].

Among these noble metals, Rh is found to be the most active metal for ethanol conversion and hydrogen production [103, 104]. The best performance of Rh-based catalysts is reported by Diagne et al. [105], up to 5.7 mol hydrogen can be produced per mol of ethanol at 723 K over a CeO_2–ZrO_2 supported Rh catalyst, which is equal

to 95 % of theoretical hydrogen yield. The density functional theory calculation and electronic structure analysis have been performed to investigate the reforming mechanism for SRE over different metal surfaces [53, 109]. Wang et al. [53] found that Rh- and Ir-based catalysts have excellent conversion efficiencies due to the lower decomposition barriers and the superior redox capabilities than other catalyst systems. However, even the metal loadings of the noble metal-based catalysts are relatively low (0.5 - 5 wt. %) compared with non-noble metal samples (typically 10 - 25 wt. %), but the extremely high unit price limits their large scale industrial application.

Due to severe mass and heat transfer limitations, conventional steam reformers are limited to an effectiveness factor for the catalyst which is typically less than 5 % [110]. It was found that the activity of catalysts is rarely the limiting factor [111]. As a result, increasing research efforts have been focused on the development of non-noble metal based catalysts. According to the publications up to date, the efforts mainly focuses on Co, Cu and Ni-based catalyst systems [39, 40, 42, 106]. As typical transition metals, the active outer layer electrons and associated valence states make it possible for these metals to be candidates for SRE. In addition, some of these catalysts have already been employed in an industrial scale steam reforming of methane [10].

Llorca et al. [112-114] studied Co-based catalysts with different supports (γ-Al_2O_3, SiO_2, TiO_2, V_2O_5, ZnO, Sm_2O_3, and CeO_2). Good activity and selectivity was found, nearly 5 mol of hydrogen can be produced per mol of ethanol converted over the Co/ZnO sample [112]. Besides, it was also proved that the cobalt phase is very efficient in C-C bond cleavage even at temperatures as low as 673 K [114]. However, it was found that Co-based catalysts can easily be deactivated within a short period during SRE [115]. It is generally believed that the deactivation can be attributed to cobalt oxidation as well as coke formation [40, 116]. In addition, temperature programmed desorption and reaction experiments have been performed by Benito et al. [117] to determine the intermediate species in the reaction mechanism for SRE over a catalyst based on La-promoted Co/ZnO. Moreover, it was found that the adsorbed ethanol is dehydrogenated to acetaldehyde producing hydrogen in the first

step. Then, the adsorbed acetaldehyde is converted into acetone by acetic acid formation. At last, acetone can be reformed to produce hydrogen and carbon dioxide.

Copper-based catalysts are frequently studied systems in the methanol synthesis and steam reforming of methanol due to the good selectivity and activity [118-120]. Steam reforming of ethanol on $CuO/ZnO/Al_2O_3$ catalyst was first investigated by Cavallaro and Freni [121]. It was found that copper is very effective for dehydrogenation of ethanol at 623 K due to its ability to maintain the C-C bond [121, 122].

However, the C–C bond cleavage for hydrogen production using ethanol instead of methanol requires much higher reforming temperatures. It was found that Cu-based catalysts always undergo a relative fast deactivation due to the aggregation of copper on the surface of the support materials at high temperatures [123]. As a result, only few studies can be found in literature where copper-based catalysts are used for SRE process [121, 124-129].

Additionally, in most cases Cu-based catalysts employed for SRE are combined with other active metals such as Ni, Fe and Co [123, 124, 126-130] or arranged as two-step process with other catalysts [39, 131] to improve the SRE performance and stability. Besides, many catalyst systems with two or more combined active metals such as Co, Ni, Fe, Zn, Cu, Pt and Cr can also be found in literature [132-137]. These catalysts can be referred as bi-metallic or alloy metal catalysts.

On the other hand, Ni-based catalysts have been most extensively investigated among all transition active metals for SRE. The relatively high C-C bond breaking activity and the low cost production make the nickel-based catalysts suitable for reforming reactions [101, 106, 107]. However, at high temperatures nickel-based catalysts can easily lose activity due to sintering and especially coke formation [36, 106, 138, 139].

At low temperatures, ethylene can be produced from ethanol dehydration reaction, and carbon may be formed by ethylene polymerization. At higher temperatures, reverse carbon gasification and hydrocarbon decomposition reactions are the main

possible sources of carbon deposition. Thermodynamic considerations indicate that carbon deposition at higher temperatures (> 473 K) can be eliminated by a high $R_{S/E}$ [140]. The acid/base property of the catalyst support is also an important effect [139, 141, 142], since suppressing surface acidity can reduce ethylene formation and hinder carbon deposition. It is worth to note that adding elements to neutralize acid sites can be a very attractive method. Alkali or earth alkali metals (e.g., Na, K and Mg) [142-146], and other rare earth elements (e.g., Sc, Y, La, Er, and Gd) [147-150] have been tested in previous studies and proved to be effective.

Metal particles should also be stabilized against sintering at higher temperatures to maintain the catalytic activity, e.g. by alloying nickel particle with a less active metal [151] or increase the oxygen storage capacity of the catalyst [152]. It was found by Vizca ́no et al. [151] that the presence of Cu eliminates the large ensembles of Ni atoms. On the other hand, oxide supports that exhibit an appropriate interaction with the active phase to preserve a small metal particle size and good dispersion [146, 148, 153] without decreasing the reducibility [154] should also be considered.

As a result, the metal loading, the support material, the preparation method, the promoter and alloying metal for nickel-based catalytic systems should be considered.

1.6.2 High Temperature Carbon Dioxide Sorbent Overview

The selection of an appropriate carbon dioxide sorbent for a SE-SRE process is not straightforward and several requirements have to be fulfilled. According to Yong et al. [155], the desired sorbent must have: (1) high selectivity and sorption capacity for carbon dioxide at high temperatures; (2) high adsorption/regeneration reaction rates for carbon dioxide at operating conditions; (3) stable adsorption capacity of carbon dioxide after repeated adsorption/regeneration cycles; (4) adequate mechanical strength of adsorbent particles after repeated adsorption/regeneration cycles. Finally, SE-SRE requires regeneration of the adsorbent after saturation with carbon dioxide. Regeneration can be carried out by temperature swing and/or pressure swing depending on the nature of the sorbent and energy efficiency.

According to the sorption temperatures, carbon dioxide sorbents can be classified into three groups: low- (< 473 K), intermediate- (473 - 673 K) and high-temperature (> 673 K) sorbents [156]. Low-temperature carbon dioxide sorbents include materials based on activated carbons, zeolites and alumina known as physisorbents. These physisorbents are sensitive to temperature changes and have relatively low carbon dioxide selectivity due to the weak physical adsorption force [157]. In order to carry out carbon dioxide adsorption processes at intermediate- and high-temperatures, chemisorbents must be used [155, 156, 158, 159]. Chemisorbents have a much higher selectivity towards carbon dioxide and relatively higher adsorption capacities compared with physisorbents [156]. Clearly, the physisorbents cannot be used for carbon dioxide sorption under operation conditions employed for SE-SRE due to the limitations discussed above, while chemisorbents, which can provide a reasonable sorption capacity and selectivity at intermediate- and high-temperatures, become ideal candidates for carbon dioxide adsorption in SE-SRE process.

Metal oxide based sorbents such as calcium oxide and alkali ceramic based sorbents such as lithium zirconate are widely used as high-temperature chemisorbents [156, 160, 161].

Due to a high sorption capacity at high temperatures, calcium oxide has been widely used for the selective adsorption of carbon dioxide in SE-SMR [162-165] and SE-SRE [61, 93] processes. The use of calcium oxide is environmental friendly and economically attractive since calcium-based materials such as limestone and dolomite are abundant and low cost [166, 167]. Calcium oxide adsorbs carbon dioxide at high temperature (~ 873 K) by the carbonation reaction:

$$CaO(s) + CO_2(g) \rightarrow CaCO_3(s) \qquad (\Delta H^0_{873K} = -171.3 kJ \cdot mol^{-1}) \quad (1.3)$$

Regeneration will take place due to the reverse carbonation reaction at elevated temperatures (> 1073 K), releasing the adsorbed carbon dioxide and regenerating the calcium-based sorbent materials.

Reaction (1.3) proceeds by a rapid surface reaction-controlled step, followed by a second stage of product layer diffusion-controlled process [168-170]. The first step

involves a rapid reaction between carbon dioxide with calcium oxide at surface. In the second step, the reaction slows down due to the formation of a layer of calcium carbonate around the adsorbent, the mass transfer resistance increases for the diffusion of carbon dioxide to reach internal calcium oxide for further carbonation [170]. The low adsorption rate in the latter step has a very limited effect on the enhancement of hydrogen production. Therefore, the initial fast step is considered to be critical in determining the reactor size, conversion and hydrogen purity [171].

The loss of sorption capacity for calcium oxide-based sorbents is a typical phenomenon during cyclic operation. Abanades et al. [172] found that the conversion of calcium oxide decreased sharply from 70 % in the first cycle to 20 % after 10 cycles when tested in a fluidized-bed. Abanades [173] fitted several series of experimental data to one equation to describe the adsorption capacity evolution of calcium oxide during extended cyclic adsorption/regeneration operations:

$$X_N = f^{N+1} + b \tag{1.4}$$

where X_N is the conversion of calcium oxide within calcium carbonate at the N^{th} cycle, with the constants f = 0.782 and b = 0.174. According to this equation, the adsorption capacity of calcium oxide as function of the number of adsorption /regeneration cycles is shown in Figure 1-7.

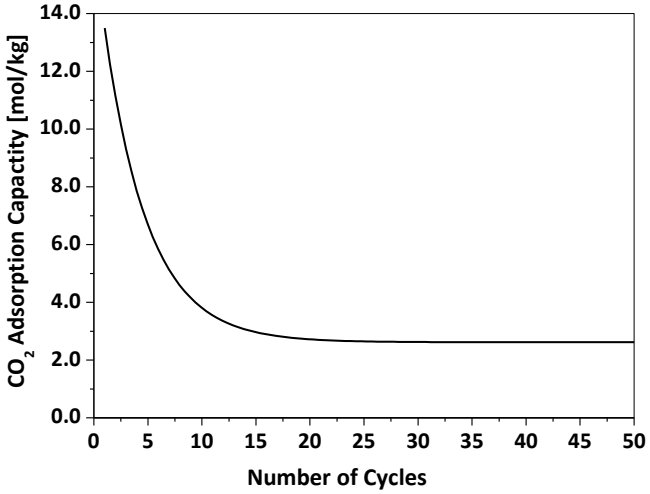

Figure 1-7 CaO adsorption capacities during adsorption/regeneration cycles.

It can be observed from Figure 1-7 that deactivation is a major concern against the

application of calcium oxide-based sorbents for their use in a SE-SRE process. It was found by Wang et al. [174] that steam can be introduced during the adsorption process to prevent the sintering of sorbents and facilitate the diffusion of carbon dioxide within the sorbent. Analysis based on simulation results for SE-SMR showed that calcium oxide must maintain at least 15 % of its thermodynamic capacity in the cyclic operation to avoid large loss in the system efficiency [171]. Another drawback associated with calcium oxide based materials is the high temperatures required for regeneration. A large temperature gap between adsorption and regeneration increases the energy consumption. In addition, high temperature can lead to the deactivation of the catalyst used in SE-SRE.

Lithium-based sorbents are another kind of high temperature selective carbon dioxide uptake material. In 1998, a sorption capacity of 4.54 $mol \cdot kg^{-1}$ for carbon dioxide was first reported by Nakagawa and Ohashi [175] using potassium carbonate promoted lithium zirconate at high temperatures (673-873 K). The reversible chemical adsorption/desorption reaction can be described as:

$$Li_2ZrO_3(s) + CO_2(g) \leftrightarrow Li_2CO_3(s) + ZrO_2(s) \quad (\Delta H^0_{873K} = -81.0 kJ \cdot mol^{-1}) \quad (1.5)$$

It is found that only little carbon dioxide can be adsorbed when using the pure lithium zirconate, and the sorption kinetics are extremely slow, approximately 250 min is required to achieve the maximum adsorption capacity [176]. By doping lithium zirconate with potassium, the sorption rate increases 40 times [175].

A double-shell mechanism for carbon dioxide sorption/desorption on lithium zirconate was proposed by Ida and Y. S. Lin [177]. During the sorption process, carbon dioxide diffuses to the surface of lithium zirconate and reacts with Li^+ and O^{2-} on the surface to form lithium oxide and lithium carbonate nuclei. When lithium oxide nuclei grow to form a shell covering unreacted lithium zirconate, the sorption rate decreases because Li^+ and O^{2-} have to diffuse through the lithium oxide shell to react with carbon dioxide. Worse still, lithium carbonate nuclei form another shell outside of lithium oxide shell. The lithium carbonate shell can also decrease the sorption rate, because carbon dioxide molecules have to diffuse through this shell before reaction. It

is found that the diffusion of carbon dioxide in solid lithium carbonate is the rate limiting step for carbon dioxide adsorption over lithium zirconate materials [177]. The whole adsorption and desorption process is illustrated in Figure 1-8.

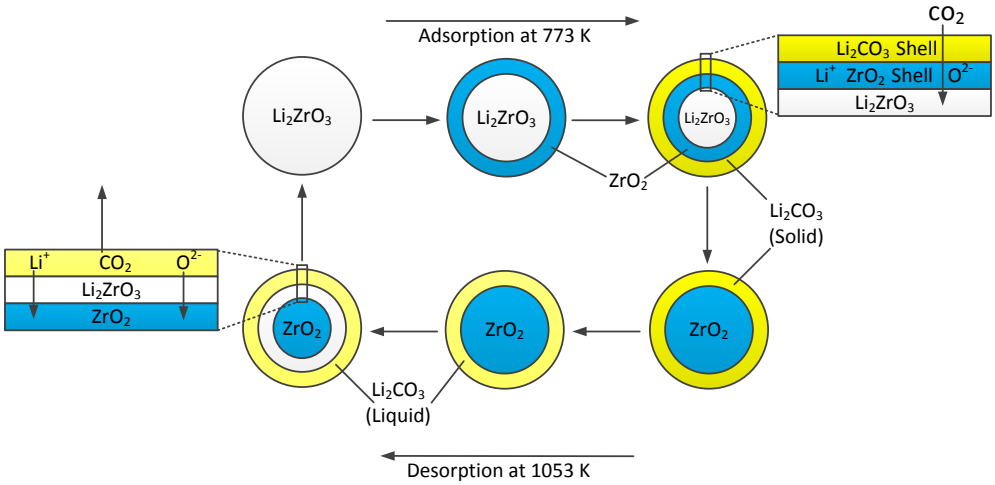

Figure 1-8 Mechanism for carbon dioxide sorption and desorption on lithium zirconate.

Besides lithium zirconate, Kato et al. [83] examined carbon dioxide adsorption performances over several different lithium-based sorbents including $LiFeO_2$, $LiNiO_2$, Li_2TiO_2, Li_2SiO_3 and Li_4SiO_4. Among these materials, lithium silicate was found to have the highest adsorption capacity (6.13 $mol \cdot kg^{-1}$). In addition, the lithium silicate sorbent has a sorption rate 30 times faster than pure lithium zirconate at 773 K, and the costs associated to this material is lower than lithium zirconate sorbent [83]. However, similar double-shell adsorption mechanism has also been found by Zhang et al. [178] for the lithium silicate material and high temperature (~ 973 K) is required for desorption.

These lithium-based materials have great potential due to their excellent carbon dioxide sorption capacity as well as stability after many adsorption/regeneration cycles [179, 180]. However, the main obstacle for the practical application for SERP of lithium-based sorbents is the kinetic limitation [156].

On the other hand, hydrotalcite-like compounds (HTlc) are typical intermediate-temperature chemisorbents, which belong to a large class of anionic and basic clays, also known as layered double hydroxides (LDH). They have been widely used as

catalysts, precursors, ion exchangers and adsorbents [181]. HTlc materials have a general formula $\left[M_{1-x}^{II}M_{x}^{III}\left(OH\right)_2\right]\left[A^{n-}\right]_{x/n}\cdot zH_2O$, where M^{II} and M^{III} are divalent (Mg^{2+}, Mn^{2+}, Fe^{2+}, Co^{2+}, Ni^{2+}, Cu^{2+}, Zn^{2+}, etc.) and trivalent (Al^{3+}, Mn^{3+}, Fe^{3+}, etc.) respectively, A^{n-} is the anion (CO_3^{2-}, Cl^-, SO_4^{2-}, etc.) and x is usually between 0.17-0.33 [182]. Their structure consists of positively charged brucite-like layers with charge compensating anions and water molecules within the interlayer space [183-185].

The most common HTlc is $\left[Mg_{1-x}Al_x\left(OH\right)_2\right]\left[CO_3\right]_{x/2}\cdot zH_2O$ occurring in nature as $\left[Mg_{0.75}Al_{0.25}\left(OH\right)_2\right]\left[CO_3\right]_{0.125}\cdot 0.5H_2O$, the mineral can be also referred as ‘‘hydrotalcite’’ or HT, where the above class of anionic clays is isostructural [186]. Hydrotalcite possess both high surface area and abundant basic sites, as a result, carbon dioxide can be adsorbed in the form of the carbonate ion (CO_3^{2-}) in the interstitial layer [187, 188]. A representation of the structure of a HTlc can be seen in Figure 1-9 [184].

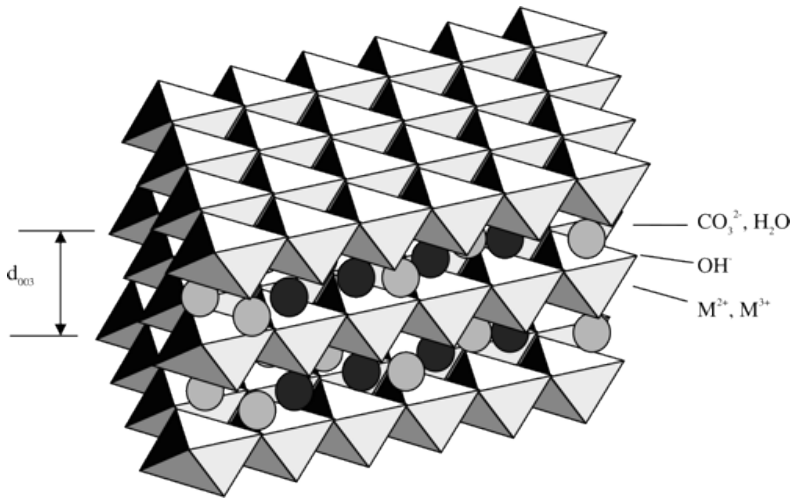

Figure 1-9 Structure diagram of a hydrotalcite sorbent [184].

Upon thermal treatment, the interlayer spacing of the hydrotalcite decreases at around 473 K due to the loss of interlayer water, but the material still remains in its layered structure. Further heating to 673 K causes the decomposition of CO_3^{2-} in the interlayer, and the material is completely dehydrated and partially dehydroxylated.

This kind of material is usually referred as layered double oxides (LDO) [189]. Comparing with HTlc, LDO has an amorphous 3-D structure with higher surface area and pore volume [189]. Samples calcinated at less than 773 K can be transformed back to the original layered structure by contacting with a carbonate solution. The phenomenon is the so-called "memory effect" of HTlcs [186]. However, if a HTlc is heated to temperatures above 773 K, the structure may change irreversibly and a spinel phase is formed [186].

The effect of the type of anion presents in the HTlc was studied by Yong et al. [190] . It was found that the amounts of adsorbed carbon dioxide on HTlc containing CO_3^{2-} are higher than those containing OH^-. Therefore, Mg-Al-CO_3 HTlc is recommended for the adsorption of carbon dioxide. The effect of calcination temperature on the carbon dioxide adsorption capacity of Mg-Al-CO_3 HTlc was investigated by Ram Reddy et al. [191], the sample calcined at 673 K had the highest adsorption capacity, due to the trade-off between the surface area and availability of active basic sites. These basic sites favor reversible carbon dioxide adsorption/desorption in a form as shown in equation (1.6):

$$Mg-O+CO_2 \leftrightarrow Mg-O\cdots CO_2(ads) \qquad (1.6)$$

The interaction between the adsorbed carbon dioxide and the basic sites is stronger than for a zeolite but weaker than alkali metal oxide [156]. As a result, the adsorption (for zeolite < 473 K) and regeneration (for calcium oxide > 973 K) process can be carried out at intermediate-temperatures (473-773 K).

Recently, a lot of studies were published regarding the sorption enhanced hydrogen production processes with HTlc as selective carbon dioxide sorbents [65, 69, 96, 186, 192-195]. It was found that when doped with potassium carbonate, HTlc is able to adsorb carbon dioxide within a temperature range 573-773 K, and the carbon monoxide concentration in the product gas from steam reforming reaction can be restrained to a ppm level [65, 196].

Comparing with SMR process, higher amounts of carbon dioxide will be produced per molar of reactant converted during SRE process. In order to employ an HTlc

material as carbon dioxide sorbent for SE-SRE process, the relative low carbon dioxide adsorption capacity becomes the biggest obstacle. Intense efforts have been devoted to improving the adsorption capacity of this material in recent years [197-200].

As a result, effects of production conditions, operation temperatures and pressures, with or without the presence of steam, regeneration methods, sorbent particle sizes and alkali promoter doping on the carbon dioxide adsorption performance should be investigated to obtain a promising HTlc sorbent material.

1.7 Scope of the Research

The objective of research on SE-SRE is to produce high purity hydrogen via the SERP at intermediate temperatures.

The tasks for SE-SRE process intensification are as follows:

- Testing and characterization of commercially available catalysts on steam reforming of ethanol within the optimization of the operating conditions. Improvement of the performance and comparison with catalysts reported in literature. Finally, developing new catalytic systems.
- The enhancement of hydrogen production in SRE by the use of a suitable carbon dioxide adsorbent, thus shifting the equilibrium reaction to the products side. Breakthrough experiments and the determination of reaction kinetics will allow the development and the validation of mathematical models.
- Development of a cyclic reactive pressure swing operation process for hydrogen production by SE-SRE. This process should be simulated and optimized, and the overall performance should be determined for economic evaluation.

1.7.1 Experimental Focus

The experimental scope can be categorized in the following research topics:

a) Experimental study for the low temperature SRE over different catalytic systems, including catalyst characterization, activity and stability testing as well as the

reaction performance study.

b) Sorption studies in terms of breakthrough tests of the prepared selective carbon dioxide adsorbents and investigating the effect of promoters on the sorption performance.
c) Experimental investigation of the SERP in a fixed bed reactor using an admixture bed consisting of catalyst/sorbent particles or hybrid material (catalyst with sorbent).
d) Regeneration process should be introduced to demonstrate adsorption/desorption cyclic operations and a process for continuous production of hydrogen.

1.7.2 Modeling and Simulation Focus

The systematic research of SERP requires a modeling and simulation section described as follows:

a) Thermodynamic study of the SRE and SE-SRE systems, and find out suitable operating conditions for further studies.
b) Deriving kinetic parameters of different catalytic systems from SRE experiments, and developing a mathematical model to simulate the reaction process.
c) Obtaining carbon dioxide adsorption/desorption kinetic parameters from produced carbon dioxide sorbent, and developing a mathematical model to simulate the adsorption process.
d) Developing a mathematical model for the SERP, improving the whole cyclic operation process and carrying out an economic study.

1.8 Outline of the Thesis

The thesis is organized as follows:

Chapter I is the introduction of thesis. The motivation of the research project, research scope and thesis outline are addressed. In addition, a brief survey on hydrogen production techniques, SRE, SERP, SE-SRE process and the materials involved for SE-SRE is provided.

Chapter II, III and IV combine a series of papers published or to be published. Each section of these chapters can be found as a stand-alone research paper.

In chapter II, a preliminary experimental study on SE-SRE with commercial materials is included. Besides, theoretical researches consist of the thermodynamic analysis of the SE-SRE system with different sorbent materials and kinetics investigation on the commercial nickel-based catalyst for SRE can be found.

Chapter III involves the development of materials for SE-SRE process. Hybrid materials with Cu or Ni as active phase and HTlc as sorbent have been prepared and employed for SRE and SE-SRE studies. Afterwards, potassium-promoted HTlc was developed to improve the carbon dioxide adsorption performance of pure HTlc material. Finally, multi-functional material consisting of K, Cu, Ni and HTlc was prepared for SE-SRE process.

SE-SRE process studies can be found in Chapter IV. In the first section, continuous cyclic SE-SRE operation was performed numerically in a column with two subsections. SE-SRE operation process by four columns with two-dimensional mathematical model has been included as the second section.

Finally Chapter V summarizes the general conclusions of this research project and some suggestions for future work.

Reference

[1] L.E. Doman, *International Energy Outlook 2013*, in, U.S. Energy Information Administration, Washington, 2013.

[2] C.-C. Lee, *Energy Econ.* **2005**, *27 (3)*, 415-427.

[3] L. Barreto, A. Makihira, K. Riahi, *Int. J. Hydrogen Energy.* **2003**, *28 (3)*, 267-284.

[4] L.W. Jones, *Toward a liquid hydrogen fuel economy*, in: Engineering Technical Report, University of Michigan, Michigan, **1970**.

[5] J.D. Holladay, J. Hu, D.L. King, Y. Wang, *Catal. Today.* **2009**, *139 (4)*, 244-260.

[6] A. Züttel, A. Borgschulte, L. Schlapbach, *Hydrogen as a future energy carrier*, Wiley, Darmstadt, Germany, **2011**.

[7] M.L. Murray, E. Hugo Seymour, R. Pimenta, *Int. J. Hydrogen Energy.* **2007**, *32 (15)*, 3223-3229.

[8] L. Carrette, K.A. Friedrich, U. Stimming, *Chemphyschem.* **2000**, *1 (4)*, 162-193.

[9] S. Lin, M. Harada, Y. Suzuki, H. Hatano, *Fuel.* **2002**, *81 (16)*, 2079-2085.

[10] P. Ferreira‐Aparicio, M.J. Benito, J.L. Sanz, *Catal. Rev.: Sci. Eng.* **2005**, *47 (4)*, 491-588.

[11] A.F. Cunha, J.J.M. Órfão, J.L. Figueiredo, *Appl. Catal., A.* **2008**, *348 (1)*, 103-112.

[12] D.L. Stojić, M.P. Marčeta, S.P. Sovilj, Š.S. Miljanić, *J. Power Sources.* **2003**, *118 (1–2)*, 315-319.

[13] W. Doenitz, R. Schmidberger, E. Steinheil, R. Streicher, *Int. J. Hydrogen Energy.* **1980**, *5 (1)*, 55-63.

[14] D. Pletcher, F.C. Walsh, *Industrial electrochemistry*, Springer, New York, **1990**.

[15] K. Sakai, Y. Kizaki, T. Tsubomura, K. Matsumoto, *J. Mol. Catal.* **1993**, *79 (1–3)*, 141-152.

[16] M. Ni, M.K.H. Leung, D.Y.C. Leung, K. Sumathy, *Renewable Sustainable Energy Rev.* **2007**, *11 (3)*, 401-425.

[17] I. Akkerman, M. Janssen, J. Rocha, R.H. Wijffels, *Int. J. Hydrogen Energy.* **2002**, *27 (11–12)*, 1195-1208.

[18] F.R. Hawkes, R. Dinsdale, D.L. Hawkes, I. Hussy, *Int. J. Hydrogen Energy.* **2002**, *27 (11–12)*, 1339-1347.

[19] M. Ni, D.Y.C. Leung, M.K.H. Leung, K. Sumathy, *Fuel Process. Technol.* **2006**, *87 (5)*, 461-472.

[20] H. Sakurai, H. Masukawa, M. Kitashima, K. Inoue, *J. Photochem. Photobiol., C.* **2013**, *1*, 1-25.

[21] J.R. Rostrup-Nielsen, *Catal. Rev.: Sci. Eng.* **2004**, *46 (3)*, 247 - 270.

[22] J.N. Armor, *Appl. Catal., A.* **1999**, *176 (2)*, 159-176.

[23] J.R. Rostrup-Nielsen, *CATTECH.* **2002**, *6 (4)*, 150-159.

[24] I. Dybkjaer, *Fuel Process. Technol.* **1995**, *42 (2–3)*, 85-107.

[25] A.J. Ragauskas, C.K. Williams, B.H. Davison, G. Britovsek, J. Cairney, C.A. Eckert, W.J. Frederick, J.P. Hallett, D.J. Leak, C.L. Liotta, J.R. Mielenz, R. Murphy, R. Templer, T. Tschaplinski, *Science.* **2006**, *311 (5760)*, 484-489.

[26] S.A. Mueller, J.E. Anderson, T.J. Wallington, *Biomass Bioenergy.* **2011**, *35 (5)*, 1623-1632.

[27] R. Sierra, A. Smith, C. Granda, M.T. Holtzapple, *Chemical Engineering Progress.* **2008**, *104 (8)*, 10-18.

[28] Y. Sun, J. Cheng, *Bioresour. Technol.* **2002**, *83 (1)*, 1-11.

[29] M.S. Buckeridge, G.H. Goldman, *Routes to cellulosic ethanol*, Springer, New York, **2011**.

[30] V. Subramani, C. Song, *Advances in catalysis and processes for hydrogen production from ethanol reforming*, in: Catalysis, The Royal Society of Chemistry, **2007**.

[31] H. Shapouri, J.A. Duffield, M.Q. Wang, *The energy balance of corn ethanol: An update*, in, United States Department of Agriculture, **2002**.

[32] G.A. Deluga, J.R. Salge, L.D. Schmidt, X.E. Verykios, *Science.* **2004**, *303 (5660)*, 993-997.

[33] T.V. Choudhary, C.B. Phillips, *Appl. Catal., A.* **2011**, *397 (1–2)*, 1-12.

[34] V.S. Bagotsky, *Fuel cells: problems and solutions*, John Wiley & Sons, Inc.,

Hoboken, New Jersey, **2012**.

[35] H. Song, *Catalytic hydrogen production from bioethanol*, in: M.A.P. Lima, A.P.P. Natalense (Eds.) Bioethanol, INTECH, Online, **2012**.

[36] L.V. Mattos, G. Jacobs, B.H. Davis, F.B. Noronha, *Chem. Rev.* **2012**, *112 (7)*, 4094-4123.

[37] A. Bshish, Z. Yaakob, B. Narayanan, R. Ramakrishnan, A. Ebshish, *Chemical Papers.* **2011**, *65 (3)*, 251-266.

[38] N. Bion, D. Duprez, F. Epron, *ChemSusChem.* **2012**, *5 (1)*, 76-84.

[39] P.D. Vaidya, A.E. Rodrigues, *Chem. Eng. J.* **2006**, *117 (1)*, 39-49.

[40] A. Haryanto, S. Fernando, N. Murali, S. Adhikari, *Energy Fuels.* **2005**, *19 (5)*, 2098-2106.

[41] P. Panagiotopoulou, C. Papadopoulou, H. Matralis, X. Verykios, *Wiley Interdiscip. Rev.: Energy Environ.* **2014**, *3(3)*, 231-253.

[42] M. Ni, D.Y.C. Leung, M.K.H. Leung, *Int. J. Hydrogen Energy.* **2007**, *32 (15)*, 3238-3247.

[43] V. Klouz, V. Fierro, P. Denton, H. Katz, J.P. Lisse, S. Bouvot-Mauduit, C. Mirodatos, *J. Power Sources.* **2002**, *105 (1)*, 26-34.

[44] S. Cavallaro, V. Chiodo, A. Vita, S. Freni, *J. Power Sources.* **2003**, *123 (1)*, 10-16.

[45] S. Velu, N. Satoh, C.S. Gopinath, K. Suzuki, *Catal. Lett.* **2002**, *82 (1)*, 145-152.

[46] J. Kugai, S. Velu, C. Song, *Catal. Lett.* **2005**, *101 (3)*, 255-264.

[47] J. Kugai, V. Subramani, C. Song, M.H. Engelhard, Y.-H. Chin, *J. Catal.* **2006**, *238 (2)*, 430-440.

[48] D.K. Liguras, K. Goundani, X.E. Verykios, *Int. J. Hydrogen Energy.* **2004**, *29 (4)*, 419-427.

[49] J.R. Salge, G.A. Deluga, L.D. Schmidt, *J. Catal.* **2005**, *235 (1)*, 69-78.

[50] A.J. Akande, *Production of hydrogen by reforming of crude ethanol*, in: Department of Chemical Engineering, University of Saskatchewan, Saskatchewan, **2005**.

[51] B. Banach, A. Machocki, P. Rybak, A. Denis, W. Grzegorczyk, W. Gac, *Catal. Today.* **2011**, *176 (1)*, 28-35.

[52] K. Kinouchi, M. Katoh, K. Nakagawa, S. Sugiyama, T. Yoshikawa, M. Wada, *J. Chem. Eng. Jpn.* **2014**, *47 (1)*, 14-20.

[53] J.-H. Wang, C. Lee, M. Lin, *J. Phys. Chem. C.* **2009**, *113 (16)*, 6681-6688.

[54] A. Le Valant, A. Garron, N. Bion, D. Duprez, F. Epron, *Int. J. Hydrogen Energy.* **2011**, *36 (1)*, 311-318.

[55] A. Le Valant, F. Can, N. Bion, D. Duprez, F. Epron, *Int. J. Hydrogen Energy.* **2010**, *35 (10)*, 5015-5020.

[56] F. Díaz Alvarado, F. Gracia, *Chem. Eng. J.* **2010**, *165 (2)*, 649-657.

[57] H. Schmidt-Traub, A. Górak, *Integrated reaction and separation operations modelling and experimental validation*, Springer-Verlag, Berlin, **2006**.

[58] K. Sundmacher, A. Kienle, A. Seidel-Morgenstern, *Integrated chemical processes : synthesis, operation, analysis, and control*, Wiley-VCH, Weinheim, **2005**.

[59] D.P. Harrison, *Ind. Eng. Chem. Res.* **2008**, *47 (17)*, 6486-6501.

[60] B.T. Carvill, J.R. Hufton, M. Anand, S. Sircar, *AIChE J.* **1996**, *42 (10)*, 2765-2772.

[61] L. He, H. Berntsen, D. Chen, *J. Phys. Chem. A.* **2009**, *114 (11)*, 3834-3844.

[62] S. G.Mayorga, J.R. Hufton, S. Sircar, T.R. Gaffney, *Sorption enhanced reaction process for production of hydrogen. Phase 1 final report*, in, U.S. Department of Energy, Washington, DC, **1997**.

[63] G.-h. Xiu, P. Li, A. E. Rodrigues, *Chem. Eng. Sci.* **2002**, *57 (18)*, 3893-3908.

[64] G.-h. Xiu, P. Li, A.E. Rodrigues, *Chem. Eng. Sci.* **2003**, *58 (15)*, 3425-3437.

[65] G.-h. Xiu, J.L. Soares, P. Li, A.E. Rodrigues, *AIChE J.* **2002**, *48 (12)*, 2817-2832.

[66] E.L.G. Oliveira, C.A. Grande, A.E. Rodrigues, *Can. J. Chem. Eng.* **2009**, *87 (6)*, 945-956.

[67] E.L.G. Oliveira, C.A. Grande, A.E. Rodrigues, *Chem. Eng. Sci.* **2010**, *65 (5)*, 1539-1550.

[68] E.L.G. Oliveira, C.A. Grande, A.E. Rodrigues, *Sep. Purif. Technol.* **2008**, *62 (1)*,

137-147.

[69] E.L.G. Oliveira, C.A. Grande, A.E. Rodrigues, *Chem. Eng. Sci.* **2011**, *66 (3)*, 342-354.

[70] M.T.D. Motay, M. Marechal, *Bull. Mensuel De La Societe Chimique De Paris.* **1868**, *9* 334.

[71] J.A. Ritter, A.D. Ebner, *Sep. Sci. Technol.* **2007**, *42 (6)*, 1123-1193.

[72] D. Chen, L. He, *ChemCatChem.* **2011**, *3 (3)*, 490-511.

[73] R. Chaubey, S. Sahu, O.O. James, S. Maity, *Renewable Sustainable Energy Rev.* **2013**, *23* 443-462.

[74] L. Barelli, G. Bidini, F. Gallorini, S. Servili, *Energy.* **2008**, *33 (4)*, 554-570.

[75] D.P. Harrison, *Energy Procedia.* **2009**, *1 (1)*, 675-681.

[76] E.R. van Selow, P.D. Cobden, P.A. Verbraeken, J.R. Hufton, R.W. van den Brink, *Ind. Eng. Chem. Res.* **2009**, *48 (9)*, 4184-4193.

[77] B. Dou, V. Dupont, G. Rickett, N. Blakeman, P.T. Williams, H. Chen, Y. Ding, M. Ghadiri, *Bioresour. Technol.* **2009**, *100 (14)*, 3540-3547.

[78] L. He, J.M.S. Parra, E.A. Blekkan, D. Chen, *Energy Environ. Sci.* **2010**, *3 (8)*, 1046-1056.

[79] J. Fermoso, L. He, D. Chen, *Int. J. Hydrogen Energy.* **2012**, *37 (19)*, 14047-14054.

[80] I. Iliuta, H.R. Radfarnia, M.C. Iliuta, *AIChE J.* **2013**, *59 (6)*, 2105-2118.

[81] J. Meyer, J. Mastin, T.-K. Bjørnebøle, T. Ryberg, N. Eldrup, *Energy Procedia.* **2011**, *4*, 1949-1956.

[82] S.D. Angeli, G. Monteleone, A. Giaconia, A.A. Lemonidou, *Int. J. Hydrogen Energy.* **2014**, *39 (5)*, 1979-1997.

[83] M. Kato, K. Nakagawa, K. Essaki, Y. Maezawa, S. Takeda, R. Kogo, Y. Hagiwara, *Int. J. Appl. Ceram. Technol.* **2005**, *2 (6)*, 467-475.

[84] K. Johnsen, H.J. Ryu, J.R. Grace, C.J. Lim, *Chem. Eng. Sci.* **2006**, *61 (4)*, 1195-1202.

[85] S.-F. Wu, T.H. Beum, J.I. Yang, J.N. Kim, *Chin. J. Chem. Eng.* **2005**, *13 (1)*,

43-47.

[86] N. Chanburanasiri, A.M. Ribeiro, A.E. Rodrigues, A. Arpornwichanop, N. Laosiripojana, P. Praserthdam, S. Assabumrungrat, *Ind. Eng. Chem. Res.* **2011**, *50 (24)*, 13662-13671.

[87] M. Broda, V. Manovic, Q. Imtiaz, A.M. Kierzkowska, E.J. Anthony, C.R. Müller, *Environ. Sci. Technol.* **2013**, *47 (11)*, 6007-6014.

[88] G.H. Xiu, P. Li, A.E. Rodrigues, *Chem. Eng. Res. Des.* **2004**, *82 (2)*, 192-202.

[89] E. Ochoa-Fernández, H.K. Rusten, H.A. Jakobsen, M. Rønning, A. Holmen, D. Chen, *Catal. Today.* **2005**, *106 (1-4)*, 41-46.

[90] D.K. Lee, I.H. Baek, W.L. Yoon, *Chem. Eng. Sci.* **2004**, *59 (4)*, 931-942.

[91] D.K. Lee, Hyun Baek, II, W. Lai Yoon, *Int. J. Hydrogen Energy.* **2006**, *31 (5)*, 649-657.

[92] A.I. Lysikov, S.N. Trukhan, A.G. Okunev, *Int. J. Hydrogen Energy.* **2008**, *33 (12)*, 3061-3066.

[93] S. Gunduz, T. Dogu, *Ind. Eng. Chem. Res.* **2012**, *51 (26)*, 8796-8805.

[94] Y. Iwasaki, Y. Suzuki, T. Kitajima, M. Sakurai, H. Kameyama, *J. Chem. Eng. Jpn.* **2007**, *40 (2)*, 178-185.

[95] K. Essaki, T. Muramatsu, M. Kato, *Int. J. Hydrogen Energy.* **2008**, *33 (22)*, 6612-6618.

[96] A.F. Cunha, Y.-J. Wu, F.A. Díaz Alvarado, J.C. Santos, P.D. Vaidya, A.E. Rodrigues, *Can. J. Chem. Eng.* **2012**, *90 (6)*, 1514-1526.

[97] A.F. Cunha, Y.-J. Wu, J.C. Santos, A.E. Rodrigues, *Chem. Eng. Res. Des.* **2013**, *91 (3)*, 581-592.

[98] Y.-J. Wu, P. Li, J.-G. Yu, A.F. Cunha, A.E. Rodrigues, *Chem. Eng. J.* **2013**, *231*, 36-48.

[99] D.K. Liguras, D.I. Kondarides, X.E. Verykios, *Appl. Catal., B.* **2003**, *43 (4)*, 345-354.

[100] A. Erdohelyi, J. Raskó, T. Kecskés, M. Tóth, M. Dömök, K. Baán, *Catal. Today.* **2006**, *116 (3)*, 367-376.

[101] J.P. Breen, R. Burch, H.M. Coleman, *Appl. Catal., B.* **2002**, *39 (1)*, 65-74.

[102] A.C.W. Koh, W.K. Leong, L. Chen, T.P. Ang, J. Lin, B.F.G. Johnson, T. Khimyak, *Catal. Commun.* **2008**, *9 (1)*, 170-175.

[103] C. Graschinsky, M. Laborde, N. Amadeo, A. Le Valant, N. Bion, F. Epron, D. Duprez, *Ind. Eng. Chem. Res.* **2010**, *49 (24)*, 12383-12389.

[104] T. Montini, L. De Rogatis, V. Gombac, P. Fornasiero, M. Graziani, *Appl. Catal., B.* **2007**, *71 (3-4)*, 125-134.

[105] C. Diagne, H. Idriss, A. Kiennemann, *Catal. Commun.* **2002**, *3 (12)*, 565-571.

[106] F. Frusteri, S. Freni, L. Spadaro, V. Chiodo, G. Bonura, S. Donato, S. Cavallaro, *Catal. Commun.* **2004**, *5 (10)*, 611-615.

[107] F. Aupr être, C. Descorme, D. Duprez, *Catal. Commun.* **2002**, *3 (6)*, 263-267.

[108] M. Koehle, A. Mhadeshwar, *Chem. Eng. Sci.* **2012**, *78*, 209-225.

[109] P. Tereshchuk, J.L. Da Silva, *J. Phys. Chem. C.* **2012**, *116 (46)*, 24695-24705.

[110] A.M. Adris, B.B. Pruden, C.J. Lim, J.R. Grace, *Can. J. Chem. Eng.* **1996**, *74 (2)*, 177-186.

[111] J.R. Rostrup-Nielsen, *Steam reforming*, in: Handbook of Heterogeneous Catalysis, Wiley-VCH Verlag GmbH & Co. KGaA, **2008**.

[112] J. Llorca, P.R. de la Piscina, J.-A. Dalmon, J. Sales, N. Homs, *Appl. Catal., B.* **2003**, *43 (4)*, 355-369.

[113] J. Llorca, N. Homs, J. Sales, P.R. de la Piscina, *J. Catal.* **2002**, *209 (2)*, 306-317.

[114] J. Llorca, N. Homs, J. Sales, J.-L.G. Fierro, P. Ram írez de la Piscina, *J. Catal.* **2004**, *222 (2)*, 470-480.

[115] S. Cavallaro, N. Mondello, S. Freni, *J. Power Sources.* **2001**, *102 (1-2)*, 198-204.

[116] I.I. Soykal, H. Sohn, U.S. Ozkan, *ACS Catal.* **2012**, *2 (11)*, 2335-2348.

[117] M. Benito, R. Padilla, A. Serrano-Lotina, L. Rodr íguez, J. Brey, L. Daza, *J. Power Sources.* **2009**, *192 (1)*, 158-164.

[118] R.M. Navarro, M.A. Pe ña, J.L.G. Fierro, *Chem. Rev.* **2007**, *107 (10)*, 3952-3991.

[119] P. Kurr, I. Kasatkin, F. Girgsdies, A. Trunschke, R. Schlögl, T. Ressler, *Appl. Catal., A.* **2008**, *348 (2)*, 153-164.

[120] X.M. Liu, G.Q. Lu, Z.F. Yan, J. Beltramini, *Ind. Eng. Chem. Res.* **2003**, *42 (25)*, 6518-6530.

[121] S. Cavallaro, S. Freni, *Int. J. Hydrogen Energy.* **1996**, *21 (6)*, 465-469.

[122] F.-W. Chang, H.-C. Yang, L.S. Roselin, W.-Y. Kuo, *Appl. Catal., A.* **2006**, *304* 30-39.

[123] D.A. Morgenstern, J.P. Fornango, *Energy Fuels.* **2005**, *19 (4)*, 1708-1716.

[124] A.E. Galetti, M.F. Gomez, L.A. Arrua, A.J. Marchi, M.C. Abello, *Catal. Commun.* **2008**, *9 (6)*, 1201-1208.

[125] A. Kaddouri, C. Mazzocchia, *Catal. Lett.* **2009**, *131 (1)*, 234-241.

[126] B. Lorenzut, T. Montini, L. De Rogatis, P. Canton, A. Benedetti, P. Fornasiero, *Appl. Catal., B.* **2011**, *101 (3-4)*, 397-408.

[127] N. Homs, J. Llorca, P.R. de la Piscina, *Catal. Today.* **2006**, *116 (3)*, 361-366.

[128] W. Grzegorczyk, A. Denis, W. Gac, T. Ioannides, A. Machocki, *Catal. Lett.* **2009**, *128 (3)*, 443-448.

[129] L.-C. Chen, S.D. Lin, *Appl. Catal., B.* **2011**, *106 (3-4)*, 639-649.

[130] I. Deinega, L.Y. Dolgykh, I. Stolyarchuk, L. Staraya, P. Strizhak, E. Moroz, V. Pakharukova, D. Zyuzin, *Theor. Exp. Chem.* **2013**, *48 (6)*, 386-393.

[131] A. Vinci, V. Chiodo, K. Papageridis, S. Cavallaro, S. Freni, P. Tsiakaras, J. Bart, *Energy Fuels.* **2013**, *27 (3)*, 1570-1575.

[132] A. Casanovas, M. Roig, C. De Leitenburg, A. Trovarelli, J. Llorca, *Int. J. Hydrogen Energy.* **2010**, *35 (15)*, 7690-7698.

[133] C. Zhang, P. Zhang, S. Li, G. Wu, X. Ma, J. Gong, *Phys. Chem. Chem. Phys.* **2012**, *14 (10)*, 3295-3298.

[134] R. Buitrago-Sierra, J. Ruiz-Martínez, J.C. Serrano-Ruiz, F. Rodríguez-Reinoso, A. Sepúlveda-Escribano, *J. Colloid Interface Sci.* **2012**, *383 (1)*, 148-154.

[135] E. Bolshak, S. Abelló, D. Montané, *Int. J. Hydrogen Energy.* **2013**, *38 (14)*, 5594-5604.

[136] V. Palma, F. Castaldo, P. Ciambelli, G. Iaquaniello, *Appl. Catal., B.* **2014**, *145*, 73-84.

[137] S. Abelló, E. Bolshak, D. Montané, *Appl. Catal., A.* **2013**, *450*, 261-274.

[138] Y. Yang, J. Ma, F. Wu, *Int. J. Hydrogen Energy.* **2006**, *31 (7)*, 877-882.

[139] I. Rossetti, C. Biffi, C.L. Bianchi, V. Nichele, M. Signoretto, F. Menegazzo, E. Finocchio, G. Ramis, A. Di Michele, *Appl. Catal., B.* **2012**, *117–118*, 384-396.

[140] Y.-J. Wu, F. Díaz Alvarado, J.C. Santos, F. Gracia, A.F. Cunha, A.E. Rodrigues, *Chem. Eng. Technol.* **2012**, *35 (5)*, 847–858.

[141] H.V. Fajardo, E. Longo, D.Z. Mezalira, G.B. Nuernberg, G.I. Almerindo, A. Collasiol, L.F. Probst, I.T. Garcia, N.L. Carreño, *Environ. Chem. Lett.* **2010**, *8 (1)*, 79-85.

[142] J.F. Da Costa-Serra, M.T. Navarro, F. Rey, A. Chica, *Int. J. Hydrogen Energy.* **2012**, *37 (8)*, 7101-7108.

[143] F. Frusteri, S. Freni, V. Chiodo, L. Spadaro, O. Di Blasi, G. Bonura, S. Cavallaro, *Appl. Catal., A.* **2004**, *270 (1–2)*, 1-7.

[144] P. Biswas, D. Kunzru, *Catal. Lett.* **2007**, *118 (1-2)*, 36-49.

[145] A. Carrero, J.A. Calles, A.J. Vizcaíno, *Chem. Eng. J.* **2010**, *163 (3)*, 395-402.

[146] R. Trane-Restrup, S. Dahl, A.D. Jensen, *Int. J. Hydrogen Energy.* **2013**, *38 (35)*, 15105-15118.

[147] M.C. Sánchez-Sánchez, R.M. Navarro, J.L.G. Fierro, *Catal. Today.* **2007**, *129 (3–4)*, 336-345.

[148] M.C. Sánchez-Sánchez, R.M. Navarro, J.L.G. Fierro, *Int. J. Hydrogen Energy.* **2007**, *32 (10–11)*, 1462-1471.

[149] J.W.C. Liberatori, R.U. Ribeiro, D. Zanchet, F.B. Noronha, J.M.C. Bueno, *Appl. Catal., A.* **2007**, *327 (2)*, 197-204.

[150] A.N. Fatsikostas, X.E. Verykios, *J. Catal.* **2004**, *225 (2)*, 439-452.

[151] A.J. Vizcaíno, A. Carrero, J.A. Calles, *Int. J. Hydrogen Energy.* **2007**, *32 (10–11)*, 1450-1461.

[152] C. Zhang, S. Li, M. Li, S. Wang, X. Ma, J. Gong, *AIChE J.* **2012**, *58 (2)*,

516-525.

[153] S. Li, M. Li, C. Zhang, S. Wang, X. Ma, J. Gong, *Int. J. Hydrogen Energy.* **2012**, *37 (3)*, 2940-2949.

[154] F. Mariño, G. Baronetti, M.a. Jobbagy, M. Laborde, *Appl. Catal., A.* **2003**, *238 (1)*, 41-54.

[155] Z. Yong, V. Mata, A.E. Rodrigues, *Sep. Purif. Technol.* **2002**, *26 (2-3)*, 195-205.

[156] Q. Wang, J. Luo, Z. Zhong, A. Borgna, *Energy Environ. Sci.* **2011**, *4 (1)*, 42-55.

[157] R.T. Yang, *Adsorbents fundamentals and applications*, Wiley-Interscience, Hoboken, N.J., **2003**.

[158] S. Choi, J.H. Drese, C.W. Jones, *ChemSusChem.* **2009**, *2 (9)*, 796-854.

[159] S. Wang, S. Yan, X. Ma, J. Gong, *Energy Environ. Sci.* **2011**, *4 (10)*, 3805-3819.

[160] A.M. Kierzkowska, R. Pacciani, C.R. Müller, *ChemSusChem.* **2013**, *6 (7)*, 1130-1148.

[161] W. Liu, H. An, C. Qin, J. Yin, G. Wang, B. Feng, M. Xu, *Energy Fuels.* **2012**, *26 (5)*, 2751-2767.

[162] K.S. Sultana, D. Chen, *Catal. Today.* **2011**, *171 (1)*, 43-51.

[163] J.A. Satrio, B.H. Shanks, T.D. Wheelock, *Ind. Eng. Chem. Res.* **2005**, *44 (11)*, 3901-3911.

[164] B. Balasubramanian, A. Lopez Ortiz, S. Kaytakoglu, D.P. Harrison, *Chem. Eng. Sci.* **1999**, *54 (15-16)*, 3543-3552.

[165] J. Comas, M. Laborde, N. Amadeo, *J. Power Sources.* **2004**, *138 (1-2)*, 61-67.

[166] J.C. Abanades, G. Grasa, M. Alonso, N. Rodriguez, E.J. Anthony, L.M. Romeo, *Environ. Sci. Technol.* **2007**, *41 (15)*, 5523-5527.

[167] A. MacKenzie, D.L. Granatstein, E.J. Anthony, J.C. Abanades, *Energy Fuels.* **2007**, *21 (2)*, 920-926.

[168] K.O. Albrecht, K.S. Wagenbach, J.A. Satrio, B.H. Shanks, T.D. Wheelock, *Ind. Eng. Chem. Res.* **2008**, *47 (20)*, 7841-7848.

[169] R. Barker, *J. Appl. Chem. Biotechnol.* **1973**, *23 (10)*, 733-742.

[170] S.K. Bhatia, D.D. Perlmutter, *AIChE J.* **1983**, *29 (1)*, 79-86.

[171] P.D. Cobden, G.D. Elzingaa, S. Booneveld, J.W. Dijkstra, D. Jansen, R.W. van den Brink, *Energy Procedia.* **2009**, *1 (1)*, 733-739.

[172] J.C. Abanades, E.J. Anthony, D.Y. Lu, C. Salvador, D. Alvarez, *AIChE J.* **2004**, *50 (7)*, 1614-1622.

[173] J.C. Abanades, *Chem. Eng. J.* **2002**, *90 (3)*, 303-306.

[174] S. Wang, H. Shen, S. Fan, Y. Zhao, X. Ma, J. Gong, *AIChE J.* **2013**, *59 (10)*, 3586-3593.

[175] K. Nakagawa, T. Ohashi, *J. Electrochem. Soc.* **1998**, *145 (4)*, 1344-1346.

[176] R. Xiong, J. Ida, Y.S. Lin, *Chem. Eng. Sci.* **2003**, *58 (19)*, 4377-4385.

[177] J.-i. Ida, Y.S. Lin, *Environ. Sci. Technol.* **2003**, *37 (9)*, 1999-2004.

[178] Z. Qi, H. Daying, L. Yang, Y. Qian, Z. Zibin, *AIChE J.* **2013**, *59 (3)*, 901-911.

[179] B.N. Nair, T. Yamaguchi, H. Kawamura, S.-I. Nakao, K. Nakagawa, *J. Am. Ceram. Soc.* **2004**, *87 (1)*, 68-74.

[180] E. Ochoa-Fernández, M. Rønning, T. Grande, D. Chen, *Chemistry of Materials.* **2006**, *18 (6)*, 1383-1385.

[181] S.M. Auerbach, K.A. Carrado, P.K. Dutta, *Handbook of Layered Materials*, Marcel Dekker Inc., Hoboken, **2004**.

[182] M.A. Ulibarri, I. Pavlovic, C. Barriga, M.C. Hermos ín, J. Cornejo, *Appl. Clay Sci.* **2001**, *18 (1-2)*, 17-27.

[183] Y. Ding, E. Alpay, *Process Saf. Environ. Prot.* **2001**, *79 (1)*, 45-51.

[184] M.K. Ram Reddy, Z.P. Xu, G.Q. Lu, J.C. Diniz da Costa, *Ind. Eng. Chem. Res.* **2006**, *45 (22)*, 7504-7509.

[185] G.R. Williams, D. O'Hare, *J. Mater. Chem.* **2006**, *16 (30)*, 3065-3074.

[186] H.T.J. Reijers, S.E.A. Valster-Schiermeier, P.D. Cobden, R.W. van den Brink, *Ind. Eng. Chem. Res.* **2005**, *45 (8)*, 2522-2530.

[187] Z. Yong, A.E. Rodrigues, *Energy Convers. Manage.* **2002**, *43 (14)*, 1865-1876.

[188] M.S. San Román, M.J. Holgado, C. Jaubertie, V. Rives, *Solid State Sci.* **2008**, *10 (10)*, 1333-1341.

[189] N.D. Hutson, S.A. Speakman, E.A. Payzant, *Chem. Mater.* **2004**, *16 (21)*,

4135-4143.

[190] Z. Yong, V.G. Mata, A.E. Rodrigues, *Ind. Eng. Chem. Res.* **2000**, *40 (1)*, 204-209.

[191] W. Yang, Y. Kim, P.K.T. Liu, M. Sahimi, T.T. Tsotsis, *Chem. Eng. Sci.* **2002**, *57 (15)*, 2945-2953.

[192] K.B. Lee, M.G. Beaver, H.S. Caram, S. Sircar, *Int. J. Hydrogen Energy.* **2008**, *33 (2)*, 781-790.

[193] M.H. Halabi, M.H.J.M. de Croon, J. van der Schaaf, P.D. Cobden, J.C. Schouten, *Chem. Eng. J.* **2011**, *168 (2)*, 872-882.

[194] M.H. Halabi, M.H.J.M. de Croon, J. van der Schaaf, P.D. Cobden, J.C. Schouten, *Fuel.* **2012**, *99*, 154-164.

[195] M.H. Halabi, M.H.J.M. de Croon, J. van der Schaaf, P.D. Cobden, J.C. Schouten, *Int. J. Hydrogen Energy.* **2012**, *37 (5)*, 4516-4525.

[196] J.R. Hufton, S. Mayorga, S. Sircar, *AIChE J.* **1999**, *45 (2)*, 248-256.

[197] J. Boon, P. Cobden, H. van Dijk, C. Hoogland, E. van Selow, M. van Sint Annaland, *Chem. Eng. J.* **2014**, *248*, 406-414.

[198] M.J. Ramírez-Moreno, I.C. Romero-Ibarra, M.d.l.Á. Hernández-Pérez, H. Pfeiffer, *Ind. Eng. Chem. Res.* **2014**, DOI: 10.1021/ie5010515.

[199] A. Hanif, S. Dasgupta, S. Divekar, A. Arya, M.O. Garg, A. Nanoti, *Chem. Eng. J.* **2014**, *236*, 91-99.

[200] O. Aschenbrenner, P. McGuire, S. Alsamaq, J. Wang, S. Supasitmongkol, B. Al-Duri, P. Styring, J. Wood, *Chem. Eng. Res. Des.* **2011**, *89 (9)*, 1711-1721.

2. Experimental and Theoretical Investigations[†]

In this chapter, the concept of sorption enhanced reaction process on steam reforming of ethanol has been demonstrated by the use of commercial materials (section 2.1). A reactor with a multilayer pattern arrangement of Ni-based catalyst and hydrotalcite sorbent has been employed to enhance the hydrogen production performance, and carbon dioxide appears in traces in the product gas stream during the initial breakthrough periods.

Theoretical investigations of the thermodynamic analysis (section 2.2) on the SE-SRE system with different high temperature carbon dioxide sorbent materials and kinetics study (section 2.3) on the commercial nickel-based catalyst for SRE can also be found. The thermodynamic analysis is performed with a Gibbs free energy minimization method to compare the conventional SRE and SE-SRE with three different sorbents, namely, calcium oxide, lithium zirconate, and HTlc. The best performance of SE-SRE is found to be at 773 K with the HTlc sorbent. Almost 6 moles hydrogen can be produced per mole ethanol converted, while the carbon monoxide content in the vent stream is less than 10 ppm, which meet the requirement of directly usage for fuel cells. On the other hand, a simplified Langmuir–Hinshelwood–Hougen–Watson kinetic model was proposed in the kinetic study, where the surface decomposition of methane is assumed as the rate determining step. Experimental results can be successfully demonstrated by simplified kinetic model over a wide temperature range (473 K – 873 K).

[†] The content of this chapter is part of the following articles:

A. F. Cunha, Y.-J. Wu, F. A. Díaz-Alvarado, J. C. Santos, P. D. Vaidya, A. E. Rodrigues, Steam Reforming of Ethanol on a Ni/Al_2O_3 Catalyst Coupled with a Hydrotalcite-like Sorbent in a Multilayer Pattern for CO_2 Uptake, Canadian Journal of Chemical Engineering, 90(6), 2012, 1514-1526.

Y.-J. Wu, F. A. Díaz-Alvarado, J. C. Santos, F. Gracia, A. F. Cunha, A. E. Rodrigues, Sorption-Enhanced Steam Reforming of Ethanol: Thermodynamic Comparison of CO_2 Sorbents, Chemical Engineering & Technology, 35(5), 2012, 847-858.

Y.-J. Wu, J. C. Santos, Ping Li, J.-G. Yu, A. F. Cunha, A. E. Rodrigues, Simplified kinetic model for steam reforming of ethanol on a Ni/Al_2O_3 catalyst, Canadian Journal of Chemical Engineering, 92(1), 2014, 116-130.

2.1 SE-SRE with Commercial Materials

2.1.1 Introduction

Environmental concerns and fossil fuels depletion led to the philosophy of a ‘‘Hydrogen economy’’ [1]. Hydrogen is a clean and efficient energy carrier, showing excellent performance in fuel cells [2]. However, fuel cell applications tolerate carbon oxides only in well-defined levels [3].

Hydrogen is mostly produced by steam reforming of light hydrocarbon fractions, obtained from fossil fuels [4]. This process involves strong emissions of carbon oxides. An adequate alternative process can be the implementation of SRE [5]; bio-ethanol is a renewable resource and, based on life cycle assessment, its use can reduce carbon emissions [6].

$$C_2H_5OH + 3H_2O \leftrightarrow 6H_2 + 2CO_2 \quad (2.1)$$

Bio-ethanol, which contains water in large excess [7], can be directly subjected to steam reforming, thereby eliminating rectification units, required to produce technical pure ethanol (azeotropic ethanol concentration 96 vol. %). Furthermore, the presence of excess water ensures sufficient supply of steam, maximizing hydrogen production and reducing ethanol dehydration ($C_2H_5OH \rightarrow C_2H_4 + H_2O$) followed by the decomposition of ethene into coke ($C_2H_4 \rightarrow 2H_2 + 2C$). It has been reported that for temperatures of ~ 573 K and higher, ethanol/water ratios above 3 are sufficient to suppress the deposition of graphitic carbon [8]. However, the support materials used, γ-Al_2O_3 and α-Al_2O_3, show different surface areas. The former one has a higher surface area than the latter. According to this finding, a higher activity was also observed for the γ-Al_2O_3 support material. In this case, the formation of ethene, promoted by γ-Al_2O_3, should not be discarded.

The catalytic SRE to produce hydrogen for fuel cells has been discussed, in depth, in recent reviews [9, 10]. Commercial catalysts for steam reforming are usually based on Ni, as active phase, supported in alumina [11]. Ni is widely used in industry, and is a low-cost non-noble metal. It is also known to work quite well for the activation of carbon-carbon, hydrogen-carbon or hydrogen-hydrogen σ-bond ś [12, 13]. However,

hydrogen production by steam reforming is limited by the thermodynamic equilibrium of the involved reversible reactions, mainly the SMR and WGS reactions [14, 15].

The SMR reaction [14] is strongly endothermic, and therefore favored by high temperatures, while the WGS reaction is moderately exothermic, meaning that it is favored by low temperatures. The reforming reaction will also be more pronounced at low pressures, whereas the WGS reaction is largely unaffected when changes in pressure are used.

Steam reforming carried out in the presence of a hybrid system, catalyst and carbon dioxide sorbent, is of great interest. An appropriate carbon dioxide sorbent can selectively remove carbon dioxide from the reaction mixture [16-19], thereby shifting the reversible reaction equilibrium according to the principle of Le Chatelier, thus, yielding more hydrogen [20, 21]. This technique is known as SERP and hereafter designated as SE-SRE. In optimal conditions, SE-SRE enables the production of pure hydrogen (CO_x-free) at low temperatures in a single-bed reactor, rather than the conventionally used ones, meaning cost minimization. The sorbent can then be regenerated in-situ, using a pressure swing [22, 23], a temperature swing [24-28] or reactive regeneration [16, 19].

In principle three groups of suitable sorbents are known to have good capacities for the sorption of carbon dioxide at high temperatures; calcium oxide-based materials, Hydrotalcite-based materials and lithium-based materials. The selection of the sorbent requires a good selectivity and capacity toward carbon dioxide, good sorption kinetics, stability for cyclic operation and mechanical strength for an operation with pressure in the presence of steam.

It has been presented earlier thermodynamic analysis for hydrogen production via SRE, using calcium oxide as a carbon dioxide sorbent [29]. However, promising classes of compounds are the hydrotalcites due to their ability to work at lower temperatures, even when the sorption capacity of these materials is lower in comparison to the other ones. Table 2-1 collects the properties of selected sorbents reported in literature, based on an updated version of the work from Oliveira et al. [40].

Table 2-1 Overview for carbon dioxide sorption capacity of selected materials.

Materials	T [K]	y_{CO2} [mol/mol]	p [kPa]	q_{sorb} [mol/kg]	References
Calcium oxides	573-973	0.05-1	100	2.1-17.3	[20, 30-39]
Hydrotalcites	573-773	0.15-1	50-300	0.2-1.8	[24, 40-49]
Basic Aluminas	573-723	1	100-300	0.4-0.8	[26, 50]
Carbons	573	1	100	0.3	[51]
Basic Zirconias	673-873	1	100	3.0-6.1	[52-55]
Basic Silicas	773-973	0.05-1	100	0.5 - 8.2	[55-58]

Previous studies on hydrotalcites made in our laboratory, showed sufficient sorption capacities for carbon dioxide at moderately high temperatures (~ 673 K) [40]. Besides, hydrotalcites are anionic clays consisting of positively charged layers of metal oxide (or metal hydroxide) with inter-layers of anions, such as carbonate [59]. These sorbents can be used to enhance the methane steam reforming process [60]. Recently, SRE has been studied in presence of nickel catalysts derived from hydrotalcite-like precursors, but SE-SRE was not the subject [61]. It is clear that SE-SRE is an important topic related with the use of a renewable raw material (bio-ethanol) and the preservation of the environment (capture of carbon dioxide).

The present work reports results obtained on a Ni/Al_2O_3 catalyst as well as a coupled system of catalyst plus hydrotalcite-like sorbent in a multilayer pattern arrangement, which is the novelty of this work. The effect of the operating conditions on the activity and selectivity were studied for these systems, and critically compared one with each other to emphasize the advantage of SE-SRE against the conventional SRE. A temperature increase was used to regenerate the sorbent.

To the best of our knowledge there is no systematic study reported in literature discussing the production of hydrogen in the presence of a commercial Ni-catalyst and a commercial hydrotalcite-like sorbent in a multilayer pattern arrangement for the capture of carbon dioxide.

2.1.2 Experimental

2.1.2.1 Materials

A commercial 15 wt. % Ni/γ-Al_2O_3 catalyst (Octolyst 1001) was supplied by Degussa AG, in form of extrudates, and used in this work. The sorbent PURAL MG30 (aluminium magnesium hydroxide, 70 % Al_2O_3) was provided by SASOL.

2.1.2.2 Reaction studies

Reaction studies were carried out in a 42 cm long tubular stainless steel fixed-bed continuous down-flow reactor (i.d. = 3.3 cm). The continuous down-flow reactor was loaded with the catalyst or catalysts plus sorbent, and placed inside a heating furnace with a PID temperature controller (Termolab, Fornos Electricos Lda).

Prior to the reaction runs, the catalyst (and sorbent) was activated with a hydrogen flow-rate of 30 cm^3 min^{-1} at 723 K during 2 h.

Each run was studied between 373 K and 873 K with 50 K intervals, until steady state conditions were achieved on stream. During these intervals, the temperature was subsequently increased exclusively in the presence of the carrier gas helium, with a heating rate of 5 K/min, to ensure total absence of product gases formed during the isothermal runs.

An HPLC pump (Merck L-2130) was used to introduce the liquid ethanol-water mixture inside the reactor. In most of the experimental runs, the premixed liquid flow rate of ethanol-water was adjusted to 0.3 ml/min with a $R_{S/E}$ of 10. Helium or Nitrogen was used as a carrier gas during experimental runs, and the flow rates (50-200 $Ncm^3 \cdot min^{-1}$) were controlled by mass flow controllers. The liquid-gas mixture was vaporized in a spider tube inside the upper part of the reactor (21 cm long). This gas stream passed over the catalyst (and sorbent) placed inside the lower part of the reactor. Blank measurements were made to ensure that no possible catalytic effects occur during the steam reforming process due to the ever presence of the inner reactor wall which consists on stainless steel. The sorbent used was also analyzed in terms of possible catalytic activity. It was found that no large amounts of products are

formed at an operating temperature of 673 K.

During the reaction, the products exiting the reactor were passed through a condenser (stainless steel heat exchanger consisting on a bundle of tubes) and an ice-cooled trap using a Dewar. The composition of the outgoing off-gas stream was determined with a gas chromatograph (GC 1000, Dani Chromatographs) equipped with an on-line multiport 16-valve system for sample injection (Valco Instruments Company Inc.), a capillary column (Carboxen 1010 Plot, Supelco) and a thermal conductivity detector. The liquid products, including the unreacted ethanol present, were periodically collected in the ice-cooled trap and separately analyzed with the same aforementioned gas chromatograph, using a capillary column (Poraplot-U) and a flame ionization detector. The water conversion was calculated via the measured amounts of carbon dioxide formed during reaction, in agreement with the global SRE equation; 2/3 mole of carbon dioxide formed may consume 1 mol of water.

Figure 2-1 depicts a schematic representation of the experimental ethanol steam reforming unit. For all the measurements made in this work, an average error of around ±5% should be taken into account.

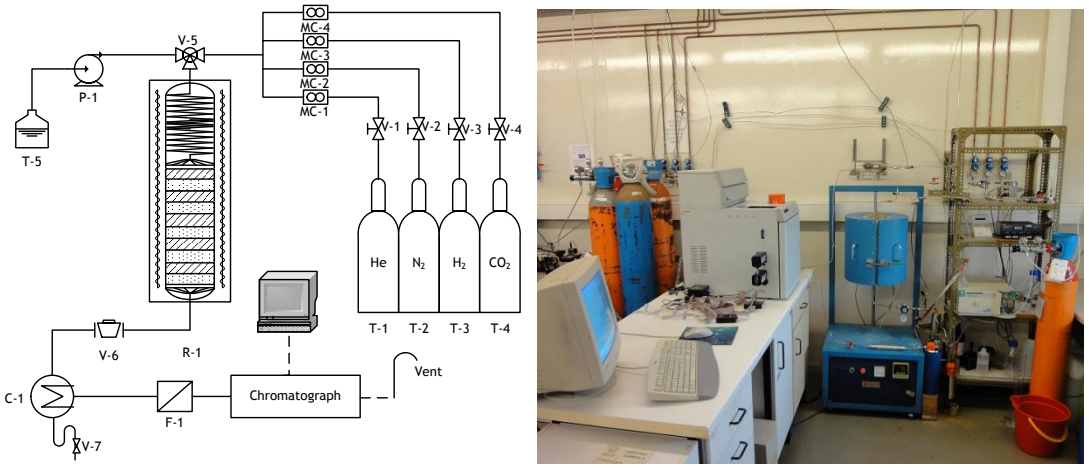

Figure 2-1 Schematic representation and picture of the experimental steam reforming unit: T-1-4 Feeding gases; MC1-4 Mass-flow controllers; T-5 Feeding ethanol-water mixture; P-1 Pump for liquids; V-5 Mixing valve; R-1 Reforming reactor; V-6 Back pressure valve; C-1 Condenser; F-1 Moisture trap.

2.1.2.3 Characterization

The materials were characterized before reaction runs, applying different physicochemical techniques. The content of nickel and alumina in the catalyst was determined with inductively coupled plasma atomic emission spectroscopy (ICP-AES) analysis (70 Plus Jobin Yvon, Unterhaching, Germany). The particle and solid density was measured with a Quantachrome PoreMaster 60 (Quantachrome, Hook, United Kingdom). A mercury porosimeter was used to determine the macro- and mesopore size distribution of the catalyst. The specific surface areas of the fresh catalysts were calculated by the BET method from the N_2 equilibrium adsorption isotherms at 77 K with a coulter Omnisorp 100 CX apparatus. The catalyst and sorbent was examined with a JEOL JSM-6301F (JEOL, Japan) scanning electron microscope (SEM) associated with an energy dispersive X-ray analyzer (EDX), Oxford INCA Energy 350 (Oxford Instruments, Oxford, United Kingdom).

Carbon dioxide sorption capacity was determined by comprising helium, carbon dioxide and water. Helium and water were employed for sorbent regeneration. The liquid water flow-rate was controlled with the HPLC pump and vaporized before entering into the column. Both carbon dioxide and helium flow-rates were controlled by independent mass flow controllers.

2.1.3 Results and Discussion

2.1.3.1 Materials characterization

A detailed discussion on the characterization of the catalyst [62] and sorbent [40] used in this work, can be found in previous reports. The properties of the catalyst and sorbent used are briefly discussed in this section, and collected in Table 2-2. The nickel and aluminum contents of the catalysts were determined by ICP-AES analysis. It was found that the catalyst is composed of nickel (15.4 wt. %) and alumina (84.6 wt. %). The results are in good agreement with the nominal value indicated by the catalyst supplier.

Table 2-2 Properties of the used materials

Materials	Ni [wt.%]	Al_2O_3 [wt.%]	MgO [wt.%]	$\bar{d}_i$ [mm]	$\bar{l}_i$ [mm]	ρ_p [kg/m^3]	ρ_s [kg/m^3]	ε_p [%]	$\bar{d}_{pore}$ [nm]	S_{BET} [m^2/g]
Octolyst	15.4	84.7	/	1.6	5	1274	3630	64.9	8.5	250
MG30	/	71.5	28.5	4.6	2.9	1139	2183	52.2	8.3	200

The catalyst has an average diameter of $\bar{d}_i$ = 1.6 mm and a length of approximately $\bar{t}_i$ = 5 mm. The advantage of this catalyst is that the pressure drop (less than 2 % of atmospheric pressure) can be limited in a certain range due to the large particle size.

The pellet density (ρ_p) of the catalyst corresponds to a value of 1274 kg·m^{-3}, while the solid density (ρ_s) was found to be 3630 kg·m^{-3}. According to this, porosity (ε_p) of 64.9 % was calculated.

SEM analyses performed in a glance of the fresh catalyst reveal that the support (γ-alumina) is covered with nickel clusters ranging from 170 to 3720 nm as shown in Figure 2-2. A large particle value variation of the Ni clusters is normally an indication for a poor dispersion during catalyst preparation (impregnation, co-precipitation, etc.), or less probably, an existing interaction between the support material used and active phase deposited.

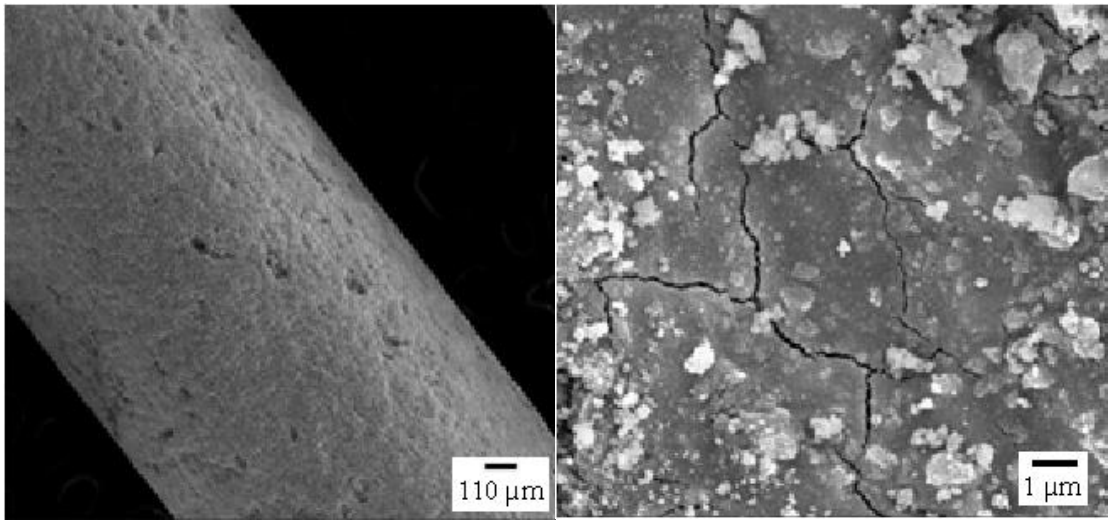

Figure 2-2 SEM micrograph of the catalyst.

The catalyst also shows a narrow pore size distribution with average diameter

($\bar{d}_{pore}$) of 8.5 nm, as shown in Figure 2-3. This is an indication that the catalyst consists mostly on mesopores (between 2 to 50 nm), rather than macropores (> 50 nm).

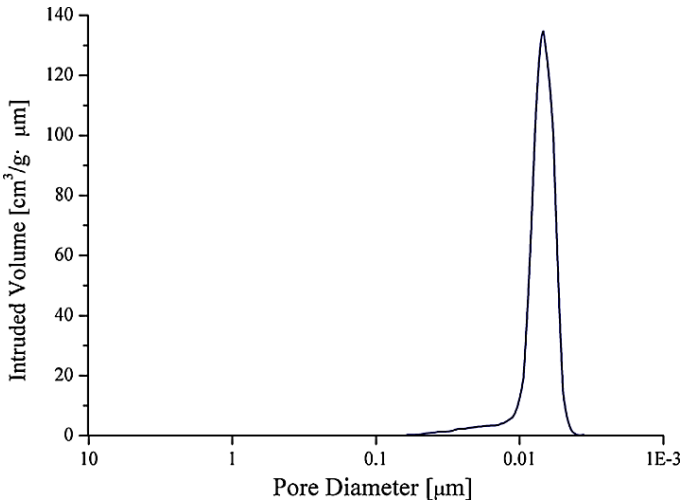

Figure 2-3 Pore size distribution of the catalyst.

The BET surface area of the catalyst, S_{BET} = 250 $m^2 \cdot g^{-1}$, is within the range of reported values for this type of catalyst [8].

The commercial hydrotalcite sorbent MG30 used shows a highly porous lamellar structure (Figure 2-4). The magnesium oxide content of 28.5 wt. % is in good agreement with the expected nominal value of the Mg content (30 wt. %).

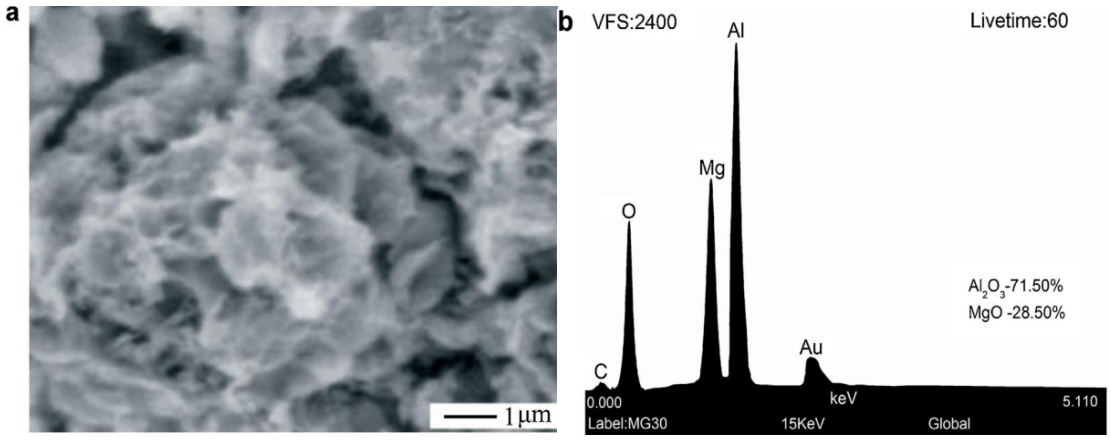

Figure 2-4 Pore size distribution of the catalyst.

The BET surface area of the sorbent was found to be S_{BET} = 200 $m^2 \cdot g^{-1}$. The MG30 sorbent was also screened in typical breakthrough experiments, employing a stream of carbon dioxide, water vapor and helium (considered as inert gas), to ensure sufficient

capacity for carbon dioxide sorption equilibrium. The experiments were conducted at 673 K with a partial pressure of carbon dioxide close to 40 kPa. The experiments carried out showed sufficient capacity for carbon dioxide sorption ($q_{sorb} \cong 0.1$ mol·kg^{-1}).

2.1.3.2 Catalyst performance

Reaction studies were carried out, and the catalyst was evaluated for 5 h on stream at each temperature interval to ensure stable operating conditions. The effects of temperature, flow-rate (contact time) and presence of sorbent during reaction and after regeneration, were investigated. To ensure total regeneration of the sorbent, a temperature increase was used as mentioned in section 2.1.2.2 (as e.g.: before a reaction was executed at 673 K with an inert gas-flow-rate of 50 or 200 Ncm^3·min^{-1}, the temperature was increased from 673 K to 693 K with an inert gas-flow-rate of 500 Ncm^3·min^{-1}, and kept during 30 min at these conditions, followed by an adjustment of the desired reaction conditions). In a real industrial technology the regeneration can be done with a temperature swing. The activity of the catalyst is assessed by comparing the conversion of ethanol and water. The conversion of ethanol and water was calculated as follow:

$$X_{EtOH}[\%] = \frac{\dot{n}_{EtOH,0} - \dot{n}_{EtOH}}{\dot{n}_{EtOH,0}} \times 100 \tag{2.2}$$

$$X_{H_2O}[\%] = \frac{\dot{n}_{H_2O,0} - \dot{n}_{H_2O}}{\dot{n}_{H_2O,0}} \times 100 \tag{2.3}$$

For convenience, the molar product distribution was calculated from the moles of one product formed divided by the total moles of products:

$$y_i[mol\%] = \frac{\dot{n}_i}{\sum \dot{n}_i} \times 100 \tag{2.4}$$

where $\dot{n}_i$ represents the molar flow rate of one product and $\sum \dot{n}_i$ represents the total molar flow rate of products in the dry product stream (water is here excluded). However, to calculate the selectivity it is required first to obtain the yield of the products, in this

case hydrogen. The hydrogen yield can be calculated from:

$$Y_{H_2}[\%] = \frac{\dot{n}_{H_2} - \dot{n}_{H_2,o}}{\dot{n}_{EtOH,o}} \cdot \frac{\nu_{EtOH}}{\nu_{H_2}} \times 100 \qquad (2.5)$$

The hydrogen selectivity can then be obtained by:

$$S_{H_2} = \frac{Y_{H_2}}{X_{EtOH}} \qquad (2.6)$$

Figure 2-5 shows the conversion of ethanol and water, as well as the product distribution (dry basis). It might be observed that conversions of both ethanol and water (Figure 2-5a), increase with temperature. However, higher reaction temperatures are required for the activation of water. For instance, when using an inert-gas flow-rate of 200 $Ncm^3 \cdot min^{-1}$ at a temperature of 623 K or above, ethanol conversion is almost complete, suggesting good activities at low temperatures, while higher temperatures are required for a moderate water conversion. Moderate water conversions have been reported previously by Resini et al. [61]. Nevertheless, in this study the low water conversion is a consequence of the high $R_{S/E}$ used (1:10), indicating that the higher the amount of water in the feed is the lower the water conversion is. However, a moderate water conversion is not a problem, since the catalyst selectivity is good enough (product purity).

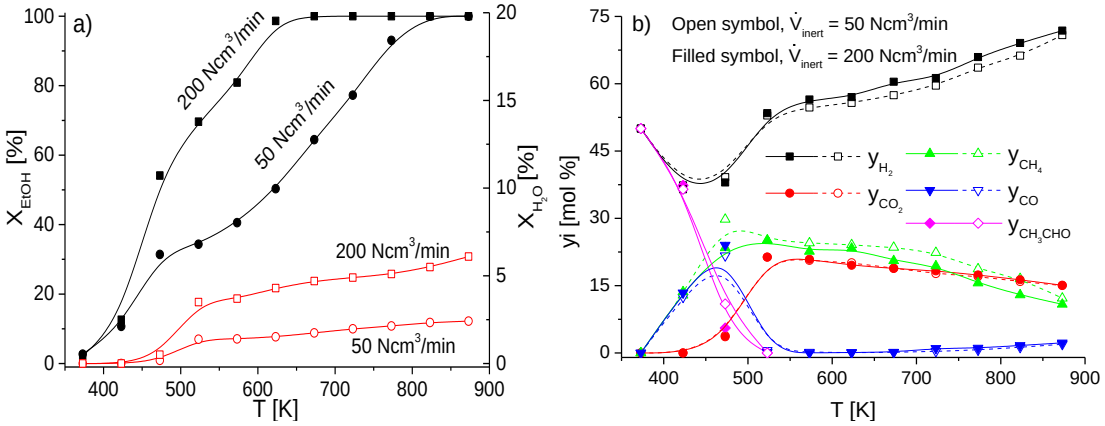

Figure 2-5 Ethanol (filled symbols) and water (open symbols) conversions (a), and product distribution (b) as function of reaction temperature at steady state conditions; operating conditions: m_{cat} = 20.0 g; p = 100 kPa;

It was also found that higher flow-rates increase the conversion of the reactants and the yield of hydrogen. Apparently this seems to be a contradiction, because a higher flow-rate means lower contact time and therefore lower conversion of the reactants. This phenomenon may be an effect of external diffusion limitations at the lower flow-rate. The presence of nickel clusters located on top of the porous γ-alumina support (SEM micrographs) may be responsible for the lower activities in the lower flow-rate regime due to external diffusion limitations.

The product distribution (Figure 2-5b) as a function of temperature during SRE in presence of the catalyst, shows that at 373 K considerable amounts of acetaldehyde are found (~ 50 mol %).

At 423 K, only carbon monoxide, methane and hydrogen are present. From these observations it can be concluded, that in a low temperature range of 373 K to 423 K, only ethanol is decomposed in the following two steps:

$$CH_3CH_2OH \leftrightarrow CH_3CHO + H_2 \tag{2.7}$$

$$CH_3CHO \leftrightarrow CO + CH_4 \tag{2.8}$$

The first step of ethanol activation goes through the formation of hydrogen and acetaldehyde as intermediate compound, and in the second step acetaldehyde decomposes partially or totally into methane and carbon monoxide. These observations are in good agreement with reports in literature [63, 64].

However, when ethanol is dehydrogenated, equal amounts of acetaldehyde and hydrogen should be expected; however, part of the formed acetaldehyde can yield equal amounts of carbon monoxide and methane so that the molar product distribution is effectively not the expected stoichiometric value of ethanol dehydration.

In the middle temperature range (473-673 K) the presence of acetaldehyde and carbon monoxide decreases strongly, while carbon dioxide and hydrogen increase in considerable amounts. The methane concentration remains constant. This observation suggests a latent WGS reaction of acetaldehyde or a direct WGS reaction after carbon monoxide formation:

$$CH_3CHO + H_2O \leftrightarrow 2H_2 + CH_4 + CO_2 \quad (2.9)$$

$$CO + H_2O \leftrightarrow H_2 + CO_2 \quad (2.10)$$

It was reported that Ni catalysts have lower WGS activities [64-67] than Cu catalysts [11, 15]. In practice the WGS process is applied in two stages, consisting of a high temperature shift (HTS) at 623 K and a low temperature shift between 463 K and 483 K. It is worth to note, the WGS reaction should not be discarded, because it is an exothermic reaction and equilibrium conversion of carbon monoxide is favored with the application of low temperatures. In this work the conversion of carbon monoxide (formed from the decomposition of ethanol) was low at 473 K, the beginning of catalyst activity for WGS, and almost complete at 573 K. However, in this temperature range only part of the ethanol is converted, so that the mass of catalyst used is enough to convert almost all the carbon monoxide formed at 573 K.

In the higher temperature range (673-873 K), the methane concentration decreases with temperature, thus indicating its activation. As a consequence, more hydrogen is generated, where SMR is most probable, as shown below:

$$CH_4 + 2H_2O \leftrightarrow 4H_2 + CO_2 \quad (2.11)$$

However, traces of carbon monoxide are always present, and their concentrations increase with temperature in the higher temperature range. This can be explained by the fact that SMR, equation (2.11), is a sum of the two individual reaction steps, already described by Xu and Froment [14]:

SMR $$CH_4 + H_2O \leftrightarrow 3H_2 + CO \quad (2.12)$$

WGS $$CO + H_2O \leftrightarrow H_2 + CO_2 \quad (2.13)$$

Since equation (2.13) is the exothermic WGS step, more carbon monoxide is generated at higher reaction temperatures (reaction (2.12)). It should be emphasized that in industrial applications the SMR is conducted over nickel catalysts at temperatures up to 1023 K to ensure complete methane conversion [11, 15]. Methane and water are thereby completely converted into hydrogen, carbon dioxide and considerable amounts of carbon monoxide which are then converted in the WGS

process into additional hydrogen and carbon dioxide.

2.1.3.3 SE-SRE results

In the following section the objective was to study a possible selective removal of carbon dioxide from the product stream by sorption. The chemical equilibrium should be shifted to the desired product hydrogen. Furthermore, the introduction of a carbon dioxide sorbent in the system should enable the production of high-purity hydrogen at a lower reaction temperature (673 K). A typical product distribution as function of the reaction time during SRE for a system consisting of pure catalyst or a coupled system of catalyst and sorbent is shown in Figure 2-6.

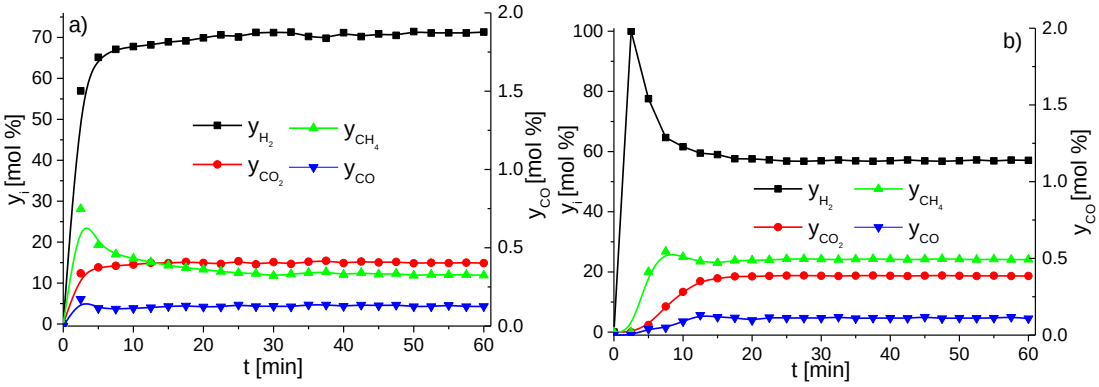

Figure 2-6 Product distribution as function of reaction time; operating conditions: p = 100 kPa; $\dot{V}_{inert}$ = 50 $Ncm^3 \cdot min^{-1}$, (a) catalyst (T = 873 K; m_{cat} = 20.0 g); (b) multilayer system of catalyst and sorbent (T = 673 K; m_{cat} = 4 × 5.0 g and m_{sorb} = 3 × 16.7 g).

In the presence of the catalyst, at 873 K and inert gas flow-rate of 50 $Ncm^3 \cdot min^{-1}$, a transient start-up period is observed during the first minutes of reaction, while steady-state conditions being recognized in the remaining period (Figure 2-6a). A relative slow increase in the hydrogen content occurs in the transient start-up period simultaneously with a constant content of carbon dioxide and a stronger decrease in the methane content. On the other hand the amounts of methane formed are lower. The concentrations of carbon dioxide are relative independent of the flow-rate applied. Traces of carbon monoxide are formed as well (~ 0.2 mol %).

The most desirable pathway of SRE produces 6 moles of hydrogen and 2 moles of

carbon dioxide. The yields of carbon dioxide, and in particular hydrogen, will only increase, if the equilibrium of the reaction is shifted to the product side. An elegant method for this purpose is the SERP. The SE-SRE is well understood, when the molar fractions of products on dry basis are plotted versus time [20, 21]. In general, four regions may be observed: a) a transient start-up period; b) a pre-breakthrough period, where the steam reforming reaction runs at maximum efficiency; c) a breakthrough period, where the efficiency of the adsorption reaction starts decreasing; d) and finally, a post-breakthrough period, where only steam reforming reaction occurs.

At this point, it is important to stress that a bi-layer system (catalyst plus sorbent) performs like a system of two separated units: a) a reaction unit (catalyst-bed), where the reactants are converted into the products which remain in equilibrium conditions, and b) a separation unit (sorption-bed), where preferentially carbon dioxide is retained, while the remaining unconverted gas mixture passes off, thus acting as a "preferential product separation". The off-gas mixture of the sorption unit, which has a different reactant composition, will pass through the third catalyst layer where the steam reforming reaction will occur in more desirable equilibrium conditions. In optimal conditions, a system of "infinite" alternated layers of catalyst and sorbent, is equivalent to a mixture of catalyst and sorbent in corresponding proportions.

The scope of this section is to demonstrate the concept of SE-SRE on a laboratory scale. The results obtained have certain relevance for further developments in engineering, especially for energy systems. In order to approach a practical SRE system with a SERP, kinetic and thermodynamic studies can be found in the following sections.

According to the results obtained with catalyst alone (Figure 2-6a), it was decided to pack the plug-flow reactor with alternated multiple layers of catalyst and sorbent. The objective was to test the concept of SE-SRE at 673 K (Figure 2-6b) in a system with four layers of catalyst (each with 5 g of mass) and three layers of sorbent (each with 16.7 g of mass).

The product distribution (hydrogen, carbon dioxide, methane and carbon monoxide)

in Figure 2-6b, shows pre-, intermediate and post-breakthrough periods. The hydrogen content in the first instants of operation is higher than in the steady state operation and higher than the one observed in the experiments with catalyst only (Figure 2-6a). This is a clear indication that the sorbent is shifting the equilibrium towards the formation of hydrogen in the transient period. A SERP can be fairly proposed for the occurring WGS reaction, and most probably also for SMR.

The plot shows an "S-shaped curve" for the carbon dioxide content vs. time. An initial absence of carbon dioxide is well visible, followed by increasing carbon dioxide content until the sorbent is completely saturated. Moreover, the levels of carbon monoxide may be reduced to a level tolerable for the application of hydrogen in proton exchange membrane fuel cells (PEMFC). In all experiments made, it was observed that breakthrough periods were only noticed for a moderate temperature of 673 K, and especially for a lower flow-rate of 50 $Ncm^3 \cdot min^{-1}$. In other words, the SERP works properly, if both reaction and adsorption rates are similar.

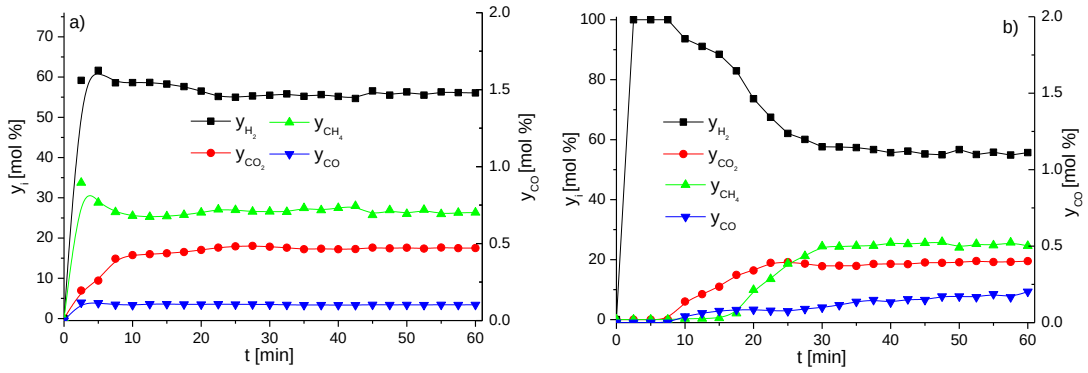

Figure 2-7 Product distribution as function of reaction time in a multilayer system; operating conditions: T = 673 K; p = 100 kPa; $\dot{V}_{inert}$ = 50 $Ncm^3 \cdot min^{-1}$; (a) m_{cat} = 4 × 10.0 g with m_{sorb} = 3 × 8.3 g; (b) m_{cat} = 4 × 1.25 g with m_{sorb} = 3 x 25.0 g.

Therefore, it is important to show the sensivity of a hybrid reactor design for a well working SE-SRE. In the following experimental sequence, it was decided to vary the mass ratio of catalyst and sorbent. Figure 2-7 depicts the effect of the mass ratio between catalyst and sorbent in a multilayer pattern arrangement. The use of the same feed flow-rate and a lower (or higher) mass of catalyst, defines the contact time which

is higher (or lower), and should decrease (increase) the conversion of the reactants and amounts of products formed. Namely of interest is hereby carbon dioxide which should appear in less amount when it leaves the sorbent layers, then the use of a higher mass of sorbent will facilitate its capture. As a result, the effect of SERP should increase. On the other hand, the employment of a higher catalyst mass, keeping the feed flow constant, should increase the amounts of carbon dioxide generated, so that the use of a lower mass of sorbent should decrease or even neutralize the desired SERP due to the less available sorption capacity of the sorbent.

At first (Figure 2-7a), the plug-flow reactor was loaded with alternated multiple layers of catalyst (4 × 10 g) and sorbent (3 × 8.3 g), using the same inert gas flow-rates, 50 $Ncm^3 \cdot min^{-1}$, and a temperature of 673 K. It is observed that the capacity of the sorbent for carbon dioxide quickly saturates. As a result, the amounts of hydrogen produced in the first instants are much lower compared with those depicted in Figure 2-7b, and the concentration of methane in the initial breakthrough period has such a high value that indeed a SERP either for WGS or SRE reaction can fairly be discarded. On the other hand, an alternated system of multiple layers, consisting of 4 × 1.25 g of catalyst and 3 × 25.0 g of sorbent (Figure 2-7b), using the same inert gas flow-rates as before, leads to higher hydrogen production in the initial breakthrough period, while carbon dioxide only starts to appear after 10 min, thus the breakthrough time increased. Moreover, during this period and especially for lower inert gas flow-rates, neither methane nor carbon monoxide appears, suggesting a SERP for WGS reaction and for the SRE reaction, respectively.

The effect of pressure and feed composition was also studied. The plug-flow reactor packed with the alternated multiple layers of catalyst (4 × 1.25g) and sorbent (3 × 25g) was tested under higher pressure conditions (p = 500 kPa) at 673 K with inert gas flow-rate of 50 $Ncm^3 \cdot min^{-1}$. The objective was to increase the sorbent capacity for carbon dioxide; however, higher pressures displace the reaction equilibrium to the reactant side so that the conversions of both ethanol and water decrease. It was found that the sorption capacity could be increased, but reaction

enhancement was not very obvious (Figure 2-8).

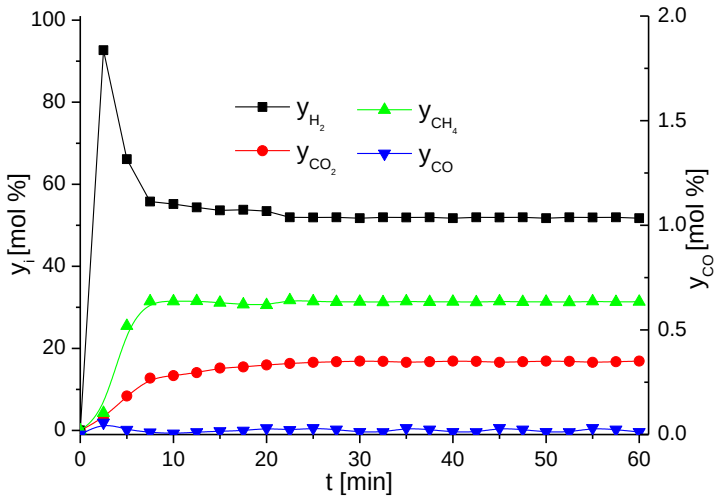

Figure 2-8 Product distribution as function of reaction time in a multilayer system; operating conditions: m_{cat} = 4 × 1.25 g with m_{sorb} = 3 × 25.0 g; T = 673 K; p = 500 kPa; $\dot{V}_{inert}$ = 50 $Ncm^3 \cdot min^{-1}$.

Finally, experiments were carried out with a water/ethanol feed ratio of $R_{S/E}$ = 3 instead of $R_{S/E}$ = 10, with the system consisting on layers of catalyst and sorbent, at 100 kPa. The idea was to ensure that the use of excess water does not disturb the performance of the hybrid system. Indeed, it seems that the use of excess water performs better than a stoichiometric feed ratio for SRE ($R_{S/E}$ = 3). Furthermore, the levels of carbon monoxide increased in the transient period, when using a low feed ratio of water/ethanol. In addition, considerable amounts of carbon deposits were detected.

We are now able to compare the results obtained at steady state conditions with those measured in the transient period, as shown in Table 2-3. The experimental conditions are listed, together with the transient conversions of both, ethanol and water, as well as yields and selectivity of hydrogen, respectively, and the steady state measurements made. Sorption enhancement can be assessed by comparing the conversions, hydrogen yields and selectivity obtained in the transient period (values obtained for the best performances ~180 s).

Table 2-3 Comparative performance between SRE and SE-SRE

Materials	Operating conditions					Transient state			Steady state		
	m_{cat} [g]	m_{sorb} [g]	T [K]	p [kPa]	$\dot{V}_{inert}$ [Ncm^3/min]	X_{EtOH} [%]	Y_{H2} [%]	S_{H2} [%]	X_{EtOH} [%]	Y_{H2} [%]	S_{H2} [%]
Octolyst	20	/	873	100	50	100	28.7	28.7	100	31.9	31.9
			873	100	200	100	60.2	60.2	100	64.6	64.6
			673	100	50	63.3	14.6	23.1	64.5	16.0	24.8
			673	100	200	100	27.1	27.1	100	31.4	31.4
Octolyst + MG30	20	50	673	100	50	76.6	16.3	21.3	65.0	16.1	24.8
	20	50	673	100	200	100	31.8	31.8	100	31.4	31.4
	40	25	673	100	50	79.1	18.0	22.8	67.5	16.4	24.2
	40	25	673	100	200	100	33.5	33.5	100	30.8	30.8
	5	75	673	100	50	100	21.8	21.8	64.2	16.1	25.1
	5	75	673	100	200	100	34.8	34.8	100	30.6	30.6
	5	75	673	500	50	71.1	13.6	19.1	49.5	12.2	24.6
	5	75	673	500	200	100	25.8	25.8	100	25.3	25.3

Among the results obtained, the introduction of the sorbent (MG30) together with the catalyst (Octolyst) in a multilayer arranged pattern show better performances in the transient period as the in the steady state periods. Even better performances reported in the present study, in terms of activity and selectivity, are those exhibited by hybrid systems consisting on low mass ratios of catalyst and sorbent (m_{cat}/m_{sorb} = 0.067) together with the use of lower inert gas flow-rates, such as a multilayer pattern system with m_{cat} = 4 × 1.25g plus m_{sorb} = 3 × 25.0 g, using a flow-rate of 50 $Ncm^3 \cdot min^{-1}$ of inert-gas in the feed.

Table 2-4 Effect of $R_{S/E}$ in the feed: hybrid system, m_{cat}/m_{sorb} = 0.067.

Operating conditions				Transient state			Steady state		
$R_{S/E}$	T [K]	p [kPa]	$\dot{V}_{inert}$ [Ncm^3/min]	X_{EtOH} [%]	Y_{H2} [%]	S_{H2} [%]	X_{EtOH} [%]	Y_{H2} [%]	S_{H2} [%]
3	673	100	50	63.4	16.4	0.259	57.0	16.4	0.288
3	673	100	200	100	24.8	0.248	84.7	23.4	0.276
10	673	100	50	100	21.8	0.218	64.2	16.1	0.251
10	673	100	200	100	34.8	0.348	100	30.6	0.306

Finally, Table 2-4 compares results obtained for the hybrid systems consisting on a low mass ratio of catalyst and sorbent (m_{cat}/m_{sorb} = 0.067), using feed ratios of $R_{S/E}$ = 3 and $R_{S/E}$ = 10, respectively. It can be seen that there is no real advantage in using a low $R_{S/E}$ = 3.

In a continuously operating cycle, the sorbent must be active for a long time. Our studies have shown that after two regeneration cycles, made with a temperature swing, the hybrid system consisting on catalyst plus sorbent (Octolyst with MG30) in multilayer pattern showed reproducibility for the isothermal reaction runs. At this stage, it must be pointed out that a stable catalyst bed was observed after carbon dioxide release by temperature increase, which is of course the key step for the application of this technology. It is now possible to elucidate the performance of the hybrid system for a practical industrial application.

2.1.4 *Conclusions*

Sorption enhanced steam reforming of ethanol can be performed on a Ni/Al_2O_3 catalyst (Octolyst 1001) coupled with a hydrotalcite based sorbent (PURAL MG30). The effects of the operating conditions (temperature and flow-rate) on the course of reaction were studied. Hydrogen was generated in the temperature range between 373 K and 873 K. A mechanism was used to explain the reaction pathways. Moreover, it was found that the hydrotalcite-like material acts as a relative good carbon dioxide sorbent at 673 K. The SERP concept was verified for this system coupling the Octolyst catalyst with the MG30 hydrotalcite sorbent. Higher amounts of hydrogen were yielded during the initial breakthrough periods. Carbon monoxide appears in traces in the product gas stream.

2.2 Thermodynamic Analysis

2.2.1 Introduction

Hydrogen is a clean energy carrier and shows an excellent performance in fuel cells [2, 3]. It is considered to have a bright future [68], because it can be produced from several sources using different methods [69]. However, PEMFC have a stringent requirement for impurities in the hydrogen carrier (10 ppm or less of carbon monoxide) [70], meaning that only selected processes are applicable for the production of hydrogen. Nowadays, the most reliable and extensively used process is the steam reforming of fossil fuels (e.g. natural gas or light hydrocarbons) [71]. However, the use of fossil raw materials has its limitations due to their depletion [72]. Therefore, the use of ethanol in steam reforming seems to be a promising alternative for hydrogen production [9, 10, 73]. Ethanol can be obtained from renewable sources such as sugar cane or lignocellulos materials [74].

SRE is an endothermic reaction, meaning that higher temperatures favor the yield of hydrogen. Unfortunately, the equilibrium conditions of the WGS inhibit the production of high purity hydrogen (absence of carbon monoxide). The hydrogen produced must be purified in cost expensive units before used in fuel cells.

Earlier studies have shown that as temperature increases, both the ethanol and water conversions as well as the hydrogen yield increase, while the methane concentration decreases at equilibrium [75, 76]. For a good hydrogen yield, SRE requires higher temperatures and higher water ratios than in methanol steam reforming [75]. Furthermore, the use of excess water in the feed can reduce undesired products such as carbon monoxide, carbon deposits and methane [76]. In addition, the effect of inert components was also considered [77], and it was found that the equilibrium can be shifted to the product side by increasing the amount of inert gas vs. ethanol ($R_{Inert/EtOH}$), minimizing the methane yield. Finally, thermodynamic calculations for SRE with an extended representation of carbon deposits were done [78, 79]; carbon deposits disappear as $R_{S/E}$ increases, mainly due to the removal of carbon nanotube (CNT) species.

Now, if carbon dioxide is selectively adsorbed by the application of a relative new technique designated as SERP [17, 80], the equilibrium can be shifted to the product side according to Le Chatelier's principle [81]. A complete conversion of ethanol can be approached [82].

SE-SRE with calcium oxides the carbon dioxide sorbent is a typical example [29], it yields higher amounts of hydrogen, higher thermal efficiency and also suppresses the formation of graphite. With optimal conditions, a relative pure hydrogen stream (97 mol %) with a carbon monoxide content of around 10 ppm can be obtained [83]. This hydrogen stream could be used directly in fuel cells. Further purification processes involving WGS, methanation and PROX would then be obsolete.

Many thermodynamic analyses on SRE and SE-SRE are available, a survey of these publications can be found in Table 2-5. The thermodynamic analyses use three main methodologies: Gibbs free energy minimization (GFEM) [75-79, 84-86], Equilibrium constants method (EQM) [87-91] or response reactions (RR) [92].

In this work, thermodynamic analysis on SRE and SE-SRE has been performed based on GFEM, with the following objectives:

- Comparison of SRE results obtained with ideal gas state vs. real gas state assumptions;
- The advantage of using SE-SRE vs. SRE;
- Comparison of equilibrium composition changes with HTlc, CaO and Li_2ZrO_3 as sorbent in the SE-SRE;
- Effect of the HTlc amount used and potassium promoted HTlc on SE-SRE;
- Comparison of the equilibrium composition with experimental results obtained.

Table 2-5 A survey of thermodynamic studies on SRE and SE-SRE.

Methodology	Condition					Research Highlights	Refs
	T [K]	p [kPa]	$R_{S/E}$	Sorbent	$R_{Inert/EtOH}$		
SRE							
GFEM	400-800	101-912	0-10	n.a.	n.a.	4.41 mol/mol_{EtOH} of hydrogen can be produced at 800 K and atmospheric pressure with $R_{S/E}$=10 in the feed.	[75]
EQM	873-973	101	2		n.a.	Molten carbonate fuel cell uses ethanol as fuel has comparable efficiency with that use methane as fuel.	[87]
GFEM	800-1200	101-507	0-80		n.a.	5.72 mol/mol_{EtOH} of H_2 can be produced at 900 K and atmospheric pressure with $R_{S/E}$=20 in the feed.	[76]
RR	400-1000	101	0-10		n.a.	Desired reaction is predominant at 800-900 K, by-products can be minimized when a high $R_{S/E}$ in the feed is used.	[92]
EQM	800-1300	101-507	3-10		n.a.	With the help of a WGS reactor, near 6 mol/mol_{EtOH} of hydrogen can be obtained at T > 1000 K, $R_{S/E}$ > 6 and atmospheric pressure.	[89]
EQM	400-1300	101	0-10		n.a.	$R_{S/E}$ higher than 3 is required to avoid coke formation when moderate temperatures are used.	[88]
EQM	300-1100	101-709	0-20		n.a.	Close to 6 mol/mol_{EtOH} of hydrogen can be obtained in a temperature range from 873 to 973 K at 101 kPa. The differences among $R_{S/E}$ are not considered.	[90]
GFEM	423-1273	101	0-10		n.a.	Optimal conditions were found to be in a temperature range from 823 to 923 K with $R_{S/E}$ > 4 in the feed.	[84]
GFEM	400-2000	101-60800	0-20		0-100	Optimal conditions: 900–1200 K, $R_{S/E}$ in the range of 3 to 6 and 101 kPa. The inert does not appreciably affect the yield of carbon monoxide.	[77]
GFEM	700-1100	100	1-10		n.a.	The maximum hydrogen yield occurs at 900 K with $R_{S/E}$ = 10 in the feed.	[85]

EQM	673-973	101	3-9		0-70	Hydrogen yield was enhanced by inert at low and moderated temperatures (< 973 K), while at high temperatures, the inert does not influence the composition of products.	[91]
GFEM	400-1200	101	0-10		n.a.	It is possible to perform SRE without carbon formation at T > 550 K with $R_{S/E}$ = 3 in the feed.	[78]
GFEM	473-1273	101	0-10		n.a.	Carbon formation only for $R_{S/E}$ < 4. In this region, graphite is formed below 673 K while CNT above 673 K.	[79]
GFEM	773-1173	101	1.6-5.2		n.a.	The optimal conditions to obtain the highest energy efficiency without carbon formation were found to be at 923 K with $R_{S/E}$ = 2.6 in the feed.	[86]
SE-SRE							
GFEM	773-1173	101-25300	2-10	CaO	n.a.	The best operating conditions for SRE with calcium oxideas carbon dioxide sorbent were found to be at 973 K, $R_{S/E}$ = 4 and p = 100 kPa.	[29]
GFEM	773-1173	101-25300	3-8	CaO	n.a.	Compare with conventional process, using sorbents increases the hydrogen yield by about 19 % and reduces the carbon dioxide content of product gas by 50.2 % at 973 K, p = 101 kPa and $R_{S/E}$ = 4.	[93]
GFEM/ EQM	773	5	3	K-HTlc	n.a.	When the carbon dioxide removal ratio exceeds 40 %, the hydrogen purity can achieve. 9.2 % at T = 773 K and $R_{S/E}$ = 3.	[94]
GFEM	573-873	100-1000	1-5	K-HTlc	n.a.	With arbon dioxideadsorption the formation of graphite can be suppressed, while the hydrogen yield can be enhanced.	[95]
GFEM	500-1450	101-507	1-14	CaO	n.a.	It is possible to obtain high purity hydrogen (97 mol %) with carbon monoxide content ~ 10 ppm. The optimal conditions: p = 507 kPa, T = 773 K and $R_{S/E}$ = 3.	[83]

2.2.2 Methodology for Thermodynamic Calculations

The prediction of the equilibrium composition was based on GFEM, which requires the total Gibbs free energy of the system expressed in equation (2.14) to be minimized [96].

$$G = G(T, P, n_1, n_2, ...n_N) \tag{2.14}$$

where n_i is the number of moles of component i and N is the number of the species in the system. The following constraint is introduced based on elemental mass balances in this system:

$$\sum_{i=1}^{N} n_i a_{ji} = b_j,\ j = 1, 2..., M \tag{2.15}$$

where a_{ji} is the number of j-type atoms in the species i, b_j is the number of j-type atoms in the feed and M refers to the types of atoms in all species.

In order to obtain the equilibrium composition at which the total Gibbs free energy is at its minimum value with the constraint (2.15), the Lagrangian multipliers λ_j were introduced to get a new function F [97]:

$$F = G + \sum_{j=1}^{M} \lambda_j \left(\sum_{i=1}^{N} n_i a_{ji} - b_j \right),\ j = 1, 2..., M \tag{2.16}$$

When G is at its minimum value, the deviation of F with respective n_i must be zero:

$$\left(\frac{\partial F}{\partial n_i} \right)_{T,P,n'} = \mu_i + \sum_{j=1}^{M} \lambda_j a_{ji} = 0, i = 1, 2..., N \tag{2.17}$$

where the subscript n' stands for keeping the amount of every component fixed except for component number i, μ_i is called the chemical potential and is defined by:

$$\mu_i = \left(\frac{\partial G}{\partial n_i} \right)_{T,P,n'} \tag{2.18}$$

For solid species, equation (2.17) can be expressed as:

$$\Delta G_{f_i}^0 + \sum_{j=1}^{M} \lambda_j a_{ji} = 0, i = 1, 2..., N \tag{2.19}$$

where ΔG_{fi}^0 is the standard Gibbs free energy of formation, which is only a function

of temperature. While for gaseous species, equation (2.17) can be further expressed as:

$$\Delta G_{f_i}^0 + RT \ln p y_i \hat{\phi}_i + \sum_{j=1}^{M} \lambda_j a_{ji} = 0, i = 1, 2..., N \tag{2.20}$$

p is the pressure of the system and y_i is the mole fraction of component i in the gas phase. $\hat{\phi}_i$ is the fugacity coefficient of component *i* in the gas mixture, which can be obtained from equation (2.21) under the assumption of real gases representation by a Virial equation of state [98].

$$\hat{\phi}_i = \exp\left[\frac{\frac{y_i p}{p_{c_i}}}{\frac{T}{T_{c_i}}} \left(B_i^0 + \omega_i B_i^1 \right) \right] \tag{2.21}$$

p_{ci} is the dimensionless critical pressure of component *i*, while T_{ci} and ω_i are the critical temperature and the acentric factor of component *i*, respectively. Terms B_i^0 and B_i^1 were calculated from Pitzer correlation, available in equation (2.22).

$$B_i^0 = 0.083 - 0.422 \cdot \left(\frac{T}{T_{c_i}} \right)^{-1.6}, B_i^1 = 0.139 - 0.172 \cdot \left(\frac{T}{T_{c_i}} \right)^{-4.2} \tag{2.22}$$

It is worth to mention that in some other publications the ideal gas state assumption has been used [29, 75, 76, 79, 83, 84, 88, 92, 94, 95].

When carbon dioxide is partially adsorbed, equation (2.20) can be modified:

$$\Delta G_{f_{CO_2}}^0 + RT \ln p y_{CO_2} (1 - f) \hat{\phi}_{CO_2} + \lambda_C + 2\lambda_O = 0 \tag{2.23}$$

where f is the fraction of adsorbed carbon dioxide, which is related with the mass and adsorption isotherm of the sorbent used:

$$f = \frac{n_{CO_2,ads}}{n_{CO_2}} = \frac{q_{eq,CO_2} \cdot m_{sorbent}}{n_{CO_2}} \tag{2.24}$$

$q_{CO_2,eq}$ is the combination of two types of adsorption, one endothermic physical adsorption and one exothermic chemical reaction. A bi-Langmuir model can be used

to describe the adsorption isotherm [40]:

$$q_{ads} = q_{\max 1}\frac{K_1 p y_{CO_2}}{1+K_1 p y_{CO_2}} + q_{\max 2}\frac{K_2 p y_{CO_2}}{1+K_2 p y_{CO_2}} \quad (2.25)$$

q_{max} is the maximum capacity for site 1 (exothermic physical adsorption) and site 2 (endothermic chemical reaction) and K is given by the equation (2.26):

$$K_1 = k_{01}\exp\left(-\Delta H_1/RT\right), K_2 = k_{02}\exp\left(-\Delta H_2/RT\right) \quad (2.26)$$

where k_{0i} is the pre-exponential factor, ΔH_1 and ΔH_2 are the enthalpies of the physical carbon dioxide adsorption and carbonation reaction, respectively.

Three different sorbents were included in this work: CaO, Li_2ZrO_3 and HTlc. For CaO and Li_2ZrO_3, only the endothermic chemical reaction was considered in the adsorption isotherm as shown in Table 2-6.

Table 2-6 Parameters used in the bi-Langmuir model for CaO, Li_2ZrO_3, HTlc and K-HTlc. [40, 102-105]

Parameters	CaO	Li_2ZrO_3	HTlc	K-HTlc
q_{max1} [mol·kg^{-1}]	n.a.	n.a.	0.0453	0.423
k_{01} [bar^{-1}]	n.a.	n.a.	$9.07\cdot10^{-3}$	$9.07\cdot10^{-3}$
ΔH_1 [kJ·mol^{-1}]	n.a.	n.a.	40.0	40.0
q_{max2} [mol·kg^{-1}]	17.83	6.53	0.0546	0.351
k_{02} [bar^{-1}]	$1.84\cdot10^{8}$	$3.83\cdot10^{8}$	$1.01\cdot10^{12}$	$1.01\cdot10^{12}$
$-\Delta H_2$ [kJ·mol^{-1}]	-171.9	-150.9	-130.8	-130.8

The values for the feed ratio of sorbent to ethanol are based on the stoichiometric ratio of carbon atoms, CaO or $Li_2ZrO_3/EtOH_{inlet}$ = 2. For HTlc, considering the destruction of the HTlc structure which occurs at ≥ 773 K [99], SE-SRE with HTlc as sorbent was performed in the temperature range from 573 to 773 K. Conventional HTlc has a small carbon dioxide sorption capacity, around 0.10 mol·kg^{-1} [100]. In order to employ HTlc as sorbent in SE-SRE process, the ratio of HTlc to ethanol is set as 1mol of EtOH vs. 20 kg of HTlc, which is in the stoichiometric ratio of carbon atoms. In addition, the effect of the ratio of HTlc and K-HTlc was also analyzed.

In total, 4 atoms, C, H, O and He as well as 9 compounds, C_2H_6O, C_2H_4O, H_2O, H_2,

CO, CO_2, CH_4, He in the gas phase and C as solid species are considered in the equilibrium system based on a previous experimental work [82].

The initial quantity of ethanol was set as 1 mol, the molar quantities of water and helium are dependent on the $R_{S/E}$ and inert-to-ethanol ratio ($R_{Inert/EtOH}$). Finally, the following explicit forms are obtained:

$$\Delta G^0_{f_C} + \lambda_C = 0, \Delta G^0_{f_{He}} + RT(\ln p \cdot \hat{\phi}_{He} \cdot y_{He}) + \lambda_{He} = 0$$
$$\Delta G^0_{f_{H_2}} + RT(\ln p \cdot \hat{\phi}_{H_2} \cdot y_{H_2}) + 2\lambda_H = 0, \Delta G^0_{f_{CO}} + RT(\ln p \cdot \hat{\phi}_{CO} \cdot y_{CO}) + \lambda_C + \lambda_O = 0$$
$$\Delta G^0_{f_{CH_4}} + RT(\ln p \cdot \hat{\phi}_{CH_4} \cdot y_{CH_4}) + \lambda_C + 4\lambda_H = 0, \Delta G^0_{f_{H_2O}} + RT(\ln p \cdot \hat{\phi}_{H_2O} \cdot y_{H_2O}) + 2\lambda_H + \lambda_O = 0$$
$$\Delta G^0_{f_{CO_2}} + RT(\ln p \cdot \hat{\phi}_{CO_2} \cdot y_{CO_2} \cdot (1 - f)) + \lambda_C + 2\lambda_O = 0,$$
$$\Delta G^0_{f_{C_2H_4O}} + RT(\ln p \cdot \hat{\phi}_{C_2H_4O} \cdot y_{C_2H_4O}) + 2\lambda_C + 4\lambda_H + \lambda_O = 0,$$
$$\Delta G^0_{f_{C_2H_6O}} + RT(\ln p \cdot \hat{\phi}_{C_2H_6O} \cdot y_{C_2H_6O}) + 2\lambda_C + 6\lambda_H + \lambda_O = 0, n_{He} = n_{C_2H_6O} \cdot R_{inert/EtOH}$$
$$n_C + n_{CH_4} + n_{CO} + n_{CO_2} + 2n_{C_2H_4O} + 2n_{C_2H_6O} = 2, n_{H_2O} + n_{CO} + 2n_{CO_2} + n_{C_2H_4O} + n_{C_2H_6O} = R_{S/E} + 1$$
$$4n_{CH_4} + 2n_{H_2} + 2n_{H_2O} + 4n_{C_2H_4O} + 6n_{C_2H_6O} = 2R_{S/E} + 6 \quad (2.27)$$

The task is to solve the above 13 non-linear equations. The calculations for this non-linear system were performed in Matlab R2010b using the *fsolve* function following the Levenberg-Marquardt algorithm [101]. All the thermodynamic data required for the calculation were taken from references [40, 102-105].

2.2.3 Results and Discussion

2.2.3.1 Real gas state vs. ideal gas state assumption

The thermodynamic equilibrium state is an important issue for any catalytic process; it provides information on how far or how close the process can reach equilibrium state. Table 2-7 shows a comparison of the thermodynamic equilibrium data calculated for SRE with real gas state and ideal gas state at a pressure of 100 kPa. It could be observed that both the conversions of water and the yields of products (hydrogen, carbon monoxide, carbon dioxide and methane) show considerable deviations with increasing temperature and decreasing $R_{S/E}$. However, at high temperatures (≥ 773 K), there are some differences between the hydrogen and carbon monoxide yields from real gas state and ideal gas state. As a result, it is recommended

to employ real gas state for thermodynamic analysis of SRE and SE-SRE. All the calculated results below were obtained from real gas state.

Table 2-7 Comparison of the thermodynamic equilibrium data for SRE with real gas state assumption and ideal gas state assumption at 100 kPa.

p [kPa]	$R_{S/E}$	T [K]	SRE (real gas)					SRE (ideal gas)				
			X_{H_2O}	Y_{H_2}	Y_{CO}	Y_{CO_2}	Y_{CH_4}	X_{H_2O}	Y_{H_2}	Y_{CO}	Y_{CO_2}	Y_{CH_4}
			[%]	[mol/mol$_{EtOH,0}$]				[%]	[mol/mol$_{EtOH,0}$]			
100	3	473	0.4	0.02	0.00	0.51	1.49	0.5	0.03	0.00	0.26	1.49
		573	3.0	0.18	0.00	0.54	1.45	3.6	0.22	0.00	0.28	1.45
		673	11.2	0.69	0.02	0.66	1.32	13.0	0.79	0.01	0.35	1.30
		773	26.3	1.72	0.14	0.83	1.04	29.5	1.85	0.08	0.45	1.02
		873	43.0	3.22	0.63	0.83	0.54	48.1	3.30	0.42	0.51	0.57
		973	51.4	4.35	1.27	0.64	0.10	58.1	4.50	1.01	0.44	0.12
	7	473	0.4	0.05	0.00	0.51	1.49	0.5	0.07	0.00	0.26	1.48
		573	2.6	0.36	0.00	0.59	1.41	3.2	0.45	0.00	0.31	1.39
		673	9.2	1.31	0.02	0.82	1.17	10.8	1.52	0.01	0.44	1.12
		773	20.7	3.04	0.14	1.16	0.71	23.1	3.31	0.08	0.64	0.65
		873	30.4	4.77	0.52	1.30	0.18	33.5	5.01	0.32	0.76	0.17
		973	30.7	5.13	0.82	1.17	0.01	34.6	5.39	0.55	0.72	0.01
	10	473	0.3	0.07	0.00	0.52	1.48	0.5	0.09	0.00	0.26	1.48
		573	2.4	0.49	0.00	0.62	1.38	3.0	0.61	0.00	0.33	1.35
		673	8.5	1.72	0.02	0.92	1.07	9.9	1.99	0.01	0.50	1.00
		773	18.2	3.78	0.13	1.34	0.52	20.2	4.11	0.08	0.74	0.45
		873	24.2	5.27	0.42	1.50	0.08	26.2	5.50	0.25	0.85	0.06
		973	23.6	5.35	0.63	1.36	0.00	26.0	5.59	0.39	0.80	0.00
	20	473	0.3	0.13	0.00	0.53	1.47	0.5	0.18	0.00	0.27	1.45
		573	2.2	0.88	0.00	0.72	1.28	2.7	1.10	0.00	0.39	1.23
		673	7.1	2.86	0.02	1.20	0.78	8.2	3.28	0.01	0.66	0.68
		773	12.7	5.21	0.11	1.72	0.17	13.6	5.48	0.06	0.92	0.12
		873	13.7	5.73	0.24	1.75	0.01	14.3	5.85	0.13	0.94	0.01
		973	13.2	5.64	0.36	1.64	0.00	14.0	5.80	0.20	0.91	0.00

2.2.3.2 Carbon deposits

It is known that carbon formation can occur during SRE [106], but at a certain $R_{S/E}$ the formation can be suppressed. This topic was considered in some previous works,

those who considered solid deposits formation, represented carbonaceous deposits simply as graphite [77, 84, 85, 107, 108]. The calculated yields for hydrogen and carbon deposits (graphite) are shown in Figure 2-9. It can be found that carbon deposits are formed below $R_{S/E}$ = 3, associated also with a low hydrogen yield in this region, fully in agreement with a previous work [79]. It must be emphasized that the ethanol used in SRE can be obtained from bio-ethanol by fermentation processes [109] where the $R_{S/E}$ is between 10 and 20, while carbon deposits may change the equilibrium composition only when the $R_{S/E}$ is low ($\leq$ 3). Therefore, carbon formation will not be a key point of our work.

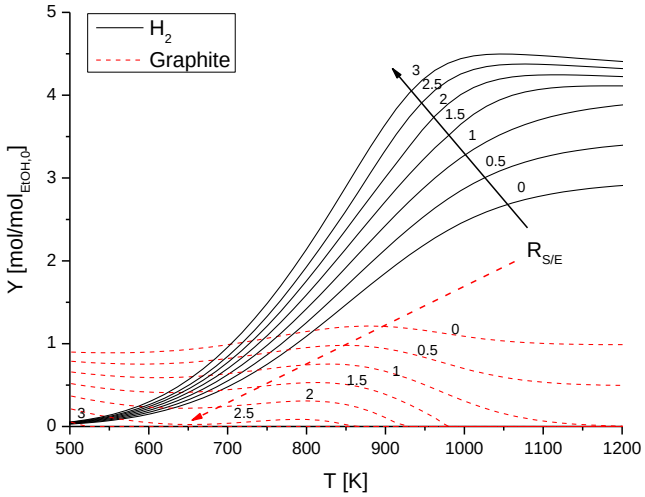

Figure 2-9 Calculated yields for hydrogen and carbon deposits supposed to be graphite.

2.2.3.3 Conversions in steam reforming of ethanol

It might be pointed out that ethanol and acetaldehyde are thermodynamically unstable; therefore, the conversions of ethanol and acetaldehyde are always very close to 100 % within the temperature range analyzed, while the conversion of water is higher at a lower pressure, lower $R_{S/E}$ and higher temperatures, as depicted in Table 2-7. This behavior is in agreement with the principle of Le Chatelier, because conversion in SRE is associated with an endothermic change and volume increase reaction, thus a temperature increase favors conversion. Not negligible, the conversion of water is a critical issue, because it enables both important processes, steam methane reforming and water-gas-shift reactions.

2.2.3.4 Steam reforming of ethanol under pressure conditions

Figure 2-10 shows the hydrogen yields at equilibrium for SRE at 100 kPa (Figure 2-10a) and 500 kPa (Figure 2-10b), respectively. The hydrogen yield at 100 kPa (Figure 2-10a) quickly increases with temperature and $R_{S/E}$ in the feed which reduces/avoids the formation of coke significantly; while for a higher pressure of 500 kPa the yield is lower, as expected from the principle of Le Chatelier. As a result, high pressures are not recommended for SRE. In addition, when steam is used in excess, the $R_{S/E}$ has no longer a strong effect on SRE, while temperature becomes the major parameter for hydrogen production.

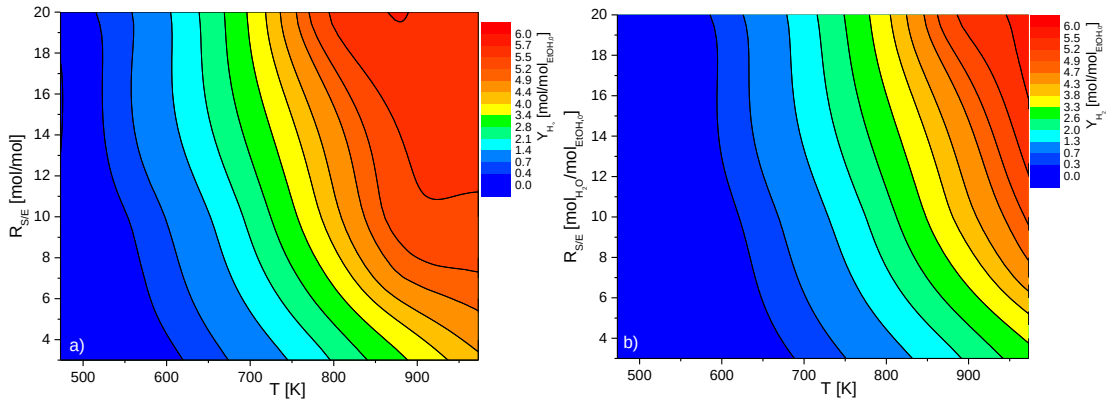

Figure 2-10 Thermodynamic calculation of hydrogen yields from SRE when p = 100 kPa (a) and p = 500 kPa (b)

In all the operating conditions analyzed, the theoretically maximum hydrogen yield (6 mols hydrogen per mol of ethanol converted) cannot be found, which can be overcome by shifting the equilibrium of SRE. Both, hydrogen and carbon dioxide can be selectively removed, thus pushing the equilibrium constant to the product side. In this work, the discussion is focused on carbon dioxide sorption, comparing different materials (CaO, Li_2ZrO_3 or HTlc) which preferentially exhibit this property.

2.2.3.5 Sorption-enhanced steam reforming of ethanol

Sorption-enhanced steam reforming of ethanol is a hybrid process involving catalytic reforming of ethanol and carbon dioxide capture with adsorbents. Table 2-8 depicts a comparison of the calculated thermodynamic equilibrium data between SRE and

SE-SRE with calcium oxide, lithium zirconate or HTlc as carbon dioxide sorption materials at a pressure of 100 kPa. The results obtained for the use of CaO provides an improvement in hydrogen equilibrium composition due to the disappearance of carbon dioxide, thus inducing a shift of the chemical equilibrium to the product side. However, this improvement is not maintained when the temperature is higher (> 873 K), because SRE without sorption already reaches high hydrogen yields in this region. Furthermore, the decrease of the hydrogen yield in this region can be a contribution of decarbonation:

$$CaCO_{3(s)} \rightarrow CO_{2(g)} + CaO_{(s)} \qquad (\Delta H^{0}_{873} = +171.3\ kJmol^{-1}) \qquad (2.28)$$

Lithium zirconate is another kind of high temperature carbon dioxide sorbent. The reversible chemical adsorption/desorption reaction can be described as:

$$Li_2ZrO_{3(s)} + CO_{2(g)} \leftrightarrow Li_2CO_{3(s)} + ZrO_{2(s)} \qquad (\Delta H^{0}_{873K} = -146.7\ kJmol^{-1}) \quad (2.29)$$

The thermodynamic equilibrium of SE-SRE with Li_2ZrO_3 as sorbent has in principle similar results towards calcium oxide as sorbent. The enhancement on hydrogen yields becomes insignificant at 973 K. In addition, from reports in literature it is known that pure Li_2ZrO_3 has extremely slow sorption kinetics [110]. As a result, employing un-promoted Li_2ZrO_3 as sorbent is not appropriate for SE-SRE.

On the other hand, HTlc show higher sorption enhancement at lower temperature ranges than CaO or Li_2ZrO_3. Therefore, the use of the former class of materials causes an increase in hydrogen production at lower temperatures, while in the latter two cases the operating temperature range is higher for a successful enhancement of the hydrogen production. The results obtained where catalyst and HTlc are coupled in a hybrid system with $R_{S/E}$ above 10 at 773 K, show high equilibrium yield of hydrogen very close to 6.

The results obtained suggest that the use of HTlc for carbon dioxide capture is recommended, because it is possible to produce hydrogen near to the stoichiometric limit with lower energy requirements for the hybrid reactor operation. However, the kinetics of sorption and SRE, as well as the regeneration of the sorbent in a cyclic process are critical issues, should be investigated in the following chapters.

Table 2-8 A comparison of SE-SRE with CaO, Li_2ZrO_3 and HTlc as carbon dioxide sorption materials at 100 kPa.

$R_{S/E}$	T [K]	SE-SRE with CaO					SE-SRE with Li_2ZrO_3					SE-SRE with HTlc				
		X_{H_2O} [%]	Y_{H_2}	Y_{CO} [mol/mol$_{EtOH,0}$]	Y_{CO_2}	Y_{CH_4}	X_{H_2O} [%]	Y_{H_2}	Y_{CO} [mol/mol$_{EtOH,0}$]	Y_{CO_2}	Y_{CH_4}	X_{H_2O} [%]	Y_{H_2}	Y_{CO} [mol/mol$_{EtOH,0}$]	Y_{CO_2}	Y_{CH_4}
3	573	13.4	0.8	$8.1\cdot10^{-6}$	0.001	1.3	9.6	0.6	$2.8\cdot10^{-5}$	0.004	1.4	7.9	0.5	$4.4\cdot10^{-5}$	0.009	1.4
	623	19.1	1.1	$1.0\cdot10^{-4}$	0.004	1.2	14.0	0.8	$2.8\cdot10^{-4}$	0.016	1.3	14.4	0.9	$2.6\cdot10^{-4}$	0.014	1.3
	673	25.4	1.5	$8.9\cdot10^{-4}$	0.014	1.1	19.6	1.2	$2.2\cdot10^{-3}$	0.049	1.2	28.4	1.7	$6.0\cdot10^{-4}$	0.008	1.1
	723	32.1	1.9	$5.8\cdot10^{-3}$	0.043	1.0	26.1	1.6	$1.3\cdot10^{-2}$	0.123	1.1	50.5	3.0	$8.9\cdot10^{-4}$	0.003	0.7
	773	39.1	2.4	$2.9\cdot10^{-2}$	0.106	0.9	33.6	2.1	$5.4\cdot10^{-2}$	0.246	1.0	72.1	4.3	$1.2\cdot10^{-3}$	0.001	0.4
	873	52.6	3.5	$3.3\cdot10^{-1}$	0.332	0.5	48.4	3.4	$4.4\cdot10^{-1}$	0.511	0.6	n.a.	n.a.	n.a.	n.a.	n.a.
	973	57.8	4.5	$1.0\cdot10^{0}$	0.441	0.1	54.9	4.4	$1.1\cdot10^{0}$	0.526	0.1	n.a.	n.a.	n.a.	n.a.	n.a.
7	573	9.6	1.3	$1.4\cdot10^{-5}$	0.002	1.2	6.8	1.0	$4.1\cdot10^{-5}$	0.010	1.3	5.7	0.8	$6.9\cdot10^{-5}$	0.018	1.3
	623	13.3	1.9	$1.7\cdot10^{-4}$	0.011	1.0	10.0	1.4	$4.6\cdot10^{-4}$	0.039	1.1	10.3	1.4	$4.1\cdot10^{-4}$	0.031	1.1
	673	17.8	2.5	$1.8\cdot10^{-3}$	0.045	0.9	13.9	2.0	$3.5\cdot10^{-3}$	0.119	1.0	19.8	2.8	$9.4\cdot10^{-4}$	0.021	0.8
	723	21.9	3.1	$9.7\cdot10^{-3}$	0.121	0.7	18.7	2.6	$1.9\cdot10^{-2}$	0.283	0.8	33.4	4.7	$1.2\cdot10^{-3}$	0.008	0.3
	773	26.7	3.8	$4.3\cdot10^{-2}$	0.278	0.5	24.0	3.4	$7.1\cdot10^{-2}$	0.519	0.6	41.6	5.8	$7.8\cdot10^{-4}$	0.003	0.0

	873	34.2	5.1	$3.0 \cdot 10^{-1}$	0.680	0.2	32.5	4.9	$3.9 \cdot 10^{-1}$	0.932	0.2	n.a.	n.a.	n.a.	n.a.	n.a.
	973	33.3	5.3	$6.5 \cdot 10^{-1}$	0.859	0.0	32.1	5.2	$7.2 \cdot 10^{-1}$	0.993	0.0	n.a.	n.a.	n.a.	n.a.	n.a.
	573	8.2	1.6	$1.8 \cdot 10^{-5}$	0.004	1.1	5.9	1.2	$5.4 \cdot 10^{-5}$	0.015	1.2	5.0	1.0	$4.5 \cdot 10^{-4}$	0.027	1.3
	623	11.3	2.3	$2.3 \cdot 10^{-4}$	0.017	0.9	8.7	1.7	$6.0 \cdot 10^{-4}$	0.059	1.1	9.0	1.8	$5.2 \cdot 10^{-4}$	0.046	1.1
	673	14.6	2.9	$2.1 \cdot 10^{-3}$	0.066	0.8	12.0	2.4	$4.5 \cdot 10^{-3}$	0.179	0.9	16.7	3.3	$1.2 \cdot 10^{-3}$	0.031	0.7
10	723	18.3	3.7	$1.2 \cdot 10^{-2}$	0.190	0.6	16.0	3.2	$2.2 \cdot 10^{-2}$	0.403	0.7	26.3	5.3	$1.2 \cdot 10^{-3}$	0.012	0.2
	773	22.0	4.5	$4.9 \cdot 10^{-2}$	0.405	0.4	20.4	4.1	$7.7 \cdot 10^{-2}$	0.694	0.4	29.5	5.9	$6.3 \cdot 10^{-4}$	0.003	0.0
	873	26.3	5.5	$2.5 \cdot 10^{-1}$	0.844	0.1	25.4	5.4	$3.3 \cdot 10^{-1}$	1.121	0.1	n.a.	n.a.	n.a.	n.a.	n.a.
	973	24.9	5.5	$5.0 \cdot 10^{-1}$	1.032	0.0	24.3	5.4	$5.6 \cdot 10^{-1}$	1.179	0.0	n.a.	n.a.	n.a.	n.a.	n.a.
	573	6.0	2.4	$3.5 \cdot 10^{-5}$	0.009	0.9	4.5	1.8	$9.7 \cdot 10^{-5}$	0.036	1.1	3.9	1.5	$1.5 \cdot 10^{-4}$	0.057	1.1
	623	8.0	3.2	$4.5 \cdot 10^{-4}$	0.048	0.7	6.4	2.6	$1.0 \cdot 10^{-3}$	0.142	0.9	6.7	2.7	$8.5 \cdot 10^{-4}$	0.103	0.8
	673	10.1	4.0	$3.6 \cdot 10^{-3}$	0.174	0.5	8.8	3.5	$6.8 \cdot 10^{-3}$	0.386	0.6	11.4	4.6	$1.7 \cdot 10^{-3}$	0.071	0.4
20	723	12.3	4.9	$1.7 \cdot 10^{-2}$	0.418	0.3	11.4	4.6	$2.8 \cdot 10^{-2}$	0.740	0.3	14.7	5.9	$1.2 \cdot 10^{-3}$	0.023	0.0
	773	13.8	5.6	$4.8 \cdot 10^{-2}$	0.701	0.1	13.3	5.4	$7.2 \cdot 10^{-2}$	1.081	0.1	15.0	6.0	$4.7 \cdot 10^{-4}$	0.006	0.0
	873	14.2	5.8	$1.5 \cdot 10^{-1}$	1.122	0.0	14.0	5.8	$1.9 \cdot 10^{-1}$	1.419	0.0	n.a.	n.a.	n.a.	n.a.	n.a.
	973	13.5	5.7	$2.9 \cdot 10^{-1}$	1.334	0.0	13.4	5.7	$3.2 \cdot 10^{-1}$	1.480	0.0	n.a.	n.a.	n.a.	n.a.	n.a.

Table 2-9 A comparison of SE-SRE with CaO, Li_2ZrO_3 and HTlc as carbon dioxide sorption materials at 500 kPa.

$R_{S/E}$	T [K]	SE-SRE with CaO					SE-SRE with Li_2ZrO_3					SE-SRE with HTlc				
		X_{H_2O}	Y_{H_2}	Y_{CO}	Y_{CO_2}	Y_{CH_4}	X_{H_2O}	Y_{H_2}	Y_{CO}	Y_{CO_2}	Y_{CH_4}	X_{H_2O}	Y_{H_2}	Y_{CO}	Y_{CO_2}	Y_{CH_4}
		[%]		[mol/mol$_{EtOH,0}$]			[%]		[mol/mol$_{EtOH,0}$]			[%]		[mol/mol$_{EtOH,0}$]		
3	573	7.6	0.5	$1.1\cdot10^{-6}$	0.000	1.4	3.0	0.3	$9.8\cdot10^{-6}$	0.001	1.5	3.9	0.2	$7.3\cdot10^{-6}$	0.002	1.4
	623	11.7	0.7	$1.3\cdot10^{-5}$	0.001	1.3	8.3	0.5	$3.8\cdot10^{-5}$	0.003	1.4	8.2	0.5	$3.7\cdot10^{-5}$	0.002	1.4
	673	16.6	1.0	$1.0\cdot10^{-4}$	0.002	1.3	12.3	0.7	$2.8\cdot10^{-4}$	0.008	1.3	18.4	1.1	$7.6\cdot10^{-5}$	0.001	1.2
	723	22.0	1.3	$6.7\cdot10^{-4}$	0.007	1.2	17.0	1.0	$1.6\cdot10^{-3}$	0.022	1.2	37.9	2.3	$1.0\cdot10^{-4}$	0.000	0.9
	773	27.7	1.7	$3.4\cdot10^{-3}$	0.017	1.1	22.3	1.3	$7.4\cdot10^{-3}$	0.050	1.2	60.2	3.6	$1.3\cdot10^{-4}$	0.000	0.6
	873	39.5	2.4	$5.1\cdot10^{-2}$	0.084	0.9	34.4	2.2	$8.6\cdot10^{-2}$	0.173	0.9	n.a.	n.a.	n.a.	n.a.	n.a.
	973	50.2	3.4	$3.5\cdot10^{-1}$	0.215	0.6	46.2	3.2	$4.6\cdot10^{-1}$	0.320	0.6	n.a.	n.a.	n.a.	n.a.	n.a.
7	573	5.5	0.8	$1.8\cdot10^{-6}$	0.000	1.3	3.8	0.5	$5.9\cdot10^{-6}$	0.002	1.4	6.8	0.1	$9.7\cdot10^{-6}$	0.003	1.4
	623	8.4	1.2	$2.1\cdot10^{-5}$	0.001	1.2	6.1	0.8	$6.1\cdot10^{-5}$	0.006	1.3	6.6	0.8	$6.1\cdot10^{-5}$	0.005	1.3
	673	11.7	1.6	$1.8\cdot10^{-4}$	0.006	1.1	8.8	1.2	$4.6\cdot10^{-4}$	0.020	1.2	6.1	1.8	$1.3\cdot10^{-4}$	0.003	1.1
	723	15.2	2.1	$1.2\cdot10^{-3}$	0.018	1.0	12.0	1.7	$2.7\cdot10^{-3}$	0.054	1.1	5.2	3.5	$1.6\cdot10^{-4}$	0.001	0.6
	773	18.9	2.7	$5.9\cdot10^{-3}$	0.050	0.8	15.7	2.2	$1.2\cdot10^{-2}$	0.126	0.9	4.3	5.3	$1.4\cdot10^{-4}$	0.000	0.2

	873	26.7	3.8	$7.6•10^{-2}$	0.227	0.5	24.2	3.5	$1.2•10^{-1}$	0.393	0.6	n.a.	n.a.	n.a.	n.a.	n.a.
	973	32.5	4.9	$3.6•10^{-1}$	0.481	0.2	30.7	4.8	$4.5•10^{-1}$	0.645	0.2	n.a.	n.a.	n.a.	n.a.	n.a.
	573	4.8	1.0	$2.4•10^{-6}$	0.000	1.3	3.4	0.7	$7.5•10^{-6}$	0.002	1.3	2.9	0.6	$1.3•10^{-5}$	0.005	1.4
	623	7.3	1.5	$2.8•10^{-5}$	0.002	1.1	5.4	1.1	$8.7•10^{-5}$	0.010	1.2	4.8	1.0	$7.8•10^{-5}$	0.007	1.3
	673	10.0	2.0	$2.4•10^{-4}$	0.009	1.0	7.6	1.5	$6.1•10^{-4}$	0.030	1.1	10.5	2.1	$1.6•10^{-4}$	0.005	1.0
10	723	12.9	2.6	$1.6•10^{-3}$	0.030	0.9	10.4	2.1	$3.5•10^{-3}$	0.084	1.0	20.4	4.1	$1.9•10^{-4}$	0.002	0.5
	773	15.8	3.2	$7.9•10^{-3}$	0.082	0.7	13.5	2.7	$1.5•10^{-2}$	0.190	0.8	28.4	5.7	$1.4•10^{-4}$	0.001	0.1
	873	21.9	4.5	$8.7•10^{-2}$	0.336	0.4	20.3	4.2	$1.3•10^{-1}$	0.542	0.4	n.a.	n.a.	n.a.	n.a.	n.a.
	973	25.2	5.4	$3.2•10^{-1}$	0.623	0.1	24.2	5.2	$4.0•10^{-1}$	0.815	0.1	n.a.	n.a.	n.a.	n.a.	n.a.
	573	3.7	1.5	$4.3•10^{-6}$	0.001	1.1	2.6	1.0	$1.3•10^{-5}$	0.005	1.2	1.8	0.7	$2.6•10^{-5}$	0.009	1.3
	623	5.3	2.1	$5.3•10^{-5}$	0.006	1.0	4.0	1.6	$1.4•10^{-4}$	0.022	1.1	3.6	1.4	$1.4•10^{-4}$	0.016	1.1
	673	7.1	2.8	$4.6•10^{-4}$	0.025	0.8	5.7	2.3	$1.1•10^{-3}$	0.075	0.9	7.5	3.0	$2.8•10^{-4}$	0.011	0.8
20	723	8.9	3.6	$2.9•10^{-3}$	0.083	0.6	7.6	3.0	$5.9•10^{-3}$	0.199	0.7	13.0	5.2	$2.7•10^{-4}$	0.004	0.2
	773	10.8	4.3	$1.3•10^{-2}$	0.212	0.4	9.7	3.9	$2.3•10^{-2}$	0.410	0.5	14.9	5.9	$1.2•10^{-4}$	0.001	0.0
	873	13.6	5.5	$8.7•10^{-2}$	0.603	0.1	13.2	5.4	$1.2•10^{-1}$	0.889	0.1	n.a.	n.a.	n.a.	n.a.	n.a.
	973	13.8	5.7	$2.1•10^{-1}$	0.895	0.0	13.6	5.7	$2.7•10^{-1}$	1.127	0.0	n.a.	n.a.	n.a.	n.a.	n.a.

2.2.3.6 SE-SRE under pressure conditions

It is expected that, in a presence of a sorbent, a pressure increase (p = 500 kPa) could enhance sorption of carbon dioxide. Then, less carbon dioxide should be present at equilibrium. The operation under pressure was analyzed to verify possible improvements in the hydrogen production at higher pressures.

Table 2-9 compares the thermodynamic equilibrium data between the SRE and the SE-SRE with CaO, Li_2ZrO_3 and HTlc as carbon dioxide sorption materials at a pressure of 500 kPa. As it can be seen for SRE, when comparing the results with Table 2-8, the maximum in hydrogen yield is reached at 973 K with a pressure of 500 kPa instead of 873 K at 100 kPa.

It can be found that the decrease of carbon dioxide yield is noticeable, but the SERP with pressure also affects methane equilibrium composition, thus reducing the hydrogen yield. The use of pressure improves the performance of the sorbent, but pressure also shifts the equilibrium to the reactants side. According to these results, the use of pressurized processes does not seem to be appropriate for hydrogen production through SE-SRE.

2.2.3.7 Influence of promoter and amount on SE-SRE with HTlc

In Figure 2-11, the effects of the HTlc amount as well as the effects of the K-promoted HTlc amount are depicted. The higher the temperature and the higher the amount of the HTlc used in the feed, the higher hydrogen yield (Figure 2-11a). Traces of carbon dioxide (Figure 2-11b) and especially carbon monoxide (Figure 2-11c) are obtained, for HTlc with an amount of 200 Kg on the feed of K-promoted HTlc with an amount of 20 Kg have shown carbon monoxide levels less than 10 ppm. Hydrogen produced under these conditions can be used directly for PEMFC [70], while further purification units (WGS, PROX, Methanation) are not required.

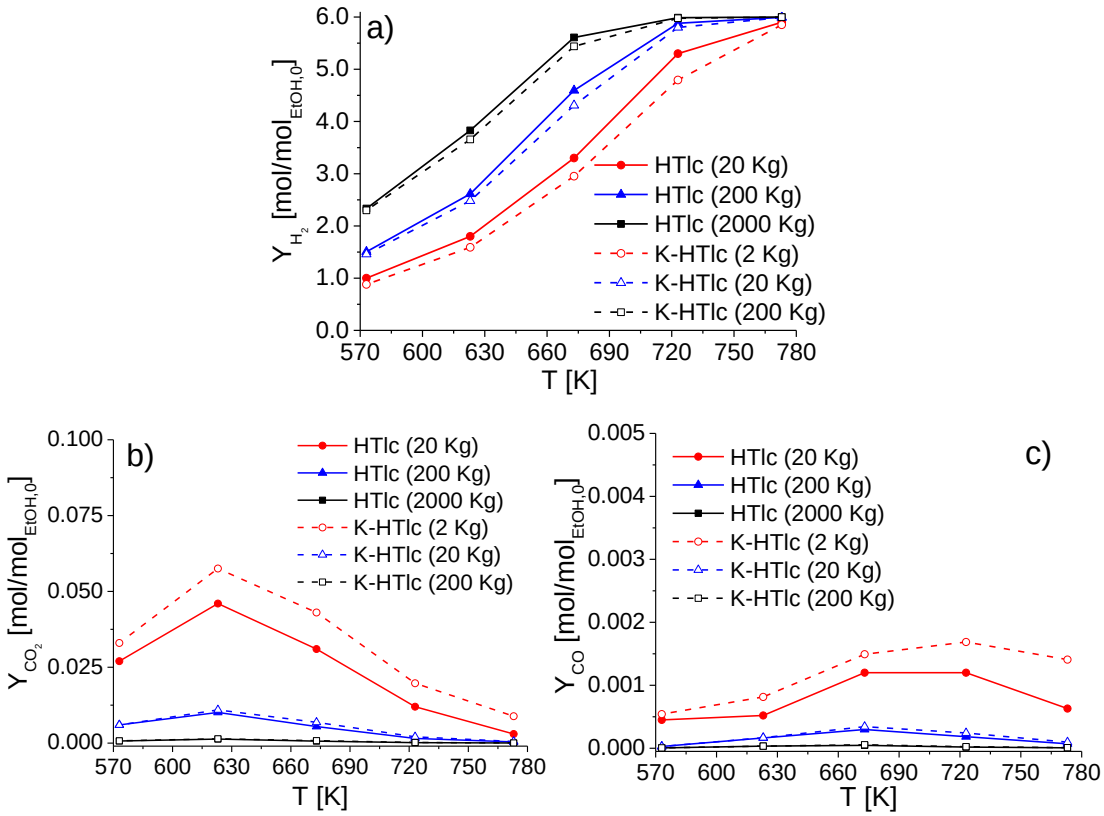

Figure 2-11 Thermodynamic equilibrium for SE-SRE with different HTlc ratios and K-promoted HTlc: Hydrogen yield (a), carbon dioxide yield (b) and carbon monoxide yield (c).

2.2.3.8 Comparison of results

The comparison of results from thermodynamic models and experimental data is quite difficult since the experimental data reported in literature are not necessarily at equilibrium conditions. However, it is useful to compare experimental results with thermodynamic data. The comparison allows us to verify how far the system is from equilibrium conditions, for possible improvements. Figure 2-12 illustrates a comparison between experimental works [82, 97] and thermodynamic calculations [83, 97].

In Figure 2-12a, the calculated product compositions regarding to the works of Silva et al. [83] and He et al. [97] for SRE at 823 K, p=100 kPa and $R_{S/E}$ = 6 can be found. Under the real gas state, the product gas from our thermodynamic analysis had a composition of 64.9 mol % hydrogen and 5.37 mol % of carbon monoxide, within a

good agreement with results from other researchers.

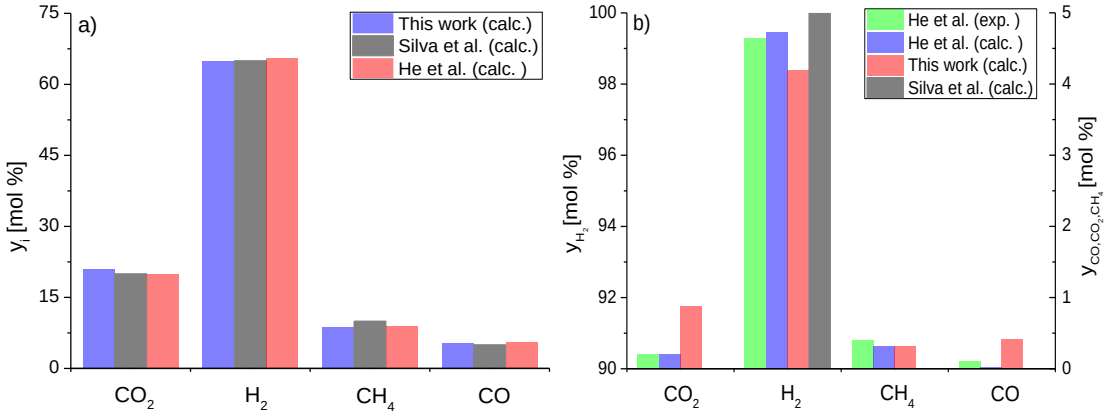

Figure 2-12 Comparison between experimental and theoretical data of He et al. [97], Silva et al. [83] and this work for the prediction of the equilibrium compositions when T = 823 K, p = 100 kPa and $R_{S/E}$ = 6, SRE (a) and SE-SRE using CaO as sorbent (b).

When CaO is used as sorbent in SE-SRE (Figure 2-12b), under the same reaction conditions, the yields of hydrogen and other undesired species calculated in this work, deviate slightly from the results of He et al. [97] and Silva et al. [83]. It might be referred that in this work the performed calculations where made with real gas state, while the works of He and Silva considered ideal gas state.

2.2.3.9 Influence of inert species

The use of inert carrier gases has to be taken into account due to the fact that most experiments are carried out with inert. Figure 2-13a shows the effect of inert gas ratios $R_{inert}/_{EtOH}$ on equilibrium compositions at 673 K, p = 100 kPa and $R_{S/E}$ = 10. It could be observed that with increasing inert gas ratios, both the conversion of water and the hydrogen equilibrium amounts increase, while methane decreases. However, the amounts of carbon dioxide and carbon monoxide remain relative constant. These results show that reactants and products diluted in inert gas could affect the conversion and product distribution.

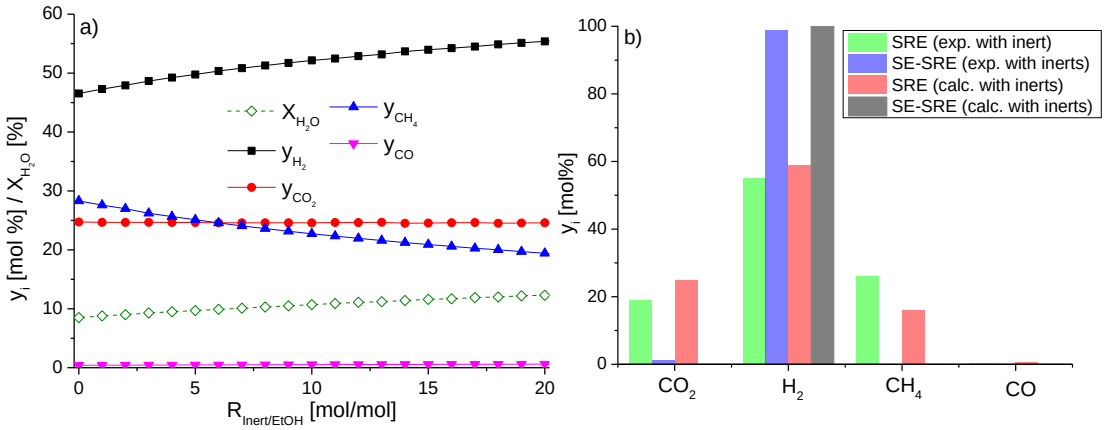

Figure 2-13 Thermodynamic equilibrium composition with inert gas at 673 K, $R_{S/E}$ = 10 and p = 100 kPa, when no sorbent is included (a) and comparison between experimental and theoretical data of Cunha et al. [82] and this work when HTlc is included (b).

The comparison between experimental results [82] and thermodynamic data of SRE with inert gas and SE-SRE with HTlc as carbon dioxide sorbent is shown in Figure 2-13b. SE-SRE results obtained from the experiments indicate that during the first 10 minutes of reaction almost all ethanol was converted along with very high hydrogen purities (~ 96 mol %). The results obtained, mostly, indicate that the catalytic SRE process is away from this theoretical work, while the SE-SRE at the same condition is close to it.

2.2.4 Conclusions

Thermodynamic equilibrium analysis of SRE indicates an improvement in hydrogen yield and purity when an HTlc sorbent is used in the system. HTlc sorbent is more preferable than CaO and Li_2ZrO_3, because HTlc has a better adsorption performance than the others at lower temperatures. The results of this work show that when enough sorbent is used, the hydrogen yield can reach close to 6 mol hydrogen per mol ethanol converted, while the content of carbon dioxide in the product gas is less than 10 ppm at 773 K and $R_{S/E} \geq 10$. According to the thermodynamic equilibrium analysis, the use of further purification units would not be necessary. These conclusions are also proved experimentally.

2.3 Kinetic Study

2.3.1 Introduction

Hydrogen is the energy carrier of the future [111, 112]. It is used in fuel cells for energy generation [2, 3]. Nowadays, steam reforming (SR) of natural gas and light oil fractions is widely used to produce hydrogen [1, 68]. Renewable resources are an alternative for the production of hydrogen via SR. Ethanol is among the candidates a good choice, because it can be produced in large amounts by the fermentation of biomass [113, 114]:

$$C_{12}H_{22}O_{11}\left(sacarose\right)+H_2O\rightarrow 4CH_3CH_2OH+4CO_2 \qquad (2.30)$$

In addition, ethanol can be directly converted into hydrogen by SRE. Since the research efforts focuses on SRE [5, 9, 10], it is clear that several reaction pathways are possible in SRE (Figure 2-14) , depending on the catalysts used [5]. The efforts are mainly focused on Co, Cu, Pt and Ni based catalysts [5, 9, 10, 63]. As typical transition metals, the active outer layer electrons and associated valence states make it possible for these metals to be candidates for SRE. It is worth noting that the conversion of the reactants used, ethanol and water, as well as the product distribution is strongly dependent on the nature of catalysts employed (active phase, promoters and support material). Therefore, it is necessary to carry out a comprehensive kinetic study on SRE to understand the nature of the reaction.

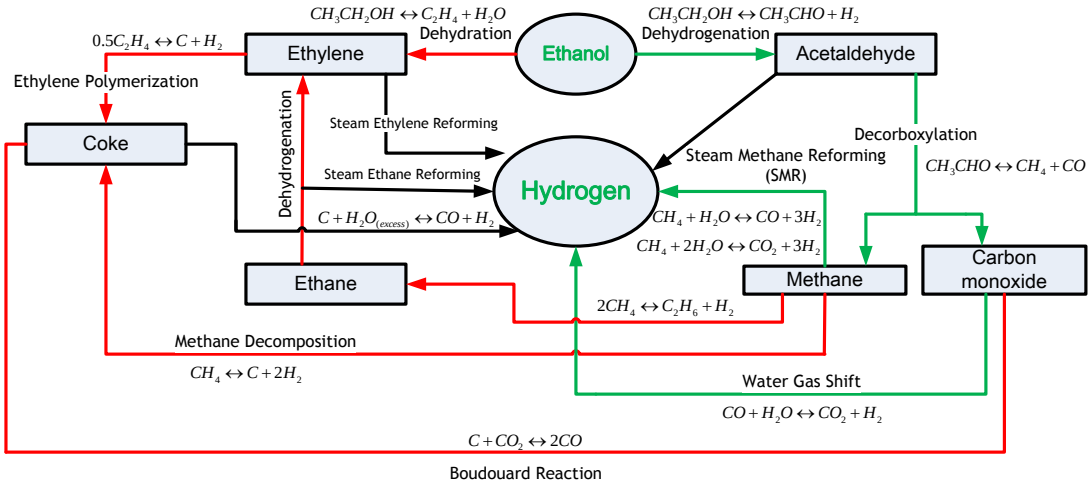

Figure 2-14 Scheme of reactions involved in SRE, pathways are dependent on catalyst and operating conditions used.

It is known that carbon formation can occur during SRE, but at a certain $R_{S/E}$ the formation can be suppressed. This topic was considered in previous works [82, 115]. It was found that carbon deposits are formed below $R_{S/E} = 3$, associated also with a low hydrogen yield in this region. In this work the simplified kinetic model proposed does not consider the formation of adsorbed carbon due to the fact that we operate SRE with excess water. In this work SRE reaction is studied in a large range of temperature (473 - 873 K) and space time (0.008 - 6.731 s) in which the ethanol conversion goes from 0 to 100 %. The goal is to prove if the established simplified kinetic model is convenient to describe the kinetic behavior of the catalyst used in SRE. The novelty of this work is that a simplified Langmuir–Hinshelwood–Hougen-Watson (LHHW) kinetic model is proposed with nine parameters, where the surface decomposition of methane is assumed as the rate determining step (RDS), while all other reaction steps are set as reversible. To the best of our knowledge there is no literature report assuming that the dissociative methane adsorption is the RDS in SRE. The purpose of this work was to develop a simplified mechanistic model to move away from empirical models (power rate model), but also to move away from other proposed models which are too complex for an applied kinetic process.

2.3.2 Kinetic Models

The kinetic behavior of the SRE reaction has been studied over various catalysts in recent years to describe the reaction rate using a power law rate expression [67, 116-125] or an equation based on certain mechanistic assumptions [121, 126-132]. However, these reports on kinetics show significant differences. This might be related with the different catalytic materials and reaction conditions used, as well as the time scale of elementary step procedures (~ 10^{-12} s); it is difficult to detect surface species with the yet available spectroscopic methods. Kinetic analysis can be classified into two groups, according to the type of kinetic expressions used for analysis; the Power rate law expressions derived from data fitting or the use of a Langmuir–Hinshelwood and/or Eley-Rideal kinetic model.

2.3.2.1 Power rate law expressions derived from data fitting

In order to have a model independent description, many of the measured kinetics are given by power law expressions without considering the mechanism of elementary steps. Data from kinetic measurements of the SRE reaction are normally fitted into the following power law expression:

$$-r_{SRE} = k_0 exp\left(\frac{-E_A}{RT}\right) p_{EtOH}^{\alpha} \cdot p_{H_2O}^{\beta} \tag{2.31}$$

A survey of reported power rate law expressions can be found in Table 2-10.

Table 2-10 Power rate law kinetics and activation energies reported.

Rate expression	E_A [kJ·mol^{-1}]	Active metal	Support/ Precursor	T [K]	$R_{S/E}$	Refs.
$r = k \cdot \dot{n}_{EtOH}$	7.0	Ni (20.6 wt. %)	Y_2O_3	403	0	[67, 116]
	5.9	after heat treated at 773 K				
	16.9	Ni (16.1 wt. %)	Al_2O_3			
	1.9	Ni (15.3 wt. %)	La_2O_3			
$r = k \cdot p_{EtOH}^{2.52} \cdot p_{H_2O}^{7.0}$	n.a.	Ni	Al_2O_3	673	4.3	[117]
$r = k \cdot p_{EtOH}^{0.8}$	144	Ni (43.6 wt. %)	Ni-Al-LDH	823-923	5.5	[118]
$r = k \cdot C_{EtOH}$	149	Raney-Type 68.9 wt. % Ni- 28.2 wt. % Cu- 2.9 wt. % Al_2O_3		523-573	1	[119]
$r = k \cdot p_{EtOH}^{0.711} \cdot p_{H_2O}^{2.71}$	23	Ni (25 wt. %)	$MgO\text{-}Al_2O_3$	673-873	3-18	[120]
$r = k \cdot \dot{n}_{EtOH}^{0.43}$	4.4	Ni (15 wt. %)	Al_2O_3	593-793	4.3	[121]
$r = k \cdot p_{EtOH}$	96	Ru (5 wt. %)	Al_2O_3	873-973	10	[122]
$r = k \cdot \dot{n}_{EtOH}^{3.64}$	51	Ni (20.6 wt. %)	n/a	673-863	4.3	[123]
$r = k \cdot C_{EtOH}^{\alpha}$ α = 0.2/1.2,	85	Rh-Pt (~4 wt. %)	monolith (BASF: SR10D)	837-973	3-10	[124]
$r = k \cdot p_{EtOH}^{\alpha} \cdot p_{H_2O}^{\beta}$ α = 0.5±0.05, β=0±0.015	18.4	Pt (1-5 wt. %)	CeO_2	573-723	1.5-6	[125]

* $\dot{n}_{EtOH}$ represents the molar flow rate of ethanol

The rate constant k_0, activation energy E_A, α and β for the reaction order vary between different studies. The reasons for the disagreement among previous research results on the values of the kinetic parameters for the investigated reaction can be explained with the use of different catalysts (active phases, supports, particle sizes, morphologies, catalyst activation/pre-treatments) and/or operating conditions (temperature ranges, feed ratios, different reactors such as differential type).

2.3.2.2 Langmuir–Hinshelwood (or Eley-Rideal) mechanism

Power rate laws provide little information about the underlying processes. Moreover, the power rate law kinetic model used in one study might not be suitable for other types of catalysts under different reaction conditions. A better understanding of the involved chemical processes can be used for the kinetic models, which can be more generic. The establishment of a kinetic model with elementary steps requires a deep knowledge of the reactions involved in the overall SRE process. Kinetic models normally use the Langmuir–Hinshelwood (or Eley-Rideal) mechanism. It assumes that all reaction species are adsorbed on the catalyst surface before they take part in network reactions, and the mechanisms proposed are based on assumptions or simplifications [133]. A survey of mechanisms can be found in Table 2-11. In Table 2-11a Ni and Co based catalysts used in SRE can be found with the corresponding kinetic models. Table 2-11b summarizes the kinetic models in SRE for Rh and Ru based catalysts. Finally, in Table 2-11c the kinetic models used in SMR with Ni based catalysts are shown for a better comparison.

It could be found that these published kinetic studies in the field of SRE processes are mainly performed in a small temperature range. In order to have an intensive investigation of SRE behavior, a systematic kinetic study of SRE was performed from 473 to 873 K, based on a Langmuir–Hinshelwood–Hougen-Watson mechanism model with nickel as the active metal phase. The kinetic model is based on the reaction pathway (green color) shown in Figure 2-14, involving four reactions. In addition, the power rate law kinetic expression was also examined for comparison purpose.

Table 2-11a Reported Langmuir–Hinshelwood and Eley-Rideal kinetics with RDS and activation energies for Ni and Co based catalysts.

Reaction Scheme	RDS	Activation Energy [kJ·mol^{-1}]	Active Metal	Support	T [K]	$R_{S/E}$	Ref.
$C_2H_5OH \rightarrow CH_4 + CO + H_2$	$\overline{C_2H_5OH} \rightarrow CO + \overline{CH_4} + H_2$	279	Ni	Ni-Al-LDH precursor	823-923	3.5-10	[118, 131]
$C_2H_5OH + H_2O \rightarrow CH_4 + CO_2 + 2H_2$	$\overline{C_2H_5OH} + \overline{H_2O} \rightarrow \overline{CH_4} + CO_2 + 2H_2 + \overline{\ }$	235					
$CH_4 + H_2O \leftrightarrow CO + 3H_2$	$\overline{CH_4} + \overline{H_2O} \leftrightarrow CO + 3H_2 + 2\overline{\ }$	124					
$CH_4 + 2H_2O \leftrightarrow CO_2 + 4H_2$	$\overline{CH_4} + 2\overline{H_2O} \leftrightarrow CO_2 + 4H_2 + 3\overline{\ }$	214					
$C_2H_5OH + H_2O \rightarrow 2CO + 4H_2$	$\overline{C_2H_5OH} + \overline{H_2O} \rightarrow 2CO + 4H_2 + 2\overline{\ }$	146					
$C_2H_5OH + 3H_2O \rightarrow 2CO_2 + 6H_2$	$\overline{C_2H_5OH} + 3\overline{H_2O} \rightarrow 2CO + 6H_2 + 4\overline{\ }$	113					
$C_2H_5OH + 3H_2O \rightarrow 2CO_2 + 6H_2$	$\overline{C_2H_5OH} + \overline{\ } \leftrightarrow \overline{CH_4O} + \overline{CH_2}$	21.0	Ni (25wt. %)	$MgO\text{-}Al_2O_3$	673-873	12	[120]
$C_2H_5OH + 3H_2O \rightarrow 2CO_2 + 6H_2$	$C_2H_5OH + \overline{\ } \leftrightarrow \overline{C_2H_5OH}$	59.7	Ni	n/a	673-863	4.3	[123]
$C_2H_5OH + 3H_2O \rightarrow 2CO_2 + 6H_2$	$\overline{C_2H_5OH} + \overline{\ } \leftrightarrow \overline{CH_4O} + \overline{CH_2}$	4.4	Ni (15wt. %)	Al_2O_3	593-793	4.3	[121]
$C_2H_5OH + 3H_2O \leftrightarrow 2CO_2 + 6H_2$	$\overline{CH_3CH_2O} + \overline{\ } \leftrightarrow \overline{CH_3CHO} + \overline{H}$	82.7	Co (10-20 wt. %)	Al_2O_3	673-873	3-8	[126]
$C_2H_5OH \leftrightarrow CH_4 + CO + H_2$	$\overline{CH_3CHO} + \overline{\ } \leftrightarrow \overline{CH_4} + \overline{CO}$	43.6					
$CO + H_2O \leftrightarrow CO_2 + H_2$	$\overline{HCOO} + \overline{\ } \leftrightarrow \overline{CO} + \overline{OH}$	71.3					

Table 2-11b Reported Langmuir–Hinshelwood and Eley-Rideal kinetics with RDS and activation energies for Ru and Rh based catalysts.

Reaction Scheme	RDS	Activation Energy [kJ·mol^{-1}]	Active Metal	Support	T [K]	$R_{S/E}$	Ref.
$C_2H_5OH \leftrightarrow CH_4 + CO + H_2$	$C_2H_5OH + \overline{)} \leftrightarrow \overline{)C_2H_5OH}$	558	Rh (5 wt. %)	CeO_2	623-933	4-8	[127]
$CH_4 + H_2O \leftrightarrow CO + 3H_2$	$\overline{)CH_4} + H_2O \leftrightarrow CO + 3H_2 + \overline{)}$	400					
$CO + H_2O \leftrightarrow CO_2 + H_2$	$\overline{)CHO} + \overline{)OH} \rightarrow \overline{)CO_2} + H_2 + \overline{)}$	496					
$C_2H_5OH + H_2O \rightarrow 2CO + 4H_2$	$\overline{)C_2H_5OH} + \overline{)H_2O} \leftrightarrow \overline{)C_2H_5OOH} + \overline{)H_2}$	110	Ru (2 wt. %)	CeO_2/Al_2O_3	723-823	4-8	[129]
$C_2H_5OH \rightarrow CH_4 + CO + H_2$	$\overline{)C_2H_5OH} \rightarrow \overline{)C_2H_4O} + H_2$	77.5					
$CH_4 + H_2O \leftrightarrow CO + 3H_2$	$\overline{)CH_4} + \overline{)H_2O} \leftrightarrow \overline{)CH_4O} + \overline{)H_2}$	162					
$CO + H_2 \leftrightarrow CO_2 + H_2$	$\overline{)CO} + \overline{)H_2O} \leftrightarrow \overline{)CO_2} + \overline{)H_2}$	90.9					
$C_2H_5OH \rightarrow CH_4 + CO + H_2$	$\overline{)CHO} + \overline{)} \rightarrow \overline{)CO} + \overline{)H}$	85.9	Rh (1 wt. %)	$MgAl_2O_4$-Al_2O_3	773-873	11.25	[132]
$C_2H_5OH + H_2O \rightarrow CH_4 + CO_2 + 2H_2$	$\overline{)CHO} + \overline{)OH} \rightarrow \overline{)CO_2} + H_2 + \overline{)}$	418					
$CH_4 + H_2O \leftrightarrow CO + 3H_2$	$\overline{)CH_3} + \overline{)OH} \rightarrow \overline{)CO} + 2H_2 + \overline{)}$	151					
$CO + H_2 \leftrightarrow CO_2 + H_2$	$\overline{)CO} + \overline{)OH} \rightarrow \overline{)CO_2} + \overline{)H}$	107					

Table 2-11c SMR kinetics with rate determining steps (RDS) and activation energies for comparison purposes.

Reaction	RDS	Activation Energy [kJ·mol^{-1}]	Active Metal	Support	T [K]	$R_{S/E}$	Ref.
$CH_4 + H_2O \leftrightarrow CO + 3H_2$	$\overline{CH_2O} + \overline{\ } \rightarrow \overline{CHO} + \overline{H}$	240.1					
$CO + H_2O \leftrightarrow CO_2 + H_2$	$\overline{CHO} + \overline{O} \rightarrow \overline{CO_2} + \overline{H}$	67.13	Ni	$MgAl_2O4$	773-848	5	[14]
$CH_4 + 2H_2O \leftrightarrow CO_2 + 4H_2$	$\overline{CO} + \overline{O} \rightarrow \overline{CO_2} + \overline{\ }$	243.9					
$CH_4 + 2H_2O \leftrightarrow CO_2 + 4H_2$	$CH_4 + 2\overline{\ } \rightarrow \overline{CH_3} + \overline{H}$	53.1 86.7	Ni	$MgAl_2O_4$ $K/MgAl_2O_4$	548-823	4	[134]
$CH_4 + 2H_2O \leftrightarrow CO_2 + 4H_2$	$CH_4 + 2\overline{\ } \rightarrow \overline{CH_3} + \overline{H}$	102	Ni	MgO	823-873	1	[135]

2.3.3 Kinetic Models Derivation

2.3.3.1 SRE and the reaction pathways

Based on results reported in literature, a schematic representation of the reactions involved in SRE was given in the introduction section (Figure 2-14). In a first step ethanol can go through dehydrogenation or dehydration reaction. Dehydration reaction is favored when the catalytic system shows acidic features (e.g. Al_2O_3-based support material), resulting in the formation of ethylene [136], which is a precursor for coke formation through polymerization. When the catalyst has basic features (e.g., MgO-based support material), dehydrogenation is preferred, leading to the formation of acetaldehyde [82, 137-139]. The acetaldehyde formed is then decomposed via decarboxylation into methane and carbon monoxide. These two reactions occur in low temperature ranges [82], but it is also possible that ethanol directly cracks into hydrogen, carbon monoxide and methane. This reaction step can be considered as a sum of the first two reactions. Hereafter, the WGS takes place in a middle temperature range. However, there is a possibility that a latent WGS occurs, that means acetaldehyde reacts directly with water [139]. Some catalysts, such as copper based systems, which have been reported in literature [140, 141], can also force acetaldehyde to react with water, so that the acetic acid formed, decomposes into methane and carbon dioxide. Indeed, these two reactions can be considered to be a latent WGS, because the sum of the individual reactions corresponds to WGS.

The remaining methane, formed upon ethanol decarboxylation, has a critical aspect in SRE; it limits the production of hydrogen at low and intermediate temperatures. For methane conversion the SMR is required. Note that SMR is the reaction which generates the highest molar amounts of hydrogen. SMR occurs when sufficiently high temperatures and excess of water is used, avoiding coke formation by methane decomposition [142], Boudouard reaction and ethylene polymerization. Furthermore, at SMR reaction conditions the WGS equilibrium becomes the limiting factor for hydrogen yield [115]. Therefore, a second low temperature WGS reaction step is necessary to complete hydrogen production. The possible reactions that can occur

during SRE are summarized in Table 2-12.

Table 2-12 Possible reactions during SRE.

Reactions	Chemical description	ΔH^{0}_{298K} [kJ·mol^{-1}]
Dehydration	$CH_3CH_2OH \leftrightarrow C_2H_4 + H_2O$	+45.4
Dehydrogenation	$CH_3CH_2OH \leftrightarrow CH_3CHO + H_2$	+68.4
Acetaldehyde Decomposition	$CH_3CHO \leftrightarrow CH_4 + CO$	-18.8
Direct Ethanol Decomposition	$CH_3CH_2OH \leftrightarrow H_2 + CH_4 + CO$	+49.7
Water-gas-shift	$CO + H_2O \leftrightarrow CO_2 + H_2$	-41.1
Latent Water-gas-shift	$CH_3CHO + H_2O \leftrightarrow CO_2 + H_2 + CH_4$	-59.9
Acetic Acid Formation	$CH_3CHO + H_2O \leftrightarrow H_2 + CH_3COOH$	-26.7
Acetic Acid Decomposition	$CH_3COOH \leftrightarrow CH_4 + CO_2$	-33.3
Steam Methane Reforming	$CH_4 + H_2 \leftrightarrow CO + 3H_2$	+205.9
Overall Steam Methane Reforming	$CH_4 + 2H_2O \leftrightarrow CO_2 + 4H_2$	+164.7

2.3.3.2 Ethanol decomposition (ETD)

Several research groups reported the production of hydrogen via ethanol decomposition under different conditions. Most of the authors suggest that the first elementary step of SRE is the molecular adsorption of ethanol [121, 123, 143]. This assumption can be described by the Langmuir adsorption (associative adsorption). The adsorbed ethanol dissociates into adsorbed ethoxy species which further decomposes into acetaldehyde and hydrogen [144]. Acetaldehyde may then be released in molecular form together with hydrogen. Infrared studies made on different catalysts have shown that ethanol adsorbs dissociative to form ethoxy species [145-147]. In these studies, the increase in temperature led to the complete disappearance of the bonds corresponding to ethoxy species at ~ 473 K [148].

2.3.3.3 Acetaldehyde decomposition (ACD)

In the next elementary step, the adsorbed acetaldehyde molecule may go again through C-C bond dissociation, forming an adsorbed methyl and aldehyde species.

The adsorbed aldehyde species further decomposes into adsorbed carbon monoxide and hydrogen species. Ni-H may then react with the adsorbed Ni-CH_3 intermolecular species to release methane and two free nickel sites. At this point the backward reaction can be set as the RDS. Finally, adsorbed carbon monoxide species may also be released as well.

Several works have reported the appearance of carbon monoxide, methane and hydrogen at the low-temperature region during temperature programmed desorption analysis of adsorbed ethanol. Such an observation can be fairly attributed to the decomposition of ethoxy species [149-151].

A pure Ni (111) surface, as Gates et al. [152] have shown, causes bond breaking of ethanol in the following order: as first, the scission of the O–H bond in the ethanol molecule to form adsorbed ethoxy species, as second, the scission of the C-H bond in the $–CH_2–$ group in the ethoxy species to form an adsorbed intermediate of acetaldehyde, and finally, the scission of the C–C bond of intermediate adsorbed acetaldehyde to form adsorbed methyl species, -CH_3, and carbon monoxide species, -CO. Therefore, it is possible to assume that the key reaction for the nickel catalyst tested at temperatures up to 573 K is the dehydrogenation of ethanol to surface adsorbed acetaldehyde. The following sequence seems to describe the transformations of acetaldehyde at this temperature range:

$$CH_3CHO_{(g)} \leftrightarrow CH_3CHO_{(ads)} \leftrightarrow CO_{(ads)} + H_{(ads)} + CH_{3(ads)} \leftrightarrow CO_{(g)} + CH_{4(g)} \quad (2.32)$$

2.3.3.4 Water gas shift reaction

The WGS reaction is an exothermic reaction without volume change, and equilibrium conversion of carbon monoxide (and water) is favored with the application of low temperatures. The WGS reaction is very fast at reforming conditions. As a result, the water-gas shift equilibrium is always established during steam reforming.

A comparison of metal-based catalysts shows that WGS depends also on the nature of the active phase. Tests made at 573 K under forward WGS feed conditions, have shown the following experimental trend for catalysts investigated on alumina oxide

support [153], which has weak support effects, Cu > Co> Rh > Ni > Pt > Au > Fe > Pd > Rh > Ir, that means Cu shows higher WGS activity than e.g. Ni.

It must be pointed out that in WGS, O or OH species tend to stick better on Fe, Mo or W, whereas Ni, Rh, Ru, Ir, Pd and Pt are covered with carbon monoxide species, and Cu, Au and Ag present only small coverage of both of these species. This is the reason why in practice the WGS process is applied in two stages, consisting of a high temperature shift (HTS) at 623 K with metaloxide catalysts such as Fe_2O_3/Cr_2O_3 for a better water activation, and a low temperature shift (LTS) between 463 and 483 K with for e.g. $Cu/ZnO/Al_2O_3$ catalysts.

The activation of water plays an important role and can follow different routes; associative adsorption of water, dissociative adsorption into OH and H [126, 154-156], or the water reacts in the gas phase with adsorbed species following an Eley-Rideal mechanism [126, 155]. It is claimed that the latter mechanism has lower probability of occurrence [157]. In this work a monomolecular water adsorption (Langmuir adsorption) is proposed. However, the manner in which water is activated is, of course, temperature dependent.

Adsorbed carbon monoxide species reacts with adsorbed hydroxyl species, forming intermediate carboxyl groups which then decompose into adsorbed hydrogen and carbon dioxide. Hydrogen and carbon dioxide are then released.

2.3.3.5 Steam methane reforming

The first known kinetic studies on SMR were published in 1950s [158, 159]. Bodrov et al. [160-162] investigated SMR kinetics on a nickel foil. The following expression was proposed to describe SMR reaction rate:

$$r_{SMR} = \frac{k_{SMR} \cdot p_{CH_4}}{1 + a \cdot p_{H_2O} \cdot p_{H_2}^{-1} + b \cdot p_{CO}} \qquad (2.33),$$

where “a” and “b” are temperature dependent constants.

Allen et al. [163] also carried out SMR experiments, using a commercial nickel catalyst and concluded that the RDS was the desorption of products. Later, De Deken

et al. [164] determined the SMR kinetics on a Ni/Al_2O_3 catalyst. Hydrogen was added to the feed stream. The kinetic model was composed of two expressions that accounted for the formation of carbon monoxide and carbon dioxide.

The proposed SMR kinetics [14, 160-162, 164] were compared by Elnashaie et al. [165]. The most important conclusion was the different dependences for the partial pressure of steam: negative [160-162], positive [164] and positive or negative [14]. The conclusion was that the work of Xu and Format [14] is the most generic kinetic model. They postulated that carbon intermediates react with adsorbed oxygen and this should be the RDS.

Another mechanism for SMR has been proposed later by Rostrup-Nielsen [166]. Hou and Hughes [167] later developed a similar model to fit the kinetics on a $Ni/\alpha\text{-}Al_2O_3$ catalyst with more parameters. Reports in literature for SMR kinetics indicate that the key-step for a successful hydrogen production must be the sufficient supply of activation energy to crack the C-H bonds in the methane molecule. It has been also reported that the theoretical "methane activation" in SMR may occur at temperatures higher than 573 K [168]. It is well known that the X-H bond strength in covalent hydrides depends on the electronegativity and element size (X = H, C, N, O). Increasing the atomic number, the bond force decreases in a group. Bonds between hydrogen, carbon, oxygen or nitrogen atoms are the most stable covalent bonds. The dissociation energy of methane is very high ($\Delta_{diss}H^o$ = 435.3 $kJ{\cdot}mol^{-1}$). Also the electronic configuration of methane is $1s^2\ 2s^2\ 2p^2$, with two unpaired electrons present in two 2p orbitals. The transfer of one electron from the 2s to the 2p orbitals results in four single filled orbital's ($1s^2\ 2s^1\ 2p^3$) for bonding. Thus, the arrangement of the four C-H bonds in the methane molecule is the result of a tetrahedral symmetry which minimizes electron repulsion.

Wei et al. [135] found that the reaction rates are only proportional to the partial pressure of methane. This observation leads to the conclusion that the dissociation of methane is the RDS for SMR. The methane dissociation is limited kinetically by the initial activation of the C–H bonds, and unaffected by the water concentration.

The current understanding of methane dissociation [134], leads to the conclusion that the reaction does not proceed via an adsorbed precursor state. It has been found that the adsorbed methyl species may decompose so far that an adsorbed carbon species is obtained [169].

The first reaction step is the dissociative adsorption of methane:

$$CH_4 + 2\overline{)} \leftrightarrow \overline{)CH_3} + \overline{)H} \qquad (2.34)$$

The $\overline{)CH_3}$ species are subsequently dissociated by many possible surface reactions until chemisorbed carbon atoms are formed on the metal surface, as shown in Figure 2-15a.

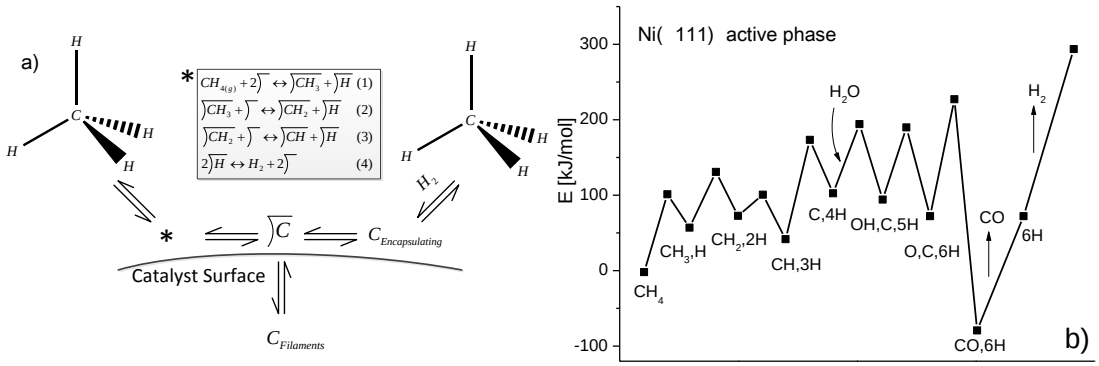

Figure 2-15 The mechanism of methane decomposing (a) and potential energy diagram based on DFT calculations [152] (b).

DFT calculations of these steps on Ni surface, which are reproduced in an energy diagram given in Figure 2-15b, were performed by Bengaard et al. [170]. They proved that the energies of the CH_x species are higher than those for methane, while the adsorbed methyl species -CH_3 show a similar energy to -CH_2 and -CH species. In addition, the energies of the chemisorbed carbon C^* species are lower than for CH_x species and CH_4, with higher activation energy for decomposition of CH_x species to C^* then to the hydrogenation of CH_x species to methane. The dissociative adsorption of methane equation (2.34) seems to be the RDS.

If water is introduced in excess, the adsorbed CH_3 species may react with the adsorbed hydroxyl species or even oxygen species intermolecular, thus forming

adsorbed carbon dioxide and hydrogen:

$$\overline{)H_3C} + \overline{)OH} \leftrightarrow \overline{)H_2COH} + \overline{)H} \quad (2.35)$$

$$\overline{)H_3C} + \overline{)OH} \leftrightarrow \overline{)H_2COH} + \overline{)H} \quad (2.36)$$

$$\overline{)H_2COH} + \overline{)} \leftrightarrow \overline{)H_2CO} + \overline{)H} \quad (2.37)$$

$$\overline{)H_2CO} + \overline{)} \leftrightarrow \overline{)CHO} + \overline{)H} \quad (2.38)$$

$$\overline{)CHO} + \overline{)} \leftrightarrow \overline{)CO} + \overline{)H} \quad (2.39)$$

As a result, these steps in this model could be simplified due to the excess water used. The adsorbed carbon dioxide species will undergo again a WGS reaction mechanism, as already proposed above, or being released.

2.3.4 Proposed Mechanism

Based on the findings in literature, the model which is associated with Figure 2-16 is proposed for SRE with excess water.

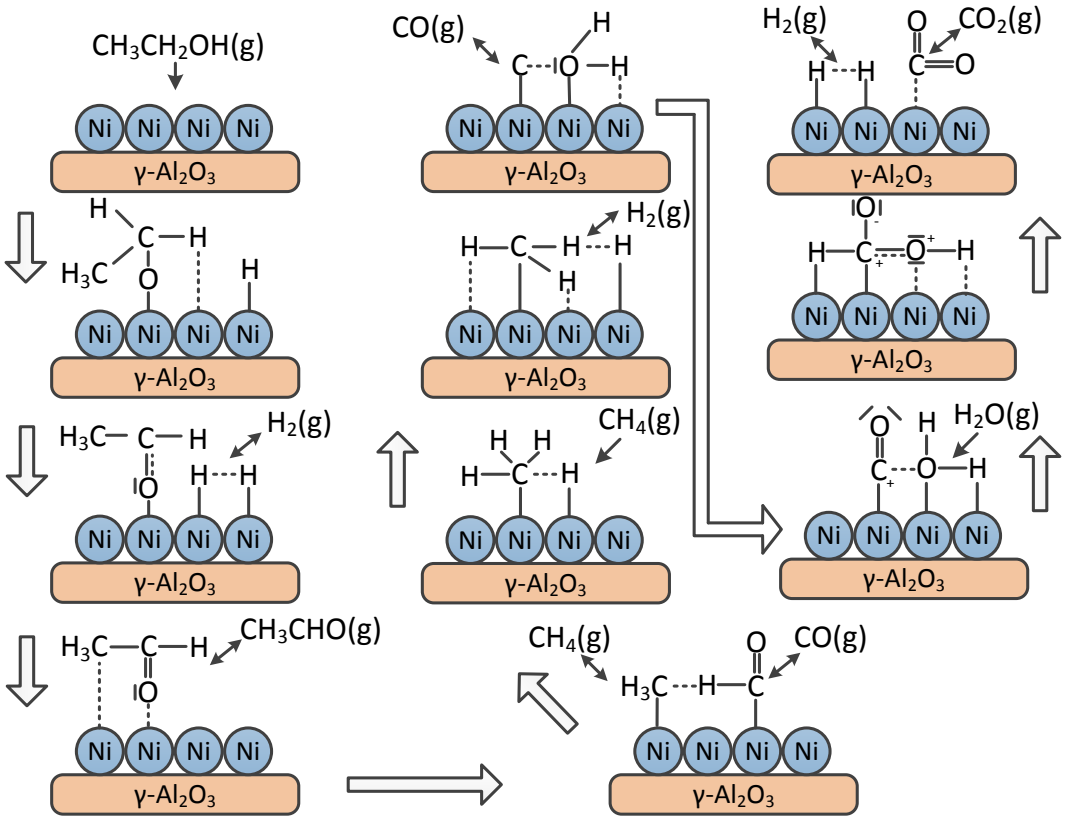

Figure 2-16 Proposed mechanism for SRE with excess water.

It is clear that the proposed SRE mechanism with excess water is too complex; therefore the establishment of a new simple kinetic model is described in the following subsection (Table 2-13), associated with the corresponding LH expressions and using the HW methodology where the dissociative adsorption of methane, equation (2.34), is set as the RDS.

In the first step (1s) ethanol reacts with a nickel site directly into adsorbed acetaldehyde and releases molecular hydrogen simultaneously.

The adsorbed acetaldehyde (2s) is released from the free active nickel site, or it further reacts (3s) to form methane and adsorbed carbon monoxide simultaneously. Here after carbon monoxide can be released (4s), while the produced methane and two free active sites can go through the reversible dissociative adsorption reaction, which is set as the RDS.

Table 2-13 Simplified mechanism and calculation of coverage expressions.

Simplified model	Number
$CH_3CH_2OH + \overline{)} \leftrightarrow \overline{)CH_3CHO} + H_2$	(1s)
$\overline{)CH_3CHO} \leftrightarrow \overline{)} + CH_3CHO$	(2s)
$\overline{)CH_3CHO} \leftrightarrow \overline{)CO} + CH_4$	(3s)
$\overline{)CO} \leftrightarrow CO + \overline{)}$	(4s)
$CH_4 + 2\overline{)} \leftrightarrow \overline{)CH_3} + \overline{)H}$	(RDS)
$H_2O + 2\overline{)} \leftrightarrow \overline{)H} + \overline{)OH}$	(5s)
$\overline{)CO} + \overline{)OH} + \overline{)H} \leftrightarrow 3\overline{)} + CO_2 + H_2$	(6s)
$2\overline{)H} \leftrightarrow 2\overline{)} + H_2$	(7s)
$\overline{)CH_3} + \overline{)OH} \leftrightarrow \overline{)} + \overline{)CO} + 2H_2$	(8s)

In the next step adsorbed carbon monoxide, hydroxyl and hydrogen react to form three active sites plus carbon dioxide and hydrogen in the gas phase (6s).

Adsorbed hydrogen species may also react with intermolecular (2Ni-H) to form two free active nickel sites and molecular hydrogen (7s).

Finally, the adsorbed methyl species, obtained in (3s) can react with adsorbed hydroxyl groups (5s) to generate the adsorbed carbon monoxide, 2 molecular hydrogen products and one active nickel site.

2.3.5 Experimental and Modeling

2.3.5.1 Reaction studies

A commercial 15 wt. % Ni/γ-Al_2O_3 catalyst (Octolyst 1001), supplied by Degussa AG in form of extrudates, was used. The experiments were performed from 473 to 873 K with 100 K intervals and atmosphere pressure with a $R_{S/E}$ of 10 in the feed. Details on the characterization of the catalyst, reaction units can be found in a previous work [82]. In addition, a Dycor ProLine Process Mass Spectrometer (AMETEK, Berwyn, USA) was used to measure all the partial pressures of products in real time. The schematic representation of the experimental units can be found in the previous section (Figure 2-1).

The catalytic results are discussed in terms of space time τ:

$$\tau = \frac{V_R}{\dot{V}_0} = \frac{m_{cat}}{\rho_b} \cdot \frac{1}{\dot{V}_0} \tag{2.40}$$

where V_R is the reactor volume, $\dot{V}_0$ is the volume flow rate of the reactants and inert under the standard condition, m_{cat} and ρ_b represents the mass of the catalyst and the bulk density of the catalyst, respectively. The reproducibility of experimental results was checked and the experimental error was around 5%. For all the measurements made in this work, an average error of around $\pm 5\%$ should be taken into account.

2.3.5.2 Kinetic modeling

Thermodynamic analysis only provides the limit of the reaction system [115]. However, kinetics must be taken into account. It is known that carbon formation can occur during SRE, but at a certain $R_{S/E}$ the formation can be suppressed. It was found

that carbon deposits are formed below $R_{S/E}$ = 3, associated also with a low hydrogen yield in this region. In this work the simplified kinetic model proposed does not consider the formation of adsorbed carbon due to the fact that we operate SRE with excess water.

The SRE reaction was investigated in an integral reactor, the reaction rates were obtained using the differential method by analyzing the conversions versus $m_{cat} / \dot{n}_{i,0}$. The initial concentration of the ethanol-water mixture is used to find the reaction rate, using the differential method of analysis.

$$r = \frac{dX_i}{d(m_{cat} / \dot{n}_{i,0})} \tag{2.41}$$

The rate of reaction is determined by the slope of dX_i versus $d(m_{cat} / \dot{n}_{i,0})$, where $\dot{n}_{i,0}$ represents the molar flow rate of reactant i in the feed.

The power rate law model can be expressed as:

$$r_{SRE} = k_0 e^{\frac{-E_A}{RT}} p_{EtOH}^n \tag{2.42}$$

where k_0 is the pre-exponential factor, E_A is the energy of activation, p_{EtOH} is the partial pressure of the reactant ethanol and n in the superscript is the reaction order with regard to the reactant. These parameters can be determined with a nonlinear regression of the experimental results.

In a next step the establishment of a simplified LHHW kinetic model for SRE was prepared:

$$r_{SRE} = k \cdot y_{CH_4} \cdot \left(1 - \frac{1}{K_{eq,SMR}} \cdot \frac{y_{CO_2} \cdot y_{H_2}^4}{y_{CH_4} \cdot y_{H_2O}^2} \right) \cdot \frac{1}{DEN^2} \tag{2.43}$$

$$DEN = 1 + K_{Ac}^* \cdot y_{Ac} + K_{CO}^* \cdot y_{CO} + K_{OH}^* \cdot \frac{y_{H_2O}}{y_{H_2}^{1/2}} + K_H^* \cdot y_{H_2}^{1/2} + K_{CH_3}^* \cdot \frac{y_{CO_2} y_{H_2}^{7/2}}{y_{H_2O}^2} \tag{2.44}$$

In order to estimate kinetic parameters, experimental data points obtained were fitted with the use of the power rate model and the LHHW model. The sums of squared residuals were used to obtain the objective function F_{obj}:

$$F_{obj} = \frac{\sum_{i}^{m}\left(r_i^{\exp} - r_i^{calc}\right)^2}{\sum_{i}^{m}\left(r_i^{\exp} - \bar{r}\right)^2} \quad (2.45)$$

where m is the total number of experimental measurements and $\bar{r}$ is the average reaction rate, $\bar{r}_i^{\exp}$ and $\bar{r}_i^{calc}$ represent the reaction rate derived from experiments and calculations, respectively. The kinetic parameters were estimated by minimizing this objective function using Levenberg–Marquardt method with the non-linear regression software (MATLAB 2010b). The values of the Levenberg–Marquardt parameters used in the optimization were function tolerance = 10^{-10}, max iterations = 10^3, and max function evaluations = 10^4.

2.3.6 Results and Discussion

2.3.6.1 Catalyst performance

Ethanol and water conversion vs. space time, at different temperatures, are shown in Figure 2-17. Dashed lines used in Figure 2-17 to Figure 2-19 were introduced to follow the experimental points. As it can be seen ethanol conversion increases with temperature and space time. Particularly at temperatures higher than 573 K, the total ethanol conversion can be reached with a space time of 0.78 s. The water conversion also increases with temperature and space time for space times lower than 0.2 s. At 873 K and space times greater than 0.2 s the water conversion remains constant in correspondence with the total conversion of ethanol or decreases slightly due to the water formation through the reverse WGS reaction favored at the higher temperature.

The intra-particle diffusion was determined with the Weisz–Prater criterion, and the calculated value was less than 1 (0.25 at 873 K and 0.0085 at 473 K), which means the concentration on the catalyst surface is very close to the concentration within its pores within our experimental conditions. Therefore, the effect of the intra-particle diffusion was eliminated. In order to eliminate the external mass transfer limitation, preliminary tests at constant space time but with varying feed rates were carried out [82]. It was found that the conversion of ethanol at constant space time

becomes independent from feed rate when the inert flow was 200 $Ncm^3 \cdot min^{-1}$. In addition, the external mass transfer effect was determined with the Mears' criterion, the calculated values are less than 0.15 (0.028 at 873 K and 0.001 at 473 K) with an inert flow of 200 $Ncm^3 \cdot min^{-1}$ in the feed. As a result, only experimental results obtained with 200 Ncm^3/min inert in the feed were used for LHHW kinetic model analysis.

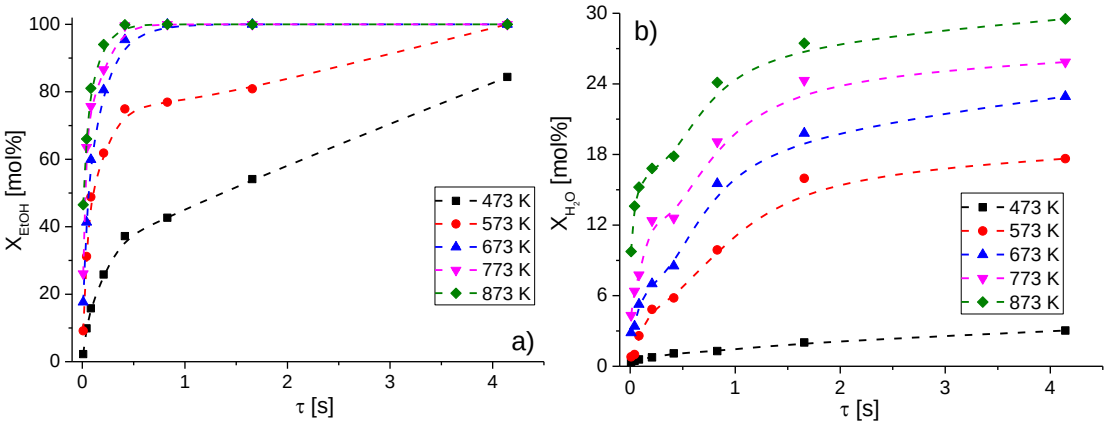

Figure 2-17 Ethanol & water conversions at different reaction temperatures with inert gas flow rates of 200 $Ncm^3 \cdot min^{-1}$ at steady-state conditions (the dash lines are drawn to help visualize the data). Operating conditions: p_{total} = 100 kPa, $R_{S/E}$ = 10.

During SRE reaction on a nickel catalyst, acetaldehyde, carbon monoxide and methane are hereby intermediate products, while hydrogen and carbon dioxide are the desired products. The variation of intermediate product distributions with space time and temperature is shown in Figure 2-18. As a result of the decomposition reaction, yields of acetaldehyde were decreased with space time in all temperatures. With increasing temperature, the methane yields first increased because of the ETD, and then decreased due to the existence of the SMR at high temperatures. Whereas the carbon monoxide yields initially decreased and then increased marginally by the temperature owing to the equilibrium of WGS reaction. On the other hand, with increasing space time, the yields of carbon monoxide decreased while methane increased slightly, which is most probably due to the methanation reaction [129]. Therefore, low space times are recommended for hydrogen production from SRE.

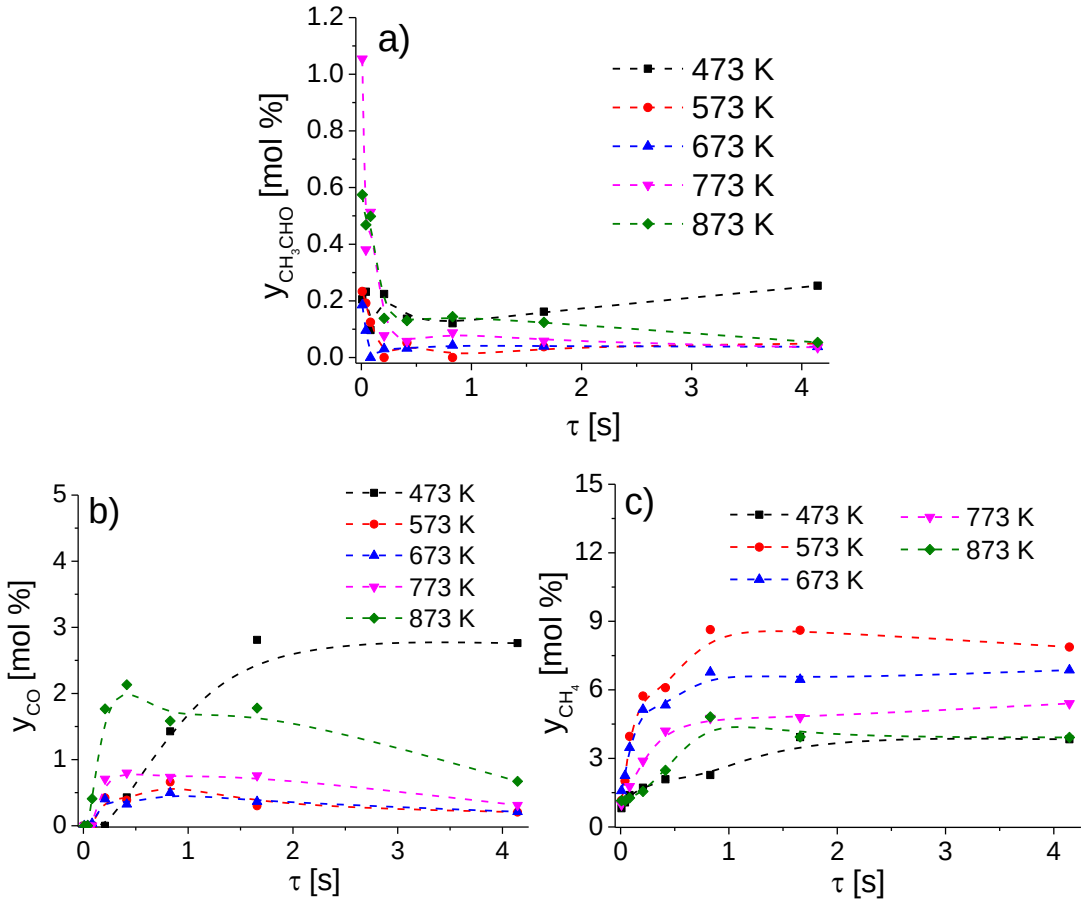

Figure 2-18 Molar fractions of the intermediate products formed at different reaction temperatures with inert gas flow rates of 200 $Ncm^3 \cdot min^{-1}$ at steady-state conditions (the dash lines are drawn to help visualize the data). Operating conditions: p_{total} = 100 kPa, $R_{S/E}$ = 10.

The distributions of the desired products vs. space time at different temperatures are shown in Figure 2-19. Below 773 K, the selectivity towards hydrogen and carbon dioxide increased with the temperature and space time, whereas above 773 K, the yields of carbon dioxide decreased due to the existence of the reverse WGS at high temperatures. At 873 K, the selectivity of hydrogen remains constant with different space times which are in agreement with the complete conversion of ethanol at these conditions.

Figure 2-17 shows results of Xi [%] vs. τ [s], while Figure 2-18 and Figure 2-19 depict results of yi [mol %] vs. τ [s]. As the conversions of the reactants increase, it was found that the molar fractions of desired products also increases, suggesting the conversions of reactants are proportional to the molar fractions of the desired

products.

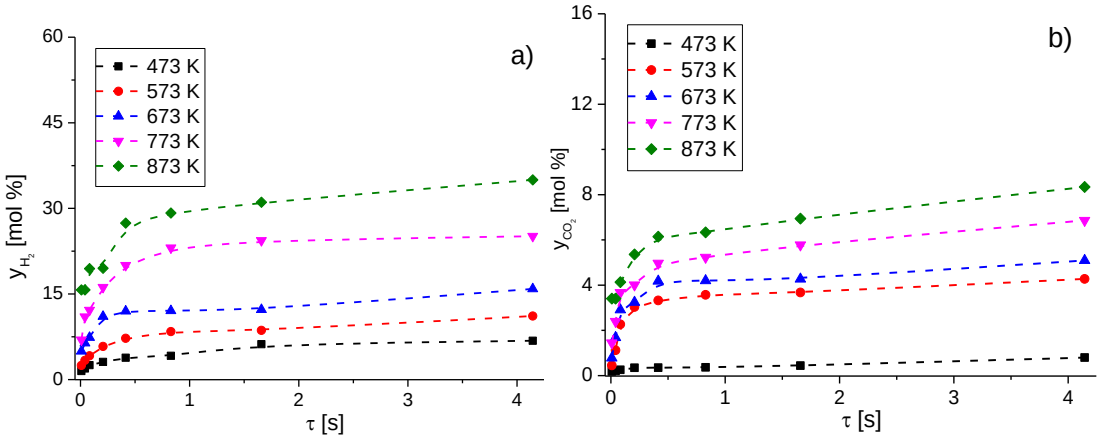

Figure 2-19 Molar fractions of hydrogen and carbon dioxide at different reaction temperatures with inert gas flow rates of 200 $Ncm^3 \cdot min^{-1}$ at steady-state conditions (the dash lines are drawn to help visualize the data). Operating conditions: p_{total} = 100 kPa, $R_{S/E}$ = 10.

2.3.6.2 Kinetic analysis

By considering the reactions and products involved mentioned in Section 2.3.3, and the simplified mechanisms of the kinetic behavior as shown in Table 2-13. The dissociative adsorption of mechanism has been considered as the RDS in this model, which is similar to the reports in literature for SMR kinetics.

Research efforts on SMR kinetics [134, 135] agree that methane is adsorbed on nickel surfaces as carbon atoms. Water is also adsorbed either as OH species or O species, and hydrogen formation is a fast reaction compared to the RDS.

However, there is no agreement in the adsorption mechanism for methane. Xu and Froment [14] found that only one Ni atom is required for the adsorption of methane. Methane is subsequently dehydrogenated, but the model predicts that three RDS are involved together with 13 reaction steps, as shown in Table 2-11c. They found also an unlikely negative heat of adsorption of steam, which is not a strong argument in favor of their mechanism, as well as it is known that the WGS reaction is very fast at reforming conditions. As a result, the WGS equilibrium is always established during steam reforming.

In contradiction to Xu and Froment [14], Rostrup-Nielsen [171] postulated that methane is not dissociative adsorbed on Ni. The RDS is assumed to be the irreversible adsorption of methane associated with substantial energy and entropy barriers, and requires at least a certain amount of active sites for carbon atoms formation, since methane is a stable and highly symmetrical molecule with low sticking coefficients for adsorption.

Wei and Iglesia [135] postulate that the reactivity of the active metal phase towards C-H bond breaking governs the overall reaction kinetics. It was found that reaction rates are proportional to methane partial pressure, but independent of carbon dioxide and water pressures, which led them to the conclusion of sole kinetic relevance of C-H bond activation steps. The catalyst surface may be uncovered by reactive intermediates, due to the fast steps of the activation of the co-reactant and methane activation through the foraging of chemisorbed carbon intermediates. Further, it is postulated that recombinative desorption steps of H atoms with OH species form hydrogen and water.

Finally, Gate et al. [152] describe the mechanism of ethanol decomposition on the Ni (111). The sequence of bond scission steps occur as ethanol undergoes dissociative reactions. Bond activation occurs in the order -O-H, -CH_2, -C-C-, -CH_3. The products observed are acetaldehyde, methane, carbon monoxide, hydrogen and surface carbon. The latter species dissolves into the Ni bulk. Acetaldehyde and methane desorb, and the formation of both of these products is controlled by scission of the methylene (CH_2 group). The CH_3 group is cleaved from the intermediate surface CH_3-CHO species to form CH_3(ads). Hydrogen exhibits a broad, the carbon-oxygen bond in ethanol remains intact and carbon monoxide ultimately desorbs in a single desorption. A small fraction of adsorbed carbon monoxide species undergo exchange with the carbidic surface carbon in a minor process observed.

Mars et al. [118] reported kinetic experiments on SRE with the formation of hydrogen, carbon monoxide, carbon dioxide and traces of methane. Experiments with different methane concentrations showed that ethanol conversion decreases as

methane concentrations increase, revealing the existence of competitiveness between both ethanol and methane for adsorption on the same active site. A power rate law was used first to estimate kinetic parameters, and then to complete the kinetic study with a LH model.

Llera et al. [130] analyzed the kinetic results on SRE, and they found that both carbon dioxide and methane are intermediate products, while carbon monoxide is a final product. They proposed a kinetic model involving two reaction steps where ethanol reacts irreversible, while the methane and carbon dioxide are reversible in the reaction. They postulate that the surface reactions are the RDS steps, and that the dissociative adsorption of methane is a reversible step in quasi-equilibrium, as well as all remaining reactions. 18 reaction steps with 4 RDS steps were used making the model quite complex. The model parameters have shown acceptable fit with a goodness of $R^2 = 0.95218$.

Sahoo et al. [126] proposed a mechanistic kinetic model using LH approach, considering the surface reactions of SRE, WGS and ETD as the RDS in the mechanism. The fitted data indicate that the formation of acetaldehyde from ethoxy is the RDS for reforming, and the correlation coefficient R^2 value for all cases was above 0.95.

Mathure et al. [120] used acquired experimental data from SRE to fit them in the power-law kinetic model. A deviation of 10.2 % was calculated, and considerable amounts of coke formation were observed during the process as well, reducing catalytic activity. Hereafter, an Eley-Rideal mechanism proposed by Akande et al. [121] was developed for a better fitting and description of reactions involved in SRE. Four RDS are proposed; adsorption of ethanol on active sites, dissociative adsorption of ethanol, surface reaction of the adsorbed oxygenated hydrocarbon fraction with no adsorbed steam, surface reaction of the adsorbed hydrocarbon fraction with non-adsorbed steam.

The values of kinetic parameters and the fitness value of objective function for power rate law model and LHHW model obtained from fitting are summarized in

Table 2-14. The coefficients of determination R^2 is obtained from:

$$R^2 = 1 - F_{obj} \tag{2.46}$$

As is shown in Table 2-14, R^2 calculated by the power rate law model and LHHW for ethanol reaction rates are 0.918 and 0.981, respectively. The comparison of reaction rates from experimental and calculated results at different temperature conditions is shown in Figure 2-20 and Figure 2-21 with a power rate law model (a) and a LHHW model (b). As can be seen from these figures, the predicted values from both models are in agreement with the experimental results under different temperature conditions, and the values of LHHW model are more close to the experimental values than the power rate law model due to the higher coefficient of determination of LHHW model (R^2 = 0.981) compared with that of power rate law model (R^2 = 0.918). These results confirmed the LHHW model with assumption of the surface decomposition of methane as the RDS has a better fit than the power rate law model.

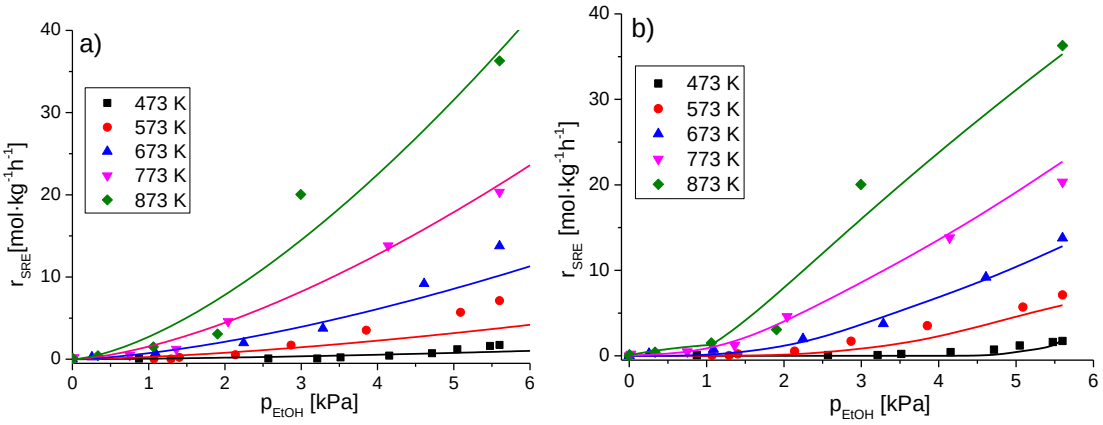

Figure 2-20 Kinetic models (lines) vs. experimental results (filled spots) at p_{total} = 100 kPa and $R_{S/E}$ = 10 with $\dot{V}_{inert}$ = 200 Ncm^3·min^{-1}: a power law model (a) and a LHHW model (b).

Table 2-14 Calculated results for the kinetic models.

Model	Relation		$k_{0,j(673.15\ K)}$ [mol·g^{-1}·h^{-1}]	E_A [kJ/mol]	n	R^2
Power law	$k(T) = k_0 \cdot e^{\frac{-E_A}{RT}}$	k_0	$(2.22 \pm 0.95) \cdot 10^2$	31.8 ±2.1	1.52 ±0.11	0.918
LHHW	$k_{RDS}(T) = k_{0,RDS} \cdot e^{\frac{-E_A}{RT}}$	k_{RDS}	$(1.67 \pm 0.54) \cdot 10^9$	31.8 ±1.6		0.981
	Equilibrium of elementary steps		$K_{j(673.15\ K)}$ [mol·g^{-1}·h^{-1}]	ΔH_j [kJ·mol^{-1}]	$\Delta S_{j,673.15\ K}$ [J·mol^{-1}K^{-1}]	
	$K_j^*(T) = K_{j(673.15)}^* \cdot e^{\frac{-\Delta H_j}{R}\left(\frac{1}{T}-\frac{1}{673.15}\right)}$	K_1	$(3.75 \pm 0.10) \cdot 10^{-5}$	$(7.20 \pm 0.58) \cdot 10^1$	22.2 ±1.0	
		K_2	$(1.66 \pm 0.29) \cdot 10^5$	$(6.55 \pm 0.41) \cdot 10^{-1}$	100.9 ±10.5	
		K_3	$(3.95 \pm 0.65) \cdot 10^{14}$	$-(2.33 \pm 0.28) \cdot 10^1$	244.8 ±34.4	
		K_4	$(4.03 \pm 0.89) \cdot 10^{-1}$	$-(5.53 \pm 0.38) \cdot 10^0$	-15.8 ±1.9	
		K_5	$(1.01 \pm 0.21) \cdot 10^0$	$(4.43 \pm 0.32) \cdot 10^0$	6.7 ±0.8	
		K_6	$(4.82 \pm 1.18) \cdot 10^2$	$-(4.82 \pm 0.35) \cdot 10^1$	-20.2 ±2.6	
		K_7	$(1.11 \pm 0.23) \cdot 10^3$	$(1.73 \pm 0.24) \cdot 10^1$	84.0 ±14.2	
		K_8	$(3.42 \pm 0.54) \cdot 10^{-12}$	$(1.23 \pm 0.18) \cdot 10^2$	-36.8 ±5.6	
	Equilibrium of adsorbed species		$K_{i(673.15\ K)}$ [mol·g^{-1}·h^{-1}]	ΔH_i [kJ·mol^{-1}]	$\Delta S_{i,673.15K}$ [J·mol^{-1}K^{-1}]	
	$K_i^*(T) = K_{i\ (673.15)}^* \cdot e^{\frac{-\Delta H_i}{R}\left(\frac{1}{T}-\frac{1}{673.15}\right)}$	K^*_{Ac}	$(6.02 \pm 0.34) \cdot 10^{-6}$	$-(6.55 \pm 0.41) \cdot 10^{-1}$	-100.9 ±6.0	
		K^*_{CO}	$(4.03 \pm 0.89) \cdot 10^{-1}$	$-(5.53 \pm 0.38) \cdot 10^0$	-15.8 ±1.9	
		K^*_{OH}	$(3.02 \pm 0.79) \cdot 10^{-2}$	$-(4.22 \pm 0.88) \cdot 10^0$	-35.4 ±8.2	
		K^*_{H}	$(3.00 \pm 0.37) \cdot 10^{-2}$	$-(8.65 \pm 0.12) \cdot 10^0$	-42.0 ±1.7	
		K^*_{CH3}	$(1.78 \pm 0.42) \cdot 10^7$	$-(1.01 \pm 0.21) \cdot 10^2$	-11.2 ±2.5	

The order values of activation energies reported for SRE has a deviation from 10^0 to 10^2 kJ·mol^{-1} the deviation of activation energies could be due to the different active phases and reaction conditions employed.

While the reaction order with respect to ethanol has a deviation from 0.43 to 3.64 over nickel based catalysts according to Akande et al. [121] and Akpan et al. [123], the large difference could be due to the presence or absence of heat and mass transfer resistances as well as a different mechanism related with the catalyst type.

The obtained energy of activation the SRE reaction in this study is 31.8 kJ·mol^{-1}, which is between the values that obtained by Mathure et al. [120] (23 kJ·mol^{-1}) and Akpan et al. [123] (51 kJ·mol^{-1}) where nickel-based catalysts were employed, while the reaction order (1.52) of the ethanol partial pressure is also in the range of the values reported by Mathure et al.[120] (0.71) and Akpan et al. [117] (2.52).

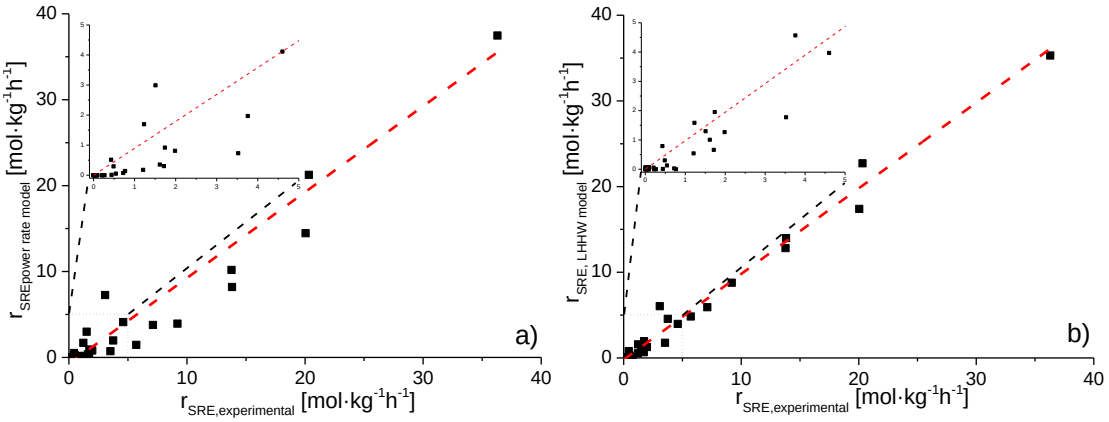

Figure 2-21 Parity plot for rates of reaction calculated using the power rate model (a) and LHHW-model (b) vs. the experimental reaction rates.

Parity plots for rates of reaction were calculated using the power rate model and LHHW-model vs. the experimental reaction rates, Figure 2-21. R-squared values were obtained from the linear fitting of the points. It might be observed that the LHHW-model has a quite good fitting, while the power rate model has stronger deviations. The relatively low activation energy obtained for LHHW model is very likely attributed to the reaction conditions, because a high water-to-ethanol molar ratio (10) was used. Mathure et al. [120] investigated a commercial Ni-based catalyst

at similar reaction conditions ($R_{S/E}$ = 12), where the gas-phase and intra-particle mass transfer resistance was eliminated, and the activation energy was determined with a value of 21 kJ·mol^{-1}.

The obtained values of K_j are listed in Table 2-14. It can be found that $K_3 >> K_1$, which indicate that the acetaldehyde decomposition reaction is much faster than the ethanol decomposition reaction. On the other hand, $K_2 > K_7 > K_4$ suggests the unreacted acetaldehyde could be released from the active phase faster than hydrogen and carbon monoxide. As a result, a low yield of acetaldehyde was obtained especially at high temperatures. It can be found that K_8 with a relatively large enthalpy value (123 kJ·mol^{-1}) increases as the temperature is raised, indicating that the elementary reaction between θ_{CH3} and θ_{OH} is also a strong endothermic reaction similar as SMR which has an average enthalpy of 180 kJ·mol^{-1} among the reaction conditions used in this study (473-873 K). In addition, the equilibrium constant (K_6) of the elementary reaction (equation 6s in Table 2-13) which is related with the reversible WGS reaction decreases with the temperature rise. As a result, the reaction temperature becomes the deterministic function of SRE process in order to obtain a high yield of hydrogen with a low yield of carbon monoxide from the product gas [79].

2.3.7 Conclusions

In this section, the kinetic behavior of SRE over a commercial nickel-based catalyst has been investigated from 473 to 873 K with a $R_{S/E}$ of 10 in the feed. The purpose of this work was to develop a simplified mechanistic model to replace empirical models (power rate model) and other proposed kinetic models which are too complex for an applied kinetic process. The following conclusions can be drawn from the analysis and discussion above.

1) The power rate law and LHHW kinetic models employed in this work both can successfully demonstrate the catalytic SRE process in a fixed-bed reactor among a large temperature range.

2) The energy of activation for SRE reaction was 31.8 $kJ \cdot mol^{-1}$ and the reaction order of the ethanol pressure obtained from the power rate law model was 1.52, which is in a good agreement with other reported results.
3) According to the comparison of experimental data between the results from two kinetic models, the LHHW model with assumption of the surface decomposition of methane as the RDS has a better fitting than that from the power rate law model.
4) The values of the parameters for LHHW kinetic model indicate that the acetaldehyde decomposition reaction is much faster than the ethanol decomposition reaction, while the elementary reaction between θ_{CH3} and θ_{OH} is also a strong endothermic reaction as the SMR.

References

[1] N.Z. Muradov, T.N. Veziroğlu, *Int. J. Hydrogen Energy.* **2008**, *33 (23)*, 6804-6839.

[2] K.V. Kordesch, G.R. Simader, *Chem. Rev.* 1995, *95 (1)*, 191-207.

[3] F. de Bruijn, *Green Chem.* **2005**, *7 (3)*, 132-150.

[4] N. Laosiripojana, S. Assabumrungrat, *Appl. Catal., A.* **2005**, *290 (1–2)*, 200-211.

[5] M. Ni, D.Y.C. Leung, M.K.H. Leung, *Int. J. Hydrogen Energy.* **2007**, *32 (15)*, 3238-3247.

[6] A.E. Farrell, R.J. Plevin, B.T. Turner, A.D. Jones, M. O'Hare, D.M. Kammen, *Science.* **2006**, *311 (5760)*, 506-508.

[7] J.R. Mielenz, *Curr. Opin. Microbiol.* **2001**, *4 (3)*, 324-329.

[8] A.L. Alberton, M.M.V.M. Souza, M. Schmal, *Catal. Today.* **2007**, *123 (1–4)*, 257-264.

[9] A. Haryanto, S. Fernando, N. Murali, S. Adhikari, *Energy Fuels.* **2005**, *19 (5)*, 2098-2106.

[10] P.D. Vaidya, A.E. Rodrigues, *Chem. Eng. J.* **2006**, *117 (1)*, 39-49.

[11] J.R. Rostrup-Nielsen, *Steam reforming*, in: Handbook of Heterogeneous Catalysis, Wiley-VCH Verlag GmbH & Co. KGaA, **2008**.

[12] S. Ahmed, A. Aitani, F. Rahman, A. Al-Dawood, F. Al-Muhaish, *Appl. Catal., A.* **2009**, *359 (1–2)*, 1-24.

[13] N. Mahata, A.F. Cunha, J.J.M. Órfão, J.L. Figueiredo, *ChemCatChem.* **2010**, *2 (3)*, 330-335.

[14] J. Xu, G.F. Froment, *AIChE J.* **1989**, *35 (1)*, 88-96.

[15] J.D. Holladay, J. Hu, D.L. King, Y. Wang, *Catal. Today.* **2009**, *139 (4)*, 244-260.

[16] G.-h. Xiu, P. Li, A. E. Rodrigues, *Chem. Eng. Sci.* **2002**, *57 (18)*, 3893-3908.

[17] G.-h. Xiu, J.L. Soares, P. Li, A.E. Rodrigues, *AIChE J.* **2002**, *48 (12)*, 2817-2832.

[18] G.-h. Xiu, P. Li, A.E. Rodrigues, *Chem. Eng. Sci.* **2003**, *58 (15)*, 3425-3437.

[19] G.H. Xiu, P. Li, A.E. Rodrigues, *Chem. Eng. Res. Des.* **2004**, *82 (2)*, 192-202.

[20] D.P. Harrison, *Ind. Eng. Chem. Res.* **2008**, *47 (17)*, 6486-6501.

[21] L. Barelli, G. Bidini, F. Gallorini, S. Servili, *Energy.* **2008**, *33 (4)*, 554-570.

[22] J.R. Hufton, S. Mayorga, S. Sircar, *AIChE J.* **1999**, *45 (2)*, 248-256.

[23] W.E. Waldron, J.R. Hufton, S. Sircar, *AIChE J.* **2001**, *47 (6)*, 1477-1479.

[24] K.B. Lee, A. Verdooren, H.S. Caram, S. Sircar, *J. Colloid Interface Sci.* **2007**, *308 (1)*, 30-39.

[25] K.B. Lee, M.G. Beaver, H.S. Caram, S. Sircar, *Ind. Eng. Chem. Res.* **2007**, *46 (14)*, 5003-5014.

[26] K.B. Lee, M.G. Beaver, H.S. Caram, S. Sircar, *AIChE J.* **2007**, *53 (11)*, 2824-2831.

[27] K.B. Lee, M.G. Beaver, H.S. Caram, S. Sircar, *Int. J. Hydrogen Energy.* **2008**, *33 (2)*, 781-790.

[28] K.B. Lee, M.G. Beaver, H.S. Caram, S. Sircar, *J. Power Sources.* **2008**, *176 (1)*, 312-319.

[29] J. Comas, M. Laborde, N. Amadeo, *J. Power Sources.* **2004**, *138 (1-2)*, 61-67.

[30] H. Gupta, L.-S. Fan, *Ind. Eng. Chem. Res.* **2002**, *41 (16)*, 4035-4042.

[31] K. Kuramoto, S. Fujimoto, A. Morita, S. Shibano, Y. Suzuki, H. Hatano, L. Shi-Ying, M. Harada, T. Takarada, *Ind. Eng. Chem. Res.* **2003**, *42 (5)*, 975-981.

[32] J.C. Abanades, D. Alvarez, *Energy Fuels.* **2003**, *17 (2)*, 308-315.

[33] E.P. Reddy, P.G. Smirniotis, *J. Phys. Chem. B.* **2004**, *108 (23)*, 7794-7800.

[34] D. Alvarez, J.C. Abanades, *Energy Fuels.* **2004**, *19 (1)*, 270-278.

[35] J.A. Satrio, B.H. Shanks, T.D. Wheelock, *Ind. Eng. Chem. Res.* **2005**, *44 (11)*, 3901-3911.

[36] Z.-s. Li, N.-s. Cai, Y.-y. Huang, *Ind. Eng. Chem. Res.* **2006**, *45 (6)*, 1911-1917.

[37] H. Lu, E.P. Reddy, P.G. Smirniotis, *Ind. Eng. Chem. Res.* **2006**, *45 (11)*, 3944-3949.

[38] H. Lu, A. Khan, P.G. Smirniotis, *Ind. Eng. Chem. Res.* **2008**, *47 (16)*, 6216-6220.

[39] S.F. Wu, Q.H. Li, J.N. Kim, K.B. Yi, *Ind. Eng. Chem. Res.* **2007**, *47 (1)*, 180-184.

[40] E. Oliveira, C. Grande, A. Rodrigues, *Sep. Purif. Technol.* **2008**, *62 (1)*, 137-147.

[41] Y. Ding, E. Alpay, *Chem. Eng. Sci.* **2000**, *55 (17)*, 3461-3474.

[42] Z. Yong, V.G. Mata, A.E. Rodrigues, *Ind. Eng. Chem. Res.* **2000**, *40 (1)*, 204-209.

[43] B. Ficicilar, T. Dogu, *Catal. Today.* **2006**, *115 (1–4)*, 274-278.

[44] M.K. Ram Reddy, Z.P. Xu, G.Q. Lu, J.C. Diniz da Costa, *Ind. Eng. Chem. Res.* **2006**, *45 (22)*, 7504-7509.

[45] H.T.J. Reijers, S.E.A. Valster-Schiermeier, P.D. Cobden, R.W. van den Brink, *Ind. Eng. Chem. Res.* **2005**, *45 (8)*, 2522-2530.

[46] A.D. Ebner, S.P. Reynolds, J.A. Ritter, *Ind. Eng. Chem. Res.* **2006**, *45 (18)*, 6387-6392.

[47] M.K. Ram Reddy, Z.P. Xu, J.C. Diniz da Costa, *Ind. Eng. Chem. Res.* **2008**, *47 (8)*, 2630-2635.

[48] J.M. Lee, Y.J. Min, K.B. Lee, S.G. Jeon, J.G. Na, H.J. Ryu, *Langmuir.* **2010**, *26 (24)*, 18788-18797.

[49] Y. Ding, E. Alpay, *Process Saf. Environ. Prot.* **2001**, *79 (1)*, 45-51.

[50] Z. Yong, V. Mata, A.E. Rodrigues, *J. Chem. Eng. Data.* **2000**, *45 (6)*, 1093-1095.

[51] Z. Yong, V.G. Mata, A.E. Rodrigues, *Adsorption.* **2001**, *7 (1)*, 41-50.

[52] E. Ochoa-Fernández, M. Rønning, T. Grande, D. Chen, *Chemistry of Materials.* **2006**, *18 (6)*, 1383-1385.

[53] J.-i. Ida, Y.S. Lin, *Environ. Sci. Technol.* **2003**, *37 (9)*, 1999-2004.

[54] A. López - Ortiz, N.G.P. Rivera, A.R. Rojas, D.L. Gutierrez, *Sep. Purif. Technol.* **2005**, *39 (15)*, 3559-3572.

[55] M. Kato, K. Nakagawa, K. Essaki, Y. Maezawa, S. Takeda, R. Kogo, Y. Hagiwara, *Int. J. Appl. Ceram. Technol.* **2005**, *2 (6)*, 467-475.

[56] M.E. Bretado, V. Guzmán Velderrain, D. Lardizábal Gutiérrez, V. Collins-Martínez, A.L. Ortiz, *Catal. Today.* **2005**, *107–108*, 863-867.

[57] K. Essaki, M. Kato, K. Nakagawa, *J. Ceram. Soc. Jpn.* **2006**, *114 (1333)*, 739-742.

[58] K. Essaki, M. Kato, H. Uemoto, *J. Mater. Sci.* **2005**, *40 (18)*, 5017-5019.

[59] A. Vaccari, *Catal. Today.* **1998**, *41 (1–3)*, 53-71.

[60] Y. Ding, E. Alpay, *Chem. Eng. Sci.* **2000**, *55 (18)*, 3929-3940.

[61] C. Resini, T. Montanari, L. Barattini, G. Ramis, G. Busca, S. Presto, P. Riani, R.

Marazza, M. Sisani, F. Marmottini, U. Costantino, *Appl. Catal., A.* **2009**, *355 (1–2)*, 83-93.

[62] E.L.G. Oliveira, C.A. Grande, A.E. Rodrigues, *Can. J. Chem. Eng.* **2009**, *87 (6)*, 945-956.

[63] F. Frusteri, S. Freni, L. Spadaro, V. Chiodo, G. Bonura, S. Donato, S. Cavallaro, *Catal. Commun.* **2004**, *5 (10)*, 611-615.

[64] S. Cavallaro, V. Chiodo, A. Vita, S. Freni, *J. Power Sources.* **2003**, *123 (1)*, 10-16.

[65] J. Comas, F. Mariño, M. Laborde, N. Amadeo, *Chem. Eng. J.* **2004**, *98 (1–2)*, 61-68.

[66] A.N. Fatsikostas, X.E. Verykios, *J. Catal.* **2004**, *225 (2)*, 439-452.

[67] J. Sun, X.-P. Qiu, F. Wu, W.-T. Zhu, *Int. J. Hydrogen Energy.* **2005**, *30 (4)*, 437-445.

[68] J.A. Turner, *Science.* **2004**, *305 (5686)*, 972-974.

[69] R.L. Peter Häussinger, Allan M. Watson, *Hydrogen*, in: Ullmann´s Encyclopedia of Industrial Chemistry, Wiley-VCH, Verlag, **2007**.

[70] C. Song, *Catal. Today.* **2002**, *77 (1-2)*, 17-49.

[71] P. Ferreira‐Aparicio, M.J. Benito, J.L. Sanz, *Catal. Rev.: Sci. Eng.* **2005**, *47 (4)*, 491-588.

[72] M. Hoel, S. Kverndokk, *Resour. Energy Econ.* **1996**, *18 (2)*, 115-136.

[73] H. Vogel, *Chem. Ing. Tech.* **2009**, *81 (8)*, 1041-1041.

[74] A. Demirbas, *Prog. Energy Combust. Sci.* **2007**, *33 (1)*, 1-18.

[75] E.Y. García, M.A. Laborde, *Int. J. Hydrogen Energy.* **1991**, *16 (5)*, 307-312.

[76] K. Vasudeva, N. Mitra, P. Umasankar, S.C. Dhingra, *Int. J. Hydrogen Energy.* **1996**, *21 (1)*, 13-18.

[77] W. Wang, Y.Q. Wang, *Int. J. Hydrogen Energy.* **2008**, *32 (15)*, 1432-1443.

[78] A. Lima da Silva, C.d.F. Malfatti, I.L. Müller, *Int. J. Hydrogen Energy.* **2009**, *34 (10)*, 4321-4330.

[79] F. Díaz Alvarado, F. Gracia, *Chem. Eng. J.* **2010**, *165 (2)*, 649-657.

[80] B.T. Carvill, J.R. Hufton, M. Anand, S. Sircar, *AIChE J.* **1996**, *42 (10)*, 2765-2772.

[81] B. Dou, V. Dupont, G. Rickett, N. Blakeman, P.T. Williams, H. Chen, Y. Ding, M. Ghadiri, *Bioresour. Technol.* **2009**, *100 (14)*, 3540-3547.

[82] A.F. Cunha, Y.-J. Wu, F.A. Díaz Alvarado, J.C. Santos, P.D. Vaidya, A.E. Rodrigues, *Can. J. Chem. Eng.* **2012**, *90 (6)*, 1514-1526.

[83] A. Lima da Silva, I.L. Müller, *Int. J. Hydrogen Energy.* **2011**, *36 (3)*, 2057-2075.

[84] G. Rabenstein, V. Hacker, *J. Power Sources.* **2008**, *185 (2)*, 1293-1304.

[85] S. Liu, K. Zhang, L. Fang, Y. Li, *Energy Fuels.* **2008**, *22 (2)*, 1365-1370.

[86] J. Li, H. Yu, G. Yang, F. Peng, D. Xie, H. Wang, J. Yang, *Energy Fuels.* **2011**, *25 (6)*, 2643-2650.

[87] S. Freni, G. Maggio, S. Cavallaro, *J. Power Sources.* **1996**, *62 (1)*, 67-73.

[88] V. Mas, R. Kipreos, N. Amadeo, M. Laborde, *Int. J. Hydrogen Energy.* **2006**, *31 (1)*, 21-28.

[89] I. Theophilos, *J. Power Sources.* **2001**, *92 (1-2)*, 17-25.

[90] A.C.C. de Souza, J. Luz-Silveira, M.I. Sosa, *J. Fuel Cell Sci. Technol.* **2006**, *3 (3)*, 346-350.

[91] L. Hernández, V. Kafarov, *J. Power Sources.* **2009**, *192 (1)*, 195-199.

[92] I. Fishtik, A. Alexander, R. Datta, D. Geana, *Int. J. Hydrogen Energy.* **2000**, *25 (1)*, 31-45.

[93] M.R. Mahishi, M.S. Sadrameli, S. Vijayaraghavan, D.Y. Goswami, *ASME Conference Proceedings.* **2005**, *2005 (42118)*, 455-463.

[94] M. Li, *Ind. Eng. Chem. Res.* **2008**, *47 (23)*, 9263-9271.

[95] M. Li, *Int. J. Hydrogen Energy.* **2009**, *34 (23)*, 9362-9372.

[96] R.G. Mortimer, *Physical chemistry*, Academic, London, **2008**.

[97] L. He, H. Berntsen, D. Chen, *J. Phys. Chem. A.* **2009**, *114 (11)*, 3834-3844.

[98] H.C.V. J.M. Smith, M. M. Abbott, *Introduction to Chemical Engineering Thermodynamics*, 7th ed., McGraw-Hill Companies, Inc., New York, **1999**.

[99] R.F.P.M. Moreira, J.L. Soares, G.L. Casarin, A.E. Rodrigues, *Sep. Purif. Technol.*

2006, *41 (2)*, 341-357.

[100] Z. Yong, V. Mata, A.E. Rodrigues, *Sep. Purif. Technol.* **2002**, *26 (2-3)*, 195-205.

[101] D.G. Luenberger, Y. Ye, *Linear and Nonlinear Programming*, Springer Science Business Media, LLC, Boston, **2008**.

[102] M.W. Chase, *NIST-JANAF thermochemical tables*, American Chemical Society, New York, **1998**.

[103] NIST, *NIST Chemistry WebBook*, in, The National Institute of Standards and Technology, U.S. Secretary of Commerce, **2011**.

[104] R.H. Perry, D.W. Green, *Perry's Chemical Engineers'Handbook*, McGraw-Hill Companies, Inc., New York, **1997**.

[105] CHERIC, *Thermophysical Properties Data Bank*, in, Chemical Engineering Research Information Center, **2009**.

[106] A.J. Vizcaíno, A. Carrero, J.A. Calles, *Int. J. Hydrogen Energy.* **2007**, *32 (10–11)*, 1450-1461.

[107] W. Wang, Y. Wang, *Int. J. Hydrogen Energy.* **2008**, *33 (19)*, 5035-5044.

[108] C.C.R.S. Rossi, C.G. Alonso, O.A.C. Antunes, R. Guirardello, L. Cardozo-Filho, *Int. J. Hydrogen Energy.* **2009**, *34 (1)*, 323-332.

[109] N. Sarkar, S.K. Ghosh, S. Bannerjee, K. Aikat, *Renewable Energy.* **2012**, *37 (1)*, 19-27.

[110] R. Xiong, J. Ida, Y.S. Lin, *Chem. Eng. Sci.* **2003**, *58 (19)*, 4377-4385.

[111] C. Hulteberg, *Int. J. Hydrogen Energy.* **2012**, *37 (5)*, 3978-3992.

[112] C. Parmesan, G. Yohe, *Nature.* **2003**, *421 (6918)*, 37-42.

[113] A. Vertès, N. Qureshi, H. Yukawa, H. Blaschek, *Biomass to Biofuels: Strategies for Global Industries*, Wiley, Hoboken, New Jersey, **2009**.

[114] C. Wyman, *Handbook on Bioethanol: Production and Utilization*, Taylor & Francis, Washington, DC, **1996**.

[115] Y.-J. Wu, F. Díaz Alvarado, J.C. Santos, F. Gracia, A.F. Cunha, A.E. Rodrigues, *Chem. Eng. Technol.* **2012**, *35 (5)*, 847–858.

[116] J. Sun, D. Luo, P. Xiao, L. Jigang, S. Yu, *J. Power Sources.* **2008**, *184 (2)*,

385-391.

[117] A. Therdthianwong, T. Sakulkoakiet, S. Therdthianwong, *ScienceAsia.* **2001**, *27* 193-198.

[118] V. Mas, M.L. Dieuzeide, M. Jobbágy, G. Baronetti, N. Amadeo, M. Laborde, *Catal. Today.* **2008**, *133-135* 319-323.

[119] D.A. Morgenstern, J.P. Fornango, *Energy Fuels.* **2005**, *19 (4)*, 1708-1716.

[120] P.V. Mathure, S. Ganguly, A.V. Patwardhan, R.K. Saha, *Ind. Eng. Chem. Res.* **2007**, *46 (25)*, 8471-8479.

[121] A. Akande, A. Aboudheir, R. Idem, A. Dalai, *Int. J. Hydrogen Energy.* **2006**, *31 (12)*, 1707-1715.

[122] P.D. Vaidya, A.E. Rodrigues, *Ind. Eng. Chem. Res.* **2006**, *45 (19)*, 6614-6618.

[123] E. Akpan, A. Akande, A. Aboudheir, H. Ibrahim, R. Idem, *Chem. Eng. Sci.* **2007**, *62 (12)*, 3112-3126.

[124] A. Simson, E. Waterman, R. Farrauto, M. Castaldi, *Appl. Catal., B.* **2009**, *89 (1-2)*, 58-64.

[125] P. Ciambelli, V. Palma, A. Ruggiero, *Appl. Catal., B.* **2010**, *96 (1-2)*, 190-197.

[126] D.R. Sahoo, S. Vajpai, S. Patel, K.K. Pant, *Chem. Eng. J.* **2007**, *125 (3)*, 139-147.

[127] O. Görke, P. Pfeifer, K. Schubert, *Appl. Catal., A.* **2009**, *360 (2)*, 232-241.

[128] P.-J. Lu, T.-S. Chen, J.-M. Chern, *Catal. Today.* **2011**, *174 (1)*, 17-24.

[129] N.R. Peela, D. Kunzru, *Ind. Eng. Chem. Res.* **2011**, *50 (23)*, 12881-12894.

[130] I. Llera, V. Mas, M.L. Bergamini, M. Laborde, N. Amadeo, *Chem. Eng. Sci.* **2012**, *71*, 356-366.

[131] V. Mas, G. Baronetti, N. Amadeo, M. Laborde, *Chem. Eng. J.* **2008**, *138 (1-3)*, 602-607.

[132] C. Graschinsky, M. Laborde, N. Amadeo, A. Le Valant, N. Bion, F. Epron, D. Duprez, *Ind. Eng. Chem. Res.* **2010**, *49 (24)*, 12383-12389.

[133] I. Chorkendorff, J.W. Niemantsverdriet, *Concepts of Modern Catalysis and Kinetics Concepts*, WILEY-VCH, Weinheim, Germany, **2003**.

[134] J.R. Rostrup-Nielsen, J. Sehested, J.K. Nørskov, *Adv. Catal.* **2002**, *47* 65-139.

[135] J. Wei, E. Iglesia, *J. Catal.* **2004**, *224 (2)*, 370-383.

[136] M.C. Sánchez-Sánchez, R.M. Navarro, J.L.G. Fierro, *Int. J. Hydrogen Energy.* **2007**, *32 (10–11)*, 1462-1471.

[137] S. Freni, S. Cavallaro, N. Mondello, L. Spadaro, F. Frusteri, *Catal. Commun.* **2003**, *4 (6)*, 259-268.

[138] F. Mariño, G. Baronetti, M. Jobbagy, M. Laborde, *Appl. Catal., A.* **2003**, *238 (1)*, 41-54.

[139] M. Akiyama, Y. Oki, M. Nagai, *Catal. Today.* **2012**, *181 (1)*, 4-13.

[140] A.F. Cunha, Y.-J. Wu, J.C. Santos, A.E. Rodrigues, *Chem. Eng. Res. Des.* **2013**, *91 (3)*, 581-592.

[141] N. Iwasa, N. Takezawa, *Bull. Chem. Soc. Jpn.* **1991**, *64 (9)*, 2619-2623.

[142] A.F. Cunha, J.J.M. Órfão, J.L. Figueiredo, *Appl. Catal., A.* **2008**, *348 (1)*, 103-112.

[143] F. Wang, Y. Li, W. Cai, E. Zhan, X. Mu, W. Shen, *Catal. Today.* **2009**, *146 (1-2)*, 31-36.

[144] J.-H. Wang, C.S. Lee, M.C. Lin, *J. Phys. Chem. C.* **2009**, *113 (16)*, 6681-6688.

[145] H. Idriss, C. Diagne, J.P. Hindermann, A. Kiennemann, M.A. Barteau, *J. Catal.* **1995**, *155 (2)*, 219-237.

[146] A. Yee, S.J. Morrison, H. Idriss, *J. Catal.* **1999**, *186 (2)*, 279-295.

[147] A. Yee, S.J. Morrison, H. Idriss, *J. Catal.* **2000**, *191 (1)*, 30-45.

[148] L.V. Mattos, F.B. Noronha, *J. Catal.* **2005**, *233 (2)*, 453-463.

[149] E.M. Cordi, J.L. Falconer, *J. Catal.* **1996**, *162 (1)*, 104-117.

[150] L.F. de Mello, F.B. Noronha, M. Schmal, *J. Catal.* **2003**, *220 (2)*, 358-371.

[151] M.A.S. Baldanza, L.F. de Mello, A. Vannice, F.B. Noronha, M. Schmal, *J. Catal.* **2000**, *192 (1)*, 64-76.

[152] S.M. Gates, J.N. Russell Jr, J.T. Yates Jr, *Surf. Sci.* **1986**, *171 (1)*, 111-134.

[153] N. Schumacher, A. Boisen, S. Dahl, A.A. Gokhale, S. Kandoi, L.C. Grabow, J.A. Dumesic, M. Mavrikakis, I. Chorkendorff, *J. Catal.* **2005**, *229 (2)*, 265-275.

[154] N. Amadeo, M. Laborde, *Trends Chem. Eng.* **1996**, *3* 159-183.

[155] F. Mariño, M. Boveri, G. Baronetti, M. Laborde, *Int. J. Hydrogen Energy.* **2004**, *29 (1)*, 67-71.

[156] J. Raskó, A. Hancz, Erdo, A. helyi, *Appl. Catal., A.* **2004**, *269 (1-2)*, 13-25.

[157] M.A. Vannice, *Kinetics of Catalytic Reactions*, Springer Science Business Media Inc, New York, **2005**.

[158] H.A. Dirksen, C.H. Riesz, *Ind. Eng. Chem. Res.* **1953**, *45 (7)*, 1562-1565.

[159] W.W. Akers, D.P. Camp, *AIChE J.* **1955**, *1 (4)*, 471-475.

[160] L.O.A. N.M. Bodrov, M.I. Temkin, *Kinet. Catal.* **1968**, *9*, 1065–1071.

[161] L.O.A. N.M. Bodrov, M.I. Temkin, *Kinet. Catal.* **1967**, *8*, 821–828.

[162] L.O.A. N.M. Bodrov, M.I. Temkin, *Kinet. Catal.* **1964**, *5*, 696–705.

[163] D.W. Allen, E.R. Gerhard, M.R. Likins, *Ind. Eng. Chem. Res.* **1975**, *14 (3)*, 256-259.

[164] C. De Deken J, F. Devos E, F. Froment G, *Steam Reforming of Natural Gas: Intrinsic Kinetics, Diffusional Influences, and Reactor Design*, in: J. Wei, C. Georgakis (Eds.) Chemical Reaction Engineering-Boston, American Chemical Society, Boston, **1982**, pp. 181-197.

[165] S.S.E.H. Elnashaie, A.M. Adris, A.S. Al-Ubaid, M.A. Soliman, *Chem. Eng. Sci.* **1990**, *45 (2)*, 491-501.

[166] J.R. Rostrup-Nielsen, *Catal. Today.* **1993**, *18 (4)*, 305-324.

[167] K. Hou, R. Hughes, *Chem. Eng. J.* **2001**, *82 (1-3)*, 311-328.

[168] A. Gritsch, G. Kolios, U. Nieken, G. Eigenberger, *Chem. Ing. Tech.* **2007**, *79 (6)*, 821-830.

[169] A.F. Cunha, *Hydrogen production by catalytic decomposition of methane*, in: Department of Chemical Engineering, Universidade do Porto, Porto, **2009**.

[170] H.S. Bengaard, J.K. Norskov, J. Sehested, B.S. Clausen, L.P. Nielsen, A.M. Molenbroek, J.R. Rostrup-Nielsen, *J. Catal.* **2002**, *209 (2)*, 365-384.

[171] J.R. Rostrup-Nielsen, *CATTECH.* **2002**, *6 (4)*, 150-159.

3. Studies on Materials Development and Evaluation[†]

In this chapter, hybrid materials with Cu (section 3.1) or Ni (section 3.2) as active phase and HTlc as sorbent have been prepared and employed for SRE and SE-SRE studies. Both the Cu- and Ni-HTlc materials show good stability during the SRE and SE-SRE tests due to the unique layered double hydroxide structure. The hydrogen production through SRE was enhanced by carbon dioxide sorption in the initial transient period. Afterwards, K-promoted HTlc (section 3.3) material with potassium nitrate as the K precursor was developed to improve the carbon dioxide adsorption performance of pure HTlc material. The synthesized material was found to have promising stability during repeated adsorption/desorption cycles.

Finally, we extend the previous results to develop a multi-functional material consisting of K, Cu, Ni and HTlc (section 3.4). It was found that Ni and Cu formed an intermetallic alloy $Ni_{0.5}Cu_{0.5}$ with the advantage of ensemble formation. The K promoter together with the hydrotalcite material ensured a successful carbon dioxide sorption performance. As a result, high purity hydrogen steam can be obtained during the pre-breakthrough period at 773 K.

[†] The content of this chapter is part of the following articles:

A.F. Cunha, Y.-J. Wu, J.C. Santos, A.E. Rodrigues, Sorption Enhanced Steam Reforming of Ethanol on Hydrotalcite-like Compounds Impregnated with Active Copper, Chemical Engineering Research and Design, 91(3), 2013, 581–592.

A.F. Cunha, Y.-J. Wu, J.C. Santos, A.E. Rodrigues, Steam Reforming of Ethanol on Copper Catalysts Derived from Hydrotalcite-like Materials, Industrial & Engineering Chemistry Research, 51(40), 2012, 13132–13143.

Y.-J. Wu, Ping Li, J.-G. Yu, A.F. Cunha, A.E. Rodrigues, Sorption-Enhanced Steam Reforming of Ethanol on NiMgAl Multifunctional Materials: Experimental and Numerical Investigation, Chemical Engineering Journal, 231, 2013, 36–48.

Y.-J. Wu, Ping Li, J.-G. Yu, A.F. Cunha, A.E. Rodrigues, K-Promoted Hydrotalcites for CO_2 Capture in Sorption Enhanced Reactions, Chemical Engineering & Technology, 36(4), 2013, 567–574.

A.F. Cunha, Y.-J. Wu, Ping Li, J.-G. Yu, A.E. Rodrigues, Sorption-Enhanced Steam Reforming of Ethanol on a K-Ni-Cu-Hydrotalcite Hybrid Material, Industrial & Engineering Chemistry Research, 53 (10), 2014, 3842–3853.

3.1 Copper-HTlc Hybrid System

3.1.1 Introduction

Nowadays, most of the energy is derived from non-renewable sources, such as fossil fuels [1]. The gradual depletion of these fossil fuel reserves as well as involved greenhouse gas emissions increased substantially the research efforts in new alternative energy systems [2]. Hydrogen is generally accepted to be the energy system of the future [3]. It is clean and efficient in fuel cells [4].

Steam reforming is the most important process for hydrogen production [5]. For a hydrogen infrastructure based on renewable resources, there is a need for efficient technologies. In late years, attentions have been given to the production of hydrogen and synthesis gas from ethanol. Bio-ethanol offers a highly attractive route, because it can be easily derived from biomass [6]. Moreover, it is abundant, renewable as an energy source, free of sulphur and it has a relatively high H/C ratio for steam reforming.

However, the research efforts on catalytic SRE are relatively young [7]. It is found that the reaction pathways of SRE differ significantly, depending on the nature of the catalyst [8] and operating conditions [9] used. Thus, it is of prime importance to design and develop a suitable material for selective hydrogen formation, with sufficient ethanol and water conversion.

Among different catalyst systems, nickel-based catalysts have been investigated extensively due to the relatively high activity and the low cost. However, the major problem for nickel-based catalysts is deactivation due to carbon deposition over nickel particles. It was found by Verykios et al. [9] that the formation of ethylene from dehydration reaction ($C_2H_5OH \rightarrow C_2H_4 + H_2O$) at high temperatures over a nickel-based catalyst could lead to polymeric deposits (coke).

In order to avoid carbon deposition, Vaidya et al. [9] proposed SRE in a two-layer fixed bed catalytic reactor (Figure 3-1). In a first layer ethanol can be converted into acetaldehyde and hydrogen ($C_2H_5OH \rightleftharpoons CH_3CHO + H_2$) on a copper-based catalyst at low temperatures, avoiding ethylene formation. The acetaldehyde may partially

decompose into methane and carbon monoxide ($CH_3CHO \rightarrow CH_4 + CO$). In addition, copper is known as an excellent active phase for the water-gas-shift reaction [10], which is reversible and exothermic. Hence, the equilibrium shifts to the right by favoring the formation of hydrogen and carbon dioxide at lower temperatures ($CO + H_2O \rightleftharpoons CO_2 + H_2$). The resulting mixture, consisting of hydrogen, acetaldehyde, methane, carbon dioxide and water is then fed into a second layer of a nickel-based catalyst, coupled with an HTlc carbon dioxide sorbent.

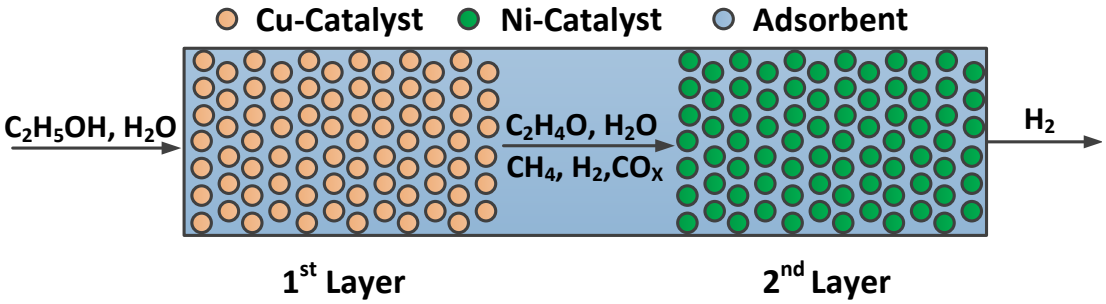

Figure 3-1 A two-layer fixed bed reactor for sorption-enhanced ethanol steam reforming

In the presence of nickel, the products of the first catalyst layer may undergo SR at lower temperatures (~ 673 K). The selective removal of carbon dioxide from the product stream by sorption further enables production of high-purity hydrogen. In a previous work, SE-SRE on a Ni/Al_2O_3 catalyst coupled with HTlc as sorbent in a multilayer pattern for carbon dioxide uptake was performed [11]. In this section, the concept of SERP on SRE was illustrated by the use of a hybrid system at 673 K.

At this point, it must be emphasized that the support material, for the copper-based catalyst in the first layer, should also have a carbon dioxide sorption capacity for sorption enhanced WGS (SE-WGS). Thus, the support material should act with at least bi-functional properties, as catalyst support and as carbon dioxide sorbent. Moreover, the use of a copper-based catalyst operating at 673 K requires a stringent operating stability (long life-time), which is at this moment quite difficult to achieve, according to the known state of the art [12]. Cu as the active phase for catalytic applications suffers mostly on deactivation phenomena, mainly provoked by thermal sintering. This is a big challenge, and to overcome this issue, an appropriated support

material is required for the stabilization of the dispersed copper crystallites.

Proper materials for metal crystallite stabilization are e.g. hydrotalcite-like compounds; they show apart from a wide range of applications as catalysts [13] and catalyst supports [14] also good capacities for the selective capture of carbon dioxide at large temperatures [15]. HTlc have layered structures with the general formula $[M^{2+}_{1-x}M^{3+}_{x}(OH)_{2x}]^{x+}(A^{n-}_{x/n})\cdot mH_2O$. Besides, HTlc has the so-called "memory effect" feature [16], which means the layered structure can be regenerated by exposure to anions after a relatively gentle calcination.

Several potential advantages of SE-SRE were found to reduce the hydrogen production cost [11, 17]. Lower reaction temperatures, less expensive construction materials, decreased heat exchanger sizes and simplified purification units [18] can be achieved when a single unit consisting on both, a reaction part (catalyst) and a separation part (sorbent for carbon dioxide capture) is used.

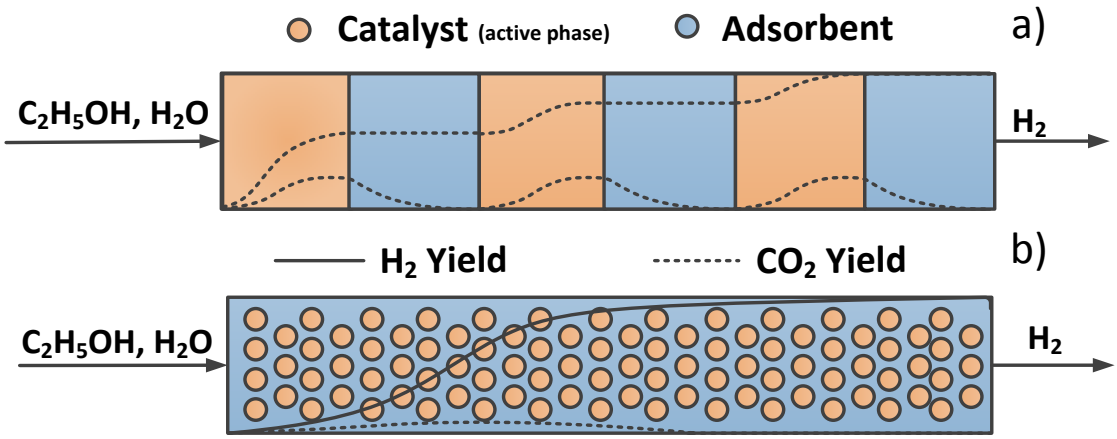

Figure 3-2 Possible arrangements of the hybrid system (catalyst plus sorbent): Multilayer pattern system of catalyst and sorbent (a) or active phase dispersed in the sorbent (b).

Thus, the material acts as a multi-functional system, as catalyst, as catalyst support and as carbon dioxide sorbent. These types of materials (hybrid systems) can be arranged in different manners and they are explained in Figure 3-2. At least two arrangements are possible for a hybrid system of catalyst plus sorbent. In Figure 3-2a the catalyst and the sorbent can be arranged in a multi-layer pattern system [11], or the active phase (catalyst for SRE) is randomly dispersed in the sorbent (catalytic support

for the active phase and selective carbon dioxide sorbent) [19]. In this section, we will focus our attention on the latter possibility.

The resulting gas mixture coming out from a copper hybrid system, consisting ideally only of hydrogen, methane, water and carbon dioxide after breakthrough [9], can then be fed into a second Ni-based hybrid system (e.g. Ni-catalyst coupled with a carbon dioxide sorbent). In the presence of Ni, the products of the first system may undergo SMR at the same low temperature range (around 673 K). The selective removal of carbon dioxide from the SMR product stream by sorption further enables the production of high-purity hydrogen [20]. Barelli et al. [21] and Harrison [22] have systematically discussed this technique.

However, the use of a copper-based hybrid system operating between 648 K and 723 K requires a stringent operating stability (long life-time), which can hardly be approached. In the present work, a hybrid system Cu-HTlc is developed for SE-SRE. This hybrid system was prepared by a novel and simple impregnation method. In addition, the calcination of HTlc creates mixed oxides [16], which are useful in catalytic applications due to their high surface area, large pores and the copper dispersion [14, 23] on surface.

In this section, two types of Cu-HTlc materials have been prepared/studied, CuZnAl and CuMgAl based hybrid materials. Relative good catalytic stability of the used active copper phase becomes another part of the improvement. Furthermore, forceful evidence of the sorption enhanced steam reforming process has been found during the first minutes of reaction in the hybrid systems. The effect of the operating conditions on the activity and selectivity was also studied for these systems and critically compared one with each other.

3.1.2 Experimental

3.1.2.1 Materials

CuMgAl samples were prepared from a commercial hydrotalcite-like compound. PURAL MG30 (Sasol) was used as support material for copper and as carbon dioxide

sorbent. The sorbent was impregnated with copper-nitrate trihydrate using a simple technique to obtain different copper loadings. The materials obtained are designated by the sorbent material used and the corresponding copper loading (e.g. CuMgAl-5HT, corresponding to a copper loading of 5 wt. %). The abbreviation HT stands for the used HTlc PURAL MG30. The calculated amounts of $Cu(NO_3)_2 \cdot 3H_2O$ were dissolved into 200 ml of water at room temperature. Hereafter, the pellets of the PURAL MG30 sorbent were added to this solution, and treated under heated ultrasonic environment at 373 K during 2 h. The obtained suspensions were further dried in an oven at 383 K for 48 h. These materials were smashed and crushed in a grinding mill into a fine powder, and then loaded into the reactor for thermal treatment during 48 h at 548 K under a nitrogen flow-rate of 50 $Ncm^3 \cdot min^{-1}$. Finally, this system was activated with a pure hydrogen flow-rate of 30 $Ncm^3 \cdot min^{-1}$ at 548 K during 24 h.

On the other hand, the CuZnAl materials used in this work were prepared in an automated laboratory reactor (Mettler-Toledo Labmax) by constant pH precipitation from aqueous metal solutions, with Na_2CO_3 as precipitating agent and a subsequent individual ageing time in the mother liquor. The continuously obtained precursor was prepared by a slightly different production method as it was precipitated accordingly from a Cu and Zn nitrate solution, using Na_2CO_3 solution to which an adequate amount of sodium aluminate was added. This slurry was continuously fed into a spray-dryer (Niro minor mobile, T_{inlet} = 473 K, T_{outlet} = 373 K). The active catalyst was obtained *in-situ* from the precursor by calcination in air and reduction in pure hydrogen. The material obtained is designated as CuZnAl-50HT.

The experimental setup, analysis and calculation methods used for the material evaluation can be found in the previous chapter II (page 46).

3.1.2.2 Characterization of the materials

The materials were characterized before and after SRE runs, applying different physical-chemical techniques.

The elemental compositions of the materials were determined with inductively

coupled plasma atomic emission spectroscopy (ICP-AAS) analysis IRIS 1000 (Thermo Elemental, Franklin, USA). The specific surface areas of the fresh materials were calculated by the BET method from the nitrogen equilibrium adsorption isotherms at 77 K, determined with ASAP2020-M (Micromeritics Instrument Co., Atlanta, USA). The decomposition behavior during calcination was simulated with Thermogravimetry analysis (TG) in a Pyris Diamond TG (Perkin-Elmer, Boston, USA) analyzer with coupled mass spectrometry (MS) in HPR-20 QIC (Hiden, Warrington, UK). X-ray powder diffraction (XRD) patterns were recorded within the range of 10–80° (2θ) by D/max2550V (Rigaku Co., Tokyo, Japan) diffract meter equipped with a Cu K_α radiation source. The materials were examined with the S-4800 (Hitachi, Tokyo, Japan) scanning electron microscope (SEM). The reducibility of CuO over the calcined materials was studied by temperature programmed reduction (TPR) technique with CATLAB (Hiden, Warrington, UK). At a rate of 5 $K \cdot min^{-1}$, 20 mg sample was heated from room temperature to 973 K, in a H_2 (5 mol %)/Ar flow (100 $cm^3 \cdot min^{-1}$). A high-resolution transmission electron microscopy (HR-TEM) study of the materials was carried out with a Philips CM200FEG microscope operated at 200 kV.

3.1.3 Results and Discussion

3.1.3.1 Materials characterization

The properties of the sorbent, PURAL MG30, used as catalyst support material for the active copper phase was described in a previous work [24].

Materials composition: The results for the composition of the materials used are collected in Table 3-1. It might be observed that the results obtained from the ICP-AAS are in good agreement with the nominal mass percentage values. The mass losses between the precursors and the reduced materials are considerable, which can be explained by the decomposition reactions which occur during the preparation of the materials.

Table 3-1 Materials composition.

Materials	m_{prec} [a] [g]	m_{cat} [b] [g]	Cu:Mg:Al [mol %]	Cu:Mg:Al[c] [mass %]
CuZnAl-50HT	15.0	7.0	50:17:33	61:21:17
CuMgAl-5HT	60.0	52.6	6:35:59	13:30:57
CuMgAl-14HT	82.0	58.4	14:32:54	28:25:47
CuMgAl-25HT	113.9	71.7	20:31:49	38:22:40

[a] Total mass of the precursor, [b] Total mass of the catalyst and [c] Mass percentage obtained by ICP-AAS for the reduced materials.

Nitrogen physisorption: The BET surface areas of precursors, calcined precursors, hydrogen reduced and materials obtained after SRE are collected in Table 3-2.

Table 3-2 Characterizations obtained by BET and pore sizes obtained by BJH.

Materials	S_{BET} [a] [m^2/g]	$\bar{d}_{pore}$ [a] [nm]	S_{BET} [b] [m^2/g]	$\bar{d}_{pore}$ [b] [nm]	S_{BET} [c] [m^2/g]	$\bar{d}_{pore}$ [c] [nm]	S_{BET} [d] [m^2/g]	$\bar{d}_{pore}$ [d] [nm]
CuZnAl-50HT	200	8	n.a.	n.a.	n.a.	n.a.	n.a.	n.a.
CuMgAl-5HT	162	7	159	9	187	9	98	15
CuMgAl-14HT	123	6	157	9	150	12	95	14
CuMgAl-25HT	85	7	48	11	104	11	67	13

[a] precursor, [b] calcined precursor, [c] reduced and [d] after SRE.

In general, all the materials show relatively high BET surface areas. It can be found that the surface areas increase during calcination as well as during reduction, and decrease after SRE which is an indication for sintering.

Associated to these results, Figure 3-3 shows the nitrogen equilibrium sorption isotherms obtained at 77 K of CuMgAl-14HT. It might be observed that the shape of all these isotherms are quite similar, which can be interpreted as a type IV isotherm associated with a hysteresis of type H1. The isotherms obtained are typical for mesoporous materials with pores in the range between 2 and 50 nm. The hysteresis of type H1 is normally an indication that the material is composed of rigid agglomerates with spherical shapes and uniform size arrangement.

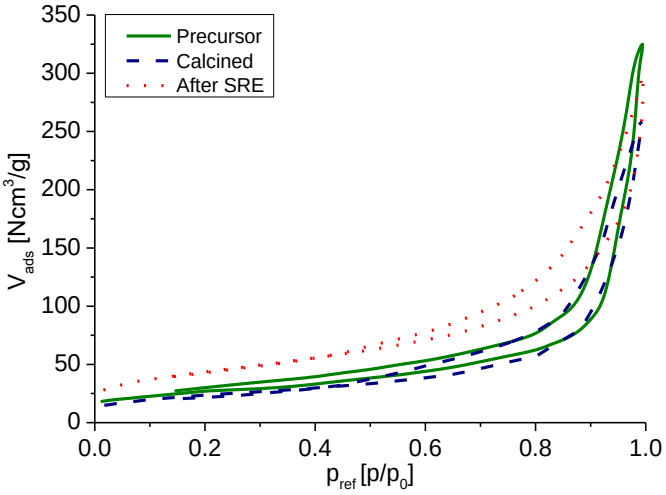

Figure 3-3 N_2 equilibrium adsorption-desorption isotherm of CuMgAl-14HT at 77 K of the precursor, calcined precursors and reduced materials before and after SRE.

The pore size distribution in the mesoporous region (2-50 nm) can be estimated from the desorption curve following the method of Barrett-Joyner-Halenda (BJH) [25]. This method assumes cylindrical pores and the results can be found in Table 3-2. The medium pore diameters of the CuMgAl based materials are within the same range, and increase with the thermal treatments applied, from around 7 nm (precursor) to around 14 nm (after SRE).

Thermogravimetry - Mass Spectrometry (TG-MS): In order to investigate the structural effects on carbon dioxide adsorption, it is important to study the dehydration and the decarbonation of the materials used. Decomposition products were monitored during the heating of the materials from room temperature to 973 K in typical TG-MS experiments which were conducted with 21 mol % oxygen in Argon at a flow rate of 100 $Ncm^3 \cdot min^{-1}$. The results are presented in Figure 3-4.

It is known that the Hydrotalcite ($Mg_6Al_2(OH)_{16}CO_3 \cdot 4H_2O$) is an anionic clay with a structure similar to brucite ($Mg(OH)_2$). However, part of the Mg cations are replaced with Al^{3+} in a HTlc and the resulting positive charge is compensated by anions, typically carbonate, in the interlayer between the brucite-like sheets [16]. Also known, the activation of HTlc involves a heat treatment wherein the layered structure is destroyed to form a mixed oxide. However, in a next step the material is rehydrated to restore the original HTlc structure to a large extent and with the exclusion of other

anions and carbon dioxide, Brønsted base sites (OH^-) are incorporated in the interlayer [26-30].

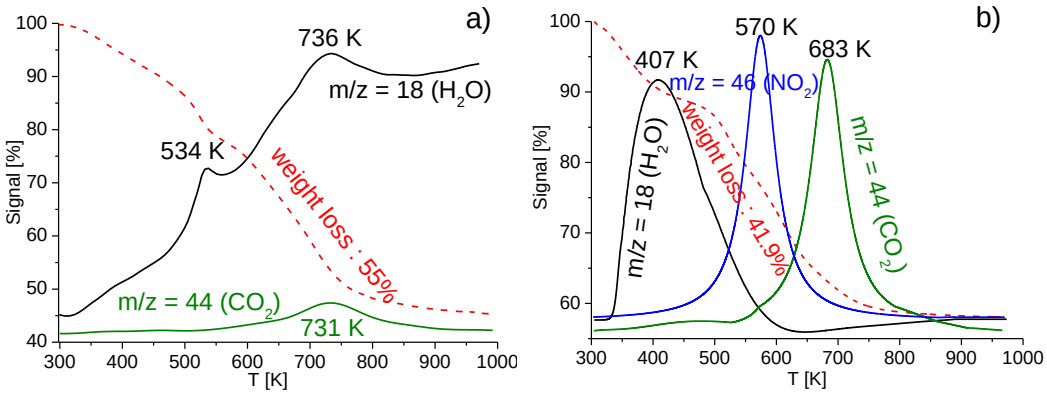

Figure 3-4 TG-MS of the sorbent MG30 (a) and the precursor CuMgAl-14HT (b).

During the calcination of precursors, hydroxyl carbonates can be released due to thermal decomposition processes, forming corresponding metal oxides. Every step corresponds to a certain process caused by the temperature increase. Nevertheless, it is possible to check whether the decomposition of hydroxyl carbonates into oxides is completed under the applied calcination conditions or if high-temperature carbonates are still present.

The water release is observed for the MG30 HTlc at around 534 K (Figure 3-4a) and, especially at 736 K where the release of carbon dioxide is also observed in the same temperature peaking. This is an indication that the structure of MG30 material is irreversibly destroyed at temperatures ≥ 723 K and in agreement with reports in literature [16].

The CuMgAl-14HT precursor material (Figure 3-4b) shows strong releases of water (peaking at 407 K), nitrogen dioxide (peaking at 570 K) and carbon dioxide (peaking at 683 K) during thermal treatment, as expected for the chemical nature of this type of materials. Remind that the HTlc was impregnated with $Cu(NO_3)_2 \cdot 3H_2O$, as the temperature increases the copper(II)-nitrate decomposes into copper(II)-oxide, while water and nitrogen dioxide is released.

X-Ray Diffraction (XRD): XRD is an important method to characterize materials in terms of catalytic behavior as well as the phase composition, structural properties of

the bulk phase and crystal sizes. The phase composition may help to interpret possible sorption effects of carbon dioxide during the first minutes of SRE (SE-SRE), if e.g. the presence of the HTlc structure is detected. Structural properties may give information of the atoms arrangement in the corresponding phase, the crystal sizes of the active phase obtained from diffraction patterns and their full width at half maximum (FWHM) through the Debye-Scherrer equation, which can be used to interpret catalytic activity and stability.

The XRD patterns of the MG30 carbon dioxide sorbent, not shown here, clearly depict an HTlc structure similar to earlier reports available in literature [31-34]. In another report [35], it is also shown that the crystallinity increases with Mg content.

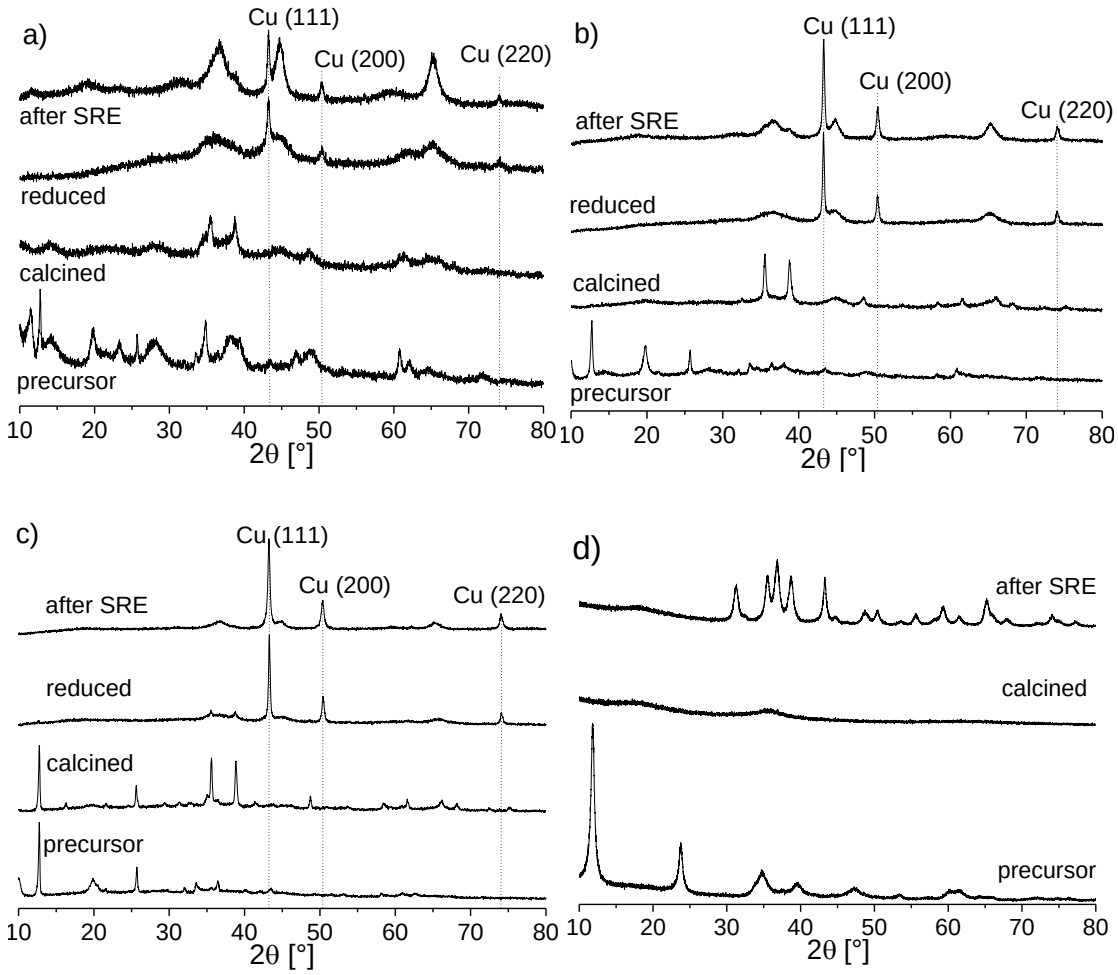

Figure 3-5 XRD patterns of the materials used; CuMgAl-5HT (a), CuMgAl-14HT (b) and CuMgAl-25HT (c) and CuMgAl-50HT (d).

However, the calcination of MG30 at 873 K results in the destruction of the LDH structure and the formation of a periclase MgO, which is also found for pure MgO [36]. Peaks of the periclase structure in MG30 are broad and low in intensity. Weak, broad peaks for $MgAl_2O_4$ (35◦, PDF no. 21-1152) and γ-Al_2O_3 (66◦) are also observed in the patterns of MG30, and a spinel phase is formed at a higher degree after calcination of MG30 at 973 K. The characterization of the bulk structure for the materials prepared for the use in SRE was obtained through the collection of XRD patterns, before and after SRE. The materials used before SRE are subdivided in their treatment features, the precursors produced, their calcined state and their reduced state. These diffraction patterns are shown in Figure 3-5, in association with the identification of the phases formed for CuMgAl can be found in Table 3-3.

The CuMgAl materials of different metal loadings (Figure 3-5) showed the presence of copper hydroxyl nitrate ($Cu_2(OH)_3NO_3$), aluminum oxide (Al_2O_3) and magnesium aluminum double hydroxide ($Mg_2Al(OH)_7$) at the precursor state. Copper(II)-oxide (CuO), Al_2O_3 and magnesium aluminium spinel ($MgAl_2O_4$) are found at the calcined state, metallic copper (Cu^0) and the HTlc structure ($Mg_6Al_2(OH)_{16}CO_3{\cdot}4H_2O$) for the reduced state. After SRE experiments, which means SRE was conducted from 473 to 873 K with a total time on stream of more than 30 h, only metallic copper, magnesium aluminium oxide ($MgAl_2O_4$) and copper(II)-oxide were detected as species in the bulk structure.

On the other hand, the precursor of CuZnAl-50HT (Figure 3-5d) can be identified as a typical hydrotalcite-like material. It matches with the patterns reported for $Cu_3Zn_3Al_2(OH)_{16}CO_3{\cdot}4H_2O$ [37]. No other crystalline phase is observed. The d-spacings of (003) and (006) reflections correspond to the FWHM of brucite-like sheets. After calcination of the CuZnAl-HT, the following phases were identified: CuO, ZnO and $CuAlO_2$. The HTlc structure was almost destroyed. The calcined CuZnAl-HT was then reduced *in-situ* with hydrogen and subjected to XRD analysis. Typical reflection planes of Cu, assigned to a metallic faced centred cubic phase were identified. This is an indication that most of the copper was reduced.

Table 3-3 Phases identified in the materials with the corresponding 2θ positions

Material	Treatment	Phase	2θ positions & reflection planes	PDF-File ICDD
CuMgAlx·HT	precursor	$Cu_2(OH)_3NO_3$	12.8 °(001), 25.8 °(111), 36.5 °(121), 39.4 °(015)	75-1779
		Al_2O_3	31.8 °(013), 34.7 °(122), 42.6 °(132), 64.8 °(135), 67.0 °(330)	88-0107
		$Mg_2Al(OH)_7$	11.6 °(003), 23.3 °(006), 34.8 °(012), 46.8 °(018), 62.0 °(113)	35-1275
	calcined	CuO	35.7 °(-111), 38.9 °(111), 49.0 °(-202)	89-5898
		Al_2O_3	31.8 °(013), 34.7 °(122), 42.6 °(132), 64.8 °(135), 67.0 °(330)	88-0107
		$MgAl_2O_4$	18.8 °(111), 36.4 °(311), 44.2 °(400), 58.5 °(511), 64.3 °(440)	77-0437
	reduced	Cu	43.2 °(111), 50.3 °(200), 73.9 °(220), 89.6 °(311)	70-3038
		$Mg_6Al_2(OH)_{16}CO_3·4H_2O$	35.0 °(012), 35.6 °(009), 60.9 °(110), 62.4 °(113)	35-0964
	after SRE	Cu	43.2 °(111), 50.3 °(200), 73.9 °(220), 89.6 °(311)	70-3038
		$MgAl_2O_4$	31.3 °(220), 36.8 °(311), 44.8 °(400), 65.2 °(440)	77-1193
		CuO	35.7 °(-111), 38.9 °(111), 49.0 °(-202)	89-5898
CuZnAl-50HT	precursor	$Cu_3Zn_3Al_2(OH)_{16}(CO_3)·3H_2O$	11.8 °(003), 23.7 °(006), 34.7 °(012), 39.4 °(015), 47.1 °(018), 60.2 °(110)	37-0629
	calcined	CuO	35.7 °(-111), 38.9 °(111), 49.0 °(-202)	65-2309
		ZnO	31.8 °(100), 34.4 °(002), 36.3 °(101), 56.6 °(110)	89-0510
		$CuAlO_2$	31.6 °(004), 37.1 °(101), 39.7 °(102), 54.9 °(105)	40-1037
	after SRE	Cu	43.3 °(111), 50.4 °(200), 74.1 °(220)	04-0836
		CuO	35.7 °(-111), 38.9 °(111), 49.0 °(-202)	89-5898
		$CuAl_2O_4$ (Spinel)	31.3 °(220), 36.9 °(311), 59.4 °(511), 65.3 °(440)	78-1605
		$Cu_2Al_4O_7$	31.6 °(004), 37.1 °(101), 39.7 °(102), 54.9 °(105)	83-1476

Before SRE runs, the precursor was calcined in air at 275 ℃, followed by activation with pure hydrogen flow. Accordingly, when SRE was started, most probably only not detectable traces of the HTlc structure remain in the bulk structure of the material. The XRD pattern taken after SRE reaction has the following phases: Cu, CuO, $Cu_2Al_4O_7$ and $CuAl_2O_4$ (corresponding to a syn-Spinel). Possible carbon dioxide sorption effects, observed in SE-SRE runs can only be explained by the fact that ZnO has the ability to adsorb carbon dioxide on its surface [38].

Table 3-4 collects the crystal sizes of copper for the materials used before and after SRE. The formation of small copper particles is desired in terms of catalytic performance. It is observed that after SRE, the crystal sizes of copper obtained become larger, which means copper has sintered.

Table 3-4 Copper crystal sizes obtained from the Cu (111) reflex.

Material	d [a] [nm]	d [b] [nm]
CuZnAl-50HT	7	17
CuMgAl-5HT	16	20
CuMgAl-14HT	20	22
CuMgAl-25HT	23	36

[a] after reduction and [b] after SRE.

Scanning Electron Microscopy (SEM): Figure 3-6 depicts the SEM micrographs of selected samples. The precursor (Figure 3-6a) and calcined precursor (Figure 3-6b) of CuMgAl-25HT show platelet-like morphologies, indicating the structure was kept.

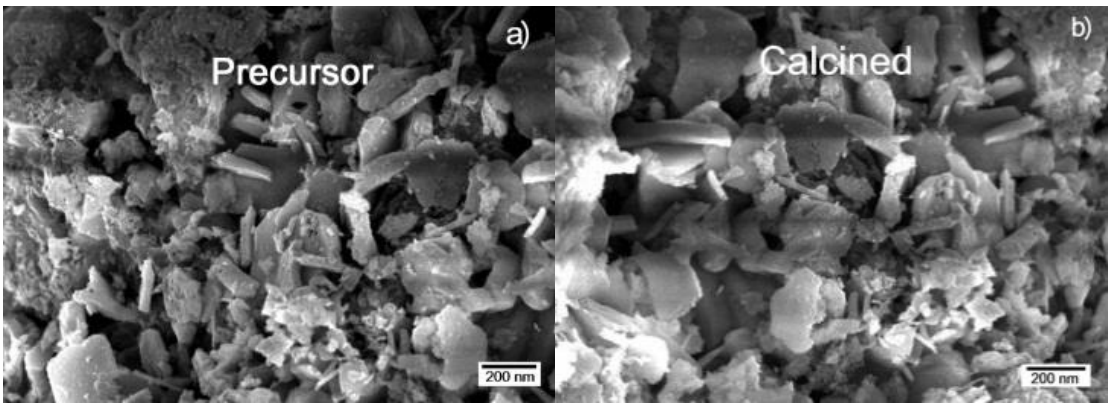

Figure 3-6 SEM micrographs of the precursor (a) and calcined precursor (b) of CuMgAl-25HT.

Temperature Programmed Reduction (TPR): TPR profiles were recorded for the CuMgAl material used. These TPR analyses were performed with 5 mol % of hydrogen in an argon inert gas at atmosphere pressure, using a total flow rate of 100 $Ncm^3 \cdot min^{-1}$ (Figure 3-7). It was found that the reduction of copper in CuMgAl-14HT starts at around 473 K, associated with a peak maximum of around 598 K and with the reduction process ending at ~ 800 K without any further reduction stages involved. For the CuZnAl-50HT sample (Figure 3-7), it can be seen that the reduction of copper starts at about 400 K. The reduction curve has a peak at a temperature of 548 K, ending at around 600 K. It is also observed that two partially resolved reduction stages are well visible, which are connected to copper oxides reduction ($CuO \rightarrow Cu_2O \rightarrow Cu$) [39].

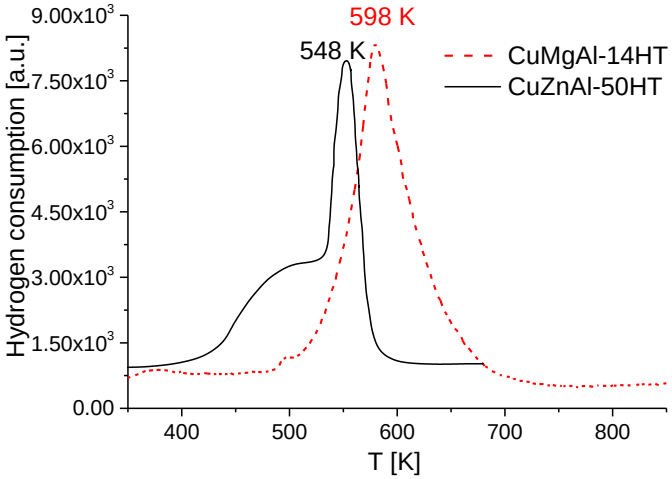

Figure 3-7 TPR on the calcined material CuMgAl-14HT.

Breakthrough Experiments: The material CuMgAl-14HT was tested to investigate the carbon dioxide adsorption performance with and without the presence of water vapor. Possible sorption properties for carbon dioxide capture on the materials used were insured by inert gas flow and steam for regeneration. The results of breakthrough experiments, for different molar fractions of carbon dioxide, are shown in Figure 3-8. Operating conditions are a helium flow-rate of 50 $Ncm^3 \cdot min^{-1}$, the presence of carbon dioxide (filled symbols) with water feed = 0.234 $ml \cdot min^{-1}$ (open symbols) at 673 K and total pressures of 1 bar.

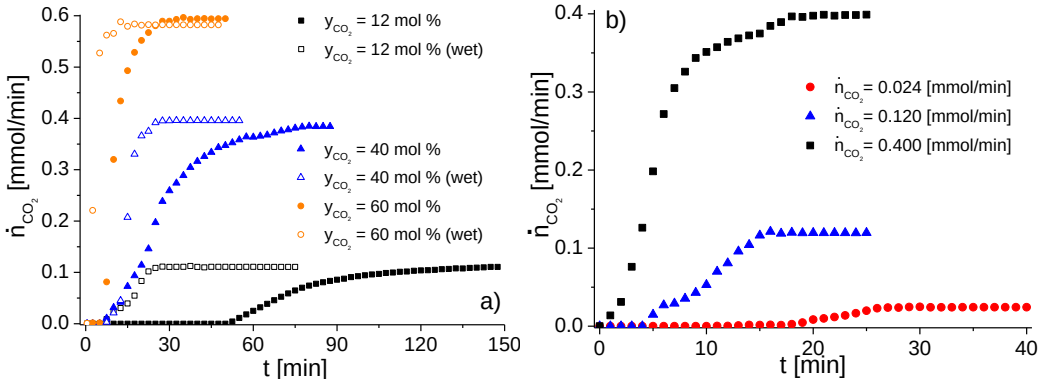

Figure 3-8 Breakthrough curves for CuMgAl-14HT material (a) and CuZnAl-50HT material (b).

It might be observed that CuMgAl-14HT has shown the ability of carbon dioxide adsorption. The breakthrough time, for each molar fraction of carbon dioxide, is directly linked to the sorption capacity of the material. The introduction of water vapor reduced the breakthrough time (and so the sorption capacity of carbon dioxide). It was found by Ficicilar and Dogu [40] that excess water vapor can cause partial pore mouth closure and increase the diffusion resistance for the transport of carbon dioxide to the active sites of the sorbent. As a result, the sorption capacity decreased from 0.11-0.18 mol·kg^{-1} to 0.03-0.10 mol·kg^{-1} in the presence of water vapor. The obtained CuMgAl materials have a similar adsorption capacity compared with pure MG30 hydrotalcites [24, 41]. This low carbon dioxide uptake was already expected since the HTlc used was not impregnated with a promoter such as potassium carbonate. In order to have a higher adsorption capacity for SE-SRE, the effects of the promoter on the adsorption and reaction performance of CuMgAl materials need to be investigated in the following sections. On the other hand, it could be observed that CuZnAl-HT had shown a similar ability of carbon dioxide sorption, as expected. It has been reported that $Cu_{1-x}Al_x$-HT-CO_3 with x = 0.43–0.48 has selectivity for carbon dioxide adsorption [42].

Transmission electron microscopy (TEM): In addition, a typical transmission electron microscopy (TEM) picture for CuZnAl-50HT was obtained (Figure 3-9a). Very small Cu particles embedded in the oxidic matrix are observed. Copper particle size distribution was also calculated, and a histogram is presented (Figure 3-9b). The

analyses show that the Cu particle of the CuZnAl-50HT material has a mean size of 7.7 nm.

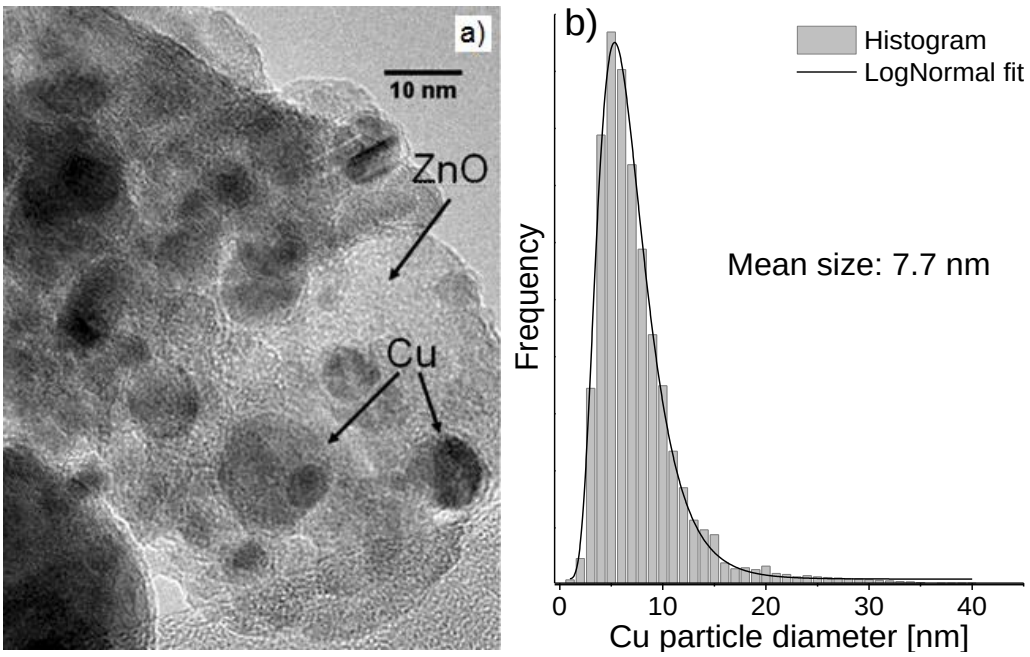

Figure 3-9 TEM image (a) and Cu particle size distribution (b) of CuZnAl-HT.

3.1.3.2 Activity of Cu-HTlc for SRE

Figure 3-10 shows the conversion of ethanol and water for SRE in the presence of the reduced Cu-HTlc materials at steady state conditions (each reaction temperature was conducted during 4h).

It can be observed that conversions of both, ethanol and water increase with the temperature. However, higher reaction temperatures are required for the activation of water, while ethanol already has a high conversion at lower temperatures. The conversion of ethanol on the Cu-HTlc materials (Figure 3-10) seems to be dependent on the copper loadings employed. For CuMgAl materials, higher metal loadings increase the catalytic activity for water conversion and especially for the ethanol conversion. No significant difference in the evolution of the conversions was observed when the inert gas flow-rate in the feed was increased from 50 $Ncm^3 \cdot min^{-1}$ (Figure 3-10a) to 200 $Ncm^3 \cdot min^{-1}$ (Figure 3-10b).

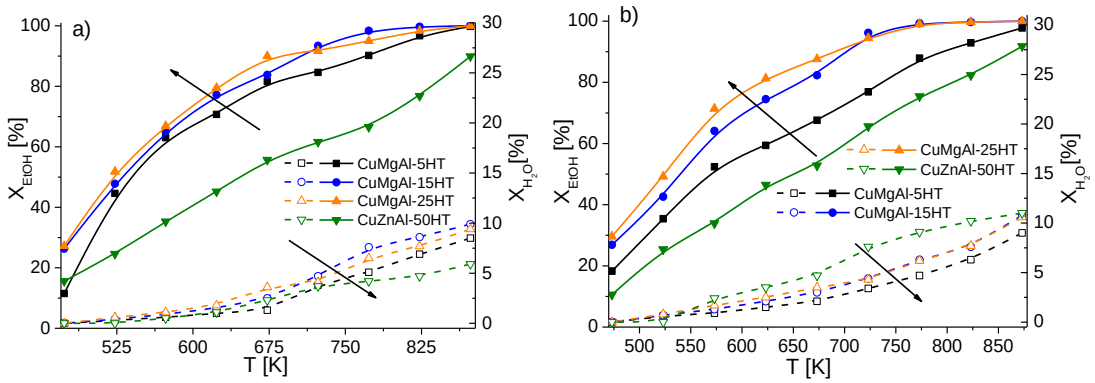

Figure 3-10 Ethanol and water conversion as function of reaction temperature at steady state conditions with m_{cat} = 5g and an inert-gas flow-rate of 50 $Ncm^3 \cdot min^{-1}$ (a) and 200 $Ncm \cdot min^{-1}$ (b) for the materials: CuMgAl-5HT, CuMgAl-14HT, CuMgAl-25HT and CuZnAl-50HT.

It was found that the Cu-HTlc materials show satisfying activities without apparent deactivation phenomena during 4 h measurement in a temperature range from 473 to 873 K. However, it must be emphasized that the temperature increase compensates in a certain level the activity loss. At this point it is also necessary to stress that compared with other active phases, copper is more likely to deactivate, especially because of thermal sintering. An increasing order of stability for metals is proposed [43]: Ag < Cu < Au < Pd < Fe < Ni < Co < Pt < Rh < Ru < Ir < Os < Re. These results are supported by the low Hüttig temperature of copper [44]. The predominant sintering mechanism in the bulk is known to be the vacancy diffusion [12]. SRE process employing copper-based catalysts should be operated at relatively low temperatures, generally lower than 573 K [18]. However, the latest report indicates that copper-based catalysts may also work at 673 K [45].

In order to investigate the stability of the copper-based materials, it was decided to carry out measurements with two selected materials at 673 K for 12 h, CuMgAl-14HT sample after SRE and the fresh CuMgAl-14HT material, as depicted in Figure 3-11. The CuMgAl-14HT material after SRE (Figure 3-11a) did not show strong deactivation behavior, because the initial activity of the sample was poor. The difference between the performances of fresh material and the material after SRE might be related with the destruction of the HTlc structure (formation of mixed oxides

and spinel) and the relative large crystal sizes after SRE at high temperatures (see Table 3-4).

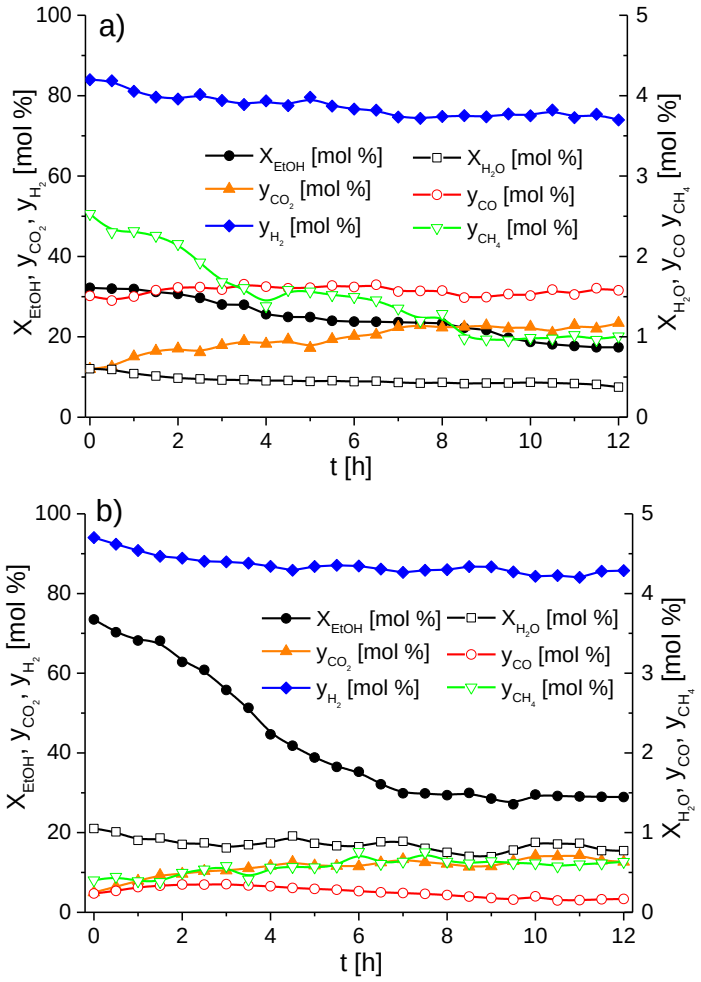

Figure 3-11 Ethanol and water conversion as well as product distribution on dry basis as function of reaction time over CuMgAl-14HT after SRE (a) and fresh CuMgAl-14HT (b). Operating conditions: m_{cat} = 3.4 g, T = 673 K, inert-gas flow-rate of 50 $Ncm^3 \cdot min^{-1}$.

In addition, the fresh CuMgAl-14HT material was also subjected to a long time measurement (Figure 3-11b). The catalytic behavior of CuMgAl-14HT during SRE was found to be close to the expected. The activity of the material was gradually decreased over time. As a result, to investigate the temperature effect on the SRE reaction performance of Cu-HTlc materials, the results of production distributions and conversions versus temperatures in the following section 3.1.3.3 were taken after 1 h of each reaction test.

This stabilization process (for the copper crystallites) can be a contribution of the HTlc structure (support material), where copper particles can have a good dispersion.

Another possible reason is the nature of the conducted reaction and respective operating conditions used, in our case the SRE. During the SRE reaction on the Cu-HTlc materials, a certain level of hydrogen is produced. This hydrogen is most probably beneficial, as it helps to maintain stable operation. Furthermore, from metallurgy it is known that oxygen containing copper can be fragmented when exposed to hot hydrogen [46]. The hydrogen diffuses through the copper and reacts with Cu_2O, forming steam and fragmented Cu. Pressurized steam bubbles are then formed at the grain boundaries. This process may cause the crystallites to literally be forced away from each other, and this is known as steam embrittlement. It may be possible that some regeneration of the copper crystallites has taken place during the SRE reaction, also because of the excess steam present in the reaction mixture which can contribute to an embrittlement. In addition, the established operating conditions for SRE where Cu-HTlc catalysts perform well are not necessarily optimal for other reactions [47]. However, some thermal stability was also observed for methane decomposition on massive Raney-Copper catalysts under severe reaction temperatures [48].

3.1.3.3 Product distribution on dry basis for SRE

The product distributions on dry basis as evolution of the reaction temperature during SRE at steady state conditions in the presence of the Cu-HTlc materials are depicted in Figure 3-12.

Ideally, SRE only generates carbon dioxide and hydrogen. In practice many other reactions take place, leading to the formation of intermediates and by-products.

The results of Cu-HTlc materials (Figure 3-12) show that at low temperatures nearly pure hydrogen was obtained from the outlet stream. The increase of the reaction temperature subsequently caused a decrease in hydrogen purity. Apart from the presence of carbon dioxide in the dried gas stream, traces of methane and carbon

monoxide were observed. At reaction temperatures higher than 673 K, the amounts of by-products increase considerable. Especially the appearance of ethylene was more notable when lower copper loaded materials were employed.

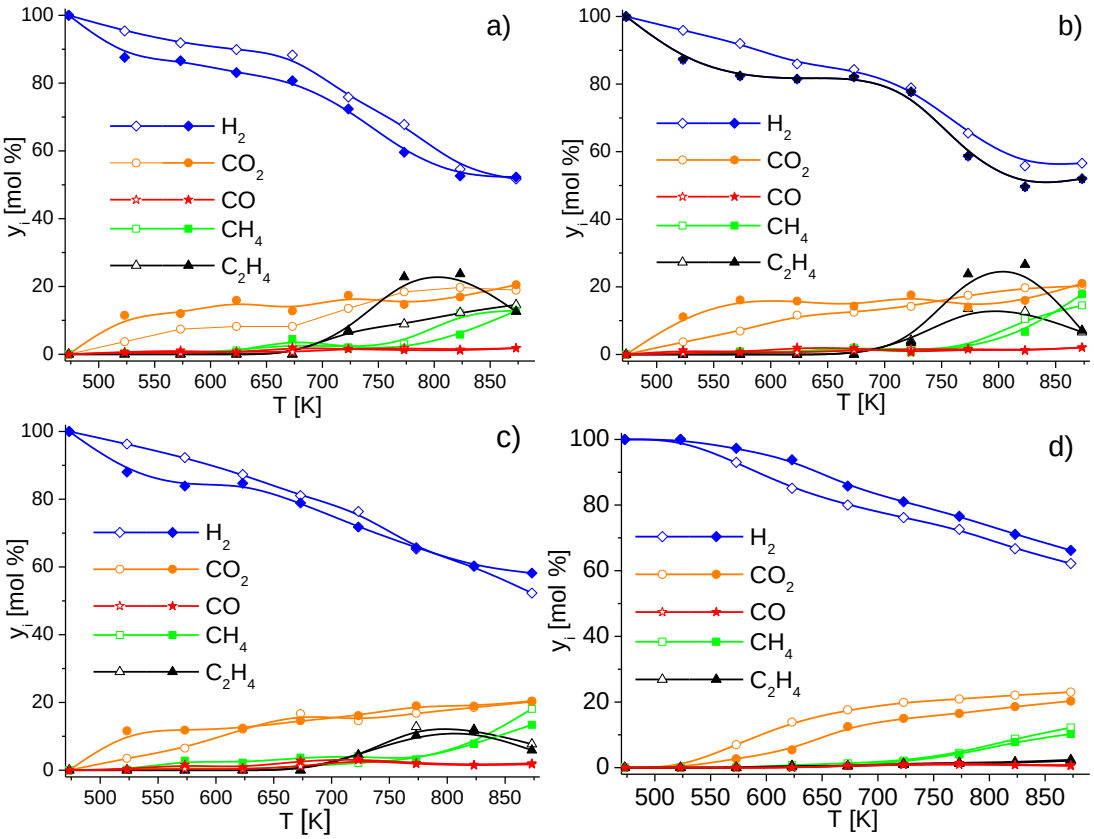

Figure 3-12 Product distribution on dry basis as function of reaction temperatures after 1 h of SRE reaction with m_{cat} = 5g and an inert-gas flow-rate of 50 $Ncm^3 \cdot min^{-1}$ (open symbols) and 200 $Ncm^3 \cdot min^{-1}$ (filled symbols) for the materials: (a) CuMgAl-5HT; (b) CuMgAl-14HT, (c) CuMgAl-25HT and (d) CuZnAl-50HT.

It is well known that two main reaction pathways can occur during SRE [8]: the dehydration and dehydrogenation route. The former one consists on the formation of ethylene (produced via dehydration of ethanol $C_2H_5OH \rightleftharpoons C_2H_4 + H_2O$), which can be further decomposed into carbonaceous species ($C_2H_4 \rightleftharpoons CH_4 + C$ or $C_2H_4 \rightleftharpoons 2H_2 + 2C_x$). Carbon deposition may also occur via Boudouard reaction ($2CO \rightleftharpoons CO_2 + C$) [49] and methane decomposition ($CH_4 \rightleftharpoons 2H_2 + C_x$) [50]. This "encapsulating" carbon blocks the active sites of the catalyst and results in deactivation. At this point it is important to stress that in this work a water/ethanol ratio of 10 was used in the feed,

while thermodynamic studies have found that high water/ethanol ratios can suppress the carbon deposition [17, 51]. As a result, the aforementioned carbon deposition has not been detected during all the experiments.

However, one disadvantage of using higher water to ethanol ratios is that more energy is required to operate the process, even when a combined heat and power system is employed. To circumvent this problem, the hot excess steam coming out from the reactor can be recycled as heating source for the same reaction unit [52].

The products found in the liquid phase mainly consist of condensed water, acetaldehyde, acetone and acetic acid. The appearance of these products is strongly dependent on the reaction temperature, copper loadings and nature of the materials used. For instance, high amounts of acetaldehyde were detected in the liquid products at low reaction temperatures, while at higher reaction temperatures acetone starts to condensate.

The formation of acetaldehyde suggests that ethanol is decomposed through the dehydrogenation route ($C_2H_5OH \rightleftharpoons CH_3CHO + H_2$). Besides, acetic acid was also detected in traces at lower temperatures, suggesting the oxidation of acetaldehyde in the presence of steam ($CH_3CHO + H_2O \rightleftharpoons CH_3COOH + H_2$). Acetic acid can further decompose into methane and carbon dioxide ($CH_3COOH \rightleftharpoons CH_4 + CO_2$). Das et al. [18] reported that the formation of acetaldehyde could be suppressed when the $R_{S/E}$ in the feed increased from 3 to 6, due to the formation of acetic acid through acetaldehyde reaction with water steam. Indeed, methane starts to appear as a result of the acetic acid decomposition reaction, which takes place at 673 K and higher.

3.1.3.4 Product distribution on dry basis vs. reaction time

Product distributions as evolution of the reaction time during SRE in the presence of the Cu-HTlc materials have been given in Figure 3-13. Two different inert gas flow-rates of 50 $Ncm^3 \cdot min^{-1}$ (open symbols) and 200 $Ncm^3 \cdot min^{-1}$ (filled symbols) were used in the tests.

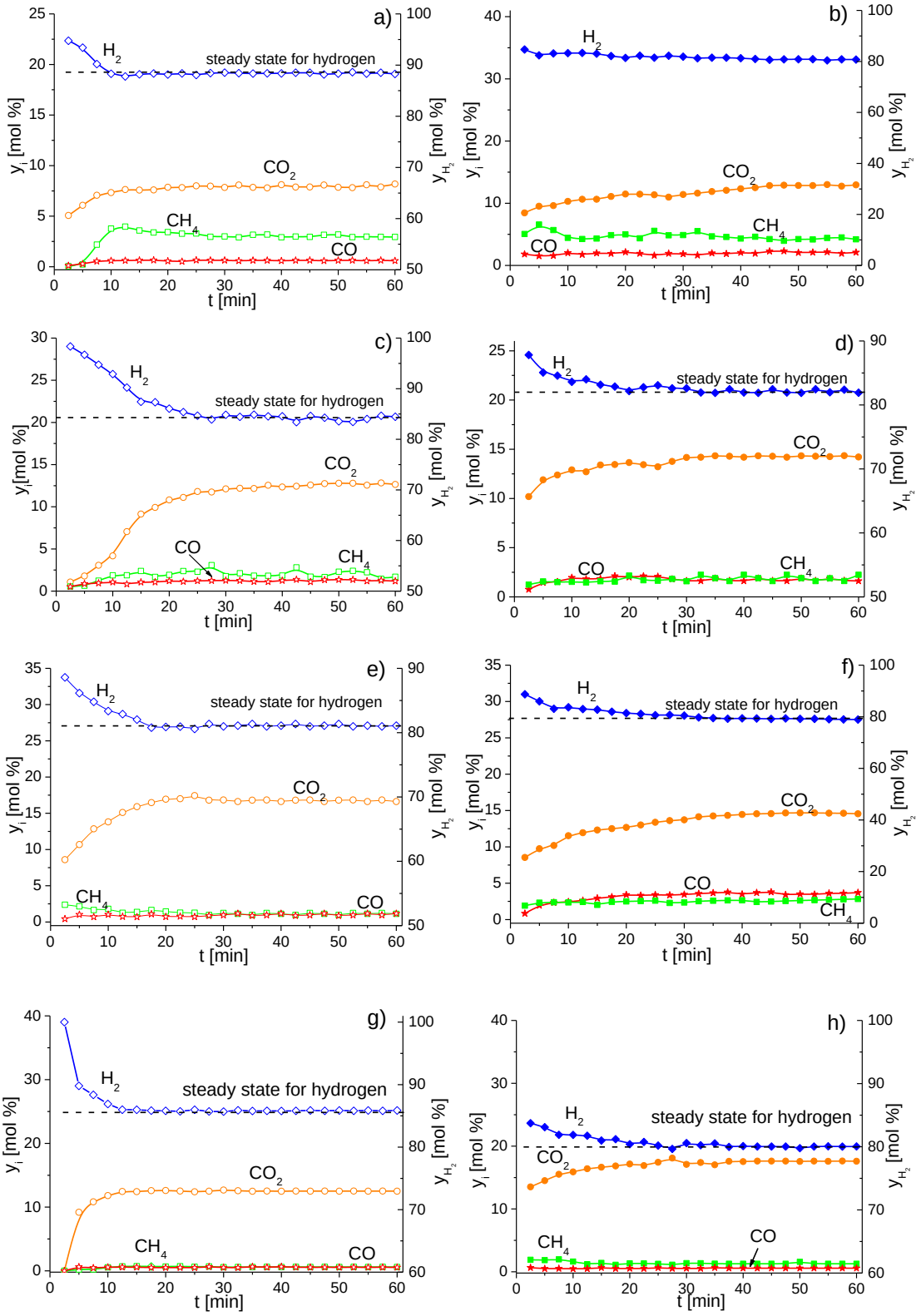

Figure 3-13 Product distribution on dry basis as function of reaction time on CuMgAl-5HT (a-b), CuMgAl-14HT (c-d), CuMgAl-25HT (e-f) and CuZnAl-50HT (g-h): m_{cat} = 5g, T = 673 K, $\dot{V}_{inert}$= 50 Ncm^3·min^{-1} (open symbols) or $\dot{V}_{inert}$ = 200 Ncm^3·min^{-1} (filled symbols).

The results collected for the materials used, depict the product compositions in the gas phase (hydrogen, carbon dioxide, methane and carbon monoxide), which reveal pre-, intermediate and post-breakthrough periods for the Cu-HTlc materials (Figure 3-13). The hydrogen content in the first minutes of operation was much higher than in the steady state operation. The enhancement in hydrogen production can be interpreted as a result of the HTlc structure within Cu-HTlc materials.

It can be found that CuMgAl-25HT shows less sorption enhancement than CuMgAl-14HT due to the loss of the surface area for carbon dioxide adsorption (Table 3-2). In addition, no obvious sorption enhancement was found with higher inert gas flow rate due to the low contact time.

HTlc are suitable to be employed as carbon dioxide sorbents [16], these materials have a satisfying sorption performance, stable capacity for cyclic operation and mechanical strength at around 673 K in the presence of steam [24]. Previous studies on HTlc at high temperatures [24, 41] have demonstrated that they can be applied to enhance the steam methane reforming [53] or SRE process [11]. Furthermore, the experiments were conducted with excess steam, so that the HTlc structure can be kept during SRE reaction [35].

It could be observed from Figure 3-13, for all the materials with HTlc structure, during the transient periods (0-10 min) either the conversions of ethanol and water, yields and selectivities of hydrogen are relative higher than in the steady state, suggesting that the carbon dioxide uptake enhances the reaction process.

Thermodynamic analysis [17] has shown that the carbon monoxide content in the obtained gas from SE-SRE with HTlc as carbon dioxide sorbent could be lower than 10 ppm. As a result, theoretically the produced hydrogen-rich gas can be directly employed for PEMFC applications. However, during the pre-breakthrough periods at 673 K with SE-SRE over CuMgAl-14HT material in this study, the carbon monoxide content was around 5000 ppm due to the limitation of the catalytic activity for WGS reaction.

3.1.4 Conclusions

Sorption enhanced steam reforming of ethanol can be performed on Cu-HTlc based materials. A new method of preparation was employed to the ensemble of catalyst and adsorbent for reaction enhancement of catalytic SRE.

The effects of the operating conditions and materials nature on the course of ethanol steam reforming products were studied. Hydrogen was generated in the temperature range between 473 K and 873 K.

Carbon dioxide uptake during the transient period of SRE is possible since an HTlc structure is kept after the synthesis of the materials used, as it was experimentally proved for the Cu-HTlc materials. Carbon dioxide uptake during the transient period of SRE was found with the CuZnAl based material derived from an HTlc precursor due to a relative good interaction of carbon dioxide formed during the initial transition period of SRE with the ZnO phase present in the CuZnAl catalyst, and also probably due to the reconstruction of HTlc structure in the presence of steam after calcination for the CuZnAl-HT catalyst. These materials have a similar carbon dioxide adsorption capacity as pure hydrotalcites at 673 K. A sorption enhanced reaction process concept may be verified for these systems. Higher amounts of hydrogen were yielded during the initial transient periods.

3.2 Nickel-HTlc Hybrid System

3.2.1 Introduction

Fossil fuels used as raw material and energy sources are limited [2]. In addition, ecological reasons become relevant due to the climatic changes caused by the carbon dioxide emission [54]. These facts lead to the idea "hydrogen economy" [55], based on hydrogen as the universal energy carrier. Hydrogen fuel cells are important in this concept due to the high efficiency and low environmental impact [56].

Hydrogen is generally produced through steam reforming of conventional fossil resources [57]. As an alternative, the use of renewable feedstock (methanol [58], bio-ethanol [59], glycerol [60], bio-oil [61], etc.) seems to be promising. Bio-ethanol,

which contains water in large excess, is an ideal feedstock that can be directly employed for steam reforming (SRE) [8]. The presence of excess water ensures sufficient supply of steam, improving hydrogen yield and reducing coke formation. Up to date, a wide range of catalytic materials have been investigated [9]. It was found that the use of nickel-based catalyst system promises success in catalytic SRE [59, 62, 63]. Nickel as active phase in a catalytic system proceeds via a complex network of reactions. Some of them are favored, depending on the catalyst and operating conditions used [64]. However, catalytic SRE is thermodynamically limited [17], the use of a carbon dioxide sorbent is required for a high hydrogen yield and has the advantage to capture carbon dioxide *in-situ* [65].

The catalyst and the sorbent can be arranged in different manners, as a multilayer pattern system of catalyst and sorbent [11, 66], mixtures of the two materials [65, 67] or the active phase (catalyst) integrated into the sorbent [68-71]. Among these methods, impregnating the active phase on the sorbent can assure a good dispersion. HTlc materials are excellent for this purpose due to the promising adsorption performance at moderate to high temperatures for carbon dioxide capture [72]. Thanks to the alkaline feature [42, 73], these materials are also useful in catalytic SRE process to avoid carbon deposition through formation of the ethylene, known as coke precursor. Therefore, HTlc can be suitable support materials for active phases in catalyst. In addition, Ni- [74-77] and Co- [78-80] based catalysts derived from HTlc precursors are found as good catalytic systems to produce hydrogen from SRE process due to the high surface areas and small crystal sizes [77]. One strategy to achieve the stabilization of Ni crystallites can be the incorporation of this active metal phase into a matrix of HTlc by a simple wet impregnation method. SE-SRE was investigated with copper as the active phase and HTlc sorbent as the support material in the previous section. The hydrogen yield increased 29 % during the initial transient period at 673 K. However, deactivation was found for the copper-based catalysts at higher temperatures due to sintering.

In this section, a systematic study was carried out for the production of hydrogen in

the presence of a Ni-HTlc hybrid material. Nickel was used as the active phase for the catalytic SRE reaction which has been impregnated in an HTlc. This later material shows bi-functional features; it is used as catalyst support material and it can capture carbon dioxide. As a result, sorption enhanced hydrogen production during SRE can be achieved. The purpose of this work is to develop the hybrid materials consist of Ni and Mg^{2+}/Al^{3+} based HTlc for SE-SRE, together with a numerical model to simulate and improve the performance for hydrogen production with the obtained materials for SE-SRE process.

3.2.2 Experimental

3.2.2.1 Materials synthesis

A commercial HTlc [81] from Sasol Germany GmbH was used as support material for the active nickel phase and as carbon dioxide sorbent. The support material was impregnated with nickel (II) nitrate hexahydrate (VWR international) to obtain different metal loadings.

The materials prepared are designated by the corresponding nickel loading (e.g. $Ni5.9^{MgAl}$ corresponds to a nickel loading of 5.9 wt. % and MgAl stands for the used HTlc based support material). The calculated amounts of $Ni(NO_3)_2\ 6H_2O$ were dissolved into 200 ml of water at room temperature. Hereafter, the HTlc pellets were added to this solution, and treated under heated ultrasonic environment at 363 K during 2 h. The obtained suspensions were further dried in an oven at 383 K for 48 h. These materials were smashed and crushed in a grinding mill into a fine powder, and then loaded into the reactor for thermal treatment during 48 h at 723 K with a nitrogen gas flow of 50 $Ncm^3 \cdot min^{-1}$. Finally, these materials have been activated at 723 K by hydrogen gas with a flow-rate of 30 $Ncm^3 \cdot min^{-1}$ for 24 h.

The experimental set-up, characterization and analysis methods used in this section can be found in previous chapter II (page 46). Altogether, six multifunctional materials each having a weight of 20 g were prepared and tested as shown in Table 3-5.

Table 3-5 Composition, pore diameter, pore volume and surface area of the materials.

Materials	metal ratios [wt./wt. %]*			before SRE			after SRE		
	Ni	Mg	Al	$\bar{d}_{pore}$ [nm]	S_{BET} [$m^2 \cdot g^{-1}$]	pore volume [$cm^3 \cdot g^{-1}$]	$\bar{d}_{pore}$ [nm]	S_{BET} [$m^2 \cdot g^{-1}$]	pore volume [$cm^3 \cdot g^{-1}$]
MG30	0	27.8	72.2	8	200.0	0.55	n.a.	n.a.	n.a.
$Ni1.0^{MgAl}$	2.8	25.9	71.3	9	182	0.33	11	130	0.34
$Ni5.9^{MgAl}$	13.2	24.1	62.7	9	152	0.31	12	112	0.29
$Ni11.5^{MgAl}$	23.5	21.6	54.9	11	119	0.29	13	86	0.26
$Ni21.5^{MgAl}$	34.4	18.3	47.3	14	105	0.27	14	80	0.27
$Ni34.0^{MgAl}$	58.8	13.4	27.8	14	95	0.28	15	75	0.25
$Ni51.0^{MgAl}$	75.1	7.9	17.0	13	87	0.27	13	67	0.23

*Mass percentage obtained by ICP-AES of the materials prepared.

3.2.2.2 Thermal efficiency

Thermal efficiency was employed to evaluate the energy suitability of SE-SRE process. In the present work, thermal efficiency evaluation method is developed from the equation proposed by He et al. [82] used for thermodynamic equilibrium conditions. For converting ethanol into hydrogen, the thermal efficiency of the process can be calculated by the following expression:

$$\eta_{SE-SRE} = \frac{\dot{n}_{H_2} LHV_{H_2}}{\dot{n}_{EtOH,0} LHV_{EtOH} + Q_{input} + \dot{n}_{mix} \Delta H_{latent}} \tag{3.1}$$

where ΔH_{latent} is the latent energy of fed stream, and LHV_{H2} (244 $kJ \cdot mol^{-1}$) and LHV_{EtOH} (1329.8 $kJ \cdot mol^{-1}$) are the lower heating value of hydrogen and ethanol. While Q_{input} is the energy input in the reaction system, which is calculated from the enthalpy change due to reaction and adsorption:

$$Q_{input} = H_{out}(T) - H_{in}(T) = \sum_i \dot{n}_i H_i(T) - \sum_i \dot{n}_{i,0} H_i(T) + \Delta H_{reg} \tag{3.2}$$

$$H_i(T) = H^{298K} + \int_{298K}^{T} C_p dT \tag{3.3}$$

where $H_{out}(T)$ and $H_{in}(T)$ are the enthalpies of the inlet and outlet streams from the reactor at temperature T, and ΔH_{reg} is the heat required for regenerating the carbon dioxide adsorbent. The enthalpy of the inlet/outlet stream depends on the enthalpy of each species i at a certain temperature, and the number of moles of each species feed into the column and obtained from the outlet, respectively.

3.2.3 Kinetic Model

A kinetic model based on the Langmuir–Hinshelwood–Hougen-Watson (LHHW) rate expression was used for the modeling; details of the mechanism, reaction scheme and model development can be found in the previous chapter II (page 95). During the SRE reaction, ethanol and water are the reactants, and carbon monoxide, carbon dioxide, hydrogen, acetaldehyde and methane are the products involved. Other intermediate species were considered as negligible. Finally, the rate expressions are:

Ethanol dehydrogenation
$$r_1 = k_1 y_{EtOH}\left(1-\frac{1}{K_1}\frac{y_{Ac}y_{H_2}}{y_{EtOH}}\right)\frac{1}{DEN} \quad (3.4)$$

Acetaldehyde decomposition
$$r_2 = k_2 y_{Ac}\left(1-\frac{1}{K_2}\frac{y_{CO}y_{CH_4}}{y_{Ac}}\right)\frac{1}{DEN} \quad (3.5)$$

Methane steam reforming
$$r_3 = k_3 y_{CH_4} y_{H_2O}\left(1-\frac{1}{K_3}\frac{y_{CO}y_{H_2}^3}{y_{CH_4}y_{H_2O}}\right)\frac{1}{DEN^2} \quad (3.6)$$

Water gas shift
$$r_4 = k_4 y_{CO} y_{H_2O}\left(1-\frac{1}{K_4}\frac{y_{CO_2}y_{H_2}}{y_{CO}y_{H_2O}}\right)\frac{1}{DEN^2} \quad (3.7)$$

where k_1 to k_4 are the reaction rate constants and K_1 to K_4 are the equilibrium constants, which can be obtained from thermodynamic data. The denominator (DEN) is given by:

$$DEN = 1 + K_{EtOH}y_{EtOH} + K_{H_2O}y_{H_2O} + K_{CH_4}y_{CH_4} + K_{OH}\frac{y_{H_2O}}{y_{H_2}^{0.5}} + K_{CH_3}\frac{y_{CH_4}}{y_{H_2}^{0.5}} + K_{CO}y_{CO} + K_H y_{H_2}^{0.5} \quad (3.8)$$

where each K_i* is the adsorption equilibrium constant of the adsorbed species and the molar fraction of hydrogen cannot be zero. Therefore, the hydrogen flow rate in the feed for the mathematical model was fixed with a flow rate of $\dot{n}_{H2,0} = 10^{-9}$ mol·s^{-1}.

3.2.3.1 Parameters estimation

Seven equilibrium constants and four rate constants in the reaction rate expressions were used. These parameters for the kinetic model are estimated based on the maximum likelihood formulation by gPROMS software (PSE Enterprise, London, UK). The values of the parameters for optimal fitting were determined and are listed in Table 3-7.

Table 3-6 Calculated results of the kinetic parameters.

Kinetic Parameters		$k_{0,j}$ [mol·kg^{-1}·s^{-1}]	$E_{A,j}$ [kJ/mol]
$k_j(T) = k_{0j} \cdot e^{\frac{-E_{A,j}}{RT}}$	k_1	(1.14±0.16)·10^4	31.8 ±3.6
	k_2	(8.42±1.03)·10^3	24.8 ±2.5
	k_3	(9.87±1.59)·10^9	119 ±8.9
	k_4	(1.06±0.13)·10^9	60.4 ±4.4
Adsorption Equilibrium		$K_i^*{}_{(673.15)}$ [mol·kg^{-1}·s^{-1}]	ΔH_i [kJ/mol]
$K_i^*(T) = K_{i\,(673.15K)}^* \cdot e^{\frac{-\Delta H_i}{R}\left(\frac{1}{T}-\frac{1}{673.15}\right)}$	K_{EtOH}*	(9.83±0.56)·10^0	-4.96 ±0.52
	K_{H2O}*	(1.32±0.11)·10^{-1}	-56.8 ±3.16
	K_{CH4}*	(1.12±0.23)·10^2	-66.8 ±4.59
	K_{OH}*	(1.73±0.16)·10^{-2}	-53.5 ±3.49
	K_{CH3}*	(1.07±0.20)·10^{-3}	-66.7 ±6.82
	K_H*	(7.35±1.02)·10^{-7}	-27.1 ±1.22
	K_{CO}*	(1.48±0.26)·10^{-2}	-79.5 ±8.21

3.2.4 Modeling and Simulation

A mathematical model was developed with the following assumptions:

- Ideal gas behavior;
- No mass or heat variations within the radial direction of the column;
- No mass or heat transfer resistance within the catalyst particle;
- Porosity is constant along the column;
- Carbon dioxide is the only species adsorbed on the HTlc support material [83].

3.2.4.1 Governing equations

With all the assumptions proposed, the mass and energy balances of the gas and solid phase in the fixed bed reactor are depicted in Table 3-7. On the other hand, the axial dispersion, transfer coefficients and diffusivities are calculated with the correlations shown in Table 3-8. In addition, the detailed correlations of the properties of the gas phase, i.e., viscosity, gas thermal conductivity and molecular diffusion are also calculated with the local conditions.

Table 3-7 Mathematical model of the fixed-bed reactor used.

Mass balance for gas phase in the column:

$$\varepsilon_c \frac{\partial C_i}{\partial t} = \varepsilon_c \frac{\partial}{\partial z}\left(D_{ax} C_t \frac{\partial y_i}{\partial z} \right) - \frac{\partial (u C_i)}{\partial z} + (1-\varepsilon_c)\alpha \rho_{cat} \sum_{j=1}^{n} \nu_{j,i} r_j - (1-\varepsilon_c) \frac{a_{cat}(1-\alpha) k_{f,cat}}{Bi+1} \left(C_i - \bar{C}_{i,cat} \right)$$

Mass balance for solid phase in the column:

$$\frac{\partial \bar{C}_{CO_2,cat}}{\partial t} = \frac{15 D_p}{r_p^2} \frac{Bi}{Bi+1} \left(C_{CO_2} - \bar{C}_{CO_2,cat} \right) - \frac{\rho_{cat}}{\varepsilon_p} \frac{\partial \bar{q}_{CO_2}}{\partial t}$$

Mass transfer coefficient of the sorbent material [84]:

$$\frac{\partial \bar{q}_{CO_2}}{\partial t} = k_{CO_2} \left(q_{CO_2,eq} - \bar{q}_{CO_2} \right), k_{CO_2} = \frac{15}{r_p^2} \cdot \frac{\varepsilon_p D_p}{\varepsilon_p + \left(1-\varepsilon_p\right) \rho_{cat} R T_s \dfrac{\partial q_{CO_2,eq}}{\partial p_{CO_2}}}$$

Momentum balance with the Ergun equation:

$$-\frac{\partial p}{\partial z} = \frac{150 \mu_g (1-\varepsilon_c)^2}{\varepsilon_c^3 d_p^2} u + \frac{1.75(1-\varepsilon_c)\rho_g}{\varepsilon_c^3 d_p} |u| u$$

Energy balance for gas phase in the column:

$$\varepsilon_c C_t C_{v,m} \frac{\partial T}{\partial t} = \frac{\partial}{\partial z}\left(\lambda \frac{\partial T}{\partial z} \right) - u C_t C_{p,m} \frac{\partial T}{\partial z} + \varepsilon_c R T \frac{\partial C_t}{\partial t} - \left(1-\varepsilon_c\right) a_{cat} h_{f,cat} \left(T - T_s \right) - \frac{2 h_w}{r_c} \left(T - T_w \right)$$

Energy balance for solid phase in the column:

$$\left[\varepsilon_p C_{v,m} \bar{C}_{t,cat} + \left(1-\varepsilon_p\right) \rho_{cat} C_{ps} \right] \frac{\partial T_s}{\partial t} = a_{cat} h_{f,cat} \left(T - T_s \right) + \varepsilon_p R T_s \frac{\partial \bar{C}_{t,cat}}{\partial t} + \rho_{cat} \sum_{j=1}^{4} R_j \left(-\Delta H_j \right)$$

Energy exchange with the surroundings:

$$\rho_w C_{pw} \frac{\partial T_w}{\partial t} = \frac{2 r_c}{l_w \left(2 r_c + l_w \right)} h_w \left(T - T_w \right) - \frac{2U \left(T_w - T_{furnace} \right)}{\left[\left(2 r_c + l_w \right) \ln \left(\dfrac{r_c + l_w}{r_c} \right) \right]}$$

Ideal gas behavior:

$$p = C_t RT \, , C_t = \sum_{i=1}^{n} C_i$$

Boundary and initial conditions

$$\varepsilon_c D_{ax} \left.\frac{\partial y_i}{\partial z}\right|_{z=0} = y_{feed,i} - y_{i,0} \, , \lambda \left.\frac{\partial T}{\partial z}\right|_{z=0} = -u_{feed} C_t C_p (T_{feed} - T_{z=0}) \text{ and } \; u_{feed} = \frac{Q}{A_{col}} \;\; \text{at}$$

z = 0. $\left.\frac{\partial y_i}{\partial z}\right|_{z=L_c} = 0$, $\left.\frac{\partial T}{\partial z}\right|_{z=L_c} = 0$ and $p_{z=L_c} = p_{out}$ at z = L_c.

Table 3-8 Calculation of transport parameters and physical properties of the gas.

Axial mass and heat dispersion coefficients by Wakao and Funazkri correlations [85]:

$$\frac{\varepsilon_c D_{ax}}{D_m} = 20 + 0.5 Sc \, \mathrm{Re}, \;\; \frac{\lambda}{k_g} = 7 + 0.5 \, \mathrm{Pr} \, \mathrm{Re}$$

Schmidt, Reynold, Prandtl and Biot numbers were calculated as follows:

$$Sc = \frac{\mu_g}{\rho_g D_m}, \;\; \mathrm{Re} = \frac{\rho_g u d_p}{\mu_g}, \;\; \mathrm{Pr} = \frac{\mu_g C_{p,m}}{k_g}, \mathrm{Bi} = \frac{r_p k_{cat}}{5 \varepsilon_p D_p}$$

Heat capacity

Molar heat capacity at constant pressure of component i was obtained with Shomate equation [86]:

$$C_{p,i} = A + Bt + Ct^2 + Dt^3 + \frac{E}{t^2}, t = \frac{T}{1000}$$

Molar heat capacity at constant pressure of the gas mixture was calculated as:

$$C_p = \sum_{i=1}^{n} y_i C_{p,i}$$

The mass heat capacity at constant pressure of component i was calculated as:

$$C_{p,m,i} = \frac{C_{p,i}}{M_i}$$

where M_i is the molecular weight of component i.

The mass heat capacity at constant pressure of the gas mixture was calculated as:

$$C_{p,m} = \frac{\sum_{i=1}^{n} y_i C_{p,i}}{\sum_{i=1}^{n} y_i M_i}$$

Viscosity

Viscosity of the gas component i was calculated according to the first order Chapman-Enskog equations [86]:

$$\mu_i = 2.67\times10^{-6}\frac{(M_iT)^{0.5}}{\varepsilon_i\Omega_\mu},\quad \Omega_\mu = 1.16\left(\frac{\varepsilon_i}{kT}\right)^{0.15} + 0.52e^{\frac{-0.77kT}{\varepsilon_i}} + 2.16e^{\frac{-2.44kT}{\varepsilon_i}}$$

where ε_i/k is the characteristic Lennard- Jones energy of component i.

The viscosity of the gas mixture was calculated with Wilke method [86]:

$$\mu_g = \sum_{i=1}^{n}\frac{y_i\mu_i}{\sum_{j=1}^{n}y_i\Phi_{ij}}\quad,\quad \Phi_{ij} = \left[8\left(1+\frac{M_i}{M_j}\right)\right]^{-0.5}\left[1+\sqrt{\frac{\mu_i}{\mu_j}}\left(\frac{M_i}{M_j}\right)^{-0.25}\right]^2$$

Thermal conductivity

The thermal conductivity of the gas component i was calculated according to the following equations proposed by Eucken [86]:

$$k_i = \left(C_{p,m,i} + 1.25\frac{R}{M_i}\right)\mu_i$$

The thermal conductivity of the gas mixture was calculated with Wassiljewa method [86]:

$$k_g = \sum_{i=1}^{n}\frac{y_ik_i}{\sum_{j=1}^{n}y_i\Phi_{ij}}$$

Molecular diffusivity

The molecular diffusivity of the mixture gas was calculated follows:

$$D_m = \sum_{i=1}^{n}D_{m,i}y_i$$

The molecular diffusivity of the gas component i was calculated as follows:

$$D_{m,i} = \frac{1-y_i}{\sum_{j=1}^{n}\frac{y_j}{D_{ij}}}$$

Where D_{ij} is obtained from the Chapman-Enskog equation [86]:

$$D_{ij} = \frac{1.18809\times10^{-7}}{P\sigma_{ij}^2\Omega_{ij}}\sqrt{T^3\left(\frac{1}{M_i}+\frac{1}{M_j}\right)},\quad \sigma_{ij} = \left(\sigma_i+\sigma_j\right)/2$$

where σ_i is the characteristic Lennard-Jones length of component i. Ω_{ij} is calculated by:

$$\Omega_{ij} = 1.06\left(\frac{\varepsilon_{ij}}{kT}\right)^{0.1561} + 0.19e^{-0.476\frac{kT}{\varepsilon_{ij}}} + 1.04e^{-1.53\frac{kT}{\varepsilon_{ij}}} + 1.76e^{-3.89\frac{kT}{\varepsilon_{ij}}},\varepsilon_{ij} = \sqrt{\varepsilon_i\varepsilon_j}$$

3.2.4.2 Numerical solution

The mathematical model consists of partial differential equations which are solved by gPROMS software (PSE Enterprise, London, UK). The discretization method for the spatial domain in the column is the orthogonal collocation with finite elements method (OCFEM) with 200 intervals in the whole column and the order of approximation is 3. The set of ordinary and algebraic equations obtained by OCFEM discretization are integrated with the DASOLV solver, and a value of 10^{-5} for absolute tolerance. The parameters used for modeling are listed in Table 3-9.

Table 3-9 Parameters used in the mathematical model.

Parameter	Unit	Values
l_c	[m]	0.21
r_c	[m]	$1.2 \cdot 10^{-2}$
l_w	[m]	$1 \cdot 10^{-2}$
m_{cat}	[kg]	$2 \cdot 10^{-2}$
U	[W m^{-2}K^{-1}]	200
c_{pw}	[J kg^{-1}K^{-1}]	500
ρ_w	[kg m^{-3}]	7750
c_{ps}	[J kg^{-1}K^{-1}]	835
h_f	[W m^{-2}K^{-1}]	80.7
d_p	[m]	$1.5 \cdot 10^{-5}$
ρ_{HTlc}	[kg m^{-3}]	1354
ρ_{Ni}	[kg m^{-3}]	8908
ε_p	[m^3 m^{-3}]	0.67
h_w	[W m^{-2} K^{-1}]	55.0
R	[J K^{-1} mol^{-1}]	8.31

3.2.5 Results and Discussion

3.2.5.1 Characterization of the materials

The properties of the sorbent, PURAL MG30, used as catalyst support material for the active nickel phase was described in previous works [24, 72, 87, 88]. Table 3-5 gives an overview of the composition of the multifunctional materials used. The actual value of Ni mass content for each prepared catalyst is given by the designated name. In the metal composition row in Table 3-5 from ICP-AES tests, the weight ratios of the metals (Ni, Mg, Al) appeared in the samples are given. Surface areas, average pore

diameters and volumes of the prepared materials are also collected. It might be found that both the surface area and pore volumes decrease as the nickel content increases, which is a clear indication that the higher the nickel loading the lower is the dispersion.

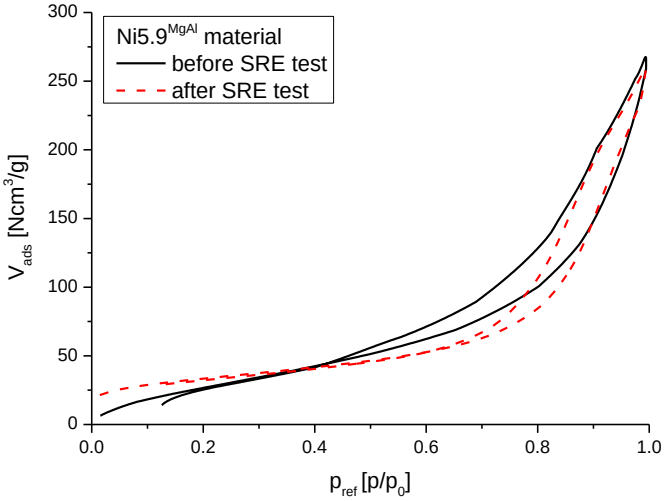

Figure 3-14 N_2 equilibrium adsorption–desorption isotherms of the Ni5.9^{MgAl}.

The N_2 adsorption isotherms of the activated Ni5.9^{MgAl} catalyst and the sample after reaction are shown in Figure 3-14. For all the materials used similar behaviors are observed, the shapes can be interpreted as the IUPAC type IV isotherm associated with a hysteresis of type H3. Isotherms of this type are characteristic of mesoporous materials, and the average pore sizes of the materials are around 10 nm, similar to the pure HTlc material [81]. On the other hand, the type of hysteresis is related with the aggregates of plate-like particles [89] due to the support material with HTlc structure.

Table 3-10 Crystal sizes obtained from the Ni (111) reflex.

Material	d [a] [nm]	d [b] [nm]
Ni1.0^{MgAl}	4	4
Ni5.9^{MgAl}	5	5
Ni11.5^{MgAl}	5	6
Ni21.5^{MgAl}	7	8
Ni34.0^{MgAl}	8	11
Ni51.0^{MgAl}	10	18

[a] before SRE and [b] after SRE.

For a good catalytic performance, small crystal sizes of nickel are desired. Table 3-10 which collects the crystal sizes of nickel for the materials used before and after reaction. It is observed that all the nickel crystal sizes increase with the metal loadings. While the nickel crystal sizes become larger after SRE due to the sintering of nickel particles at high temperatures.

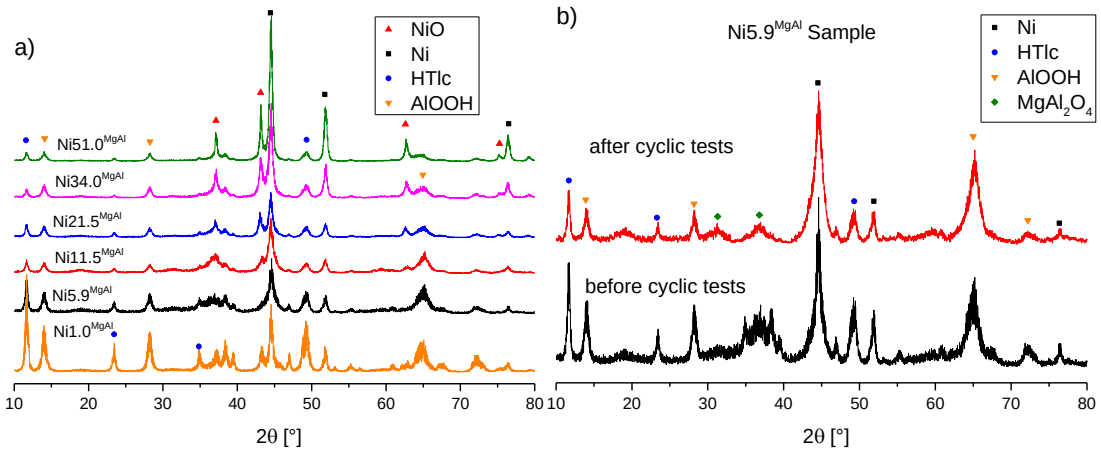

Figure 3-15 XRD patterns of the reduced materials before (a) and Ni5.9^{MgAl} after cyclic tests (b))

XRD patterns of the material can be found in Figure 3-15, and Table 3-11 identifies the bulk structure of the materials with the corresponding 2θ positions. The NiMgAl materials with different nickel loadings reduced before SRE (Figure 3-15a) showed the presence of Ni, NiO and HTlc structure support, as expected. It can be found that the NiO phase becomes dominate especially on the samples with high metal loadings. Since the samples have been activated before SRE and XRD reflects the structure of the bulk phase rather than the surface, the NiO phase is most probably due to the very high loadings of the catalyst, where NiO in the bulk phase has not been reduced. A similar behavior was found by Al-Ubaid and Wolf [90] on Ni-based catalysts with high metal loadings. For the sample after cyclic SE-SRE operations carried out at 773 K (Figure 3-15b), most of the HTlc structure was kept during and only a small amount of magnesium aluminum oxide ($MgAl_2O_4$) was found. In addition, the carbon deposition was not detected from the XRD pattern which is due to the relatively high $R_{S/E}$ (10) used in the feed. According to a previous thermodynamic study [15], carbon deposition can be suppressed with $R_{S/E} > 4$ in the feed.

Table 3-11 Phases identified in the materials with the corresponding 2θ positions

Material	Treatment	Phase	2θ positions & reflection planes	PDF-File ICDD
Ni^{MgAl}*	reduced samples	Ni	44.5 (111), 51.8 (200), 76.4 (220)	70-1849
		NiO	37.2 (111), 43.3 (200), 2.8 (220), 75.3 (311), 79.3 (222)	73-1523
		$Mg_6Al_2(CO_3)(OH)_{16}\cdot 4H_2O$	11.3 (006), 22.7 (018), 4.4 (024), 48.9 (211)	41-1428
		AlO(OH)**	14.0 (010), 28.2 (110), 8.4 (101), 49.3 (210), 65.0 (002)	49-0133
	after cyclic tests	Ni	44.5 (111), 51.8 (200), 76.4 (220)	70-1849
		$Mg_6Al_2(CO_3)(OH)_{16}\cdot 4H_2O$	11.3 (006), 22.7 (018), 4.4 (024), 48.9 (211)	41-1428
		AlO(OH)**	14.0 (010), 28.2 (110), 8.4 (101), 49.3 (210), 65.0 (002)	49-0133
		$MgAl_2O_4$	31.3 (220), 36.8 (311), 4.8 (400), 65.2 (440)	77-1193

* Materials with different nickel loadings.

** Due to the high aluminum content, PURAL MG30 contains a significant amount of boehmite [81].

3.2.5.2 Materials performance

Catalytic activity at steady state conditions: SRE reaction was performed with different nickel loadings in a temperature range of 478 K to 891 K. The catalytic activity can be described in terms of ethanol and water conversion. The results obtained with different Ni loadings are depicted in Figure 3-16. Lines have been introduced to follow the experimental points. The results collected correspond to a steady state (taken after 1 h).

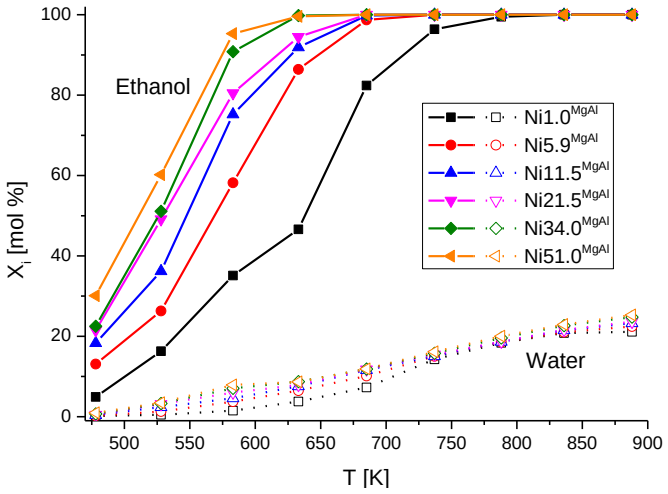

Figure 3-16 Ethanol and water conversions on the prepared catalysts at different temperatures.

The conversion of ethanol increases with increasing nickel loading as well as reaction temperatures due to ethanol dehydrogenation (endothermic reaction). The conversion of water also increases along with the temperature; however, the conversion of water requires higher temperatures (> 650 K) due to the highly endothermic methane steam reforming. In addition, the use of Ni as active phase shows quite higher potential for the conversion of water as in comparison the use of Cu [91]. Besides, the molar ratio of water-to-ethanol ($R_{S/E}$ = 10) used in the feed was above the stoichiometric ratio. A previous thermodynamic study has shown that higher $R_{S/E}$ favors hydrogen yield, while other by-products, such as carbon monoxide or carbon deposition, can be suppressed [92].

Nevertheless, the theoretically maximum water conversion at the established $R_{S/E}$ conditions can only reach a maximum of 30 %. The water conversion obtained

experimentally (~ 25 %) becomes stable at temperatures higher than 823 K, which can be attributed to the backward effect of WGS. As a result, the highest hydrogen yield during the activity test was 5.05 moles per mole of ethanol at 891 K.

Product distribution on dry basis at steady state conditions: The product distribution of SRE as function of reaction temperature T [K] in the presence of $Ni5.9^{MgAl}$, is shown in Figure 3-17a. The results show that at 478 K a considerable amount of acetaldehyde is found as expected [11, 64]. However, part of the formed acetaldehyde is cracked into carbon monoxide and methane so that the molar product distribution is effectively not the expected stoichiometric value of ethanol dehydrogenation. As the temperature increases, the presence of acetaldehyde and carbon monoxide decreases strongly, while carbon dioxide and hydrogen increase in considerable amounts due to water-gas-shift and acetaldehyde decomposition reaction.

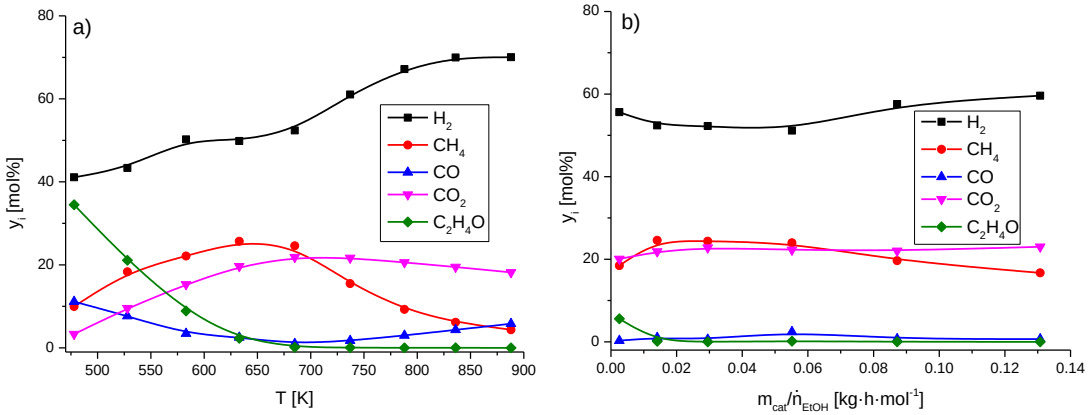

Figure 3-17 Product distributions under different reaction temperatures (a); with different m_{cat}/n_{EtOH} ratios (b).

It can be found that the selectivity to carbon dioxide and hydrogen increases with temperatures below 723 K, whereas above these temperatures the selectivity towards carbon dioxide decreases. The selectivity towards hydrogen, however, first increases and then remains unchanged. In the same figure it is also observed that the carbon monoxide concentration decreases and then slightly increases with temperature. Finally, the concentration of methane increases, but then it decreases with temperatures higher than 685 K. These results suggest that the reaction rates of

ethanol dehydrogenation and acetaldehyde decomposition are higher than the reaction rates for the water-gas-shift at low temperatures. As a result, the concentration of carbon monoxide becomes higher than that of carbon dioxide. The relative higher increase of the water-gas-shift reaction rate is responsible for the higher selectivity towards carbon dioxide and hydrogen. However, the selectivity towards carbon monoxide is low at intermediate temperatures (478 K - 683 K). Higher reaction temperatures favor the methane steam reforming which is responsible for methane selectivity decrease, and increase in carbon monoxide selectivity above 683 K.

The product distribution at 685 K as a function of $m_{cat}/\dot{n}_{EtOH}$ [kg·h·mol^{-1}] is depicted in Figure 3-17b. It is worth to note that the hydrogen concentration first slightly decreases and then increases with increasing $m_{cat}/\dot{n}_{EtOH}$, while undesired by-products such as methane and carbon monoxide increase slightly in its concentrations and then decrease with increasing $m_{cat}/\dot{n}_{EtOH}$. These results are due to the acetaldehyde decomposition reaction ($C_2H_4O = CH_4 + CO$). The total molar flow rate increases with the contact time as the acetaldehyde being converted, and the hydrogen concentration may decreases at the beginning. As the contact time increases, more hydrogen can be obtained from the steam methane reforming and water-gas-shift reactions, and the concentration of hydrogen increases with the decrease of methane as can be found from the Figure 3-17b.

3.2.5.3 Model Verification

Kinetic parameters were fitted according to the obtained experimental results with the method described in section 3.2.3.1. The values obtained are listed in Table 3-6. A comparison between predicted ethanol conversions simulated from the mathematical model and obtained from experimental results, is given in the parity plot shown in Figure 3-18a.

The partial pressures predicted by the model and obtained from the experiments are shown in Figure 3-18b. It can be found that the predicted values match well with the experimental data obtained within a large range of operating conditions, which means

the kinetic model proposed can also be used for further sorption enhanced reaction process study.

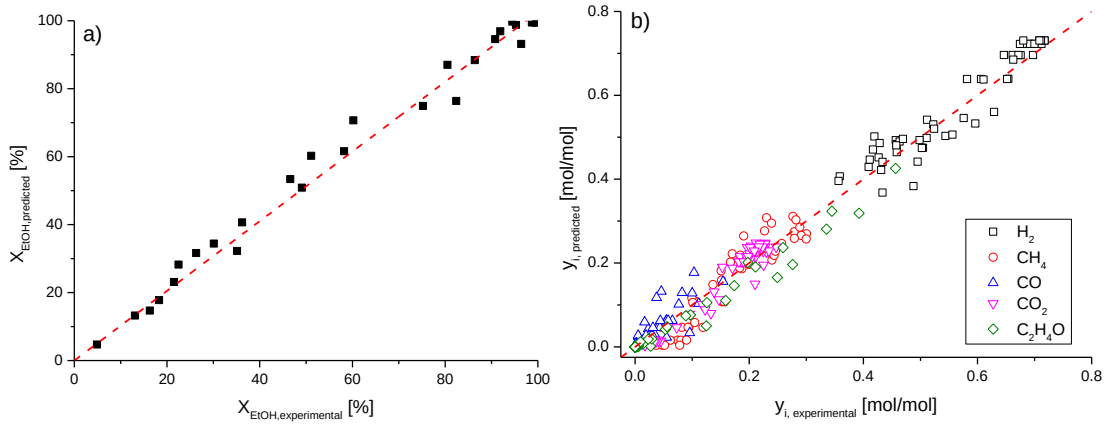

Figure 3-18 Parity plots for ethanol conversions (a) product distribution (b).

The investigation on the adsorption performance of the support material can be found in previous studies [88, 93]. Fixed-bed breakthrough experiments were carried out to investigate the adsorption performance on the prepared multifunctional material. The applicability of the mathematical model for adsorption should be validated before the simulation of sorption enhanced reaction process. The carbon dioxide breakthrough tests were carried out over the $Ni5.9^{MgAl}$ sample at 723 K and 773 K, p_{H2O} = 50 kPa with different carbon dioxide partial pressures. Helium was used as the balance gas to maintain $\dot{V}_{total}$ = 50 $Ncm^3 \cdot min^{-1}$ in the feed.

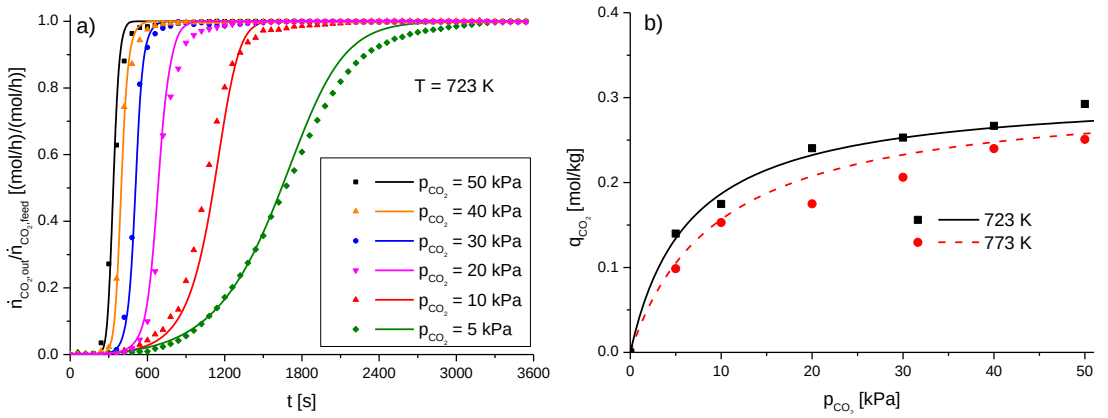

Figure 3-19 Adsorption performance: breakthrough curves (a); adsorption isotherm (b).

Results of the breakthrough experiments for different carbon dioxide molar

fractions at 723 K can be found in Figure 3-19a; the plots are the normalized carbon dioxide mole flow rates at the column outlet as a function of time. The carbon dioxide adsorption isotherms at 723 K and 773 K are shown in Figure 3-19b. Experimental data was described by the Langmuir isotherm according to the following equation:

$$q_{CO_2} = q_{\max} \frac{b_{CO_2} p_{CO_2}}{1 + b_{CO_2} p_{CO_2}}, b_{CO_2} = b_{CO_2,0} e^{\frac{-\Delta H_{ads}}{RT}} \quad (3.9)$$

where q_{max} = 0.31 mol·kg^{-1} is the maximum capacity, $b_{CO2,0}$ = 3.2·10^{-4} kPa^{-1} and ΔH = - 37.16 kJ·mol^{-1} is the adsorption enthalpy. It could be found that the support material of the multifunctional catalyst has a similar adsorption capacity compared with the pure HTlc sample [88, 94], since the support material used for the multifunctional catalyst was not impregnated with an alkaline promoter such as K or Cs. In order to improve the SE-SRE performance of the material, effects of the promoter on the adsorption and reaction performance of NiMgAl materials need to be investigated in following sections.

3.2.5.4 Sorption enhanced reaction process

The economic feasibility of SERP depends on its ability to work in cyclic mode, which is a requisite for a well SE-SRE. The material used for SE-SRE has to be periodically regenerated without affecting the catalytic and sorption properties (activity, selectivity, stability, selective carbon dioxide capture, etc.). Each column with SE-SRE promoting material swings between two different states; reaction and carbon dioxide sorption, where the mixture of ethanol and steam is fed into the reactor to produce ultra-pure hydrogen, and regeneration, where the operating conditions are twisted to regenerate the sorbent. In the design of a cyclic SE-SRE process, the longer the pre-breakthrough period, the less parallel columns are required for operation which may be an advantage in the fixed cost structure and a possible disadvantage in the variable cost structure. In this section the SE-SRE process on the synthesized material was first simulated to find the desired and/or required reaction conditions, and then the prediction was verified experimentally.

According to previous research, SE-SRE with HTlc material as sorbent can be performed in the temperature range up to 773 K due to irreversible destruction of HTlc structure [95]. While the yield of hydrogen is relativity low at temperature lower than 723 K [17]. It could be found from Figure 3-16 that the Ni5.9^{MgAl} sample has a good reaction performance under this temperature condition and a high sorbent-to-catalyst ratio which was chosen for SE-SRE study.

Effect of $m_{cat}/\dot{n}_{EtOH}$: The concentrations of hydrogen and carbon dioxide as function of reaction time at 773 K with a steam-to-ethanol molar ratio of 10 in the feed under different $m_{cat}/\dot{n}_{EtOH}$ conditions are shown in Figure 3-20. It could be found that the concentration of carbon dioxide in the product gas is kept low during the pre-breakthrough period due to selective *in situ* removal by the multifunctional catalyst in the reactor bed.

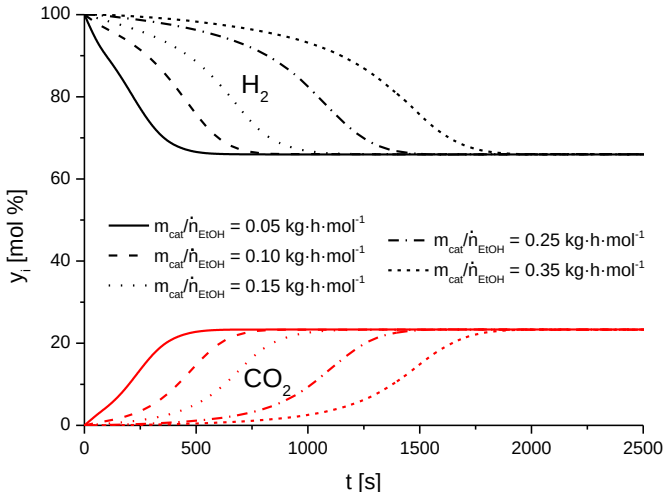

Figure 3-20 Molar fractions of hydrogen and carbon dioxide at different $m_{cat}/\dot{n}_{EtOH}$ conditions.

The reaction enhancement can be observed for all these $m_{cat}/\dot{n}_{EtOH}$ conditions. The sorption enhanced reaction region increases with increasing $m_{cat}/\dot{n}_{EtOH}$, especially when $m_{cat}/\dot{n}_{EtOH}$ rises from 0.15 to 0.25 kg·h·mol^{-1}.

Under $m_{cat}/\dot{n}_{EtOH}$ = 0.25 kg·h·mol^{-1} condition, a clear reaction enhancement is observed. The hydrogen produced has an initial purity higher than 99 mol % during the first 150 s, which is kept higher than 90 mol % for the remaining 800 s.

The concentration of hydrogen decreases in the non-enhanced regime after sorbent

saturation with carbon dioxide. Here, the purity of hydrogen reaches ~ 66 mol %, the same as the hydrogen concentration during SRE at steady state. For both the initial and post-breakthrough periods, the product gas compositions were found to be close to thermodynamic equilibriums for SE-SRE and SRE, respectively [17]. This is an indication that the multifunctional material prepared has a promising reaction and adsorption performance.

Effect of the steam/ethanol ratio: Most of the experimental investigations made on SRE were performed with a $R_{S/E}$ molar ratio of 3 in the feed [8, 9, 96]. However, high ratios such as 21 or even up can be used for SRE process [97] due to the fact that the crude bio-ethanol which contains 14 vol. % of ethanol has an $R_{S/E}$ around 20. The advantages of using such high feeding $R_{S/E}$ were previously discussed. The use of higher $R_{S/E}$, the generation of higher purity hydrogen and the suppression of carbon monoxide and carbon deposit formation. The four most widely used steam-to-ethanol molar ratios (3, 6, 10, and 20) among several studies were tested.

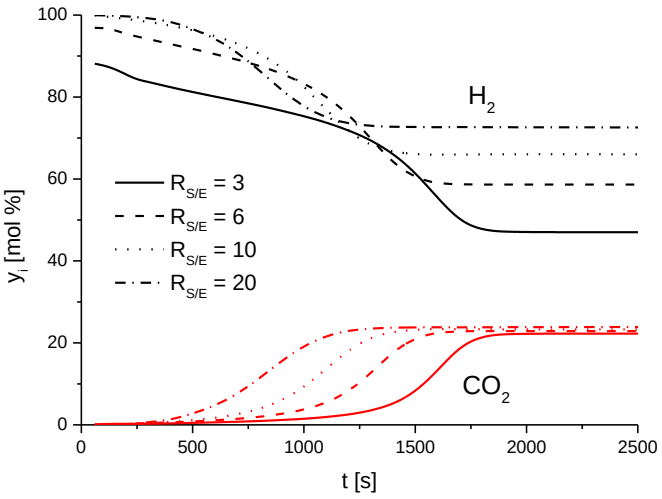

Figure 3-21 Molar fractions of hydrogen and carbon dioxide at different $R_{S/E}$ conditions.

The concentrations of hydrogen and carbon dioxide as a function of reaction time at 773 K with $m_{cat}/\dot{n}_{EtOH}$ = 0.25 kg·h·mol^{-1} under different $R_{S/E}$ feeding ratios conditions are shown in Figure 3-21. It could be found from the figure that the feed $R_{S/E}$ has an effect on both SRE reaction and carbon dioxide adsorption rate. The hydrogen concentrations at both the transient state and steady state increase with

increasing $R_{S/E}$. Therefore, a high $R_{S/E}$ is favored in order to obtain hydrogen with high purity during the SE-SRE process. However, the breakthrough times of carbon dioxide in Figure 3-21 decrease with the $R_{S/E}$ increase, and the concentration of hydrogen with $R_{S/E}$ = 20 after pre-breakthrough (540 s) is even lower than that with $R_{S/E}$ = 10 in the feed. At this point it must be pointed out that the higher the $R_{S/E}$ used in the feed the lower is the obtained partial pressure of carbon dioxide, and simultaneously carbon dioxide adsorption capacity of the material used decreases with the decrease of p_{CO2}. Nevertheless, the overall thermal efficiency may decrease with a higher $R_{S/E}$ [82]. As a result, the practical $R_{S/E}$ for this multifunctional material can be fairly attributed to a value of around 10 in terms of improving the hydrogen purity and efficiency.

Effect of sorbent mass fraction: The effect of the sorbent mass fraction on the carbon dioxide breakthrough curves are shown in Figure 3-22a. It can be detected that with increasing sorbent mass fractions, longer transition times are required for the equilibrium approach of the carbon dioxide concentration at the outlet of the column.

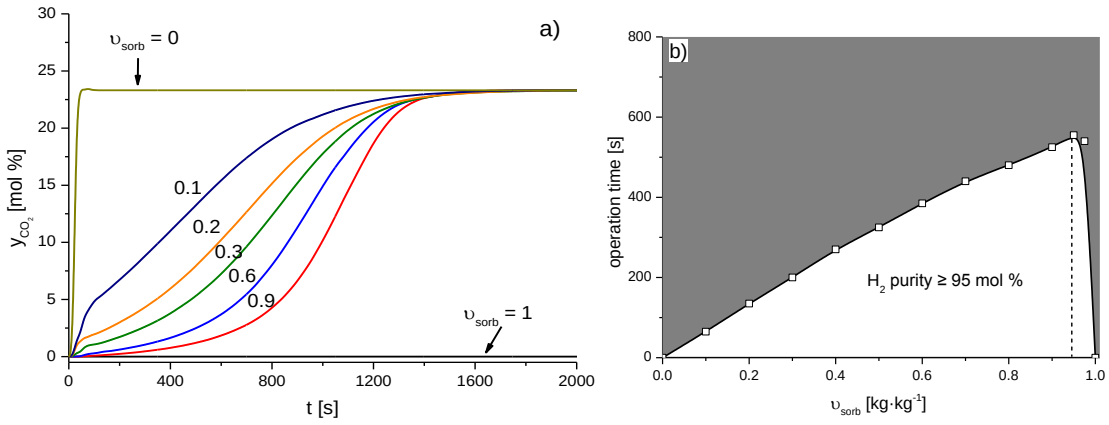

Figure 3-22 Effects of sorbent mass fraction on CO_2 breakthrough (a) and operation time (b).

During the breakthrough period the hydrogen purity can be enhanced to a higher level. Figure 3-22b depicts the relationship of the operation windows [98] with υ_{sorb} ratios at 773 K, $R_{S/E}$ = 10 and a contact time of 0.25 kg·h·mol^{-1}. The constraint is the hydrogen purity higher than 95 mol %. It can be seen that the operating window increases almost in a linear manner with the adsorbent fraction increases initially, and an optimum appears near to the position of υ_{sorb} = 0.945. In other words, the simulated

nickel loading for the optimal multifunctional material is around 1.1 g. This is close to one of the materials ($Ni5.9^{MgAl}$, corresponding to 1.2 g of nickel loading) prepared in this work. However, with further increase of the sorbent fraction, the operation time drastically decreases due to the reduction of catalyst efficiency [99]. These results suggest that the operation window for SERP can be greatly affected by the catalyst/sorbent ratios. It is recommended that the ratio should be properly chosen to obtain an optimal design the SE-SRE process.

Sorption enhanced reaction results According to the previously simulated results, experimental tests were carried out with the following conditions: T = 773 K, υ_{sorb} = 0.94, $m_{cat}/\dot{n}_{EtOH}$ = 0.25 kg·h·mol^{-1} and $R_{S/E}$ = 10. Comparisons of the product distribution as a function of reaction time from experiment and simulation are depicted in Figure 3-23a.

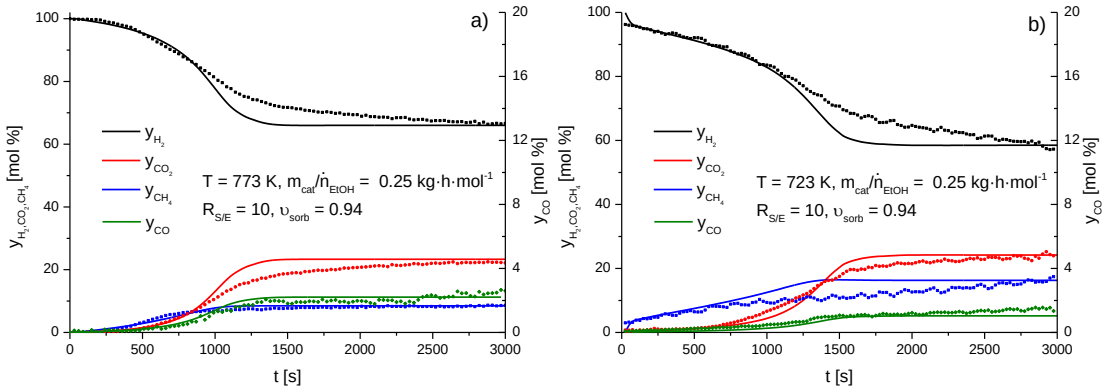

Figure 3-23 Product distributions as function of the reaction time for SE-SRE.

From the experimental results obtained, it can be seen that the carbon dioxide breakthrough happens between 300 and 350 s after reaction start. On the other hand, hydrogen with purities higher than 95 mol % was directly produced from the reactor for more than 500 s, where the most abundant impurity in the product gas was methane. After saturation approach of the material, carbon dioxide sorption enhancement was no longer effective and the post-breakthrough period began. The carbon dioxide molar fraction reaches the final value ~ 23 mol % after 2000 s, while both the molar fractions of methane and carbon monoxide also increased to equilibrium state conditions during the post-breakthrough period. The lines in the

figure correspond to the simulated values in the reactor. On the other hand, experimental test performed at lower temperature (723 K) is shown in Figure 3-23b. A similar SE-SRE performance can be found from the result. However, the purity of hydrogen is relatively low (< 95 mol %) during the pre-breakthrough period due to the thermodynamic limitation of SMR [92]. Therefore, the applicable temperature in this study is 773 K in terms of hydrogen purity and HTlc structure stability. It can be found that the numerical simulation can describe the experimental points during the pre- and post-breakthrough periods well. The relatively good agreement confirms the validity of the mathematical model proposed for SE-SRE process simulations.

In addition, products yields and thermal efficiencies of the SE-SRE process are calculated and compared with the results obtained from conventional SRE process, which is shown in Table 3-12. The results for SRE process are obtained at steady state, while results of SE-SRE are calculated for the products obtained during the initial 500 s. It could be found that under both temperature conditions, the yields of hydrogen and thermal efficiencies from SE-SRE process are higher than that from conventional SRE process. Therefore, the use of a carbon dioxide sorbent can increase not only the yield of hydrogen, and also improve the overall thermal efficiency.

Table 3-12 Yields of products and thermal efficiencies during SRE and SE-SRE.

T [K]	Process	Y_{H2}	Y_{CH4}	Y_{CO}	Y_{CO2}	Thermal Efficiency
		[$mol \cdot mol_{EtOH,0}^{-1}$]				
773	SRE	3.98	$4.92 \cdot 10^{-1}$	$1.29 \cdot 10^{-1}$	$1.39 \cdot 10^{0}$	0.51
	SE-SRE	5.74	$7.00 \cdot 10^{-2}$	$4.55 \cdot 10^{-3}$	$2.96 \cdot 10^{-2}$	0.71
723	SRE	2.76	$7.37 \cdot 10^{-1}$	$4.73 \cdot 10^{-2}$	$1.12 \cdot 10^{0}$	0.36
	SE-SRE	4.81	$2.32 \cdot 10^{-1}$	$2.14 \cdot 10^{-3}$	$2.53 \cdot 10^{-2}$	0.61

3.2.5.5 Stability of the material

One technological challenge of SE-SRE process is its cyclic nature. The material has to be regenerated without affecting the catalytic activity. Therefore, investigations on the catalytic stability of the material used are required. The $Ni5.9^{MgAl}$ was first tested

for long time-on-stream performance, the results can be found in the Figure 3-24. Conversions of ethanol fluctuated from 98 % to 100 % for an overall run time of 48 h, while water conversion changed from 18.0 % to 19.1%. Besides, the compositions of products were not affected by the run time.

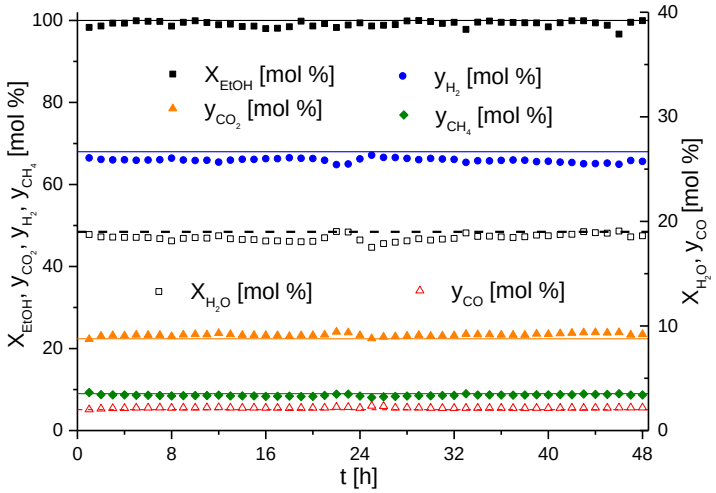

Figure 3-24 Time-on-steam performance of the Ni5.9^{MgAl} material.

On the other hand, the stability of Ni5.9^{MgAl} for cyclic operation at 773 K was also investigated. Five operation cycles have been carried out as can be seen from Figure 3-25. Each cycle consists of two steps: sorption-enhanced reaction with ethanol and steam in the feed for 3000 s with $\dot{n}_{EtOH}= 4.8\cdot10^{-3}$ mol·h^{-1} and $\dot{n}_{H2O}= 4.8\cdot10^{-2}$ mol·h^{-1} in the feed; Regeneration by introducing only steam to the column for 5400 s with $\dot{n}_{H2O}= 5.3\cdot10^{-2}$ mol·h^{-1} in the feed.

It can be found from the experimental results that the reaction and adsorption/desorption performance of the Ni5.9^{MgAl} material had not been changed much during these cycles. Besides, the major composition and structure of the sample after cyclic tests were also preserved according to the characterization results (section 3.2.5.1). Because excess steam had been used during the reaction and regeneration steps, which can help to preserve the HTlc structure [51] and avoid the carbon deposition [15]. While hydrogen gas produced during the reaction can maintain the activation of the nickel phase at the same time. Therefore, the prepared material can have good stability under the conditions employed in the cyclic process.

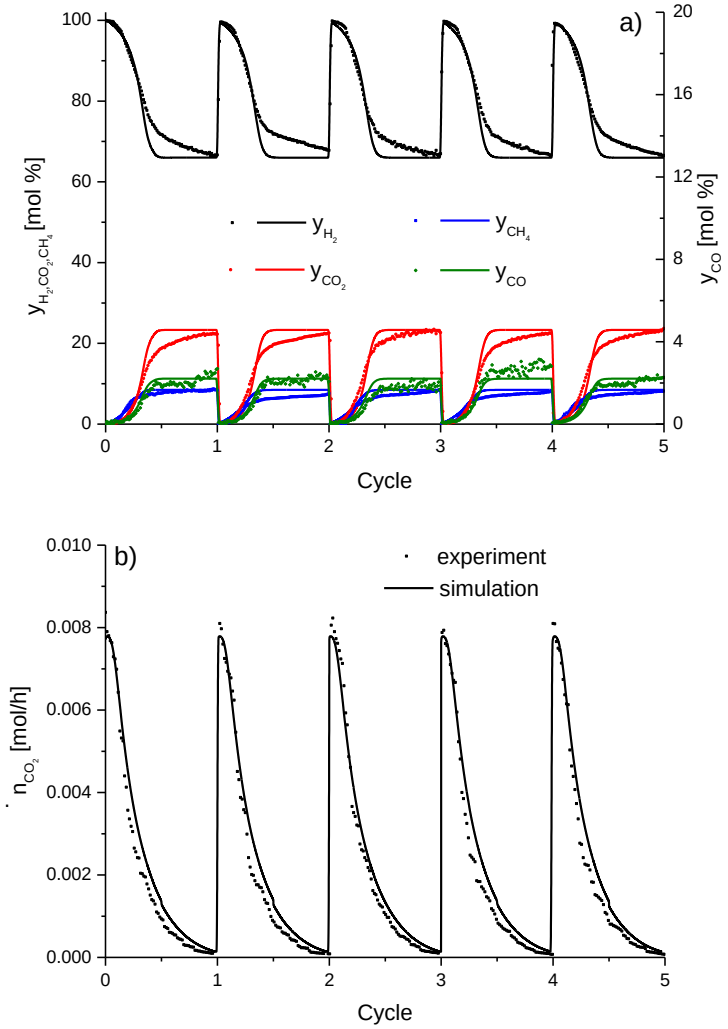

Figure 3-25 Cyclic performance of the Ni5.9^{MgAl} material at 773 K. Product distribution during the breakthrough period (a) and carbon dioxide desorption curve (b) as a function of the cycle numbers.

The good stability of the obtained material (for the nickel crystallites) can be a contribution of the metal support interaction effect [75] and HTlc structure of the support material where the active metal can have a good dispersion [68, 76]. In addition, the relativity high $R_{S/E}$ used in the feed can also suppress the carbon formation which can lead to deactivation. Therefore, the prepared multifunctional material with a good stability performance becomes an attractive material for SERP study in the future.

3.2.6 Conclusion

A novel impregnation method was used to create a multifunctional material with bivalent properties, catalytic and selective carbon dioxide sorption for SE-SRE. The kinetic behavior of the NiMgAl multifunctional material obtained was investigated and simulated with a previously developed kinetic model. The model employed successfully predicts the SRE reaction and carbon dioxide adsorption for a selected multifunctional material. The support material with nickel impregnation has a similar carbon dioxide adsorption capacity as pure hydrotalcites.

The SERP with the multifunctional material in the fixed-bed reactor was simulated to investigate the effects of different reaction conditions. The reaction conditions were found as $R_{S/E}$ = 10 and with a $m_{cat}/\dot{n}_{EtOH}$= 0.25 kg·h·mol^{-1} at 773 K where the material can achieve the highest possible enhancing performance. It was found that the hydrogen produced during the sorption-enhanced reaction period had an initially high purity (> 99 mol %). The concentration was kept higher than 95 mol % for the first 500 s. The use of a carbon dioxide adsorbent can improve the yield of hydrogen and the thermal efficiency of the hydrogen production process. Experimental SE-SRE tests were carried out to confirm the simulated predictions which were in a good agreement.

Finally, the catalytic stability at steady state conditions and cyclic operations for the chosen material has been investigated. It was found that the prepared material have good reaction and adsorption/desorption stability under the conditions employed, the composition and structure of the sample were preserved.

According to these results, numerical studies can successfully predict experimental behavior of the materials NiMgAl multifunctional synthesized for a SE-SRE process. In addition, a further extension to the cyclic operation as well as material improvement is required in the following sections.

3.3 Potassium-Promoted HTlc Sorbent

3.3.1 Introduction

Since the last century development grew up exponentially. Along with the growth, the carbon dioxide concentration in the atmosphere has raised up, which enhances the greenhouse effect [100]. The majority of the simulated scenarios preview a temperature increase [54].

In order to solve the environmental impact of carbon dioxide, research efforts have been devoted to capture carbon dioxide from fossil fuel-fired power plants [101-103] or to replace fossil fuels with a hydrogen based system, known as "Hydrogen Economy" [55]. Steam reforming of hydrocarbons is currently the process of choice for hydrogen production [104], which also releases strong amounts of carbon dioxide. Recently, the use of biomass-derived feedstock's e.g. bio-ethanol [105], which allows an almost closed carbon cycle, is becoming attractive [106].

Sorption enhanced reaction process was developed [22, 107] for hydrogen production with *in situ* carbon dioxide capture formed during the steam reforming process [108] and water-gas-shift process [109], which shifts the equilibrium towards the product side. Apart from lower reaction temperatures, less expensive construction materials, decreased heat exchanger sizes, and the elimination of undesired by-products such as carbon deposition [110] and carbon monoxide [17], carbon dioxide can be captured and afterwards be stored and/or be used.

Sorption-enhanced steam reforming of ethanol can be carried out in a single reaction step [11]. An efficient catalytic system coupled with an adequate carbon dioxide sorbent, such as HTlc, is required. The later material is going to be studied in this work extensively on its ability to capture carbon dioxide. Specific properties of HTlc can be found in previous works [72, 84, 88].

Recently, many studies were published regarding SERP [11, 66, 95, 111, 112]. It is known that HTlc doped with potassium carbonate is able to adsorb carbon dioxide within a temperature range of 573 to 773 K. In addition, the carbon monoxide

concentration in the product gas of steam reforming can be restrained to a ppm level at these temperatures [108, 112].

However, the relatively low carbon dioxide adsorption capacity becomes the biggest obstacle for SE-SRE. Intense efforts have been devoted to improve the adsorption capacity of HTlc. Effects of synthetic conditions, operating temperatures and pressures, with or without the presence of steam, particle sizes and alkali (especially K) doping were widely investigated. Previous studies focused heavily on the use of potassium carbonate as the precursor for K as promoter. The present work reports novel results employing potassium nitrate as the K precursor with a new impregnation method [68] to obtain a K-promoted HTlc (K-HTlc) for carbon dioxide sorption.

A commercial HTlc was impregnated with KNO_3, breakthrough tests were performed with p_{total} = 1 bar (p_{H2O} = 0.5 bar, T = 608 - 711 K and different p_{CO2} conditions). The modified HTlc was submitted to cyclic sorption and regeneration steps for stability evaluation. The information collected for the carbon dioxide sorption kinetics were examined through an own developed mathematical model, the simulation of the experimental SERP unit.

3.3.2 Experiments

3.3.2.1 Materials

The sorbent, PURAL MG30 provided by Sasol (Germany) was impregnated with potassium nitrate (≥ 99 mol % KNO_3) from Sigma-Aldrich. The fresh material was calcined at 673K for 4 h with a helium flow-rate of 50 $Ncm^3 \cdot min^{-1}$ before impregnation. After calcination, the obtained 100 g sorbent was impregnated with an aqueous solution of 51.7 g potassium nitrate to achieve a potassium loading of 20 wt.%, and treated under heated ultrasonic environment at ~ 363 K for 2 h. The obtained suspension was dried over night at 383 K. Hereafter, the sample was loaded into the reactor and thermally treated at 723 K with a helium flow-rate of 50 $Ncm^3 \cdot min^{-1}$ for 48 h. Finally, the sample was subjected to a hydrogen treatment at 723

K with a hydrogen flow-rate of 30 $Ncm^3 \cdot min^{-1}$ for 24 h to convert the remaining potassium nitrite. This material is hereafter designated as MG30-K^N; MG30 stands for its origin (PURAL MG30), K for the cationic potassium promoter and the superscript N for the anionic nitrate origin of the precursor (KNO_3).

3.3.2.2 Experimental set-up

Sorption studies were carried out in a stainless steel fixed-bed continuous down-flow reactor. The continuous down-flow reactor was loaded with 40 g of the obtained K-HTlc sorbent. Details on the experimental units can be found in the previous chapter II (page 46). Prior to the sorption tests, the sorbent was activated with a hydrogen flow rate of 30 Ncm^3/min and helium flow rate of 50 $Ncm^3 \cdot min^{-1}$ at 723 K for 24h.

3.3.2.3 Adsorption and desorption experiments

The carbon dioxide adsorption isotherms on the material used were determined at three temperatures from 608 to 711 K, with helium as balance gas during experiments to ensure a total feed flow rate equal to 200 $Ncm^3 \cdot min^{-1}$ and p_{total} = 1 bar with different p_{CO2}. The carbon dioxide sorption capacity of the material is defined as:

$$q_{CO_2} = \frac{n_{co_2,adsorbed}}{m_{sorb}} = \frac{\dot{n}_{CO_2,feed} \cdot t_s - \int_0^{t_s} \dot{n}_{CO_2,out} dt}{m_{sorb}} \qquad (3.10)$$

where q_{CO2} is the sorption capacity of the material, m_{sorb} is the mass of the sorbent material, $n_{CO2,adsorbed}$ is the mol number of adsorbed carbon dioxide on the material, $\dot{n}_{CO2,feed}$ is the molar flow rate of the carbon dioxide feed, $\dot{n}_{CO2,out}$ is the molar flow rate of the carbon dioxide outlet and t_s is the time for stabilization.

After carbon dioxide adsorption, desorption was carried out until $\dot{n}_{CO2} \leq 0.1$ $mmol \cdot min^{-1}$ without variation for 5 min in the outlet stream with water (p_{H2O} = 0.5 bar), helium (p_{He} = 0.5 bar) and a total feed flow rate equal to 200 $Ncm^3 \cdot min^{-1}$. Detailed operating conditions used for the breakthrough tests can be found in Table 3-14.

Table 3-13 Operation condition used in the breakthrough tests.

Temperature [K]			608, 656, 711
Total pressure [bar]			1
Total flow rate [cm^3/min, 298 K, 1 bar]			200
Sorbent Mass [kg]			0.04
Operation	p_{CO2} [bar]	p_{H2O} [bar]	p_{He} [bar]
Adsorption	0.05	0.5	0.45
	0.10		0.40
	0.20		0.30
	0.30		0.20
	0.40		0.10
	0.50		0
Desorption	0	0.5	0.5

3.3.2.4 Mathematical modeling

A mathematical model was developed to analyse the sorbent performance under different operation conditions, the detailed facts of the model and the numerical solution used for the simulation can be found in the previous section 3.2.4 (page 147).

3.3.3 Results and Discussion

3.3.3.1 Carbon dioxide sorption isotherm

In order to employ a carbon dioxide sorbent for a SE-SRE process, the sorption capacity must be determined at different temperatures. It is also necessary to determine the operating conditions at which the carbon dioxide sorbent possesses the highest carbon dioxide capacity in the presence of steam. For this reason, sorption equilibrium isotherms at 608 K, 656 K and 711 K were measured. The isotherms were determined by measuring the breakthrough curves of carbon dioxide. The measured gas effluent in the breakthrough experiments is considered at equilibrium when the carbon dioxide concentration did not vary for at least 5 min. The obtained isotherms at three different temperatures are shown in Figure 3-26.

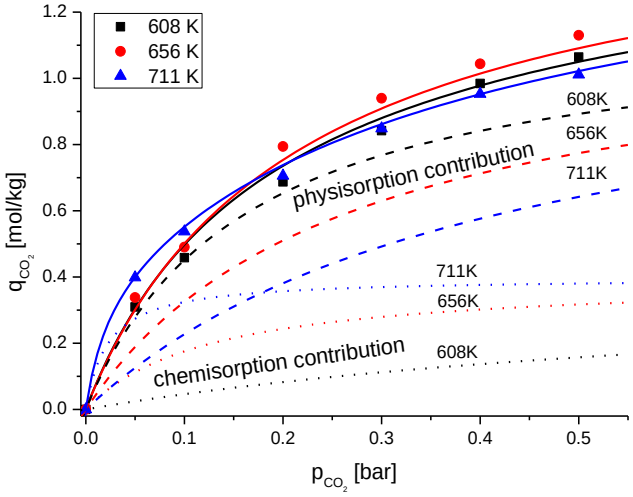

Figure 3-26 Carbon dioxide sorption equilibrium isotherms on MG30-K^N at 608, 656 and 711 K. Solid lines - bi-Langmuir model; dashed lines - physical contribution; dotted lines - chemical contribution.

The solid curves correspond to the fitted results obtained with a bi-Langmuir model [24]:

$$q_{CO_2} = q_{\max 1}\frac{K_1 p_{CO_2}}{1+K_1 p_{CO_2}} + q_{\max 2}\frac{K_2 p_{CO_2}}{1+K_2 p_{CO_2}} \tag{3.11}$$

where q_{max} the maximum capacity for site 1 (physical adsorption) and site 2 (chemical adsorption) and K_i is given by the Van't Hoff equation:

$$K_1 = k_{01}e^{\frac{-\Delta H_1}{RT}}; K_2 = k_{02}e^{\frac{-\Delta H_2}{RT}} \tag{3.12}$$

where k_{0i} is the pre-exponential factor, ΔH_1 is the enthalpy of physical adsorption and ΔH_2 is the enthalpy of chemical reaction.

The dashed and dotted curves correspond to the contribution of the physical and chemical sorption terms of the model, respectively. The fitting parameters of the bi-Langmuir model are listed in Table 3-14.

Table 3-14 Fitting parameters of the bi-Langmuir isotherm.

Parameters	q_{max1} [mol·kg^{-1}]	k_{01} [bar^{-1}]	ΔH_1 [kJ·mol^{-1}]	q_{max2} [mol·kg^{-1}]	k_{02} [bar^{-1}]	ΔH_2 [kJ·mol^{-1}]
values	1.2 ±0.3	(8.0 ±0.2) ·10^{-3}	-33.6 ±1.6	0.4 ±0.1	(5.9 ±0.9) ·10^{10}	123.8 ±8.1

The large value of k_{02} means the prepared sorbent has a large number of active chemisorption sites. The highest CO_2 adsorption capacity (1.13 mol·kg^{-1}) of this material was obtained at 656 K with p_{CO2} = 0.5 bar. The sorption capacity for p_{CO2} = 0.4 bar was found to be 1.04 mol·kg^{-1} which is around 37 % higher than the K-HTlc used in a previous study (0.76 mol·kg^{-1}) where similar conditions have been used [24]. When KNO_3 is thermally decomposed the following reaction occurs:

$$2KNO_3 \rightarrow K_2O + 2NO_2 + 0.5O_2 \tag{3.13}$$

The released nitrogen dioxide and oxygen gas have an additional calcination effect on the HTlc, and potassium oxide incorporates better into the HTlc, since no ”needle-like” morphology [24] was found in the SEM micrographs. The increased adsorption capacity can be attributed to a better interaction between the potassium oxide promoter and HTlc sorbent.

It could be found in Figure 3-26 that the adsorption capacities at 711 K with p_{CO2} = 0.05 and 0.1 bar were higher than those at 608 K and 656 K, while the adsorption capacities with higher p_{CO2} at 711 K were lower than for other temperature conditions. This “crossing” phenomenon in isotherms at different temperatures and p_{CO2} cannot be explained by physical adsorption alone. Hutson et al. [113] found that the adsorption capacity is a combination of physisorption and chemisorption. The physisorption has a strong correlation with the number of basic sites on the sorbent, while the relationship between the surface basicity and the chemisorption capacity is absent. Physisorption is an exothermic spontaneous process ($\Delta H < 0$) attributed to van der Waals and electrostatic forces. The typical value of physical adsorption enthalpy is ~ -25 kJ·mol^{-1} [114]. However, in the case of HTlc, the value for the heat of physical adsorption can be higher due to the electrostatic contribution of the positively charged metal layers [24]. In this work, the heat of physical adsorption was 33.6 kJ·mol^{-1}.

The adsorption isotherms in the low p_{CO2} region indicate the presence of strong adsorption sites, this major portion can be attributed to chemisorption sites, while in the high p_{CO2} region the majority appears to be physical adsorption sites. The physical adsorption capacities decrease with the temperature rise due to the negative enthalpy,

while the chemical contribution increases as the temperature is raised. This contrast becomes even more obvious at a low p_{CO2} region (p_{CO2} < 0.1 bar). As a result, a maximum in the carbon dioxide sorption equilibrium capacity (1.13 $kJ \cdot mol^{-1}$) was obtained at 656 K with p_{CO2} = 0.5 bar.

However, we cannot simply go to the conclusion that the optimal temperature to operate the SE-SRE process is 656 K. When the SRE reaction is performed at atmospheric pressure, the p_{CO2} can only reach a maximum of ~ 0.25 bar, supposing that ethanol and water are totally converted.

In addition, the molar ratio between ethanol and water used for SRE is always higher than the stoichiometric ratio of 3. This was done in most of the studies to avoid carbon deposition [17]. Therefore, the p_{CO2} region of interest for SE-SRE is lower than 0.25 bar, where the adsorption capacities at 711 K are higher than for 656 K or 608 K. At this point it must be stressed that the operating conditions for SE-SRE need to be established according to the catalyst performance. That means the reaction rate must be similar to the sorption rate for carbon dioxide.

3.3.3.2 Carbon dioxide adsorption kinetics

The coupling of SRE with an *in situ* separation unit is innovative. A hybrid configuration consisting of a catalyst for chemical reaction and a sorbent for selective carbon dioxide separation can improve the operating unit [108, 112]. Reversible reactions, such as the SRE, are of interest for this purpose. More favorable reaction equilibrium can be reached as under a conventional regime; higher reactant conversions and product selectivities can also be achieved. Moreover, this reaction enhancement may enable a lower temperature of operation. For a gas-phase catalytic reaction such as the SRE, the separation can be based on the sorption of carbon dioxide generated during the reaction [11]. In order to develop a mathematical model for the SE-SRE process, the carbon dioxide sorption kinetics on the sorbent is required. Therefore, carbon dioxide sorption breakthrough curves were used to investigate the kinetic behavior of MG30-K^N.

Carbon dioxide sorption breakthrough curves were measured on the synthesized MG30-K^N. The sorption kinetics was determined in the temperature range of 676 to 783 K, which is in the range of interest for SERP, especially on SE-SRE. The p_{H2O} was always kept at 0.5 bar during the experimental runs due to two main reasons; on the one hand, steam is always in excess during SE-SRE process with the advantage to avoid the carbon deposition [11], and on the other hand Ding and Alpay [84] found that the adsorption capacity of HTlc is approximately 10% higher with the presence of steam than under dry feeding conditions, and this is likely attributed to the maintenance of the hydroxyl groups on HTlc surface [84].

Simulations were performed on MG30-K^N with 6 different feed p_{CO2}, 0.05; 0.1; 0.20; 0.30; 0.40 and 0.50 bar. The experimental and simulated breakthrough curves associated with the temperature profile during breakthrough time at a temperature of 656 K are shown in Figure 3-27a and b. The plots are the normalized carbon dioxide mole flow rates [$\dot{n}_{CO_2,out}$ (t)/ $\dot{n}_{CO_2,feed}$] at the column outlet as a function of time.

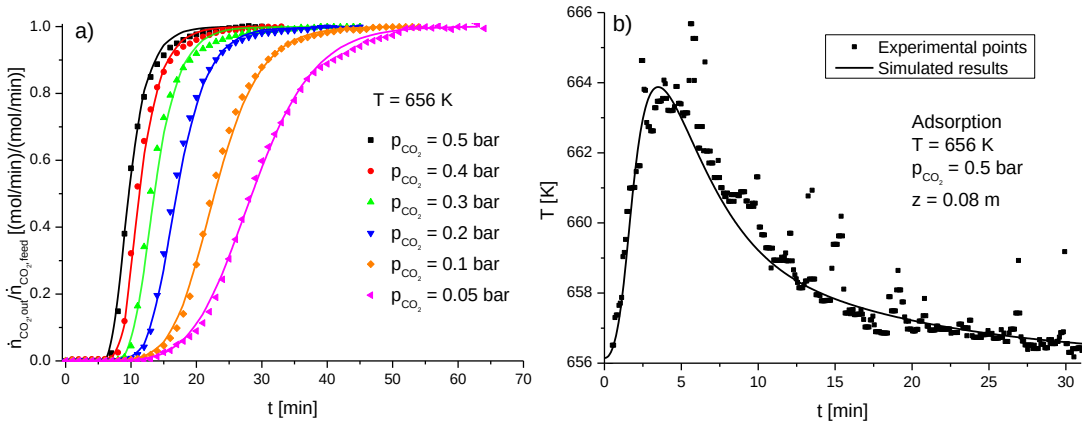

Figure 3-27 Carbon dioxide breakthrough curves for pco_2 = 0.5 bar in the feed at 656 K in a column packed with MG30-K^N: mole flow rate of the carbon dioxide effluent at the outlet (a) and temperature wave measured at 8 cm from top of the column (b). Symbols correspond to experimental points and lines represent simulated results.

As it can be seen from Figure 3-27a, the curves exhibit a dispersed front when the carbon dioxide mole flow rate approaches equilibrium at the outlet of the column, which is a result of the mass transfer effects [115]. The breakthrough curve as well as

the shape of the carbon dioxide front was successfully simulated with the proposed mathematical model in most of the experimental runs. The simulated curves closely follow the experimental results indicting the equilibrium points which correspond to the carbon dioxide isotherms at different temperatures. It is proved that the bi-Langmuir model can be employed to simulate the adsorption performance during the breakthrough period.

The temperature profiles in the column are depicted in Figure 3-27b for the experimental and simulated case, with 0.5 bar feed p_{CO2} at 656 K. The sorbent temperature in the bed was measured at 8 cm from top during the breakthrough experiments inside the column. Comparing the carbon dioxide mole flow rate fronts in Figure 3-27a, the prolonged slope of the temperature line in Figure 3-27b suggests that a longer time was required for the complete release of the temperature wave.

3.3.3.3 Stability tests

The stability of the sorbent was assessed by submitting the obtained K-HTlc material to cyclic adsorption and regeneration operations. In SE-SRE, catalyst and sorbent are mixed in the column to capture carbon dioxide *in situ*, displacing the thermodynamic equilibrium towards higher yields of hydrogen [11]. After sorbent saturation, regeneration is required. In practice, the adsorption/desorption cyclic process is performed in several columns operating in parallel for a continuous operation. Therefore, the sorbent must resist to the feed and operational variations during the sorption/desorption cycles without great changes in sorption capacity or kinetics to maintain stable conditions. For all these reasons, the obtained fresh sorbent was submitted to an adsorption/desorption cyclic operation for 10 cycles at 656 K. The operating conditions used in the cyclic tests can be found in Table 3-15.

The results obtained for the stability tests at 656 K with a p_{CO2} = 0.5 bar over ten adsorption/desorption cycles is shown in Figure 3-28a and b. From the calculation of Figure 3-28a it can be found that after 10 cycles the carbon dioxide adsorption capacity slightly decreases (~ 7 %), from 1.13 mol·kg^{-1} to 1.05 mol·kg^{-1}. The capacity

loss can be attributed to partial unavailability of K promoter (K_2O or KOH), which was partially converted into potassium carbonate (K_2CO_3). In addition, by comparing the breakthrough plots from the first and tenth tests, it can be seen that the kinetic behavior of the material is kept during the cyclic operations.

Table 3-15 Operation condition used in the cyclic tests.

Temperature [K]		656	
Total pressure [bar]		1	
Total flow rate [cm^3/min, 298 K, 1 bar]		200	
Sorbent Mass [kg]		0.04	
Number of cycles		10	
Operation	p_{CO2} [bar]	p_{H2O} [bar]	p_{He} [bar]
Adsorption	0.5	0.5	0
Desorption	0	0.5	0.5

Previous investigations have found that K-HTlc have a good stability after several numbers of cyclic operations [116]. In a recent study it was found that the capacity loss (8 %) of K-HTlc occurs during the initial cycles, but the capacity stabilizes after many number of cycles [115]. Comparing the previous cyclic operation results with the newly developed K-HTlc, it can be fairly admitted that this material is adequate to be employed for a cyclic SE-SRE process.

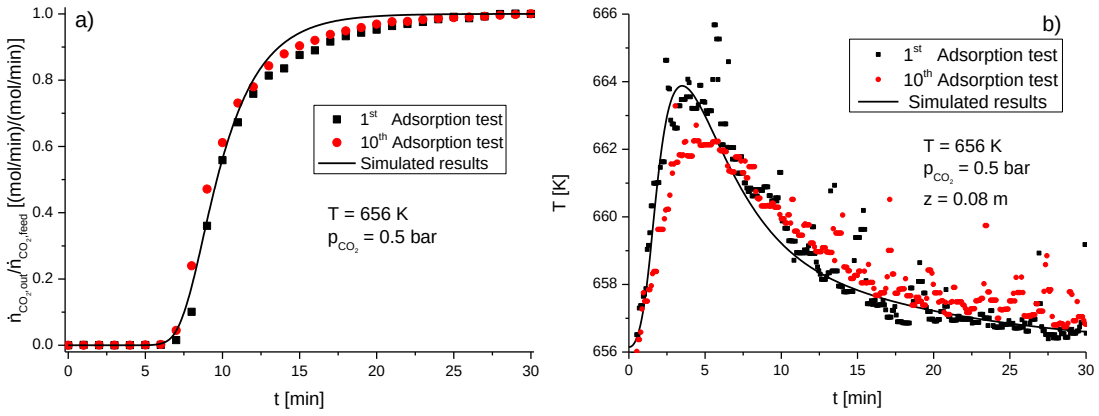

Figure 3-28 Carbon dioxide breakthrough curve with MG30-K^N (a) and temperature wave with MG30-K^N (b) at 656 K after the tenth adsorption/desorption cycle.

3.3.3.4 Carbon dioxide desorption experiments

The experiments for carbon dioxide desorption in the presence of steam were also performed and simulated as well. As a representative example, Figure 3-29a shows the curve of desorption at 656 K corresponding to the sorption test for p_{CO2} = 0.50 bar. It can be found that during the initial minutes, the released carbon dioxide mole flow rate at the outlet of the column which was 9 % higher than the carbon dioxide feed flow rate during the breakthrough period, which can be attributed to purging of the remaining carbon dioxide in the gas phase. The mathematical model proposed is able to describe this desorption behavior. Also the temperature curve was measured and simulated during the desorption process, as shown in Figure 3-29b. During the first 10 min of desorption, the temperature in the bed decreased ~ 2 K due to the fact that desorption is an endothermic process. The temperature then gradually increases to 656 K after 30 min.

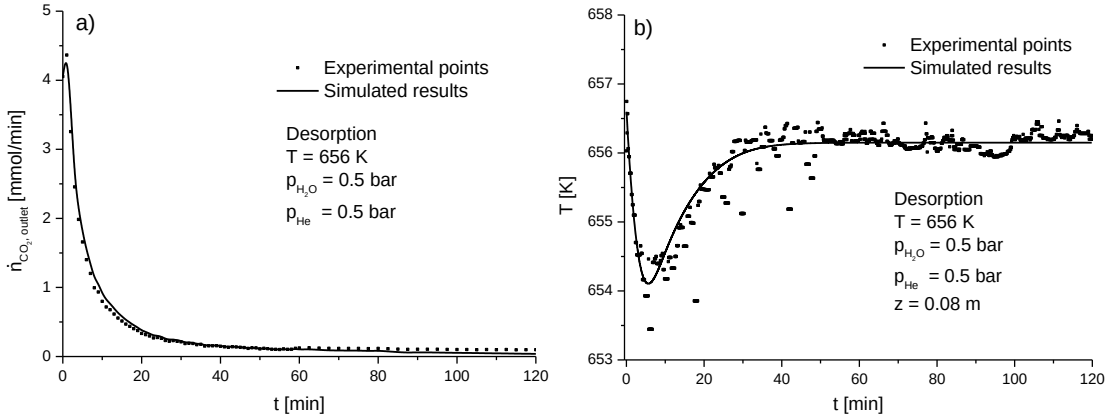

Figure 3-29 Desorption curve for pco_2 = 0.5 bar at 656 K: The mole flow rate of the CO_2 effluent at the outlet (a) and temperature wave measured at 8 cm from top of the column (b) Symbols correspond to experimental points and lines represent simulated results.

It can be seen from experimental and simulated results that the carbon dioxide desorption front is of dispersive nature. The equilibrium theory of fixed bed adsorption [117] says that the velocity of propagation of a given concentration is inversely proportional to the slope of the isotherm; for a favorable isotherm (as it is the case here) it means lower concentrations travel through the column at lower velocities and therefore take longer time to appear at the column outlet. The result is a

dispersive front; in fact in desorption step the initial state corresponds to the column saturated with carbon dioxide at given concentration and the final state will be zero gas concentration and clean adsorbent when the regeneration is made with inert gas. The main message is that the shape of the desorption front is mainly determined by the shape of the isotherm being mass transfer effects of second-order. Therefore, the time required for desorption (~ 120 min or more) was always one order of magnitude higher than the time required for complete sorption (~ 30 min). In the design of a cyclic SE-SRE process, the longer the time required for desorption, the more parallel columns are required for operation which is a disadvantage in the cost.

Most of the regenerative operations reported in literature were carried out at isothermal conditions. However, time consumption associated with desorption process can be reduced if a temperature swing is employed for cyclic adsorption/desorption operation. Temperature swing desorption was achieved by heating the sorbent up to the desorption temperature for carbon dioxide release. The most significant aspect of this design is to reduce the time required for regeneration [118]. Lee et al. [119] have found that a relatively simple and very compact unit can be developed for sorption-enhanced steam reforming of methane with the use of temperature swing desorption, whereas the conventional desorption process uses steam at isothermal conditions to purge the saturated sorbent.

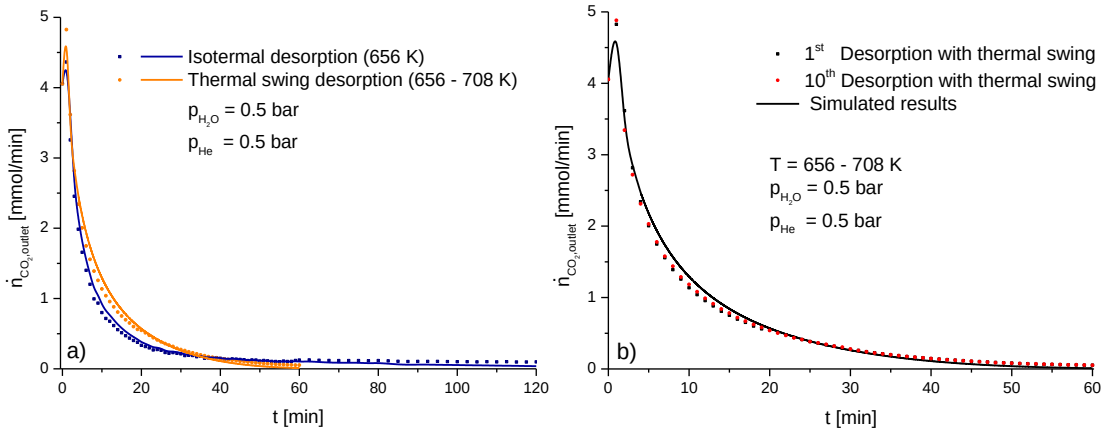

Figure 3-30 Desorption curve with temperature swing regeneration and isothermal regeneration (a) and Curves of desorption after the tenth adsorption/desorption cycle with temperature swing regeneration (b). Symbols correspond to experimental points and lines represent simulated results.

The desorption experiments made in this work after breakthrough tests with a p_{CO2} = 0.50 bar in the feed at 656 K, uses a temperature increase of the column to 708 K with a heating rate of 5 K·min^{-1}. After 30 min, the temperature in the column was decreased to 656 K with a cooling rate of 2.5 K·min^{-1} before the next adsorption test. Desorption conditions were kept as described in Table 3-15. A comparison between obtained desorption results from temperature swing and isothermal regeneration is shown in Figure 3-30a. It can be seen that the time required for desorption process can be reduced to 60 min by the use of a temperature swing, as shown in Figure 3-30a. However, desorption kinetics was not affected after ten temperature swing cycles according to Figure 3-30b.

Finally, the recovered adsorption capacity Figure 3-31 of the sorbent with temperature swing and isothermal regeneration shows a similar decrease (~ 7 %) after ten cycles. The experimental desorption results with temperature swing and isothermal operation can both be successfully simulated, which indicates that the proposed model is able to design a cyclic operations for SERP.

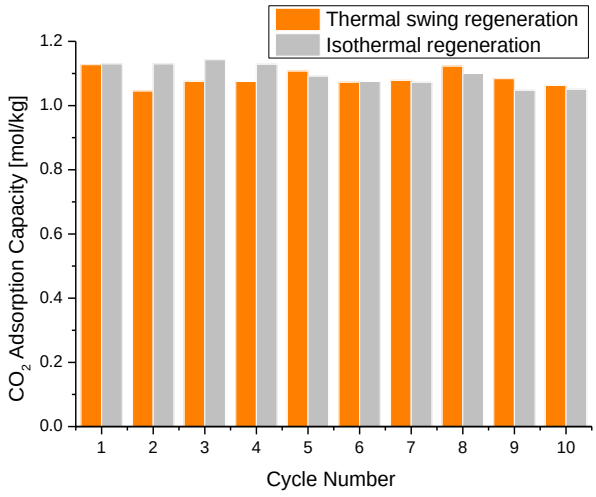

Figure 3-31 Adsorption capacities of carbon dioxide on MG30-K^{N} at 656 K with temperature swing regeneration and isothermal regeneration for ten adsorption /desorption cycles.

3.3.4 Conclusions

Potassium promoted HTlc was prepared by a novel impregnation method with potassium nitrate as the K precursor. The carbon dioxide adsorption isotherms of the

obtained material were investigated at 608 K, 656 K and 711 K with p_{CO2} from 0.05 bar to 0.5 bar. A bi-Langmuir adsorption isotherm model combining physical adsorption and chemical reaction was used to fit the equilibrium data. It was found that the equilibrium adsorption results can be successfully described by a bi-Langmuir isotherm. The highest ever reported carbon dioxide adsorption capacity (1.13 $mol \cdot kg^{-1}$) at 656 K with the p_{CO2} = 0.5 bar for K-HTlc was found.

Breakthrough curves at different conditions were also investigated experimentally and numerically. A mathematical model was developed to simulate the adsorption and desorption process, the model satisfactorily predicts the breakthrough curves of carbon dioxide in the column packed with the K-HTlc.

The stability of the K-HTlc was studied with repeated adsorption/desorption cycles. It was found that both the carbon dioxide adsorption capacity and kinetics were not that much affected after ten cycles. Additionally, carbon dioxide desorption experiments were also conducted with temperature swing regeneration. The temperature swing regeneration can be achieved within 60 min which reduce half of the time required for regeneration at isothermal condition. The K-HTlc material used was found to have very good thermal and cyclic stability, which becomes an attractive carbon dioxide sorbent for SERP.

3.4 Potassium-Nickel-Copper-HTlc Multifunctional Material

3.4.1 Introduction

Energy demands and environmental impacts are the major concerns of civilization since the past century [120]. As a result, a new concept of "hydrogen economy" [121], where hydrogen is used as universal energy carrier, has been proposed.

Several most commonly employed processes such as steam reforming [122], oxidative reforming [123] and its combination auto-thermal reforming [124] can be used to produce hydrogen from different sources [57] such as natural gas, naphtha and other renewable feedstock such as ethanol [79]. Among these processes, steam reforming can produce the highest amount of hydrogen from the ethanol feedstock,

where ethanol reacts with water steam to produce carbon dioxide and hydrogen.

However, other side reactions also exist [64]. The major challenge is to produce high purity hydrogen with carbon monoxide content in ppm level for its application in fuel cells [125]. SERP was regarded as a promising method to produce pure hydrogen in a single step which has been extensively studied [11, 22, 108, 126, 127]. This concept is the combination of reaction and adsorption in a single column packed with a mixture of catalyst and adsorbent. In order to achieve a good dispersion of the catalyst along the column, hybrid multifunctional materials consisting on a selective carbon dioxide adsorption support material and catalytic phase have been developed in some recent studies [69-71, 128, 129]. It was found that the hybrid material with nickel as the active phase and HTlc as the carbon dioxide adsorbent [130] can improve the yield of hydrogen and the thermal efficiency of SRE process [128]. However, reaction performance of this hybrid material can be further improved on this nickel-based catalyst. Previous studies have found that nickel based catalysts favor the methanation reaction [131], which can lead to a low hydrogen yield. Fortunately, it has been proved that copper can restrain the reaction by suppressing the carbon monoxide dissociation step on Ni [132], which is the rate-determining step of the methanation reaction. As a result, copper, which has also been regarded as an excellent active phase for WGS [133] as well as SRE [68, 91] was employed to improve the hydrogen yield.

On the other hand, potassium promoter [87] has been used to enhance the carbon dioxide adsorption performance on the HTlc material. In this work where HTlc has been used as the support, the possible acid sites would be the Al_2O_3 due to the high aluminium content in the unpromoted material [81]. As an acidic support, Al_2O_3 has the disadvantage of favoring ethanol dehydration reaction to produce the ethylene by-product [134], which is considered as the source of graphite/coke [135] that can deposit on the catalyst and causes catalyst deactivation. It has been found that the presence of the alkaline metal can neutralize the acid sites in the support material and improve the selectivity towards hydrogen [136, 137].

The major challenge is to combine the HTlc with potassium for carbon dioxide uptake, and nickel copper active phases for the catalytic SRE reaction to achieve SERP. In the present work a K-Ni-Cu-HTlc hybrid system has been prepared with a simple synthesis method. During the thermal treatment of the precursor, oxygen and NO_x were released, which were responsible for simultaneous volatile expansion of the material surface and calcination [68, 87, 128]. Afterwards, the material consisting of K_2O, NiO and CuO together with the HTlc was reduced in a hydrogen atmosphere.

The synthesized hybrid material was systematically studied on its performance. The effects of the operating conditions on the activity and selectivity for hydrogen production from SRE with nickel and copper as active catalyst phase were investigated. The carbon dioxide adsorption capacity was further examined by carrying out carbon dioxide breakthrough tests in a fixed-bed reactor with the feed of helium, carbon dioxide and steam. Finally, the synthesized hybrid material was also analyzed on selective carbon dioxide sorption for hydrogen production by SE-SRE.

3.4.2 Experimental

A commercial HTlc, also known as LDH, from Condea (now Sasol), with the designation PURAL MG30 was used as support material for potassium, nickel and copper. The selective carbon dioxide sorbent was mixed with potassium-nitrate, nickel-nitrate hexahydrate and copper-nitrate trihydrate. The preparation method developed in our research group can be found in several previous publications [68, 87, 128].

Previous studies found that high catalytic performance for SRE can be obtained when a mass ratio of Cu/Ni = 1 is used [75, 138], while promising carbon dioxide adsorption performance was achieved on HTlc with 20 wt.% of K-promoter [24]. Therefore, the material prepared is designated by the compounds used (K-Ni-Cu-HTlc) and the corresponding loadings were 20 wt. % for K, 5 wt. % for Ni and 5 wt. % for copper. The abbreviation HTlc stands for the used PURAL MG30 sample. The calculated amounts of KNO_3, $Ni(NO_3)_2$ $6H_2O$ and $Cu(NO_3)_2$ $3H_2O$ were dissolved in

200 ml of distilled water at room temperature. Hereafter, the pellets of the PURAL MG30 sorbent were added to this solution, and treated under heated ultrasonic environment at 373 K during 2 h. The obtained suspension was further dried in an oven at 383 K for 48 h. These materials were smashed and crushed in a grinding mill into a fine powder, and then loaded into the reactor for thermal treatment during 48 h at 723 K under a nitrogen flow-rate of 50 $Ncm^3 \cdot min^{-1}$. Finally, this system was activated with a pure hydrogen flow-rate of 30 $Ncm^3 \cdot min^{-1}$ at 723 K during 24 h.

The experimental set-up, characterization and analysis methods can be found in previous chapter II (page 46).

3.4.3 Results and Discussion

3.4.3.1 Characterization of the materials

The properties of the sorbent, PURAL MG30, used as the support material for potassium, nickel and copper phases was described in previous sections. The results obtained are compared with the previously used systems.

The metal composition of the multifunctional material together with other physico-chemical properties can be found in Table 3-16. The results obtained from ICP-OES are found to have a good agreement with the nominal mass percentage values.

Table 3-16 Properties of the prepared K-Ni-Cu-HTlc material

$m_{cat.}$[a]	[g]	45.1
K:Ni:Cu:Mg:Al[b]	[mass %]	25:16:11:15:33
S_{BET}	$[m^2 \cdot g^{-1}]$	38
$\bar{}_{pore.}$	[nm]	16
V_{pore}	$[cm^3 \cdot g^{-1}]$	0.14

a: Total mass of the catalyst; b: Metal mass fraction from ICP-OES.

Water release and decomposition reactions during thermal treatment can be explained by:

$$Ni\left(NO_3\right)_2\, 6H_2O \rightarrow NiO + NO_2 + NO + O_2 + 6H_2O \qquad (3.14)$$

$$Cu(NO_3)_2\ 3H_2O \rightarrow CuO + NO_2 + NO + O_2 + 3H_2O \quad (3.15)$$

$$KNO_3 \rightarrow KNO_2 + 0.5O_2 \quad (3.16)$$

$$2KNO_2 \rightarrow K_2O + NO_2 + NO \quad (3.17)$$

The release of the NO_x species together with oxygen improved the volatile expansion of the material (higher surface area and better dispersion) and calcination in a single step.

The N_2 adsorption isotherm of the activated K-Ni-Cu-HTlc hybrid material is given in Figure 3-32. It can be found that the shapes of the obtained isotherms can be interpreted as the IUPAC type IV isotherm associated with a hysteresis of type H3. Isotherms of this type are characteristic of mesoporous materials, and the average pore sizes of the materials are around 16 nm, similar to the K-promoted HTlc material [87]. In addition, it must be pointed out that this type of hysteresis is related with the aggregates of plate-like particles [89], because the PURAL MG30 sample used in this work as sorbent and as support material has such a layered structure.

Comparing the BET surface area of the K-Ni-Cu-HTlc hybrid material with previously used materials [68, 87, 128], it is clear that a subsequent decrease in surface area can be observed. The physico-chemical properties of this prepared material were found to be more close to the K-promoted HTlc sample. While the physico-chemical properties of the other hybrid materials (Ni-based [128] or Cu-based [68]) without K promoters were found to be close to the PURAL MG30 [81]. The HTlc MG30 with a 100 % available surface area of 200 $m^2\ g^{-1}$, decreases in its surface area to 76 % after the loading with Ni [128], 75 % after the loading with Cu [68] and 14.5 % after incorporation of the K promoter [87]. The percentage of the surface area decrease for the K-Ni-Cu-HTlc hybrid material was 19 % (this work). The average pore diameter obtained for the K-Ni-Cu-HTlc hybrid material (16 nm) was also in good agreement with the previously used materials (between 8 and 15 nm). On the other hand the pore volume of the hybrid material (0.14 $cm^3\ g^{-1}$) was in the range of the K-promoted HTlc [87], which is reasonable since the loadings are similar.

For nickel [128] and copper [68]incorporated HTlc materials the pore volumes were 0.31 and 0.32, respectively, since the metal loadings of these materials were much smaller (~5 wt. %).

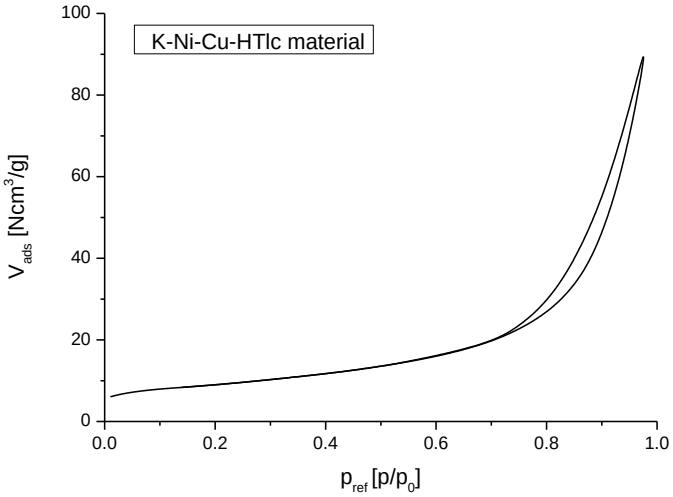

Figure 3-32 N_2 adsorption–desorption equilibrium isotherm of the prepared K-Ni-Cu-HTlc material at 77 K.

As previously mentioned, the adsorption-desorption isotherm indicated that the material was mostly composed by plate-like particles, as shown in the SEM micrograph depicted in Figure 3-33. In previously published studies [68, 87, 128], the same morphology was also observed. From Figure 3-33, it is clear that the morphology was kept for the K-Ni-Cu-HTlc hybrid material, while the diameter of the multifunctional material particle varies from 30 to 50 μm.

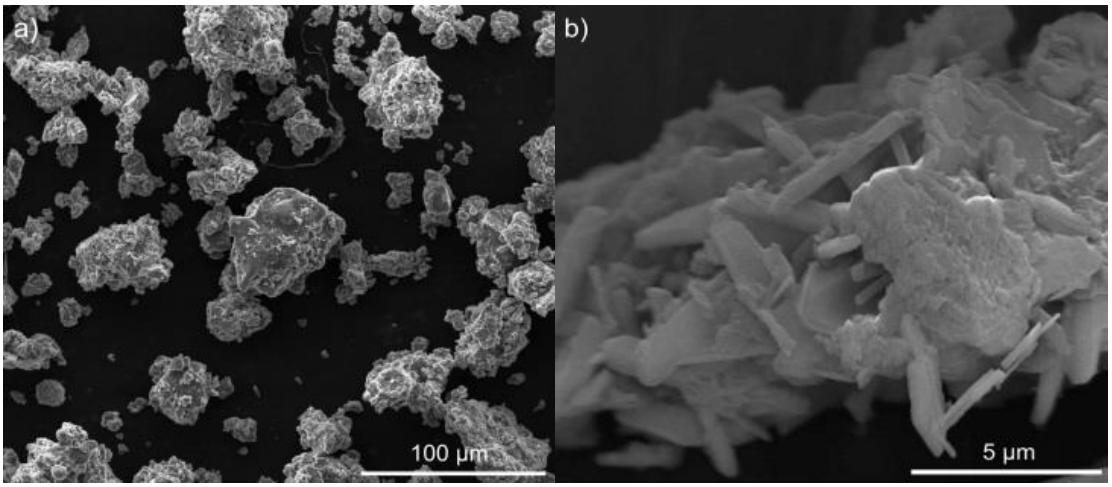

Figure 3-33 SEM micrograph of the prepared K-Ni-Cu-HTlc material.

XRD patterns of the synthesized hybrid material before and after SRE tests can be found in Figure 3-34, and Table 3-17 identified the phases of the bulk with the corresponding 2θ positions.

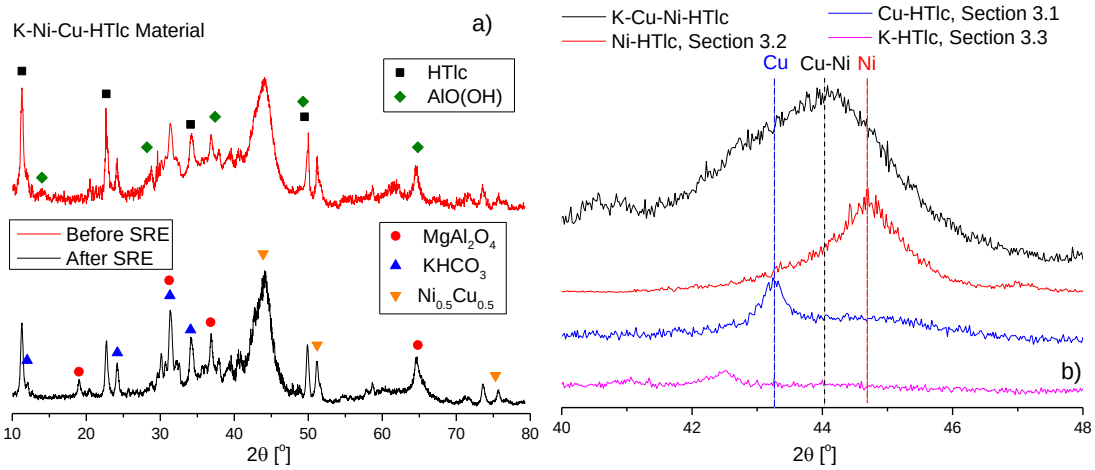

Figure 3-34 XRD patterns of the K-Ni-Cu-HTlc material before and after SRE tests (a) and comparison of K-HTlc [87], Ni-HTlc [128], Cu-HTlc [68] and the K-Ni-Cu-HTlc material synthesized for this work (b).

The material reduced before SRE consisted of multiphase compositions and had the presence of boehmite (AlO(OH)), potassium bicarbonate ($KHCO_3$) and HTlc material ($Mg_6Al_2(CO_3)(OH)16{\cdot}4H_2O$), as expected. However, the 2θ positions of the characteristic reflections corresponding to the Ni phase at 44.5 º(PDF#70-1849) and Cu phase at 43.4 º (PDF#65-9743) cannot be distinguished, because a strong overlapping peak can be observed between the 2θ positions from 41 º to 47.5 º. Previous researches have shown that a strong overlapping peak can only be found when a well formed Ni-Cu alloy was obtained [139], otherwise two separated peaks can be found when an incipient alloy is synthesized [140] or a physical mixture is prepared [139]. Besides, the alumina (PDF#29-0063) content did not appear since the strongest peak for this material at 67 ºwas not found. Therefore, the results from XRD in this work clearly indicated the formation of a nickel-copper alloy ($Ni_{0.5}Cu_{0.5}$). These results are in agreement with a former report by Cunha et al. [141], where the formation of nickel-copper alloys has been studied thoroughly.

Table 3-17 Phases identified in the materials with the corresponding 2θ positions

Materials	Phase	2θ positions & reflection planes	PDF ICDD
K-Ni-Cu-HTlc	HTlc	11.3 (006), 22.7 (018), 34.4 (024), 48.9 (211)	41-1428
	$MgAl_2O_4$	19.0 (111), 31.2 (220), 36.8 (311), 65.2 (440)	77-1193
	$KHCO_3$	12.0 (200), 24.2 (400), 31.3 (111)	89-2369
	$Ni_{0.5}Cu_{0.5}$	44.5 (111), 51.8 (200), 76.4 (220)	70-1849
	AlO(OH)	14.0 (010), 28.2 (110), 37.4 (111), 49.3 (210)	49-0133

On the other hand, it can be found from the samples before and after SRE that most HTlc structure was kept during the SRE tests. Only traces of magnesium aluminium oxide ($MgAl_2O_4$) were detected (2θ = 19º) after SRE. Due to the high aluminium content, the prepared material contained a significant amount of boehmite [81], the peaks from boehmite overlapped with the peaks from $MgAl_2O_4$ except the peak at 19 º.

As previously calculated from thermodynamic equilibrium [17, 92], carbon deposition can be suppressed with a water-to-ethanol ratio higher than 4. It is in good agreement with the XRD results reported in Figure 3-34b, since no carbon deposition can be detected due to the relatively high molar ratio of water-to-ethanol (10) used in the feed. Another method to avoid carbon deposition and other undesired side reactions is the formation of small ensembles of nickel surface atoms. These small ensembles of surface atoms have the benefit to minimize interactions of adsorbed species formed during a catalytic process.

For a good catalytic activity, small crystal sizes of the active phases are desired. Table 3-18 collects the crystal sizes of the formed nickel-copper alloy in the hybrid material used for SRE. Additionally, crystal sizes of previously used materials were introduced for comparison purposes.

Table 3-18 Metal crystal sizes obtained from the Ni, Cu and $Ni_{0.5}Cu_{0.5}$ reflections by the Scherrer equation.

Materials	d_{Ni} [nm]	d_{Cu} [nm]	d_{NiCu} [nm]
K-Ni-Cu-HTlc	n.a.	n.a.	15
Cu-HTlc [68]	n.a.	16	n.a.
Ni-HTlc [128]	5	n.a.	n.a.

The broad peak of around 45 ºindicated a small crystal size obtained for the nickel copper alloy [142], and the average metal crystal size was found to be 15 nm in the K-Ni-Cu-HTlc hybrid material, which was in approximation with 16 nm obtained from the crystal size of Cu for Cu-HTlc system [68]. This phenomenon is related with the incorporation of copper in the nickel lattice and the lower melting point of copper (Tamman and Hüttig criteria) [143].

3.4.3.2 Catalytic performance

Catalytic activity under steady state conditions SRE tests were performed with different feeding rates in a temperature range between 570 K and 753 K. The catalytic activity was investigated in terms of ethanol and water conversion. The results obtained with different feeding rates are depicted in Figure 3-35. Lines were introduced to follow the experimental points, and the results were collected at steady state conditions, taken within post-breakthrough regions at least after 1 h since the start of reaction, and when the concentrations of the products did not vary more than 5 mol % for at least 5 min. Higher temperatures have not been tested in order to avoid the irreversible destruction of the hydrotalcite-like structure at temperatures higher than 773 K [144]. The external and intra-particle diffusion limitations were determined (at lowest and highest temperatures) with the Mears' criterion and the Weisz–Prater criterion, respectively. It was found that the catalytic tests were performed under kinetic control regime and the effect of the external and intra-particle diffusion can be neglected. In addition, it was found that the pressure drop with highest feeding flow rate at 773 K was around 2 % of the atmospheric pressure. Therefore, the effect of pressure drop on the reaction performance was not considered. Heat transfer effects in the hybrid material particles and temperature gradients in the bed can also be discarded since they were not found.

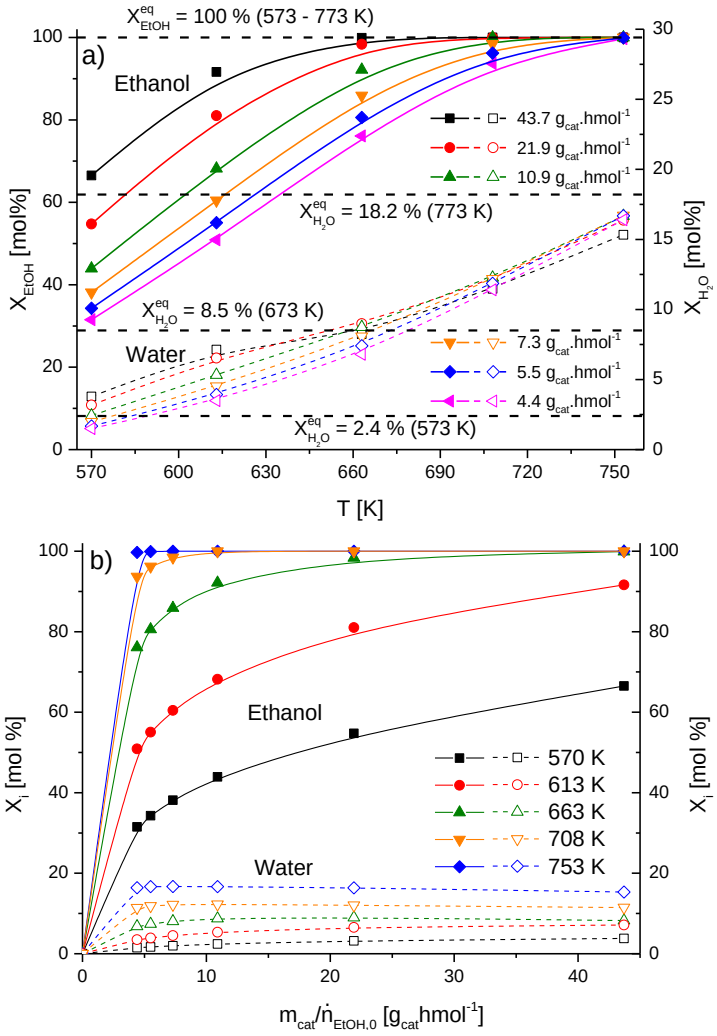

Figure 3-35 The effect of reaction temperature (a) and contact time (b) on the ethanol and water conversions at steady state conditions, where X_i^{eq} stands for the equilibrium conversions of the reactants from the thermodynamic study [17].

Previous thermodynamic studies [17, 145] have found that ethanol is a thermodynamically unstable compound at temperatures higher than 523 K. Therefore, the equilibrium conversion of ethanol was always 100 % within the temperature range used in this work. The equilibrium water conversions at three different temperatures are also included in Figure 3-35 according the thermodynamic calculations with real gas model [17]. The conversions of ethanol from the experiments increased with the rise of reaction temperatures (Figure 3-35a) and contact times (Figure 3-35b). According to the reaction scheme given in Table 3-19, this fact is expected since the fast endothermic ethanol dehydrogenation (ETD) reaction [146] is the first reaction

step in SRE. Because copper was present as active catalyst phase, ETD was even more favored [147]. However, conversions of ethanol can decrease with increasing feeding flow rates due to the shorter contact times.

Table 3-19 Reaction scheme of ethanol steam reforming

Reactions	Chemical description	ΔH^0_{298K} [kJ·mol^{-1}]
Ethanol dehydrogenation (ETD)	$C_2H_6O \leftrightarrow C_2H_4O + H_2$	+68.4
Acetaldehyde decomposition (ACD)	$C_2H_4O \leftrightarrow CH_4 + CO$	-18.8
Water-gas-shift (WGS)	$CO + H_2O \leftrightarrow CO_2 + H_2$	-41.4
Steam methane reforming (SMR)	$CH_4 + H_2O \leftrightarrow CO + 3H_2$	+205.9

The conversion of water also increased with temperature increases (Figure 3-35a), while the feeding rate of the liquid reactant (contact time, Figure 3-35b) had a negative effect on the conversions. It is also important to stress that the activation of water is higher than for ethanol, which means higher temperatures are required to convert water. The maximum thermodynamic conversion of water at 773 K and with a molar ratio of water-to-ethanol ($R_{S/E}$ = 10) used in the feed can only reach a maximum of 18.2 %. This phenomenon can be attributed to the thermodynamic equilibrium limitation of the SMR as well as the WGS reaction [17, 92]. In these experimental tests the highest water conversion of around 17 % was reached with the K-Ni-Cu-HTlc hybrid material.

With the presence of nickel as active phase, the propensity of activating the endothermic steam methane reforming (SMR) at higher temperature levels can be obtained, while the presence of copper favors the activation of the exothermic WGS [127]. No acetaldehyde was found at a reaction temperature of 753 K, as shown in Figure 3-36, which is a good indication that nickel is suitable for acetaldehyde decomposition (ACD) [136, 148].

It has been observed from XRD results that between nickel and copper an alloy

was formed. The formation of small ensembles of nickel atoms and copper atoms on surface can avoid the interaction of adsorbed species, the catalytic decomposition of methane and catalytic carbon monoxide decomposition can be avoided. The generated carbon monoxide from SMR by the nickel active phase can be converted by the neighboring copper active phase in the WGS reaction. It was also found that the crystal sizes of the Ni-Cu alloy are very small, which can be the explanation for the high activities of the hybrid material synthesized. Finally, there is also a good possibility that the K species used in the hybrid material acted as an electronic promoter for WGS reaction [149].

Product distribution on dry basis at steady state condition: The selectivities of intermediate compounds formed during SRE as function of the reaction temperature in the presence of the hybrid material is shown in Figure 3-36.

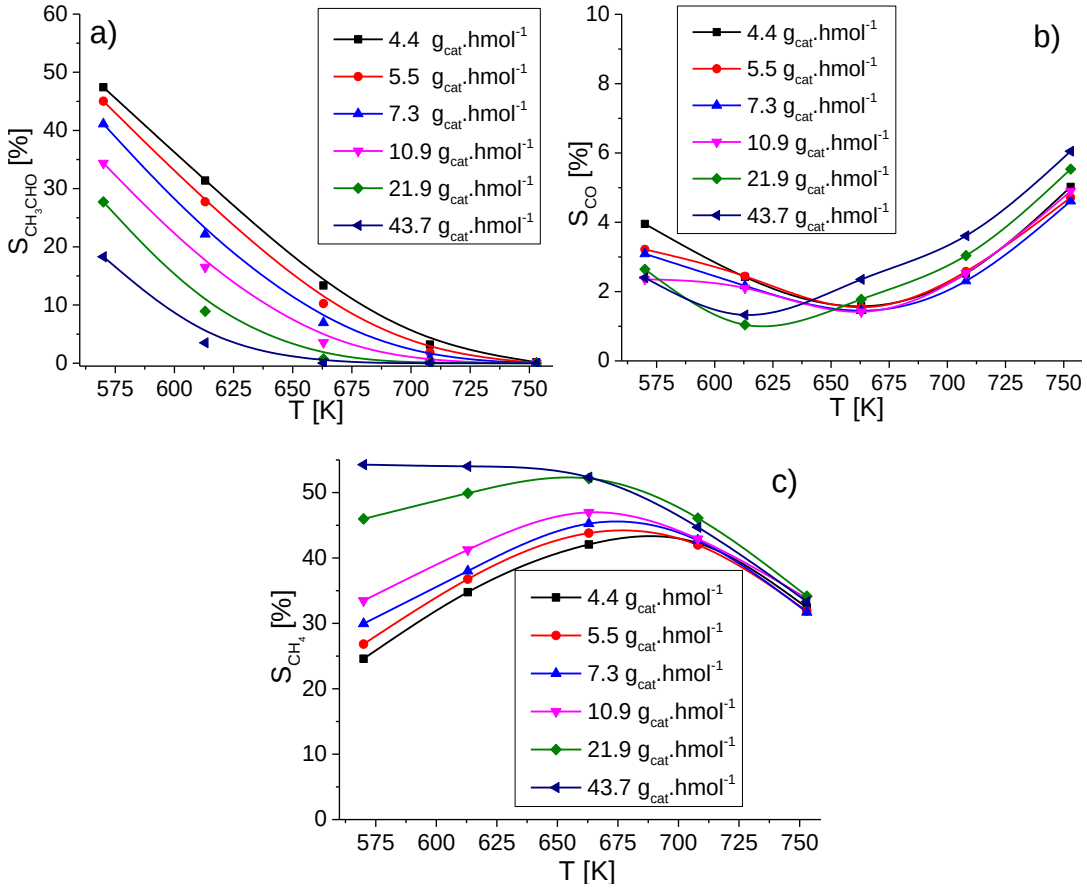

Figure 3-36 Selectivities of the intermediate products under different reaction temperature and feeding flow rate at steady state conditions: CH_3CHO (a), CO (b) and CH_4 (c).

The results showed that at lower temperatures high selectivity towards acetaldehyde was observed (Figure 3-36a). The high selectivity towards acetaldehyde suggests a fast ETD, which can be the contribution of the active copper phase [91], while nickel as the active phase was more responsible for the C–C bond cleavage [150] by catalytic cracking of acetaldehyde into methane and carbon monoxide, known as ACD. These deductions can be confirmed by the selectivities of acetaldehyde and carbon monoxide which were not the stoichiometric ratio of ETD reaction.

The presence of acetaldehyde decreased strongly with temperature increase and lower amounts of reactant feeding. It could be an indication that the bimetallic Ni-Cu alloy system improves the ACD reaction [138]. Previous study found that the addition of a second metal (copper) can lead to a promoting effect on Ni for the decomposition of C_2^+ species [132]. The presence of potassium may also electronically promote [151] both ETD and ACD since the selectivity of acetaldehyde decreased rapidly.

Carbon monoxide appeared with low selectivities (Figure 3-36b) during all the SRE measurements (less than 6 %), which is important for pure hydrogen production. It is also clear that WGS was promoted since the selectivity towards carbon monoxide for the hybrid material used in this work is much lower than for the previously used material (without copper) [128] within the low temperature region. However, the selectivity of carbon monoxide first decreased with the rise of temperature, reaching a minimum at ~ 660 K. The result suggested that the forward reaction rate of WGS was higher than ACD at intermediate temperatures, since the lowest selectivity towards carbon monoxide under different feeding flow rates was obtained between 600 K and 700 K.

The backward WGS and the backward SRM (known as reverse WGS and methanation reaction) are the main side reactions in SRE, leading to the consumption of hydrogen. In Figure 3-36c it can be observed that higher reaction temperatures favor SMR due to the thermodynamic equilibrium of this reaction, which is the major reason for the decrease of methane selectivity, and increase in hydrogen selectivity. In

addition, Cu could suppress the methanation reaction by suppressing the dissociation of carbon monoxide on the Ni surface [132]. Comparing a previous study where a Ni-HTlc material [128] was used at 673 K with similar reaction conditions, the selectivity towards methane decreased with the use of Ni-Cu alloy as active phase, from 62 % to 45 % in this study. On the other hand, the reverse WGS reaction became significant at high temperatures and the selectivity of carbon monoxide increased as methane selectivity decrease. Besides, it was found that the WGS closely reached equilibrium at high temperature conditions, the experimental results from the test performed at 753 K with 4.4 $g_{cat}hmol^{-1}$ (lowest contact time) in the feed was calculated, and the WGS reaction constant from our study (5.71) was close to the equilibrium constant (5.87), while at low temperature (T = 570 K, with the longest contact time 43.7 $g_{cat}hmol^{-1}$) the reaction constant (1.76) was found to be much lower than the equilibrium value at 570 K (42.2).

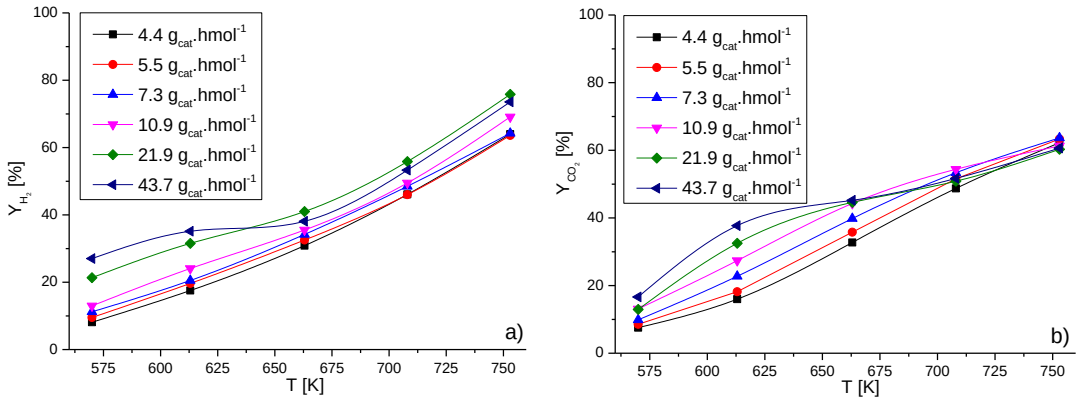

Figure 3-37 Product yields of hydrogen (a) and carbon dioxide (b) under different reaction temperature and feeding flow rate at steady state conditions.

The yields for hydrogen and carbon dioxide produced during SRE as function of reaction temperatures in the presence of the K-Ni-Cu-HTlc hybrid material is shown in Figure 3-37. The yield for hydrogen (Figure 3-37a) increased with temperature rise under different feeding flow rates. The yield of hydrogen with the longest contact time (43.7 $g_{cat}molh^{-1}$) was found to be highest at low temperatures, because more ethanol can be converted (Figure 3-35a) into hydrogen and acetaldehyde under the low feeding flow rate condition. Under high temperature conditions, the effect of contact

time became less obvious, since the ethanol reactant and the intermediate product acetaldehyde (Figure 3-36a) were already converted.

On the other hand, the yield of carbon dioxide (Figure 3-37b) first increased rapidly with temperature rise, and then the increase with temperature slowed down due to the reverse WGS at these conditions. Meanwhile more carbon monoxide appeared at higher temperatures (Figure 3-36b).

Finally, for all the reaction conditions used, no carbon deposition was found. Carbon deposition, generated by the carbon monoxide dissociation [43] at low temperatures (< 573–648 K), can be suppressed when $R_{S/E} \geq 4$. In addition, a graphitic carbon film only appears at higher temperatures (> 873 K) due to thermal cracking of methane [141]. Since SRE tests were carried out between 570 and 753 K the carbon film formation can be avoided.

3.4.3.3 Carbon dioxide adsorption

SE-SRE for pure hydrogen production requires a multifunctional material with the ability to capture carbon dioxide selectively, especially when the hybrid material was incorporated with catalytic active phases as in this work. The influence of the active copper and active nickel phase on the carbon dioxide sorption behavior for the hybrid material used in this work was studied and also compared with previous results [24, 84, 87]. For the implementation of the obtained multifunctional material on a SE-SRE study, the carbon dioxide sorption capacity must be determined at different temperatures.

The sorption isotherms were obtained by measuring the breakthrough curves of carbon dioxide. The measured gas effluent in the breakthrough test was considered at equilibrium when the carbon dioxide concentration at the outlet of the column did not vary for at least 5 min. The detailed conditions can be found in Table 3-20.

The carbon dioxide sorption capacity of the prepared material is defined as:

$$q_{CO_2} = \frac{n_{co_2,adsorbed}}{m_{sorb}} = \frac{\dot{n}_{CO_2,feed} \cdot t_s - \int_0^{t_s} \dot{n}_{CO_2,out} dt}{m_{sorb}} \tag{3.18}$$

where q_{CO2} is the sorption capacity of the material, m_{sorb} is the mass of the sorbent material, $n_{CO2,adsorbed}$ is the mol number of adsorbed carbon dioxide on the hybrid material, $\dot{n}_{CO2,feed}$ is the molar flow rate of the carbon dioxide feed, $\dot{n}_{CO2,out}$ is the molar flow rate of the carbon dioxide outlet and t_s is the time for stabilization.

Table 3-20 Operation condition used in the breakthrough tests

Temperature [K]		669, 721, 763	
Total pressure [kPa]		100	
Flow rate [$cm^3 \cdot min^{-1}$, 298 K, 100 kPa]		200	
Material Mass [kg]		0.04	
Operation	p_{CO2} [kPa]	p_{H2O} [kPa]	p_{He} [kPa]
Adsorption	5	50	45
	10		40
	20		30
	30		20
	40		10
	50		0
Desorption	0	50	50

After carbon dioxide adsorption and SE-SRE reaction, regeneration was carried out until $\dot{n}_{CO2,out} \leq 0.1$ mmol·min^{-1} without variation for 5 min in the outlet stream with water (p_{H2O} = 50 kPa), helium (p_{He} = 50 kPa) and a total feed flow rate equal to 200 $Ncm^3 \cdot min^{-1}$. During all the tests, a steam feed with the partial pressure of 50 kPa has been used. As had been reported [84], the adsorption process on an HTlc material with the presence of steam favors carbon dioxide capture. Furthermore, the layered structure of the HTlc can be recovered or maintained when contacted with ambient moisture, which is known as the memory effect [16]. Finally, sorption equilibrium isotherms at 669 K, 721 K and 763 K were measured, as depicted in Figure 3-38.

The plots are the experimental data and the solid curves correspond to the Langmuir isotherm at different conditions:

$$q_{CO_2} = q_{\max} \frac{b_{CO_2} p_{CO_2}}{1 + b_{CO_2} p_{CO_2}}, b_{CO_2} = b_{CO_2,0} e^{\frac{-\Delta H_{ads}}{RT}} \quad (3.19)$$

where q_{max} = 1.21 mol·kg^{-1} is the theoretical maximum capacity, $b_{CO2,0} = 2.11 \cdot 10^{-3}$ kPa^{-1} and ΔH_{ads} = - 18.7 kJ·mol^{-1} is the heat of carbon dioxide adsorption.

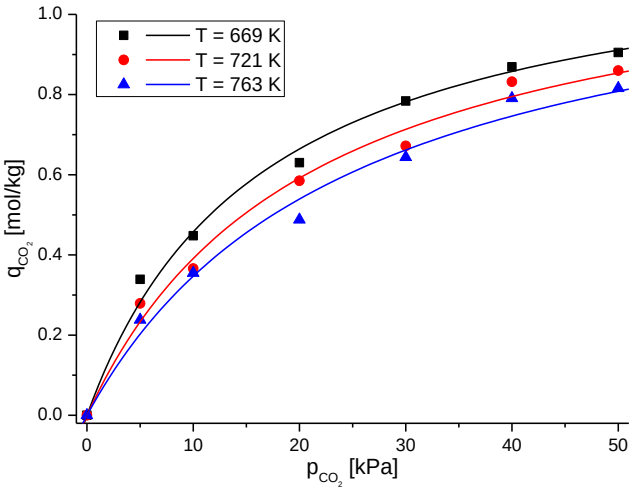

Figure 3-38 CO_2 adsorption equilibrium isotherms on K-Ni-Cu-HTlc at 669, 721 and 763 K.

The adsorption heat of this material was close to results obtained by Ding and Alpay (-17 $kJ \cdot mol^{-1}$) [84] on a K_2CO_3 promoted HTlc material under similar conditions. The adsorption capacity was found to be much higher than the unpromoted Ni-HTlc sample in section 3.2. The carbon dioxide adsorption capacity of the hybrid material with K-promoter in this study was 0.83 $mol \cdot kg^{-1}$ at 721 K and p_{CO2} = 40 kPa, while the Ni-HTlc material has a capacity of 0.26 $mol \cdot kg^{-1}$ at 723 K and p_{CO2} = 40 kPa. The possible explanation for the improvement on the carbon dioxide sorption capacity can be found in a previous report [87]. It seems also that the active phases, Ni and Cu, do not influence the sorption behavior of the support material.

It can be found from the sorption isotherms that the highest carbon dioxide adsorption capacity was obtained under the lowest temperature condition (669 K) due to the exothermic carbon dioxide adsorption process. However, we cannot simply come to the conclusion that low temperature favors the SE-SRE process, since the operating conditions for a successful SE-SRE process should be established in combination with both promising catalytic and adsorption performance of the hybrid material.

3.4.3.4 Sorption enhanced reaction process

The feasibility of operating regions on SE-SRE for a high purity hydrogen production should be investigated. The K-Ni-Cu-HTlc hybrid material was studied at different

reaction conditions. Figure 3-39 depicts the molar fractions obtained for hydrogen, carbon dioxide, carbon monoxide and methane at 723 K and 773 K for the same contact time during the transient time period and steady state period.

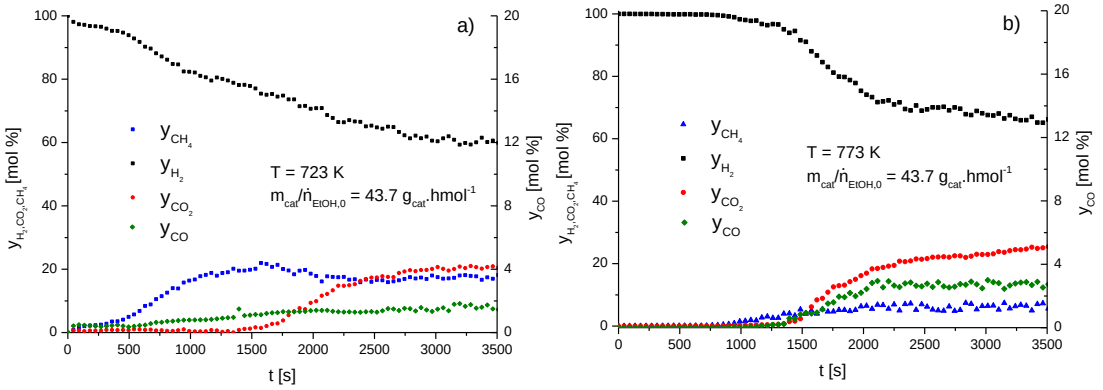

Figure 3-39 Product distributions as a function of reaction time at 723 K (a) and 773 K (b) with a $m_{cat}/\dot{n}_{0,EtOH}$ = 43.7 gcat·h·mol^{-1}.

It is important to note that in this study the highest reaction temperature applied for SE-SRE tests was 773 K, where an irreversible HTlc structure destruction can be avoided [16]. In a previous study [17] it was also found from thermodynamic equilibrium conditions that the performance of SE-SRE benefits from a low pressure operation, because the overall SRE reaction is a volume increase reaction. Therefore, atmospheric pressure was used during SE-SRE tests.

At a lower temperature, 723 K (Figure 3-39a), the yield of hydrogen produced during the transient period was relatively lower than for 773 K (Figure 3-39b). On the other hand, the breakthrough time for methane (and carbon monoxide) was shorter as for a lower temperature. This means that at 723 K mainly SE-WGS occurred, while at 773 K SE-SMR and SE-WGS were both performed simultaneously. As a result, the yield of hydrogen for the latter case was higher and the carbon dioxide breakthrough time was longer. After breakthrough, the outlet concentrations observed at steady state conditions corresponding to the previously observed SRE experiments. In addition, a comparison between the results, both SE-SRE and SRE tests, from the prepared K-Ni-Cu-HTlc material and other studies can be found in Table 3-21, where y_{H2} [mol %] represents the concentration of hydrogen in the product gas (dry basis).

Table 3-21 Comparative performances of the materials used for SE-SRE (Pre-breakthrough state) and SRE (Post-breakthrough state).

Materials	Pre-breakthrough state			Post-breakthrough state		
	X_{EtOH} [%]	y_{H2} [mol %]	S_{H2} [%]	X_{EtOH} [%]	y_{H2} [mol %]	S_{H2} [%]
[1]Thermodynamic [17]		99.9	98.3	100	66.0	63.0
[2]Co−Ni/HTlc with CaO [65]		>99	n.a.	100	66	n.a.
[3]Ni/Al_2O_3 with Li_4SiO_4 [152]		~98	~87	100	~61	~58
[4]Ni/Al_2O_3 with HTlc [11]	100	98.7	21.8	64.2	56.0	25.1
[4]Cu-HTlc [68]		91.7	24.4	83.8	84.4	22.6
[1]Ni-HTlc [128]		98.2	95.7	100	66.4	66.3
[1]K-Ni-Cu-HTlc		99.8	96.5	100	67.1	66.7

Operating conditions: p = 101 kPa, [1]T = 773 K and $R_{S/E}$ = 10, [2]T = 823 K and $R_{S/E}$ = 6, [3]T = 800 K and $R_{S/E}$ = 6, [4]T = 673 K and $R_{S/E}$ = 10.

Among the SE-SRE studies published, many pairs of catalyst-sorbent systems have been developed. These configurations can be classified into two groups: alternate layers of catalyst and sorbent; or uniform mixture of the two materials. By packing the bed with several layers of catalyst and sorbent sequentially, the column is just a combination of several reactors and adsorbers in series. The arrangement can affect the overall performance [153]. Rawadieh and Gomes [154] compared different layered systems, they found that a well-mixed configuration can produce higher hydrogen purity with lower carbon monoxide content compared to other layered configurations, which is in agreement with the result found by Lu and Rodrigues [155]. However, in practice it is very difficult to obtain an ideal mixed catalyst-sorbent system due to the differences in particle size, shape and density of the catalyst and sorbent materials. Alternatively, recent studies suggested that a homogenous mixture can be achieved by synthesis of sorbent material together with an active phase [68, 128, 156].

It could be found that the use of a carbon dioxide adsorbent can improve the hydrogen production performance in the reforming process, since under all these different operating conditions, the yields and selectivity of hydrogen were much

higher during the pre-breakthrough period (SERP region) than that obtained from conventional reforming process. According to the results collected from K-Ni-Cu-HTlc material (Table 3-21), for both the pre- and post-breakthrough periods, the hydrogen concentrations and selectivity were found to be close to thermodynamic calculations for SE-SRE and SRE, respectively. It is an indication of the promising reaction and adsorption performance of the multifunctional material. In addition, hydrogen with a higher concentration can be produced from the use of a K-HTlc material as carbon dioxide sorbent than the other high temperature carbon dioxide sorbents.

It can be observed that the developed multifunctional material can offer promising hydrogen production performance (y_{H2} = 99.8 mol % and S_{H2} = 96.5 %) during the pre-breakthrough region, comparing the conventional operation [65, 152] of the bed packed with a mixture of catalyst and sorbent. As a result, the development of a multifunctional material can eliminate the use of additional catalyst support and offers the advantage of reducing the reactor size [156].

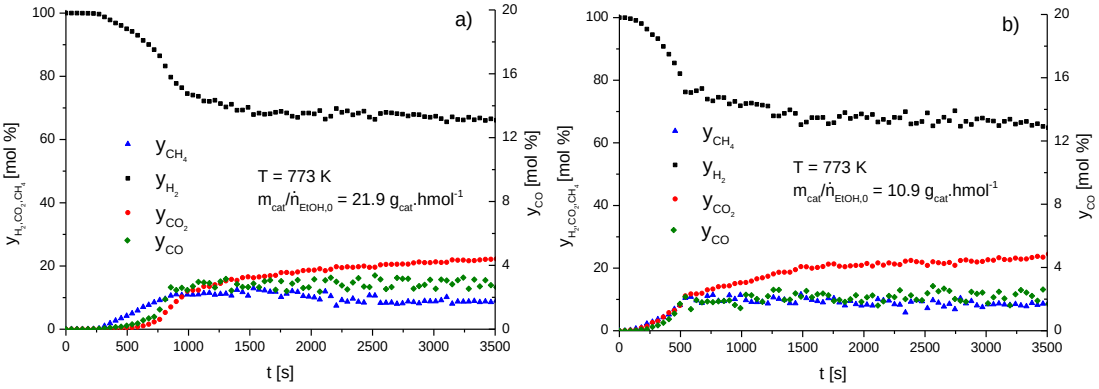

Figure 3-40 Product distributions as a function of time at 773 K with $m_{cat}/\dot{n}_{0,EtOH}$ = 21.9 $g_{cat}\cdot h\cdot mol^{-1}$ (a) and 10.9 $g_{cat}\cdot h\cdot mol^{-1}$.

Comparing Figure 3-39a with Figure 3-40a and Figure 3-40b, we can find that at a temperature of 773 K, the higher of the reactant mixture feeding rates, the shorter were the breakthrough times during SE-SRE. These breakthrough times were very important for the design of a SE-SRE process in order to employ this hybrid material for hydrogen production. In the design of a cyclic SE-SRE process, the longer the

pre-breakthrough period, the less parallel columns would be required for a continuous operation, which can be an advantage in the fixed construction cost [128]. Therefore, a detailed investigation will be carried out in the following chapter to design a cyclic SE-SRE operation process with the material synthesized in this work.

3.4.4 Conclusions

A multifunctional hybrid material was synthesized with multivalent properties, catalytic activity and selectivity as well as the selective sorption towards carbon dioxide for SE-SRE. The catalytic behavior obtained for SRE was investigated and found to be more promising than the previously used HTlc materials incorporated with Ni or Cu alone. The multifunctional hybrid material used in this work kept a similar carbon dioxide adsorption capacity as the K-promoted hydrotalcite studied in former studies. It is found that the K-HTlc structure was kept in the multiphase material similar like the previously used individual materials. In this work, the formation of a nickel-copper alloy phase has been observed, which can be very helpful in the catalytic property due to the formation of small ensembles of nickel and copper that reduce in considerable amounts the interactions of adsorbed species on the specific metallic surfaces. The metallic crystallite size of the $Ni_{0.5}Cu_{0.5}$ alloy was found to be very small which has the benefit of high catalytic activity. The hybrid material consisted of a multiple phase composition used for SRE was found to have promising activity and selectivity, together with the excellent selective carbon dioxide sorption capacity. This multifunctional material was found as one of the most promising SERP materials, which is ripe for a scale up SE-SRE process design to produce high purity hydrogen in a single reaction unit.

References

[1] J.D. Arndt, S. Freyer, R. Geier, O. Machhammer, J. Schwartze, M. Volland, R. Diercks, *Chem. Ing. Tech.* **2007**, *79 (5)*, 521-528.

[2] N. Lior, *Energy.* **2008**, *33 (6)*, 842-857.

[3] N. Muradov, T. Veziroglu, *Int. J. Hydrogen Energy.* **2008**, *33 (23)*, 6804-6839.

[4] F. de Bruijn, *Green Chem.* **2005**, *7 (3)*, 132-150.

[5] R.L. Peter Häussinger, Allan M. Watson, *Hydrogen*, in: Ullmann´s Encyclopedia of Industrial Chemistry, Wiley-VCH, Verlag, **2007**.

[6] C. Wyman, *Handbook on Bioethanol: Production and Utilization*, Taylor & Francis, Washington, DC, **1996**.

[7] M. Ni, D.Y.C. Leung, M.K.H. Leung, *Int. J. Hydrogen Energy.* **2007**, *32 (15)*, 3238-3247.

[8] A. Haryanto, S. Fernando, N. Murali, S. Adhikari, *Energy Fuels.* **2005**, *19 (5)*, 2098-2106.

[9] P.D. Vaidya, A.E. Rodrigues, *Chem. Eng. J.* **2006**, *117 (1)*, 39-49.

[10] C. Ratnasamy, J. Wagner, *Catal. Rev.* **2009**, *51 (3)*, 325-440.

[11] A.F. Cunha, Y.-J. Wu, F.A. Díaz Alvarado, J.C. Santos, P.D. Vaidya, A.E. Rodrigues, *Can. J. Chem. Eng.* **2012**, *90 (6)*, 1514-1526.

[12] M.V. Twigg, M.S. Spencer, *Top. Catal.* **2003**, *22 (3)*, 191-203.

[13] S. Velu, K. Suzuki, M.P. Kapoor, F. Ohashi, T. Osaki, *Appl. Catal., A.* **2001**, *213 (1)*, 47-63.

[14] J.C.J. Bart, R.P.A. Sneeden, *Catal. Today.* **1987**, *2 (1)*, 1-124.

[15] S. Choi, J.H. Drese, C.W. Jones, *ChemSusChem.* **2009**, *2 (9)*, 796-854.

[16] F. Cavani, F. Trifirò, A. Vaccari, *Catal. Today.* **1991**, *11 (2)*, 173-301.

[17] Y.-J. Wu, F. Díaz Alvarado, J.C. Santos, F. Gracia, A.F. Cunha, A.E. Rodrigues, *Chem. Eng. Technol.* **2012**, *35 (5)*, 847–858.

[18] N.K. Das, A.K. Dalai, R. Ranganathan, *Can. J. Chem. Eng.* **2007**, *85 (1)*, 92-100.

[19] Z.P. Lu, J.M. Loureiro, A.E. Rodrigues, *Simulation of pressure swing adsorption reactors* in: CHEMPOR'93, 6th International Chemical Engineering Conference,

Porto, Portugal, **1993**.

[20] W.E. Waldron, J.R. Hufton, S. Sircar, *AIChE J.* **2001**, *47 (6)*, 1477-1479.

[21] L. Barelli, G. Bidini, F. Gallorini, S. Servili, *Energy.* **2008**, *33 (4)*, 554-570.

[22] D.P. Harrison, *Ind. Eng. Chem. Res.* **2008**, *47 (17)*, 6486-6501.

[23] G.C. Chinchen, P.J. Denny, J.R. Jennings, M.S. Spencer, K.C. Waugh, *Appl. Catal.* **1988**, *36* 1-65.

[24] E.L.G. Oliveira, C.A. Grande, A.E. Rodrigues,, *Sep. Purif. Technol.* **2008**, *62 (1)*, 137-147.

[25] E.P. Barrett, L.G. Joyner, P.P. Halenda, *J. Am. Chem. Soc.* **1951**, *73 (1)*, 373-380.

[26] A. Guida, M.H. Lhouty, D. Tichit, F. Figueras, P. Geneste, *Appl. Catal., A.* **1997**, *164 (1-2)*, 251-264.

[27] F. Prinetto, D. Tichit, R. Teissier, B. Coq, *Catal. Today.* **2000**, *55 (1-2)*, 103-116.

[28] K.K. Rao, M. Gravelle, J.S. Valente, F. Figueras, *J. Catal.* **1998**, *173 (1)*, 115-121.

[29] J.C.A.A. Roelofs, D.J. Lensveld, A.J. van Dillen, K.P. de Jong, *J. Catal.* **2001**, *203 (1)*, 184-191.

[30] D. Tichit, M. Naciri Bennani, F. Figueras, R. Tessier, J. Kervennal, *Appl. Clay Sci.* **1998**, *13 (5-6)*, 401-415.

[31] D. Tichit, M.H. Lhouty, A. Guida, B.H. Chiche, F. Figueras, A. Auroux, D. Bartalini, E. Garrone, *J. Catal.* **1995**, *151 (1)*, 50-59.

[32] M.J. Climent, A. Corma, S. Iborra, K. Epping, A. Velty, *J. Catal.* **2004**, *225 (2)*, 316-326.

[33] A. Corma, V. Fornes, F. Rey, *J. Catal.* **1994**, *148 (1)*, 205-212.

[34] G. Fornasari, M. Gazzano, D. Matteuzzi, F. Trifirò, A. Vaccari, *Appl. Clay Sci.* **1995**, *10 (1-2)*, 69-82.

[35] R.F.P.M. Moreira, J.L. Soares, G.L. Casarin, A.E. Rodrigues, *Sep. Purif. Technol.* **2006**, *41 (2)*, 341-357.

[36] H.A. Prescott, Z.-J. Li, E. Kemnitz, A. Trunschke, J. Deutsch, H. Lieske, A. Auroux, *J. Catal.* **2005**, *234 (1)*, 119-130.

[37] P. Kurr, I. Kasatkin, F. Girgsdies, A. Trunschke, R. Schlögl, T. Ressler, *Appl. Catal., A.* **2008**, *348 (2)*, 153-164.

[38] X. Xia, *Experimental and Theoretical Aspects of Adsorption Microcalorimetry Applied to Characterize Hetereogeneous Catalysts*, in: Lehrstuhl fur Technische Chemie, Ruhr-Universitaet Bochum, 2006.

[39] P. Mierczynski, T.P. Maniecki, K. Chalupka, W. Maniukiewicz, W.K. Jozwiak, *Catal. Today.* **2011**, *176 (1)*, 21-27.

[40] B. Ficicilar, T. Dogu, *Catal. Today.* **2006**, *115 (1–4)*, 274-278.

[41] Z. Yong, A.E. Rodrigues, *Energy Convers. Manage.* **2002**, *43 (14)*, 1865-1876.

[42] S.M. Auerbach, K.A. Carrado, P.K. Dutta, *Handbook of Layered Materials*, Marcel Dekker Inc., Hoboken, **2004**.

[43] C.H. Bartholomew, *Appl. Catal., A.* **2001**, *212 (1-2)*, 17-60.

[44] M.S. Spencer, *Nature.* **1986**, *323 (6090)*, 685-687.

[45] J.-H. Lin, V.V. Guliants, *ChemCatChem.* **2011**, *3 (9)*, 1426-1430.

[46] M. Louthan, *J. Fail. Anal. Prev.* **2008**, *8 (3)*, 289-307.

[47] C. Wu-Hsun, *Appl. Catal., A.* **1995**, *130 (1)*, 13-30.

[48] A.F. Cunha, J.J.M. Órfão, J.L. Figueiredo, *Fuel Process. Technol.* **2009**, *90 (10)*, 1234-1240.

[49] D.L. Trimm, *Catal. Today.* **1997**, *37 (3)*, 233-238.

[50] N. Mahata, A.F. Cunha, J.J.M. Órfão, J.L. Figueiredo, *ChemCatChem.* **2010**, *2 (3)*, 330-335.

[51] A. Lima da Silva, C.d.F. Malfatti, I.L. Müller, *Int. J. Hydrogen Energy.* **2009**, *34 (10)*, 4321-4330.

[52] G. Emig, E. Klemm, *Technische chemie einführung in die chemische reaktionstechnik*, Springer-Verlag, Berlin, Heidelberg, **2005**.

[53] Y. Ding, E. Alpay, *Chem. Eng. Sci.* **2000**, *55 (18)*, 3929-3940.

[54] S. Solomon, C. Intergovernmental Panel on Climate, I. Intergovernmental Panel on Climate Change. Working Group, *Climate Change 2007: The Physical Science Basis : Contribution of Working Group I to the Fourth Assessment Report of the*

Intergovernmental Panel on Climate Change, Cambridge University Press, Cambridge; New York, **2007**.

[55] G.W. Crabtree, M.S. Dresselhaus, M.V. Buchanan, *Phys. Today.* **2004**, *57 (12)*, 39-44.

[56] C. Song, *Catal. Today.* **2002**, *77 (1-2)*, 17-49.

[57] P. Ferreira‐Aparicio, M.J. Benito, J.L. Sanz, *Catal. Rev.: Sci. Eng.* **2005**, *47 (4)*, 491-588.

[58] C.-C. Chang, J.-W. Wang, C.-T. Chang, B.-J. Liaw, Y.-Z. Chen, *Chem. Eng. J.* **2012**, *192*, 350-356.

[59] J. Comas, F. Mariño, M. Laborde, N. Amadeo, *Chem. Eng. J.* **2004**, *98 (1–2)*, 61-68.

[60] C. Wang, B. Dou, H. Chen, Y. Song, Y. Xu, X. Du, T. Luo, C. Tan, *Chem. Eng. J.* **2013**, *220*, 133-142.

[61] F. Seyedeyn Azad, J. Abedi, E. Salehi, T. Harding, *Chem. Eng. J.* **2012**, *180*, 145-150.

[62] G. Wu, C. Zhang, S. Li, Z. Huang, S. Yan, S. Wang, X. Ma, J. Gong, *Energy Environ. Sci.* **2012**, *5 (10)*, 8942-8949.

[63] A.N. Fatsikostas, X.E. Verykios, *J. Catal.* **2004**, *225 (2)*, 439-452.

[64] Y.-J. Wu, J.C. Santos, P. Li, J.-G. Yu, A.F. Cunha, A.E. Rodrigues, *Can. J. Chem. Eng.* **2014**, *92 (1)*, 116-130.

[65] L. He, H. Berntsen, D. Chen, *J. Phys. Chem. A.* **2009**, *114 (11)*, 3834-3844.

[66] E.L.G. Oliveira, C.A. Grande, A.E. Rodrigues, *Chem. Eng. Sci.* **2011**, *66 (3)*, 342-354.

[67] S. Gunduz, T. Dogu, *Ind. Eng. Chem. Res.* **2011**, *51 (26)*, 8796-8805.

[68] A.F. Cunha, Y.-J. Wu, J.C. Santos, A.E. Rodrigues, *Chem. Eng. Res. Des.* **2013**, *91 (3)*, 581-592.

[69] M.H. Halabi, M.H.J.M. de Croon, J. van der Schaaf, P.D. Cobden, J.C. Schouten, *Fuel.* **2012**, *99*, 154-164.

[70] J.-N. Kim, C.H. Ko, K.B. Yi, *Int. J. Hydrogen Energy.* **2013**, *38 (14)*, 6072-6078.

[71] H.Z. Feng, P.Q. Lan, S.F. Wu, *Int. J. Hydrogen Energy.* **2012**, *37 (19)*, 14161-14166.

[72] Z. Yong, V. Mata, A.E. Rodrigues, *Sep. Purif. Technol.* **2002**, *26 (2-3)*, 195-205.

[73] M.K. Ram Reddy, Z.P. Xu, G.Q. Lu, J.C. Diniz da Costa, *Ind. Eng. Chem. Res.* **2006**, *45 (22)*, 7504-7509.

[74] V. Mas, M.L. Dieuzeide, M. Jobbágy, G. Baronetti, N. Amadeo, M. Laborde, *Catal. Today.* **2008**, *133-135* 319-323.

[75] F. Mariño, G. Baronetti, M. Jobbagy, M. Laborde, *Appl. Catal., A.* **2003**, *238 (1)*, 41-54.

[76] V. Mas, G. Baronetti, N. Amadeo, M. Laborde, *Chem. Eng. J.* **2008**, *138 (1-3)*, 602-607.

[77] C. Resini, T. Montanari, L. Barattini, G. Ramis, G. Busca, S. Presto, P. Riani, R. Marazza, M. Sisani, F. Marmottini, U. Costantino, *Appl. Catal., A.* **2009**, *355 (1–2)*, 83-93.

[78] A.F. Lucrédio, J.A. Bellido, E.M. Assaf, *Catal. Commun.* **2011**, *12 (14)*, 1286-1290.

[79] R. Espinal, E. Taboada, E. Molins, R.J. Chimentao, F. Medina, J. Llorca, *RSC Adv.* **2012**, *2 (7)*, 2946-2956.

[80] R. Guil-López, R.M. Navarro, M.A. Peña, J.L.G. Fierro, *Int. J. Hydrogen Energy.* **2011**, *36 (2)*, 1512-1523.

[81] Sasol, Product information, www.sasoltechdata.com/tds/PURAL-MG.pdf, in, Sasol, Germany, **2013**.

[82] L. He, J.M.S. Parra, E.A. Blekkan, D. Chen, *Energy Environ. Sci.* **2010**, *3 (8)*, 1046-1056.

[83] M.H. Halabi, M.H.J.M. de Croon, J. van der Schaaf, P.D. Cobden, J.C. Schouten, *Chem. Eng. J.* **2011**, *168 (2)*, 872-882.

[84] Y. Ding, E. Alpay, *Chem. Eng. Sci.* **2000**, *55 (17)*, 3461-3474.

[85] N. Wakao, T. Funazkri, *Chem. Eng. Sci.* **1978**, *33 (10)*, 1375-1384.

[86] B.E. Poling, J.M. Prausnitz, J.P. O'Connell, *The properties of gases and liquids*,

McGraw-Hill, New York, **2001**.

[87] Y.-J. Wu, P. Li, J.-G. Yu, A.F. Cunha, A.E. Rodrigues, *Chem. Eng. Technol.* **2013**, *36 (4)*, 567-574.

[88] Z. Yong, Mata, A.E. Rodrigues, *Ind. Eng. Chem. Res.* **2000**, *40 (1)*, 204-209.

[89] K.A. Carrado, R. Csencsits, P. Thiyagarajan, S. Seifert, S.M. Macha, J.S. Harwood, *J. Mater. Chem.* **2002**, *12 (11)*, 3228-3237.

[90] A. Al-Ubaid, E.E. Wolf, *Appl. Catal.* **1988**, *40*, 73-85.

[91] A.F. Cunha, Y.-J. Wu, J.C. Santos, A.E. Rodrigues, *Ind. Eng. Chem. Res.* **2012**, *51 (40)*, 13132-13143.

[92] F. Díaz Alvarado, F. Gracia, *Chem. Eng. J.* **2010**, *165 (2)*, 649-657.

[93] J.L. Soares, R.F.P.M. Moreira, H.J. José, C.A. Grande, A.E. Rodrigues, *Sep. Purif. Technol.* **2005**, *39 (9)*, 1989-2010.

[94] J.L. Soares, C.A. Grande, Z. Yong, R.F.P.M. Moreira, A.E. Rodrigues, *Adsorption of Carbon Dioxide at High Temperatures onto Hydrotalcite - like Compounds (HTlcs)*, in: K. Kaneko, H. Kanoh, Y. Hanzawa (Eds.) Proceeedings of Fundamentals of Adsorption 7, IK International Ltd, Chiba, Japan, **2002**.

[95] H.T.J. Reijers, S.E.A. Valster-Schiermeier, P.D. Cobden, R.W. van den Brink, *Ind. Eng. Chem. Res.* **2005**, *45 (8)*, 2522-2530.

[96] J.P. Breen, R. Burch, H.M. Coleman, *Appl. Catal., B.* **2002**, *39 (1)*, 65-74.

[97] B. Banach, A. Machocki, P. Rybak, A. Denis, W. Grzegorczyk, W. Gac, *Catal. Today.* **2011**, *176 (1)*, 28-35.

[98] Y.-N. Wang, A.E. Rodrigues, *Fuel.* **2005**, *84 (14–15)*, 1778-1789.

[99] Y. Chen, Y. Zhao, C. Zheng, J. Zhang, *Chem. Eng. Sci.* **2013**, *92 (5)*, 67-80.

[100] M. Tomkiewicz, *C. R. Chim.* **2006**, *9 (2)*, 172-179.

[101] M. Finkenrath, *Chem. Eng. Technol.* **2012**, *35 (3)*, 482-488.

[102] C. Luo, Q. Shen, N. Ding, Z. Feng, Y. Zheng, C. Zheng, *Chem. Eng. Technol.* **2012**, *35 (3)*, 547-554.

[103] R.J. Notz, I. Tönnies, N. McCann, G. Scheffknecht, H. Hasse, *Chem. Eng. Technol.* **2011**, *34 (2)*, 163-172.

[104] J.A. Turner, *Science.* **2004**, *305 (5686)*, 972-974.

[105] G.A. Deluga, J.R. Salge, L.D. Schmidt, X.E. Verykios, *Science.* **2004**, *303 (5660)*, 993-997.

[106] A.J. Liska, H.S. Yang, V.R. Bremer, T.J. Klopfenstein, D.T. Walters, G.E. Erickson, K.G. Cassman, *J. Ind. Ecol.* **2009**, *13 (1)*, 58-74.

[107] B.T. Carvill, J.R. Hufton, M. Anand, S. Sircar, *AIChE J.* **1996**, *42 (10)*, 2765-2772.

[108] J. Hufton, S. Mayorga, S. Sircar, *AIChE J.* **1999**, *45 (2)*, 248-256.

[109] H.M. Jang, K.B. Lee, H.S. Caram, S. Sircar, *Chem. Eng. Sci.* **2012**, *73*, 431-438.

[110] A.F. Cunha, J.J.M. Órfão, J.L. Figueiredo, *Appl. Catal., A.* **2008**, *348 (1)*, 103-112.

[111] K.B. Lee, M.G. Beaver, H.S. Caram, S. Sircar, *Int. J. Hydrogen Energy.* **2008**, *33 (2)*, 781-790.

[112] G.-h. Xiu, J.L. Soares, P. Li, A.E. Rodrigues, *AIChE J.* **2002**, *48 (12)*, 2817-2832.

[113] N. Hutson, B. Attwood, *Adsorption.* **2008**, *14 (6)*, 781-789.

[114] R.T. Yang, *Adsorbents fundamentals and applications*, Wiley-Interscience, Hoboken, N.J., **2003**.

[115] M.H. Halabi, M.H.J.M. de Croon, J. van der Schaaf, P.D. Cobden, J.C. Schouten, *Int. J. Hydrogen Energy.* **2012**, *37 (5)*, 4516-4525.

[116] S. G.Mayorga, J.R. Hufton, S. Sircar, T.R. Gaffney, *Sorption enhanced reaction process for production of hydrogen. Phase 1 final report*, in, U.S. Department of Energy, Washington, DC, **1997**.

[117] D. DeVault, *J. Am. Chem. Soc.* **1943**, *65 (4)*, 532-540.

[118] S. Sircar, *Rapid Thermal Swing Adsorption*, in, U.S. Patent 20030037672, **2003**.

[119] K.B. Lee, M.G. Beaver, H.S. Caram, S. Sircar, *Ind. Eng. Chem. Res.* **2007**, *46 (14)*, 5003-5014.

[120] L.E. Doman, *International Energy Outlook 2013*, in, U.S. Energy Information Administration, Washington, **2013**.

[121] L. Barreto, A. Makihira, K. Riahi, *Int. J. Hydrogen Energy.* **2003**, *28 (3)*, 267-284.

[122] K. Liu, C. Song, V. Subramani, *Hydrogen and syngas production and purification technologies*, Wiley, Hoboken, NJ, **2010**.

[123] Z. Wang, H. Wang, Y. Liu, *RSC Adv.* **2013**, *3 (25)*, 10027-10036.

[124] R. Chakrabarti, J.S. Kruger, R.J. Hermann, L.D. Schmidt, *RSC Adv.* **2012**, *2 (6)*, 2527-2533.

[125] J. Divisek, H.F. Oetjen, V. Peinecke, V.M. Schmidt, U. Stimming, *Electrochim. Acta.* **1998**, *43 (24)*, 3811-3815.

[126] G.-h. Xiu, P. Li, A.E. Rodrigues, *Chem. Eng. Sci.* **2002**, *57 (18)*, 3893-3908.

[127] Y. Li, Q. Fu, M. Flytzani-Stephanopoulos, *Appl. Catal., B.* **2000**, *27 (3)*, 179-191.

[128] Y.-J. Wu, P. Li, J.-G. Yu, A.F. Cunha, A.E. Rodrigues, *Chem. Eng. J.* **2013**, *231*, 36-48.

[129] M.A. Nahil, X. Wang, C. Wu, H. Yang, H. Chen, P.T. Williams, *RSC Adv.* **2013**, *3 (16)*, 5583-5590.

[130] Q. Wang, Y. Gao, J. Luo, Z. Zhong, A. Borgna, Z. Guo, D. O'Hare, *RSC Adv.* **2013**, *3 (10)*, 3414-3420.

[131] M.P. Andersson, F. Abild-Pedersen, I.N. Remediakis, T. Bligaard, G. Jones, J. Engbæk, O. Lytken, S. Horch, J.H. Nielsen, J. Sehested, J.R. Rostrup-Nielsen, J.K. Nørskov, I. Chorkendorff, *J. Catal.* **2008**, *255 (1)*, 6-19.

[132] C. Zhang, P. Zhang, S. Li, G. Wu, X. Ma, J. Gong, *Phys. Chem. Chem. Phys.* **2012**, *14 (10)*, 3295-3298.

[133] E. Poggio-Fraccari, F. Mariño, M. Laborde, G. Baronetti, *Appl. Catal., A.* **2013**, *460–461*, 15-20.

[134] J.R. Rostrup-Nielsen, N. Hojlund, *Deactivation and Poisoning of Catalysts*, Taylor & Francis, New York, **1985**.

[135] H. Nakano, J. Ogawa, J. Nakamura, *Surf. Sci.* **2002**, *514 (1–3)*, 256-260.

[136] F. Mariño, M. Boveri, G. Baronetti, M. Laborde, *Int. J. Hydrogen Energy.* **2001**,

26 (7), 665-668.

[137] J.F. Da Costa-Serra, M.T. Navarro, F. Rey, A. Chica, *Int. J. Hydrogen Energy.* **2012**, *37 (8)*, 7101-7108.

[138] L.-C. Chen, S.D. Lin, *Appl. Catal., B.* **2011**, *106 (3-4)*, 639-649.

[139] I. Ban, J. Stergar, M. Drofenik, G. Ferk, D. Makovec, *J. Magn. Magn. Mater.* **2011**, *323 (17)*, 2254-2258.

[140] F. Bonet, S. Grugeon, L. Dupont, R. Herrera Urbina, C. Guéry, J.M. Tarascon, *J. Solid State Chem.* **2003**, *172 (1)*, 111-115.

[141] A.F. Cunha, J.J.M. Órfão, J.L. Figueiredo, *Int. J. Hydrogen Energy.* **2009**, *34 (11)*, 4763-4772.

[142] H. Natter, M. Schmelzer, R. Hempelmann, *J. Mater. Res.* **1998**, *13 (5)*, 1186-1197.

[143] J.A. Moulijn, A.E. van Diepen, F. Kapteijn, *Appl. Catal., A.* **2001**, *212 (1–2)*, 3-16.

[144] K.L. Erickson, T.E. Bostrom, R.L. Frost, *Mater. Lett.* **2005**, *59 (2–3)*, 226-229.

[145] V. Mas, R. Kipreos, N. Amadeo, M. Laborde, *Int. J. Hydrogen Energy.* **2006**, *31 (1)*, 21-28.

[146] F. Mariño, M. Boveri, G. Baronetti, M. Laborde, *Int. J. Hydrogen Energy.* **2004**, *29 (1)*, 67-71.

[147] C. Ampelli, R. Passalacqua, C. Genovese, S. Perathoner, G. Centi, T. Montini, V. Gombac, J.J. Delgado, P. Fornasiero, *RSC Adv.* **2013**, *3(44)*, 21776-21788.

[148] M.A. Ebiad, D.R. Abd El-Hafiz, R.A. Elsalamony, L.S. Mohamed, *RSC Adv.* **2012**, *2 (21)*, 8145-8156.

[149] R.I. Wijngaarden, K.R. Westerterp, A. Kronberg, A. Bos, *Industrial catalysis: optimizing catalysts and processes*, Wiley-VCH, Weinheim, **1998**.

[150] J. Xu, X. Zhang, R. Zenobi, J. Yoshinobu, Z. Xu, J.T. Yates Jr, *Surf. Sci.* **1991**, *256 (3)*, 288-300.

[151] J. Hagen, *Industrial catalysis: a practical approach*, John Wiley & Sons, Mannheim, **2006**.

[152] K. Essaki, T. Muramatsu, M. Kato, *Int. J. Hydrogen Energy.* **2008**, *33 (22)*, 6612-6618.

[153] S. Rawadieh, V.G. Gomes, *Int. J. Chem. React. Eng.* **2007**, *5 (1)*, 1428.

[154] S. Rawadieh, V.G. Gomes, *Int. J. Hydrogen Energy.* **2009**, *34 (1)*, 343-355.

[155] Z.P. Lu, A.E. Rodrigues, *AIChE J.* **1994**, *40 (7)*, 1118-1137.

[156] N. Chanburanasiri, A.M. Ribeiro, A.E. Rodrigues, A. Arpornwichanop, N. Laosiripojana, P. Praserthdam, S. Assabumrungrat, *Ind. Eng. Chem. Res.* **2011**, *50 (24)*, 13662-13671.

4. Process Study †

In this chapter, a four-step pressure swing operation process in one column with two subsections for SE-SRE has been developed by simulation for high purity hydrogen production in section 4.1. Within the two subsections, two different volumetric ratios (1:2 and 1:4) between the Ni impregnated hydrotalcite catalyst and K-promoted hydrotalcite sorbent have been employed. Various reaction conditions and operating parameters have been tested to improve the hydrogen production performance. The product gas with hydrogen purity above 99 mol % and carbon monoxide content of 30 ppm can be produced at 773 K with swing pressure from 101.3 to 304 kPa. The yield of hydrogen in SE-SRE (78.5 %) is found to be much higher than in SRE (38.3 %) at the same reaction conditions.

In the following section, a two-dimensional adsorptive reactor model has been developed for SE-SRE. The product distributions from simulations match well with experimental data obtained from a laboratory-scale fixed-bed reactor. In addition, the performance of sorption enhanced reaction is found to be sensitive to the temperature gradient in the radial direction in a scale-up reactor. Afterwards, four reactors with a seven steps cycle operation scheme have been employed in a continuous hydrogen production process. It is found that high purity hydrogen with 0.95 $mol \cdot kg^{-1} \cdot h^{-1}$ productivity can be produced under cyclic steady state operation, the ratio between energy output and input is around 1.7. Besides, high purity carbon dioxide can also be captured as a by-product during the sorbent regeneration step in this process.

† The content of this chapter is part of the following articles:

Y.-J. Wu, Ping Li, J.-G. Yu, A.F. Cunha, A.E. Rodrigues, High-Purity Hydrogen Production by Sorption-Enhanced Steam Reforming of Ethanol: A Cyclic Operation Simulation Study, Industrial & Engineering Chemistry Research, 53 (20), 2014, 8515–8527.

Y.-J. Wu, Ping Li, J.-G. Yu, A.F. Cunha, A.E. Rodrigues, Sorption-enhanced Steam Reforming of Ethanol for Continuous High-Purity Hydrogen Production: 2D Adsorptive Reactor Dynamics and Process Design, Chemical Engineering Science, 2014, DOI: 10.1016/j.ces.2014.07.005.

4.1 SE-SRE Operation in a Single Column System

4.1.1 Introduction

Until now, most of the SERP researches are focused on the use of methane (natural gas) as feedstock, while only a small number of experimental studies have been carried out on SE-SRE. Among these studies, calcium oxide-based materials have been widely used as the high temperature carbon dioxide sorbents. Lysikov et al. [1] compared different feedstocks for hydrogen production via SERP over a mixture of a commercial nickel-based catalyst and calcium oxide sorbent. It was found that ethanol exhibits the best performance among all the feedstocks studied, a 98 vol. % purity of hydrogen-rich gas, with impurities of carbon monoxide and carbon dioxide less than 20 ppm, was obtained. With ethanol as feedstock, He et al. [2] carried out SERP over a mixture of a HTlc derived Co−Ni catalyst and calcined dolomite as carbon dioxide sorbent. A good performance was observed at 823 K, where the product gas contains 99 mol % hydrogen with only 0.1 mol. % of carbon monoxide. Besides, a study on SE-SRE with Ni- and Co-incorporated MCM-41 catalysts, with calcium oxide as carbon dioxide sorbent, was performed by Gunduz and Dogu [3]. They found that the yield of hydrogen can reach 94 % at 873 K with a steam-to-carbon molar ratio ($R_{S/C}$) of 1.6 in the feed.

On the other hand, other high temperature carbon dioxide sorbents such as lithium-based materials and HTlc materials are also used. Iwasaki et al. [4] performed SE-SRE reaction with lithium silicate as sorbent over 1 wt. % Rh/CeO_2 catalyst. A product gas with 96 mol % hydrogen was obtained at 823 K, atmospheric pressure and $R_{S/C}$ = 1.5. In addition, Essaki et al. [5] reported that the concentration of hydrogen can reach 99 mol. % along with carbon monoxide below 0.12 mol % by SE-SRE over a commercial nickel-based catalyst, with lithium silicate as sorbent at similar conditions. Besides, a commercial nickel-based catalyst with an HTlc sorbent was employed by Cunha et al. [6] as a hybrid system. The results of SE-SRE at 673 K with $R_{S/C}$ = 5 in the feed showed that pure hydrogen was produced in the first 10 min of reaction. In addition, hybrid materials with Cu [7] and Ni [8] as the active metal

phase, HTlc material as the catalyst support have also been developed for SE-SRE. These materials were found to have good catalytic performance to produce hydrogen from SE-SRE due to the relatively high surface areas and small crystal sizes.

However, one technological challenge of SERP is its cyclic nature. The sorbent has to be periodically regenerated without affecting both the activity of the catalyst and the sorbent. Each column with sorbent and catalyst swings between at least two states: Reaction, where ethanol together with steam is fed to the reactor to produce hydrogen; Regeneration, operating conditions are modified to regenerate the saturated carbon dioxide sorbent. Previous studies on SE-SRE only have the reaction stage where SERP was performed with different catalysts and sorbents, while the results from a cyclic operation process have not been reported. Therefore, investigations on sorbent regeneration and cyclic process should be performed to develop a continuous SE-SRE operation. Fortunately, strategies developed for cyclic sorption-enhanced steam methane reforming [9-22] and sorption-enhanced water-gas-shift [23-25] operations can be taken into consideration. A brief survey of these operation strategies can be found from Table 4-1.

The aim of the work in this section is to find suitable cyclic steady-state operation parameters to produce hydrogen with sufficiently high purity, traces of carbon monoxide less than 30 ppm for fuel cell applications [26]. The development of a mathematical reactor model with two subsections to analyze the SE-SRE reaction is given in the first step. Within the two-subsections, different ratios between the Ni impregnated hydrotalcite catalyst and K-promoted hydrotalcite sorbent are employed. Afterwards, the model is constructed to investigate the whole cyclic process. In addition, reaction conditions and operating parameters have been investigated to improve the overall performance of the process. Finally, the energy analysis of the predicted process for hydrogen production has also been taken into account.

Table 4-1 A survey of cyclic operations developed for sorption enhanced reaction process

Operation Strategy	Conditions						Product		Ref.
	T [K]	p [kPa]	$R_{S/C}$ [mol/mol]	Feedstock	Sorbent	Catalyst	y_{H2} [mol%]	y_{CO} [ppm]	
Pressure swing (4 steps)	723	126-446	6	CH_4	K-HTlc [27]	$Ni/MgAl_2O_4$ [28]	86	33	[17]
Pressure swing with reactive regeneration (5 steps)	673-723						89	28	
Pressure swing (5 steps)	723						~81	<30	[18]
Pressure swing with subsection-controlling strategy (4 steps)	673-763						93	18	[19]
Thermal swing (2 steps)	673-733						~86	<30	[20]
Pressure-thermal swing with multi-section strategy (5 steps)	763-863	150	4	CO	K- HTlc [27] /Na-promoted alumina [29]	$Cu/ZnO/Al_2O_3$	>99	<10	[21]
	673-823	1520-2179					99	~10	[23-25]

Pressure swing (4 steps)	723	126-446	6	CH_4	K-HTlc [27]	$Ni/MgAl_2O_4$ [28]	81	24	[22]
Thermal swing (2 steps)	903-1123	101	5		$CaO/Ca_{12}Al_{14}O_{33}$	Ni-based	>90	n.a.	[9]
Pressure swing (4 steps)	763	35-455	6		K-HTlc [30]	Noble metal/Al_2O_3	94.4	<30	[10]
Concentration swing with pulsing feed (4 steps)	~803	129	3		K-HTlc (PURALOX® MG70)	Rh/CeO_2	97.3	10	[11]
Concentration swing (2 steps)	773	450	6		K-HTlc [31] (PURAL MG61)	$Rh/Ce_aZr_{1-a}O_2$	>99	<95	[12]
Pressure swing (4 steps)	1013-1033	101-202			Li_2CO_3-CaO	Ni-based (NIAP-18-02)	99.8	130	[13]
Thermal swing (2 steps)	923-1123	101	4		CaO/ $Ca_{12}Al_{14}O_{33}$	NiO/Al_2O_3	> 90	n.a.	[14]
Pressure swing (4 steps)	778	101-400			K-HTlc [32]	Ni/Al_2O_3 (Octolyst 1001)	76.4	n.a.	[15]

4.1.2 Process Development

4.1.2.1 Materials for sorption enhanced reforming reaction

Ethanol steam reforming catalyst: Several reaction pathways can occur during the reforming process depending on the catalysts and reaction conditions used [33, 34]. Due to the relatively low cost and good activity compared with other metals [35], nickel-based catalysts is one of the most studied active phases for catalytic SRE process. A previously developed nickel-based catalyst (Ni/HTlc) [8] has been employed in this work. According to previous researches [36, 37], four most important reactions and species involved should be included in the reaction scheme when a nickel-based catalyst is used (Table 4-2).

Table 4-2 Reaction scheme of the ethanol reforming process.

Reactions	Chemical description	ΔH_{298K} [kJ·mol^{-1}]	Number
Ethanol dehydrogenation	$C_2H_6O \leftrightarrow C_2H_4O + H_2$	+68.4	(I)
Acetaldehyde decomposition	$C_2H_4O \leftrightarrow CH_4 + CO$	-18.8	(II)
Methane steam reforming	$CH_4 + H_2O \leftrightarrow CO + 3H_2$	+205.9	(III)
Water-gas-shift	$CO + H_2O \leftrightarrow CO_2 + H_2$	-41.4	(IV)

The rate expressions of reactions are:

Ethanol dehydrogenation
$$r_1 = \frac{k_{ETD} p_{C_2H_6O}}{DEN}\left(1 - \frac{1}{K_{ETD}}\frac{p_{C_2H_4O} p_{H_2}}{p_{C_2H_6O}}\right) \quad (4.1)$$

Acetaldehyde decomposition
$$r_2 = \frac{k_{ACD} p_{C_2H_4O}}{DEN}\left(1 - \frac{1}{K_{ACD}}\frac{p_{CO} p_{CH_4}}{p_{C_2H_4O}}\right) \quad (4.2)$$

Methane steam reforming
$$r_3 = \frac{k_{SMR} p_{H_2O} p_{CH_4}}{DEN^2}\left(1 - \frac{1}{K_{SMR}}\frac{p_{CO} p_{H_2}^3}{p_{H_2O} p_{CH_4}}\right) \quad (4.3)$$

Water-gas-shift
$$r_4 = \frac{k_{WGS} p_{H_2O} p_{CO}}{DEN^2}\left(1 - \frac{1}{K_{WGS}}\frac{p_{CO_2} p_{H_2}}{p_{H_2O} p_{CO}}\right) \quad (4.4)$$

where y_i is the molar fraction of the species in the gas phase, and k_1 to k_4 are the reaction rate constants. At last, K_{ETD}, K_{ACD}, K_{SMR} and K_{WGS} are the equilibrium constants, which can be obtained from thermodynamic data. The denominator (DEN) is given by:

$$DEN = 1 + K_{EtOH} p_{EtOH} + K_{H_2O} p_{H_2O} + K_{CH_4} p_{CH_4} + K_{OH} p_{H_2O} p_{H_2}^{-0.5} + K_{CH_3} p_{CH_4} p_{H_2}^{-0.5} + K_{CO} p_{CO} + K_H p_{H_2}^{0.5} \quad (4.5)$$

where each K_i is the adsorption equilibrium constant of the adsorbed species. Parameters used for the Ni/HTlc catalyst [8] can be found from chapter III (page 147).

High temperature carbon dioxide sorbent: Numerous sorbents have been developed for carbon dioxide capture [38-41]. However, most commonly used physisorbents (zeolites, activated carbons, etc.) may suffer from capacity loss at elevated temperatures. On the other hand, chemisorbents can be used to carry out carbon dioxide adsorption processes at high temperatures. These materials include calcium oxide [42], lithium-based materials [43] and HTlc (also referred as layered double hydroxide, LDH) [27]. Among these materials, HTlc sorbents have fast sorption kinetics, very good cyclic stability and can be easily regenerated due to the weak bonding towards carbon dioxide [44]. On the other hand, very high regeneration temperature and energy consumption are required when lithium-based and calcium oxide-based materials are used as carbon dioxide adsorption materials due to the strong chemisorption. Therefore, lithium-based and calcium oxide-based materials were not used in this work.

The major challenge for HTlc sorbents is to increase the relatively low carbon dioxide adsorption capacity, which can be improved with an alkaline promoter. It can be found in Table 4-1 that K-promoted HTlc sorbents have been employed in most cases. K-HTlc material [45] with promising adsorption and desorption performance at high temperatures has been used as carbon dioxide sorbent in this work. The adsorption isotherm of the material is given by the bi-Langmuir model [32]:

$$q_{CO_2} = q_{\max 1}\frac{K_1 p_{CO_2}}{1+K_1 p_{CO_2}} + q_{\max 2}\frac{K_2 p_{CO_2}}{1+K_2 p_{CO_2}} \quad (4.6)$$

where q_{max} is the maximum capacity for site 1 (physical adsorption) and site 2 (chemical adsorption), respectively. And K_i is given by the Van't Hoff equation:

$$K_1 = k_{01}e^{\frac{-\Delta H_1}{RT}}; K_2 = k_{02}e^{\frac{-\Delta H_2}{RT}} \quad (4.7)$$

where k_{0i} is the pre-exponential factor, ΔH_1 is the enthalpy of the physical adsorption and ΔH_2 is the enthalpy of the chemical adsorption. The parameters involved in the adsorption isotherm and kinetic of the sorbent material [45] can be found from chapter III (page 172).

4.1.2.2 Arrangement within the column

Among the works published, many pairs of catalyst-sorbent systems have been developed in SERP. Two typical configurations can be found: alternate layers of catalyst and sorbent; or uniform mixture of the two materials. By packing the bed with several layers of catalyst and sorbent sequentially, the column is just a combination of several reactors and adsorbers in series, and the arrangement can affect the overall performance [46]. Rawadieh and Gomes [22] compared different layered systems, they found that a well-mixed configuration can produce higher hydrogen purity with lower carbon monoxide content compared to other layered configurations, which is in agreement with the result found by Lu and Rodrigues [47]. However, in practice it is very difficult to obtain such a well-mixed catalyst-sorbent system due to the differences in particle size, shape and density of the materials. Alternatively, recent studies found that a homogenous mixture can be achieved by impregnating the sorbent material with an active phase [7, 48-53].

On the basis of the homogeneously packed column, the subsection-controlling strategy [19, 20] and a similar multi-section column concept [54] are proposed to improve the performance of the sorption-enhanced reaction. By using different packing ratios of sorbent/catalyst and wall temperature in each section, the concentration of impurity can be decreased further in the produced gas. As a result,

additional degree of freedom can be obtained for flexible operation [54]. Therefore, a column with two subsections and homogeneously packed with Ni/HTlc catalyst and K-HTlc sorbent has been developed and used for SE-SRE process.

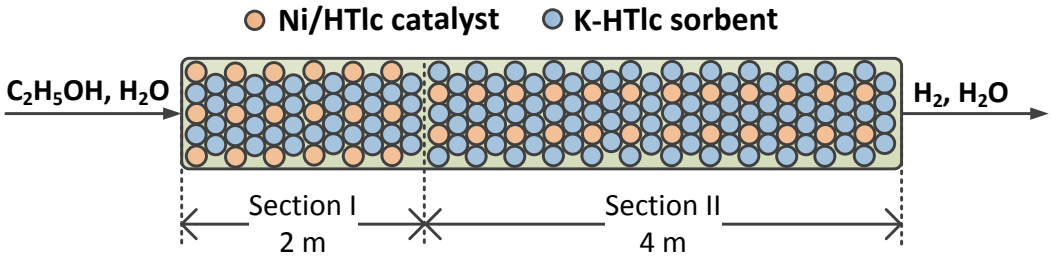

Figure 4-1 Scheme of the fixed-bed reactor developed with two subsections for cyclic SE-SRE process.

A scheme of the reactor is shown in Figure 4-1. In the inlet zone of the column (subsection I), the SRE reaction is more intensive with a high reaction rate, so it is packed with more catalyst than that in subsection II. In subsection II, the sorption-enhanced reaction becomes dominant, and the reforming reaction rate is slower than in subsection I, therefore more adsorbent can be packed in this section. The detailed parameters for the reactor column and subsections can be found in Table 4-3. It has been found that promising reaction performance can be achieved within a short first subsection [54], which is around 2 m in this work. Therefore, the use of a longer second subsection (4 m) is found to be favorable rather than increase the length of the first section where ethanol dehydrogenation and acetaldehyde decomposition reactions dominantly occurs.

Table 4-3 Parameters used for the reactor column and subsections.

Reactor		
Parameter	Unit	Values
l_c	[m]	6
r_c	[m]	$1.25 \cdot 10^{-2}$
l_w	[m]	$1 \cdot 10^{-2}$
ε_c	[m^3 m^{-3}]	0.5
U	[W m^{-2} K^{-1}]	71
c_{pw}	[J kg^{-1} K^{-1}]	500
ρ_w	[kg m^{-3}]	7750
ρ_c	[kg m^{-3}]	900
c_{ps}	[J kg^{-1} K^{-1}]	835
h_f	[W $m^{-2}K^{-1}$]	80.7
k_f	[m^2 s^{-1}]	$1.03 \cdot 10^{-1}$
d_p	[m]	$2 \cdot 10^{-3}$
h_w	[W m^{-2} K^{-1}]	55.0
R	[J K^{-1} mol^{-1}]	8.31
Subsections		
l_1	[m]	2
l_2	[m]	4
m_{cat}/m_{sorb1}	[kg kg^{-1}]	1:2
m_{cat}/m_{sorb2}	[kg kg^{-1}]	1:4

4.1.2.3 Operation strategy

The schematic diagram of cyclic configuration of the process is presented in Figure 4-2. Each cycle of the overall SE-SRE process can be carried out with four steps: sorption-enhanced reaction with ethanol and steam in the feed at high pressure; the rinse of the column with steam to remove the residual products within the gas phase

with a pressure decrease; the regeneration of the carbon dioxide adsorbent by steam at low pressure; and finally the purge of the column with hydrogen gas and steam with a pressure increase occurs before the next cycle.

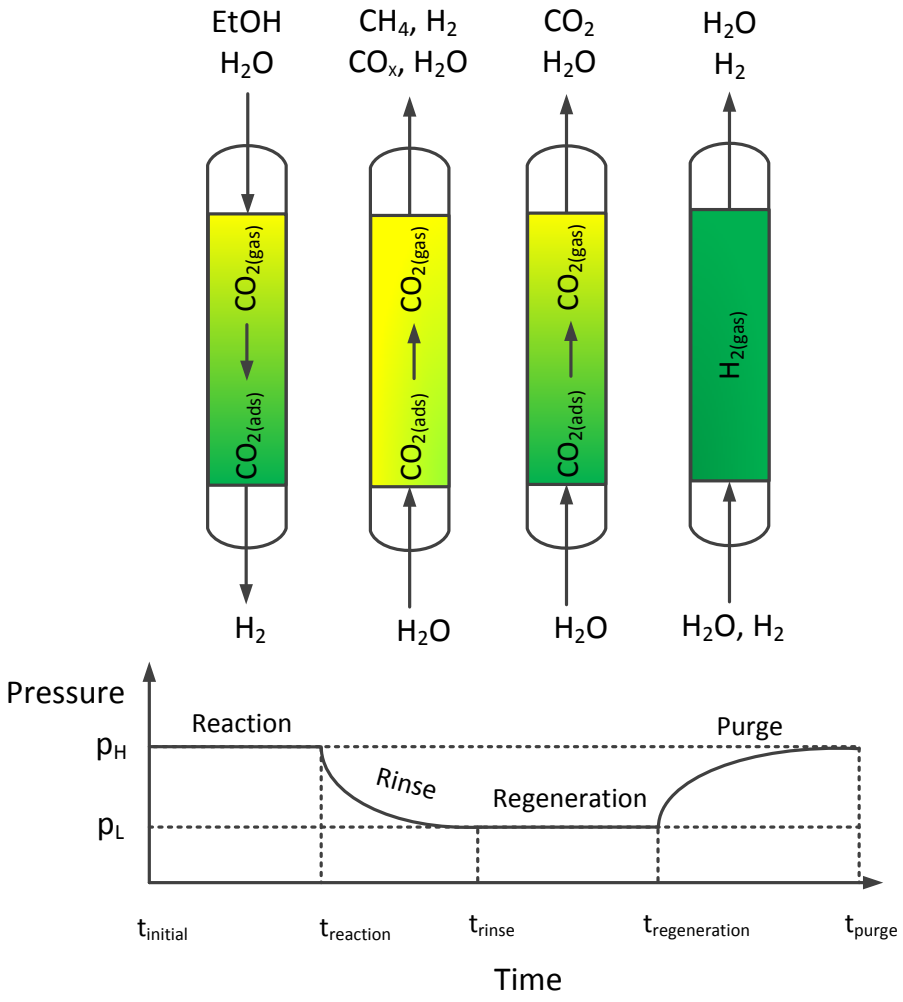

Figure 4-2 Operation scheme of the SE-SRE cyclic process: sorption-enhanced reaction; rinse; regeneration; and product purge.

The detailed operating parameters of the cyclic SE-SRE process, the initial and boundary conditions for different steps are given in Table 4-4.

Table 4-4 Initial and boundary conditions for different steps.

Initial conditions		
$\bar{q}_{CO_2}(\bar{z})=0,\ \bar{C}_{i,sorb}(\bar{z})=0,\ y_{H_2}(\bar{z})=1, T(\bar{z})=T_s(\bar{z})=T_w(\bar{z})=T_{feed}=T_{furnace}$		
Boundary conditions		
Steps	z = 0	z = l_c
	$\frac{\varepsilon_c D_z}{u}\frac{\partial y_i}{\partial z}\Big\|_{z+} = y_i\|_{z-} - y_i\|_{z+}$	$\frac{\partial y_i}{\partial z}\Big\|_{z-} = 0$
Reaction	$u_0 = \frac{Q}{A_{col}}, Q = \frac{RT_{feed}}{p_0}\sum_i \dot{n}_{i,0}$	$\frac{\partial T}{\partial z}\Big\|_{z-} = 0$
	$\frac{\lambda}{u}\frac{\partial T}{\partial z}\Big\|_{z+} = C_t C_p T\|_{z-} - C_t C_p T\|_{z+}$	$p_{z=l_c} = 304kPa$
	$\frac{\partial y_i}{\partial z}\Big\|_{z+} = 0$	$\frac{\varepsilon_c D_{ax}}{u}\frac{\partial y_i}{\partial z}\Big\|_{z-} = y_i\|_{z+} - y_i\|_{z-}$
Rinse	$\frac{\partial T}{\partial z}\Big\|_{z+} = 0$	$u_0 = -\frac{Q}{A_{col}}, Q = \frac{RT_{feed}}{p_0}\sum_i \dot{n}_{i,0}$
	$p_{z=0} = 101kPa$	$\frac{\lambda}{u}\frac{\partial T}{\partial z}\Big\|_{z-} = C_t C_p T\|_{z+} - C_t C_p T\|_{z-}$
	$\frac{\partial y_i}{\partial z}\Big\|_{z+} = 0$	$\frac{\varepsilon_c D_{ax}}{u}\frac{\partial y_i}{\partial z}\Big\|_{z-} = y_i\|_{z+} - y_i\|_{z-}$
Regeneration	$\frac{\partial T}{\partial z}\Big\|_{z+} = 0$	$u_0 = -\frac{Q}{A_{col}}, Q = \frac{RT_{feed}}{p_0}\sum_i \dot{n}_{i,0}$
	$p_{z=0} = 101kPa$	$\frac{\lambda}{u}\frac{\partial T}{\partial z}\Big\|_{z-} = C_t C_p T\|_{z+} - C_t C_p T\|_{z-}$
	$\frac{\partial y_i}{\partial z}\Big\|_{z+} = 0$	$\frac{\varepsilon_c D_{ax}}{u}\frac{\partial y_i}{\partial z}\Big\|_{z-} = y_i\|_{z+} - y_i\|_{z-}$
Purge	$\frac{\partial T}{\partial z}\Big\|_{z+} = 0$	$u_0 = -\frac{Q}{A_{col}}, Q = \frac{RT_{feed}}{p_0}\sum_i \dot{n}_{i,0}$
	$p_{z=0} = 304kPa$	$\frac{\lambda}{u}\frac{\partial T}{\partial z}\Big\|_{z-} = C_t C_p T\|_{z+} - C_t C_p T\|_{z-}$

4.1.2.4 Performance Assessment

To assess the performance of the SE-SRE process, the hydrogen purity [mol %] and the carbon monoxide content [ppm] during the first sorption enhanced reaction step are employed as follows:

$$H_2\ purity\left[mol\%\right]=\frac{\int_{t_{initial}}^{t_{reaction}}\dot{n}_{H_2}dt}{\int_{t_{initial}}^{t_{reaction}}\left(\dot{n}_{CO}+\dot{n}_{CO_2}+\dot{n}_{H_2}+\dot{n}_{CH_4}\right)dt}\times 100,$$
$$CO\ content\left[ppm\right]=\frac{\int_{t_{initial}}^{t_{reaction}}\dot{n}_{CO}dt}{\int_{t_{initial}}^{t_{reaction}}\left(\dot{n}_{CO}+\dot{n}_{CO_2}+\dot{n}_{H_2}+\dot{n}_{CH_4}\right)dt}\times 10^6 \quad (4.8)$$

where $\dot{n}_i$ is the molar flow rate of the compound i at the outlet during the sorption enhanced step. While the hydrogen yield [mol %] during the reaction and carbon dioxide yield [mol %] during the regeneration step are calculated by:

$$H_2\ yield\left[mol\%\right]=\frac{\int_{t_{initial}}^{t_{reaction}}\dot{n}_{H_2}dt-\int_{t_{regeneration}}^{t_{purge}}\dot{n}_{H_2,0}dt}{6\int_{t_{initial}}^{t_{reaction}}\dot{n}_{EtOH,0}dt}\times 100,$$
$$CO_2\ yield\left[mol\%\right]=\frac{\int_{t_{rinse}}^{t_{regeneration}}\dot{n}_{CO_2}dt}{2\int_{t_{initial}}^{t_{reaction}}\dot{n}_{EtOH,0}dt}\times 100 \quad (4.9)$$

where $\dot{n}_{EtOH,0}$ represents the molar flow rate of the ethanol reactant during the sorption enhanced reaction step. Finally, the amounts of the hydrogen and carbon dioxide produced in a cycle are calculated by:

$$H_2\ produced\left[mol\cdot kg^{-1}\right]=\frac{\int_{t_{initial}}^{t_{reaction}}\dot{n}_{H_2}dt-\int_{t_{regeneration}}^{t_{purge}}\dot{n}_{H_2,0}dt}{m_{cat}+m_{sorb}},$$
$$CO_2\ produced\left[mol\cdot kg^{-1}\right]=\frac{\int_{t_{rinse}}^{t_{regeneration}}\dot{n}_{CO_2}dt}{m_{cat}+m_{sorb}} \quad (4.10)$$

where $\dot{n}_{H_2,0}$ is the molar flow rate of hydrogen in the feed during the purge step, and m_{cat} and m_{sorb} are the weight of the catalyst and sorbent materials, respectively.

The energy balance of the hydrogen production process is an important issue for the economic evaluation. Therefore, thermal efficiency has been employed to evaluate

the energy feasibility of the process. In this work, thermal efficiency evaluation method is developed from the model proposed by He et al. [55]. For hydrogen production from ethanol, the thermal efficiency of the process can be calculated by:

$$\eta_{SE-SRE} = \frac{n_{H_2} LHV_{H_2}}{n_{EtOH,0} LHV_{EtOH} + Q_{input} + n_{mix,0} \Delta H_{latent}} \tag{4.11}$$

where n_{H2} is the molar amount of hydrogen collected at outlet, $n_{EtOH,0}$ and $n_{mix,0}$ are the molar amounts of ethanol and feed stream used, respectively. ΔH_{latent} is the latent energy of the feed stream, and LHV_{H2} (244 kJ/mol) and LHV_{EtOH} (1329.8 kJ/mol) are the lower heating value of hydrogen and ethanol. Q_{input} is the energy input, which is calculated from the enthalpy change due to reaction and adsorption:

$$Q_{input} = H_{out}(T) - H_{in}(T) = \sum_i \dot{n}_i H_i(T) - \sum_i \dot{n}_{i,0} H_i(T) + \Delta H_{reg} \tag{4.12}$$

where $H_{out}(T)$ and $H_{in}(T)$ are the enthalpies of the inlet and outlet streams from the reactor at temperature T, and ΔH_{reg} is the heat required for carbon dioxide regeneration. The enthalpy of the inlet and outlet stream depends on the enthalpy of each species i under operating conditions, the amount of each species fed into the column, and obtained from the outlet.

4.1.3 Mathematical Modeling

The mathematical model adopted for the cyclic SE-SRE process is developed from mass, energy and momentum balances, including the following assumptions:

- Axial dispersed plug flow, momentum balance is simplified by the Ergun equation;
- Ideal gas behavior;
- No mass, velocity or heat variations in the radial direction of the column;
- The column porosity, cross sectional area are constant along the column;
- Carbon dioxide is the only species adsorbed on the sorbent material [56].

Based on the above assumptions, the following governing equations and the corresponding initial conditions and general boundary conditions for the SE-SRE process are derived. The overall mass balance equation in the fixed-bed is:

$$\varepsilon_c \frac{\partial C_i}{\partial t} = \varepsilon_c \frac{\partial}{\partial z}\left(D_{ax} C_t \frac{\partial y_i}{\partial z} \right) - \frac{\partial (u C_i)}{\partial z} + (1-\varepsilon_c)\alpha\rho_c \sum_{j=1}^{n} \nu_{j,i} r_j - (1-\varepsilon_c)\frac{a_p(1-\alpha)k_f}{Bi+1}\left(C_i - \bar{C}_{i,sorb}\right) \tag{4.13}$$

where C_i is the gas-phase concentration, D_{ax} is the axial dispersion coefficient, u is the superficial gas velocity, ε_c is the column porosity. ρ_c is the solid density within the column, where the density of catalyst and sorbent is assumed as the same due to the relativity low metal loadings. α is the volume fraction of catalyst, α = 1/3 in subsection I and 1/5 in subsection II. $\upsilon_{j,i}$ is the stoichiometric number of species i in reaction j, r_j is the reaction rate of reaction j, a_p is the specific area of pellet, k_f is the film mass transfer resistance, Bi is the Biot number, $\bar{C}_{i,sorb}$ is the averaged concentration in the adsorbent, t is the time, and z is the axial coordinate.

The mass transfer from the gas phase to the macropores in the adsorbent is given by:

$$\frac{\partial \bar{C}_{i,sorb}}{\partial t} = \frac{15 D_p}{r_p^2}\frac{Bi}{Bi+1}\left(C_i - \bar{C}_{i,sorb}\right) - \frac{\rho_c}{\varepsilon_p}\frac{\partial \bar{q}_i}{\partial t} \tag{4.14}$$

where $\bar{q}_i$ represents the average adsorbed species concentration in the pellet, D_p is the pore diffusivity, r_p is the radius of pellet, ε_p is the porosity of the adsorbent.

Since carbon dioxide is the only species adsorbed, the mass balance for the adsorbed carbon dioxide in the sorbent can be expressed by:

$$\frac{\partial \bar{q}_{CO_2}}{\partial t} = \frac{15 D_{\mu,CO_2}}{r_{crystal}^2}\left(q_{eq,CO_2} - \bar{q}_{CO_2}\right) \tag{4.15}$$

where $D_{\mu,CO2}$ is the crystal diffusivity, $r_{crystal}$ is the crystal radius and $q_{CO_2,eq}$ is the carbon dioxide adsorbed concentration in the equilibrium state.

The momentum balance in the fixed bed is given by Ergun equation as:

$$-\frac{\partial p}{\partial z} = \frac{150\mu_g(1-\varepsilon_c)^2}{\varepsilon_c^3 d_p^2}u + \frac{1.75(1-\varepsilon_c)\rho_g}{\varepsilon_c^3 d_p}|u|u \tag{4.16}$$

where d_p is the diameter of the adsorbent, μ_g and ρ_g are the bulk gas mixture viscosity and density, respectively. The total pressure p is given by:

$$p = C_t RT \tag{4.17}$$

where $C_t = \sum C_i$ is the total concentration, T is the gas temperature and R is the ideal gas constant.

The energy balance includes three phase (gas, solid, and column wall). The energy balance for gas phase in the fixed-bed is given by:

$$\begin{aligned}\varepsilon_c C_t C_v \frac{\partial T}{\partial t} = \frac{\partial}{\partial z}\left(\lambda \frac{\partial T}{\partial z}\right) - uC_t C_p \frac{\partial T}{\partial z} + \varepsilon_c RT \frac{\partial C_t}{\partial t} \\ -\left(1-\varepsilon_c\right) a h_f \left(T - T_s\right) - \frac{2h_w}{r_c}\left(T - T_w\right)\end{aligned} \tag{4.18}$$

where C_v and C_p are the specific molar heat at constant volume and the specific molar heat at constant pressure of the gas mixture, respectively. λ is the axial heat dispersion coefficient, h_f is the film heat transfer coefficient, h_w is the film heat transfer coefficient between the gas phase and the wall. r_c is the radius of the column and T_w is the temperature of the wall.

The solid phase energy balance in the fixed bed is expressed by:

$$\begin{aligned}\left[\varepsilon_p C_{v,ads} \bar{C}_{t,sorb} + \left(1-\varepsilon_p\right)\rho_c C_{ps}\right]\frac{\partial T_s}{\partial t} = a h_f \left(T - T_s\right) + \varepsilon_p RT_s \frac{\partial \bar{C}_{t,sorb}}{\partial t} \\ + \rho_c \left[\sum_{j=1}^{4} R_j \left(-\Delta H_j\right) + \frac{\partial \bar{q}_{CO_2}}{\partial t}\left(-\Delta H_{ads}\right)\right]\end{aligned} \tag{4.19}$$

where $C_{v,ads}$ is the molar specific heat in the adsorbed phase at constant volume, $\bar{C}_{t,sorb}$ is the average total gas concentration within the adsorbent, C_{ps} is the particle specific heat at constant pressure, R_j and ΔH_j are the reaction rate and reaction enthalpy of reaction j, respectively. ΔH_{ads} is the isosteric heat of adsorption.

Finally, the energy balance for the column wall is given by:

$$\rho_w C_{pw} \frac{\partial T_w}{\partial t} = \frac{2r_c}{l_w\left(2r_c + l_w\right)} h_w \left(T - T_w\right) - \frac{2U\left(T_w - T_{furnace}\right)}{\left[\left(2r_c + l_w\right)\ln\left(\frac{r_c + l_w}{r_c}\right)\right]} \tag{4.20}$$

where ρ_w and C_{pw} are the density and the specific heat of the column wall (stainless steel), respectively. l_w is the thickness of the column wall, $T_{furnace}$ is the temperature of

the furnace and U is the overall heat transfer coefficient between the column wall and the external air in the furnace.

The values of transport parameters are calculated with the following correlations: axial mass and heat dispersion coefficients and the mass transfer and heat convective coefficient are estimated using the Wakao and Funazkri correlations [57]. The internal convective heat transfer coefficient between gas and the column wall is calculated with the Wasch and Froment correlation [58]. On the other hand, properties of the gas mixture, such as density, viscosity, and molar specific heat are obtained according to Poling et al. [59]. The molar specific heat of the adsorbed gas is assumed to be equal to the molar specific heat in the gas phase.

The mathematical model consists of partial differential equations which are solved by gPROMS software (PSE Enterprise, London, UK). The discretization method for the spatial domain in the column is the orthogonal collocation with finite elements method (OCFEM) with 200 intervals and the order of approximation is 3. The set of ordinary and algebraic equations obtained by OCFEM discretization are integrated with the DASOLV solver, and a value of 10^{-5} for absolute tolerance.

4.1.4 Results and Discussions

4.1.4.1 Sorption enhanced steam reforming of ethanol

In order to probe feasible operation regions to fulfill carbon monoxide free and high purity hydrogen production, the effects of reaction conditions on the performance of SE-SRE reaction have been investigated. The evolution adjustments are performed sequentially with the following route: steam-to-carbon molar ratio, operating pressure and residence time. It must be pointed out that the temperature applied in this study is fixed at 773 K, where the reforming catalyst can achieve a high activity [8] and avoiding the irreversible HTlc structure destruction [60].

Effect of steam-to-carbon ratio: Most of the previous SRE investigations were performed with a stoichiometric steam-to-carbon molar ratio ($R_{S/C}$) of 1.5 in the feed [33, 34, 61]. However, high ratios up to 10.5 [62] can also be used, since the crude

bio-ethanol contains 14 vol. % ethanol has an $R_{S/C}$ around 10. Both thermodynamic analyses [63-65] and experimental studies [6, 36, 66] found that the use of high feeding $R_{S/C}$ can help to generate hydrogen with higher purity, while carbon monoxide and carbon formation are suppressed at the same time. Several $R_{S/C}$ (0.5, 1.5, 3, 5 and 10) that have been used among previous studies are tested, the pressure is kept at 101.33 kPa and the feed gas velocity was $u_0 = 0.1$ m·s^{-1}, corresponding to a residence time of 60 s in a column with $l_c = 6$ m.

The dynamic behavior of the hydrogen and carbon monoxide molar fractions under different $R_{S/C}$ conditions are given in Figure 4-3a. It can be found that by increasing the $R_{S/C}$ from 0.5 to 3 enhances the average hydrogen purity in the transient sorption enhanced regime from ~ 50 mol % to ~ 95 mol %, and the prebreakthrough time rises with the $R_{S/C}$ increase. For fuel cell application, the content of carbon dioxide in hydrogen product should be controlled less than 30 ppm [26]. Therefore, the allowable operation regions under different $R_{S/C}$ conditions are investigated, two constraints (CO content < 30 ppm and H_2 purity > 99 mol %) were imposed to determine the operation window (prebreakthrough time), the results are shown in Figure 4-3b.

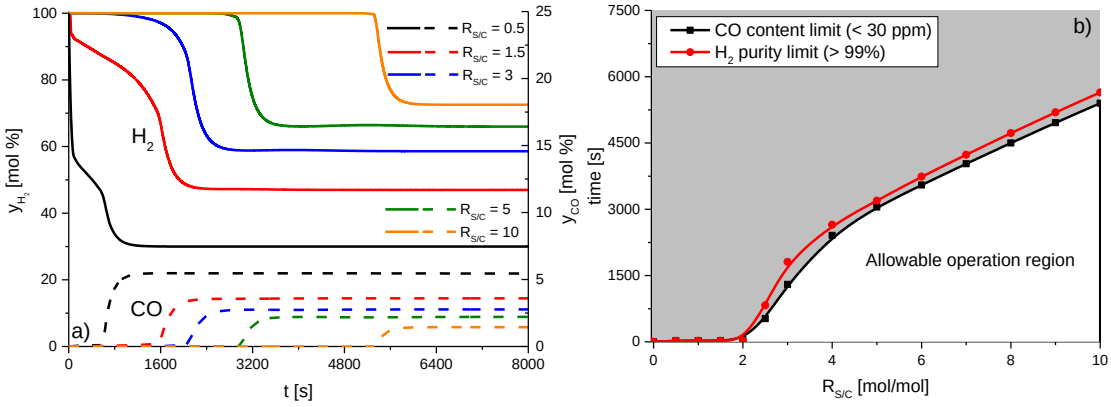

Figure 4-3 The effect of $R_{S/C}$ conditions on dry basis H_2 (solid line) and CO (dashed line) concentrations at the outlet stream (a) and operation window (b) for H_2 purity (> 99 mol %) and CO content (< 30 ppm) limits with $u_0 = 0.1$ m·s^{-1}, p = 101.3 kPa and T = 773 K.

From the Figure 4-3b, we can find that the limits in the operation window for the carbon monoxide content is always smaller than that for hydrogen purity, *i.e.*, to fulfill

carbon monoxide content limit was more difficult than to obtain high purity hydrogen. In addition, it can be found that a feasible operation window to produce carbon monoxide free hydrogen gas cannot be achieved when $R_{S/C}$ is lower than 2, and the operation window is increasing with the $R_{S/C}$ rise. However, we cannot simply come to the conclusion that high $R_{S/C}$ favors the performance of SE-SRE reaction. The effect of $R_{S/C}$ on the amount of hydrogen produced and thermal efficiency within the operation windows is given in Figure 4-4.

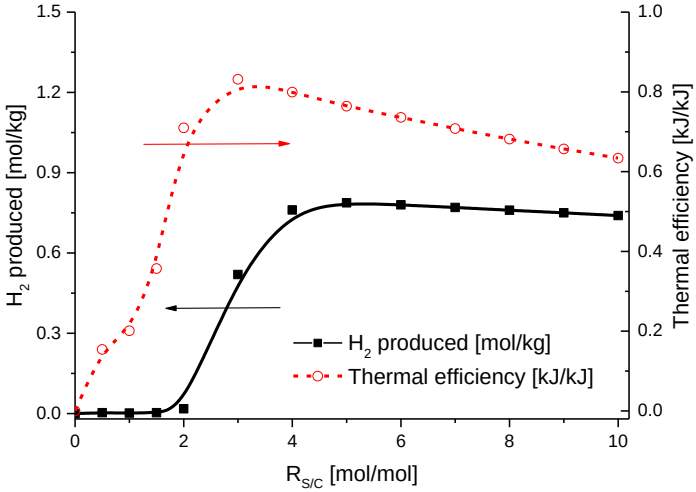

Figure 4-4 Thermal efficiency and H_2 produced with different $R_{S/C}$, u_0 = 0.1 m·s^{-1}, T = 773 K and p = 101.3 kPa conditions

It can be found from Figure 4-4 that both the thermal efficiency and hydrogen productivity are enlarged drastically with the increase of $R_{S/C}$ from 2 to 3 due to the positive effect of high $R_{S/C}$ on SRE reaction performance, which is in agreement with the operation window shown in Figure 4-3b. On the other hand, the hydrogen produced slightly decrease when $R_{S/C}$ is larger than 5. Because the higher $R_{S/C}$ used in the feed, the lower is the obtained partial pressure of carbon dioxide, and simultaneously carbon dioxide adsorption capacity of the material used decreased with the decrease of p_{CO2}. Therefore, the adsorption performance of the material is suppressed by increasing $R_{S/C}$. While both adsorption and reaction performances can affect SE-SRE process. As a result, further increase $R_{S/C}$ from 5 to 10 causes a negative effect on the amount of hydrogen produced, and the overall thermal

efficiency decreased in a linear manner due to the excess latent heat required for the feed stream [55]. The practical $R_{S/C}$ for SE-SRE process can be fairly attributed to a value of around 4 in terms of improving the amount of hydrogen produced and thermal efficiency.

Effect of pressure: A previous report [64] found that the performance of SRE reaction under thermodynamic equilibrium conditions benefit from lower pressure operation, since the overall SRE reaction is a volume increase reaction. However, carbon dioxide adsorption capacity of the sorbent can be enhanced and consequently improve the SE-SRE reaction performance under higher pressure operations. Therefore, the pressure effect on the SE-SRE performance has been investigated at pressure conditions in a range from 101.3 kPa to 506.5 kPa, two constraints CO content < 30 ppm and H_2 purity > 99 mol % are imposed. The results are given in Table 4-5.

Table 4-5 Operating performance in sorption-enhanced reaction step during the operation time under different pressure conditions at 773 K, $u_0 = 0.1$ m·s^{-1} and $R_{S/C} = 4$.

p [kPa]	Operation time [s]	H_2 produced [mol·kg^{-1}]	Thermal efficiency [kJ/kJ]
101.3	2410	0.761	0.799
202.7	1365	0.850	0.795
304.0	930	0.853	0.791
405.3	665	0.804	0.785
506.6	485	0.717	0.778

It could be found that the amount of hydrogen produced during the sorption enhanced reaction step increase when operation pressure increases from 101.3 kPa to 304.0 kPa. In addition, the operation time required can be dramatically reduced from 2410 s to 930 s with only a small loss of thermal efficiency. However, hydrogen

production during the reaction step cannot benefit from further pressure increases from 304.0 kPa to 506.6 kPa. This behavior can be explained with the results presented in Figure 4-5 where the solid lines correspond to the adsorbed carbon dioxide profile along the reactor at the end of each allowable operation region under different pressure conditions and dashed lines represent the equilibrium carbon dioxide adsorption capacity of the sorbent at given conditions.

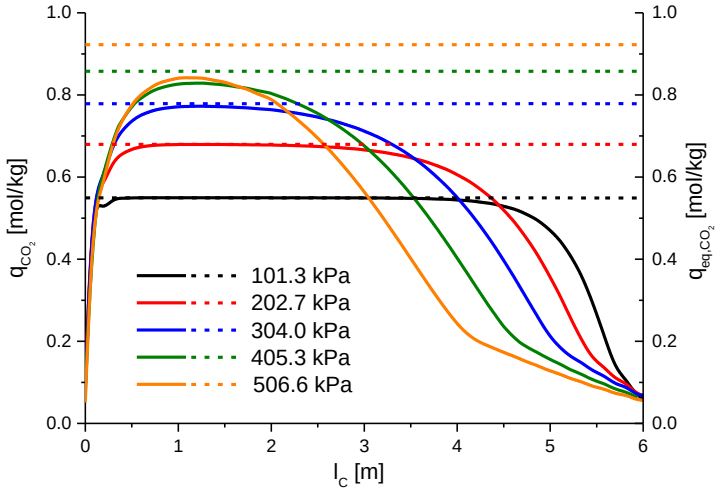

Figure 4-5 CO_2 adsorption performance along the reactor under different pressure conditions, $R_{S/C}$ = 4 and u_0 = 0.1 $m \cdot s^{-1}$. Solid lines correspond to the CO_2 adsorbed along the reactor and dashed lines represent the equilibrium CO_2 adsorption capacity after breakthrough period.

Even though the equilibrium carbon dioxide adsorption capacity along the reactor can be enhanced with increased pressure conditions as shown in Figure 4-5, the additional carbon dioxide adsorption capacity has not been fully used within the operation time due to the kinetic limitation [15] (caused by the intra-particle diffusion resistance) of the sorbent material. Therefore, an operation pressure of 304.0 kPa is employed for further studies where the highest hydrogen production and carbon dioxide adsorption performance can be achieved.

Effect of the feed gas velocity: The feed gas velocity is a key operation parameter for SE-SRE. Figure 4-6 shows the concentration profiles on dry-basis of hydrogen and

carbon monoxide with several different feed gas velocity conditions, the operation pressure is kept at 304.0 kPa and $R_{S/C}$ is 4.

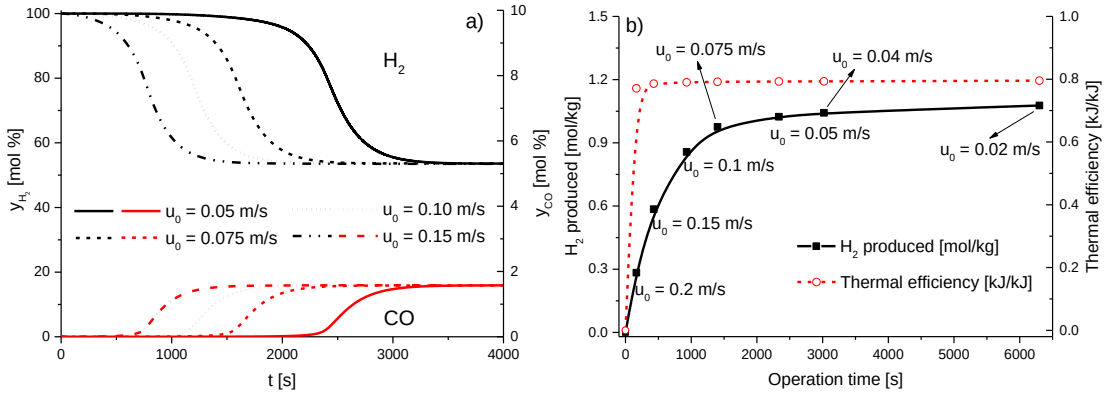

Figure 4-6 The effect of feed gas velocity on dry basis H_2 (black) and CO (red) concentrations at outlet stream (a); and the amount of H_2 produced and thermal efficiency (b). p = 304.0 kPa, T = 773 K and $R_{S/C}$ = 4

It can be found from Figure 4-6a that higher residence time can give longer pre-breakthrough periods. However, decrease the feed gas velocity results in a longer operation time to obtain the required amount of hydrogen. The relationship between the operation times, which depends on the feed gas velocity, with the performance of SE-SRE has been investigated. Figure 4-6b shows the amount of hydrogen produced and thermal efficiency under different operation times; these operation times (from left to right) correspond to u_0 = 0.2, 0.15, 0.1, 0.075, 0.05, 0.04 and 0.02 $m \cdot s^{-1}$. The operation pressure is kept at 304.0 kPa and $R_{S/C}$ is 4.

As shown in Figure 4-6b, we can find that decreasing the feed gas velocity (increasing the time for operation) resulted in an enhancement for the amount of hydrogen produced and thermal efficiency. However, this enhancement became insignificant after 1405 s (corresponding to u_0 = 0.075 $m \cdot s^{-1}$). In addition, a much longer operation time will be required to obtain the same amount of hydrogen, when a lower feed gas velocity has been used. As a result, a feed gas velocity of 0.075 $m \cdot s^{-1}$ is employed to improve the hydrogen production and thermal efficiency within a practical operation time.

On the other hand, the performance of a single-section column system (with the same amount of catalyst and sorbent) has been compared with the results obtained from the column with two subsections, the reaction conditions are T = 773 K, p = 304 kPa, u_0 = 0.075 m/s and $R_{S/C}$ = 4. It is found that the prebreakthrough period (CO content < 30 ppm and H_2 purity > 99 mol %) of the single-section column is shorter than (1290 s vs. 1405 s) the results from the column with two-subsections. As a result, the hydrogen produced from the single-section column (0.89 mol) is lower than that from the column with two-subsections (0.97 mol). These results are in a good agreement with the results found by Jang et al. [54] .

4.1.4.2 Other operation steps in a cyclic operation

Rinse step: In order to achieve a cyclic operation, the saturated carbon dioxide adsorbent should be regenerated before the following cycle. The rinse step followed the sorption-enhanced reaction step first. The column is depressurized from 304.0 kPa to atmospheric pressure by switching the feed to pure steam (counter currently) at atmospheric pressure. Even lower pressures has not been employed, because the use of a vacuum pump and sub-atmospheric steam will be the cost intensive [21].

During this period, only steam is introduced into the column and the feeding molar flow rate has been kept the same as in the reaction step. It is found that the pressure at the outlet of the reactor dropped rapidly to 101.3 kPa within 90 s. The outlet stream consisted of interspace gas in the column and some desorbed carbon dioxide, the concentrations of hydrogen, carbon monoxide and methane first decreases and then increases during the initial several seconds. Because the change of pressure decreases concentrations of the produces, and increases the outlet gas velocity at the same time to flush higher amounts of the residual products out of the column. Afterwards, the carbon dioxide molar fraction among the gas phase (dry basis) can be enriched by removing the remaining products within the column. After 90 s, the carbon dioxide molar fraction on the dry basis reached 99 mol % and the pressure along the reactor became atmospheric, the rinse step finished.

Regeneration step: A regeneration step is carried out to desorb the carbon dioxide adsorbent and produce pure carbon dioxide at the same time. It is found that the amount of regeneration steam required for complete desorption should be considered as the key parameter to characterize the efficiency of the regeneration step [24]. Therefore, the effect of the regenerating steam velocity on the regeneration performance has been investigated in this step. The concentration of carbon dioxide at the outlet of the column and the adsorbed carbon dioxide concentration profiles through the column as a function of regeneration time are given in Figure 4-7.

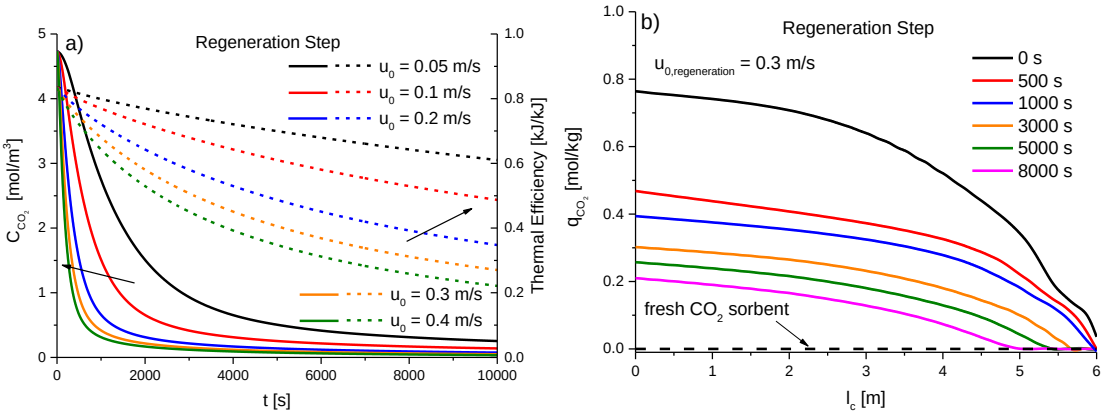

Figure 4-7 The effect of feed steam velocity on the CO_2 desorption performance during the regeneration step (a), and CO_2 loading profiles inside the column during the regeneration step with a feed steam velocity of 0.3 $m \cdot s^{-1}$ (b).

It can be found that the initial carbon dioxide desorption rates under different feed velocities are very rapid, especially when a high u_0 was used. However, the improvement of desorption rates by increasing feed velocities became insignificant when $u_0 \geq 0.3$ $m \cdot s^{-1}$, while thermal efficiency of the regeneration step decreases more rapidly when a high feed velocity has been used. On the other hand, the adsorbed carbon dioxide concentration profiles through the column as a function of regeneration time are given in Figure 4-7b. When the carbon dioxide concentration at the outlet reaches ~ 0.5 $mol \cdot m^{-3}$ and regeneration time over 1000 s, a much slower desorption rate can be observed according to Figure 4-7a. The recovered carbon dioxide adsorption capacity is related with the carbon dioxide concentration at the end of regeneration step. However, the adsorbent is regenerated slowly during this period

due to the strong steepness of the carbon dioxide isotherms in the low-pressure range, while the thermal efficiency for the regeneration step decreases continuously. Therefore, an unavoidable decay in adsorption capacity should be taken into consideration in the cyclic operation to perform the process with a practical regeneration time and thermal efficiency. As a result, a feed velocity of $u_0 = 0.3\ m{\cdot}s^{-1}$ was used in terms of regeneration time, carbon dioxide yield and thermal efficiency.

Purge step: A product purge step is typically added in the cyclic operation to obtain pure product in the following cycle [18]. Besides, an excess steam is required to maintain the HTlc structure in the K-promoted HTlc sorbent material used in this study. Therefore, a gas mixture of hydrogen and steam is fed into the column during this product purge step. At the same time, the column is pressurized from atmospheric pressure back to 304.0 kPa. The total molar flow rate of hydrogen and steam feed had been kept the same as in the reaction step, with $y_{H2} = y_{H2O} = 50$ mol % in the feed stream. By switching the feed steam into a mixture of hydrogen and steam, the remaining carbon dioxide gas within the column can be removed, and hydrogen molar fraction among the gas phase (dry basis) can be enriched. It is found that after 120 s, the hydrogen molar fraction on dry basis reached 99 mol % and the pressure along the reactor became 304.0 kPa, the purge step finishes and the reactor becomes ready for the next operation cycle.

4.1.4.3 Cyclic steady state

In this work, a cyclic steady state (CSS) is considered to be achieved when the difference between profiles of the mole fractions during the last two cycles reaches the following criterion:

$$\left| \frac{y_i^{(n)} - y_i^{(n-1)}}{y_i^{(n)}} \right| \leq 10^{-4} \tag{4.21}$$

where n is the number of the cycles.

A cyclic operation has been tested with reaction time ($t_{reaction}$) 1405 s, rinse time (t_{rinse}) 90 s, regeneration time ($t_{regeneration}$) 3000 s and purge time (t_{purge}) 120 s, with the

operating parameters obtained in previous sections. Figure 4-8a shows the effluent mole fractions of the products from the reactor in the reaction step during the cyclic operation process. Figure 4-8b shows the purity of the hydrogen and carbon monoxide content in the product gas obtained from the reaction step during the cyclic operation process as a function of the cycle number n. The cyclic steady state is obtained after 5 cycles.

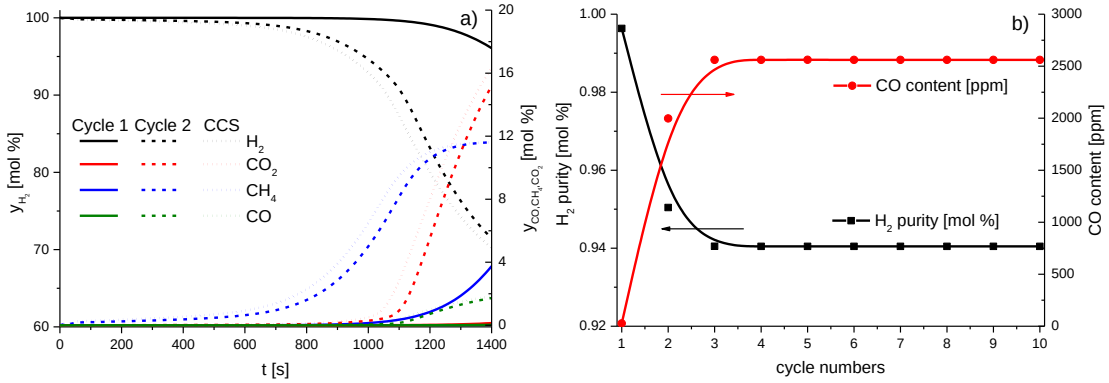

Figure 4-8 Molar fractions of products at the outlet as a function of time in the cyclic operation (a). The H_2 purity and CO content in the produced gas as a function of the number of cycles (b)

It can be found from Figure 4-8a that the purity of hydrogen in the product gas in the first cycle is higher than that in the following cycles since the first cycle uses the fresh sorbent. After regeneration, the recovered adsorption capacity of the adsorbent is smaller than the fresh sample due to the remaining carbon dioxide in the sorbent (Figure 4-7b). As a result, with an increase in the cycle number, the prebreakthrough time decreases due to the decay in the carbon dioxide adsorption capacity. Sorption enhancement becomes no longer effective after the prebreakthrough period, and the molar fractions of by-products methane and carbon monoxide at the outlet stream increases. The purity of the hydrogen decreases with an increase in the cycle number, as shown in Figure 4-8b. At the cyclic steady state, hydrogen-rich product with an average hydrogen purity of around 94 mol % and a carbon monoxide content of 2561 ppm can be obtained.

In order to produce hydrogen product with an acceptable level of carbon monoxide content, the reaction step should be performed within the prebreakthrough period,

which is mainly determined by the cyclic adsorption capacity of the sorbent. The recovered adsorption capacity of the sorbent in the regeneration step is directly related with carbon dioxide concentration at the outlet stream from the column during the regeneration step. Therefore, the effect of carbon dioxide concentration at the outlet stream on the cyclic operation performance has been investigated. In addition, two constraints, CO content < 30 ppm and H_2 purity > 99 mol %, were imposed to determine the prebreakthrough period. The time of reaction step ($t_{reaction}$) is the length of the prebreakthrough period where pure hydrogen (with the constraints) can be obtained, which means that when the carbon monoxide content in the produced gas reached 30 ppm, the reaction step is finished and the time becomes $t_{reaction}$. Therefore, the carbon monoxide content in the obtained hydrogen product is kept as 30 ppm. The rinse and following steps have been carried out after the prebreakthrough period. On the other hand, $t_{regeneration}$ is the time consumed to reach the required carbon dioxide concentration at outlet during the regeneration step.

Table 4-6 The effect of CO_2 concentration at the end of regeneration step on the performance of the cyclic operation at CSS. Operation conditions: T = 773 K, $u_{0,reaction}$ = 0.075 $m \cdot s^{-1}$, $u_{0,regeneration}$ = 0.3 $m \cdot s^{-1}$, $R_{S/C}$ = 4, p_H = 304.0 kPa, p_L = 101.3 kPa, t_{rinse} = 90 s and t_{purge} = 120 s.

C_{CO2} [$mol \cdot m^{-3}$]	$t_{regeneration}$ [s]	$t_{reaction}$ [s]	t_{total} /$t_{reaction}$ [$s \cdot s^{-1}$]	H_2 yield [mol%]	CO_2 yield [mol%]	Thermal efficiency [$kJ \cdot kJ^{-1}$]
0.20	1581	567	4.16	84.1	78.7	0.43
0.25	1033	432	3.88	78.5	75.0	0.45
0.30	702	329	3.77	72.4	72.0	0.46
0.35	483	260	3.67	64.6	68.5	0.47
0.40	382	216	3.75	58.3	65.4	0.48

From the results given in Table 4-6, we can find that the carbon dioxide concentration at the end of regeneration step has a major effect on the performance of

the cyclic operation at CSS. In other words, the higher is the carbon dioxide adsorption capacity recovered during the regeneration step, the longer is prebreakthrough period. As a result, more pure hydrogen and carbon dioxide can be produced with an extended prebreakthrough. However, the thermal efficiency of the overall process decreases due to the longer regeneration period required (more steam used) to recover the carbon dioxide adsorption capacity. In addition, the ratio between the whole cyclic period (reaction, rinse, regeneration and purge steps) and the prebreakthrough period also increases with the decrease of the C_{CO2}. In the design of a cyclic process, for higher ratio between the whole operating period and the prebreakthrough period, more parallel columns are required for a continuous operation, which is a disadvantage in the fixed cost structure. Finally, a carbon dioxide concentration at the end of regeneration step of 0.25 $mol \cdot m^{-3}$ is chosen, where high hydrogen productivity and a relatively low ratio between the whole operating period and the prebreakthrough period can be achieved.

4.1.4.4 Hydrogen production performance

A continuous hydrogen production process was proposed with four columns as can be found in the Figure 4-9, and the operating parameters are listed in Table 4-7. The time of purge step has been increased to 173 s to achieve a ratio between the whole operating period and the prebreakthrough period equal to 4.

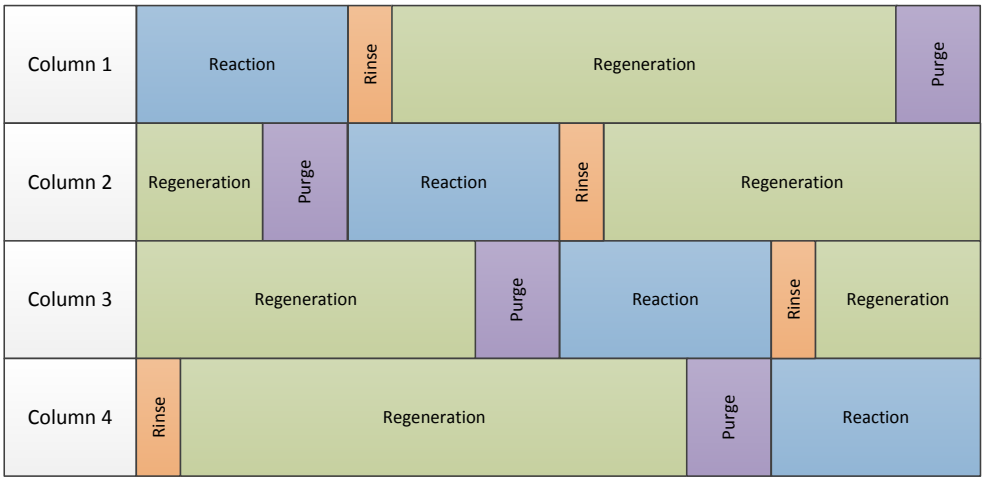

Figure 4-9 A continuous hydrogen production by SE-SRE operating scheme with four columns.

The simulated hydrogen production performance from SE-SRE under CCS is given in Table 4-8. Around 0.25 mol·kg^{-1} of fuel cell grade hydrogen (CO content = 30 ppm) and 0.08 mol·kg^{-1} of pure carbon dioxide as by-product can be produced in within one column in a cycle. The yields of hydrogen and carbon dioxide are 78.5 % and 75 %, respectively, which are much higher than the results (hydrogen yield 38.3 % and carbon dioxide yield 51.0 %) from a conversional SRE process under the same reaction conditions. The thermal efficiency (0.45) of SE-SRE is much higher than the thermal efficiency (0.33) of the SRE process. In addition, numerous separation steps are required to produce pure hydrogen and carbon dioxide from the product gas mixture obtained from a conversional reforming process, which can greatly increase the cost and reduce the efficiency. Therefore, comparing with a conversional reforming process, better energy efficiency can be achieved with SE-SRE.

Table 4-7 Operating parameters and reaction conditions used for CSS test.

Parameters	unit	values
T	K	773
p_H	kPa	304.0
p_L	kPa	101.3
$R_{S/C}$	mol·mol^{-1}	4
$t_{reaction}$	s	432
t_{rinse}	s	90
$t_{regeneration}$	s	1033
t_{purge}	s	173
$u_{0,reaction}$	m·s^{-1}	0.075
$u_{0,regeneration}$	m·s^{-1}	0.3
$\dot{n}_{H_2O,0,rinse}$	mol·s^{-1}	$1.0 \cdot 10^{-3}$
$\dot{n}_{H_2O,0,purge}$	mol·s^{-1}	$3.47 \cdot 10^{-4}$
$\dot{n}_{H_2,0,purge}$	mol·s^{-1}	$3.47 \cdot 10^{-4}$

Another important result of the SE-SRE process simulations described by Table 4-8 is the steam cost. It can be found that in an operating cycle, the steam required per unit amount of H_2 produced is 8.44 $mol_{H2O}mol^{-1}_{H2}$ (corresponds to 0.076 $ton_{steam}kg^{-1}_{H2}$) which is a little less than the result (9.86 $mol_{H2O}mol^{-1}_{H2}$) obtained from a thermal-swing sorption-enhanced water-gas-shift H_2 production process by Lee et al. [24]. The cost of this steam at 773 K with an energy cost of $3.6 per MMBtu (13/9/2013) [67] is \$ 11.5 ton^{-1}_{steam} according to the steam cost calculator [68]. Therefore, the cost of steam is \$ 0.87 per kilogram of hydrogen, which is around 38 % of the cost goal by DOE (\$ 2.3 per kg) for hydrogen production from biomass-derived renewable liquids in 2020 [69]. It must be noted that in this preliminary design, the excess energy from the outlet stream has not been recycled. Therefore, the steam cost of SE-SRE can be reduced even further. However, the energy cost is only part of the overall cost of in a whole reforming process [70]. A more detailed economic analysis of this design will be investigated in the following section.

Table 4-8 Comparison of hydrogen production performance for SRE process and cyclic SE-SRE process under CSS. Operating conditions: T = 773 K, $u_{0,reaction}$ = 0.075 $m{\cdot}s^{-1}$, $u_{0,regeneration}$ = 0.3 $m{\cdot}s^{-1}$ $R_{S/C}$ = 4, p_H = 304.0 kPa, p_L = 101.3 kPa, $t_{reaction}$ = 432 s, t_{rinse} = 90 s, $t_{regeneration}$ = 1033 s, t_{purge} = 173 s.

Operation	H_2 yield [mol %]	CO_2 yield [mol %]	H_2 produced [$mol{\cdot}kg^{-1}$]	CO_2 produced [$mol{\cdot}kg^{-1}$]	Thermal efficiency [$kJ{\cdot}kJ^{-1}$]	H_2 productivity [$mol{\cdot}kg^{-1}h^{-1}$]	Steam requirement [mol_{H2O}/mol_{H2}]
SE-SRE[1]	78.5	75.0	0.245	0.078	0.45	0.51	8.44
SRE[2]	38.3	51.0	0.446	0.188	0.33	0.93	3.74

[1] The performance of SE-SRE is based on the total amount of material (catalyst+ adsorbent) and refers to hydrogen product with 30 ppm carbon monoxide content.

[2] The performance of SRE is based on the amount of catalyst only, and PSA separation units are required after SRE to meet the purity requirement (hydrogen purity > 99 mol %, carbon monoxide content < 30 ppm).

4.1.5 Conclusion

In this section, a four-step pressure swing sorption-enhanced steam reforming of ethanol (SE-SRE) process has been investigated by numerical analysis to produce fuel-cell-grade hydrogen and pure carbon dioxide at the same time.

A reactor column with two subsections is developed, within the two-subsections, two different volumetric ratios (1:2 and 1:4) between the Ni impregnated hydrotalcite catalyst and K-promoted hydrotalcite sorbent are employed. Various reaction conditions and operating parameters have been tested to improve the hydrogen production performance of the cyclic SE-SRE operation process. According to the results obtained with the most promising operating parameters, it is possible to produce the hydrogen product with purity higher than 99 mol % with carbon monoxide content of 30 ppm by conducting the SE-SRE and carbon dioxide sorbent regeneration in a cyclic manner at 773 K and the swing pressure from 101.3 to 304 kPa. In addition, better SE-SRE performance has been found by the use of a column within the two-subsections compared with a single section column.

This cyclic SE-SRE operation process is predicted to have a great potential to produce fuel-cell-grade hydrogen with a high yield (78.5 %) and thermal efficiency (0.45). At the same time, pure carbon dioxide can also be obtained as a by-product with a yield of 75 %. The cost of steam ($ 0.87 per kilogram of hydrogen) for the SE-SRE have also been calculated, which can be reduced even further by recycling the exhaust energy. As a result, further extension to a multi-bed continuous hydrogen production process will be performed in the next section.

4.2 SE-SRE Operation in a Multi-Column System

4.2.1 Introduction

One-dimensional fixed-bed adsorptive reactor is the most widely used model for SERP in previous researches [15, 17-20, 49, 56, 71-73], where multifunctional reactors with small diameters have been employed. However, Rostrup-Nielsen [74] found that the radial temperature difference within a typical industrial reformer can be as large as 40 K, and the effect of energy transport in the radial direction might be significant when a large diameter reactor is used [69, 75-78]. An accurate design of SE-SRE reactors requires an adequate description of the reaction/adsorption kinetics, momentum, heat and mass transfer processes, and a two-dimensional model has therefore been developed in this study, where the size of reactors is intended to be enlarged from experimental to industrial scale.

The aim of this research is to find a feasible multi-bed SE-SRE process for continuous hydrogen production with traces of carbon monoxide (no more than 30 ppm) in the high purity product for fuel cell applications [26]. The development and validation of a two-dimensional heterogeneous fixed-bed adsorptive reactor model can be found in this section. Afterwards, the reaction dynamics of SE-SRE in an industrial scale reactor has been reported. In addition, a seven-step pressure swing process with four reactors has been constructed to investigate the overall cyclic operation performance for continuous hydrogen production. Finally, a brief energy analysis of the predicted process for hydrogen production has also been taken into consideration.

4.2.2 Adsorptive Reactor Modeling and Validation

The development of a fixed-bed adsorptive reactor model is described in this section. Based on the reactor geometry illustrated in Figure 4-10, differential mass, energy, and momentum balances are considered as a function of time (t), axial (z) and radial (r) positions inside the reactor with 2-D cylindrical coordinates system, including the following assumptions:

- Ideal gas behavior;
- The column porosity, cross sectional area and solid density are constant;
- Carbon dioxide is the only species adsorbed on the sorbent material [56].

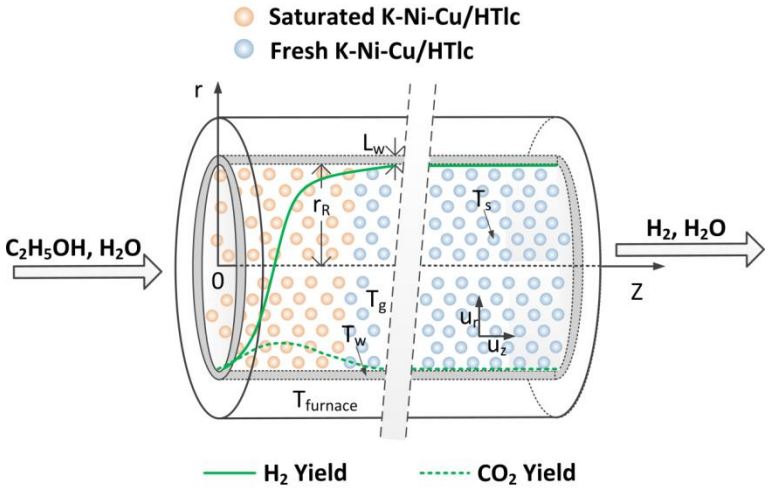

Figure 4-10 Scheme of the 2-D fixed-bed adsorptive reactor.

4.2.2.1 Governing equations

The overall mass balance equation for the gas phase in the reactor can be expressed as:

$$\varepsilon_c \frac{\partial C_i}{\partial t} = \varepsilon_c \frac{\partial}{\partial z}\left(D_z C_t \frac{\partial y_i}{\partial z} \right) + \frac{\varepsilon_c}{r} \frac{\partial}{\partial r}\left(D_r C_t \frac{\partial y_i}{\partial r} r \right) - \frac{\partial (u_z C_i)}{\partial z} - \frac{1}{r} \frac{\partial (u_r C_i r)}{\partial r} - (1-\varepsilon_c) \frac{k_f a_p}{Bi+1} \left(C_i - \bar{C}_{p,i} \right) \tag{4.22}$$

where C_i and $\bar{C}_{p,i}$ are the concentration of species i in the bulk gas phase and the average concentration of gas phase within the pellet ($mol \cdot m^{-3}$). D_z and D_r are the axial and radial effective mass diffusivity ($m^2 \cdot s^{-1}$), respectively. u_z and u_r are the velocities of gas phase in the axial and radial direction ($m \cdot s^{-1}$), respectively. ε_c is the column porosity. a_p is the surface area to volume ratio of the pellet (m^{-1}), Bi is the Biot number and k_f is the film mass transfer coefficient ($m \cdot s^{-1}$).

The mass balance equation for the pellet can be obtained from:

$$\varepsilon_p \frac{\partial \bar{C}_{p,i}}{\partial t} = \varepsilon_p \frac{15 D_p}{r_p^2} \frac{Bi}{Bi+1} \left(C_i - \bar{C}_{p,i} \right) + \rho_p \left(\sum_{j=1}^{n} \nu_{j,i} \bar{r}_j - \frac{\partial \bar{q}_i}{\partial t} \right) \tag{4.23}$$

Where ε_p is the porosity of the solid, D_p is the pore diffusivity ($m^2 \cdot s^{-1}$) and r_p is the radius of the pellet (m), ρ_p is the density of the pellet ($kg_{pellet} \cdot m^{-3}$). $\upsilon_{j,i}$ is the stoichiometric number of species i in reaction j. $\bar{r}_j$ is the average reaction rate of reaction j in the pellet ($mol \cdot kg_{pellet}^{-1} \cdot s^{-1}$), which is calculated according to the reaction kinetics. Since only CO_2 is the only species adsorbed on the sorbent material, $\bar{q}_i$ represents the average adsorbed CO_2 concentration in the sorbent ($mol \cdot kg_{pellet}^{-1}$), which is calculated by:

$$\frac{\partial \bar{q}_{CO_2}}{\partial t} = k_{CO_2}\left(q_{eq,CO_2} - \bar{q}_{CO_2}\right) \tag{4.24}$$

Where $q_{CO_2,eq}$ is the CO_2 adsorbed concentration at equilibrium state ($mol \cdot kg_{pellet}^{-1}$), which can be obtained from the Langmuir CO_2 adsorption isotherms and k_{CO2} is the CO_2 mass transfer coefficient (s^{-1}).

The momentum balances in both axial and radial direction are given by Ergun equation as:

$$-\frac{\partial p}{\partial z} = \frac{150\mu_g(1-\varepsilon_c)^2}{\varepsilon_c^3 d_p^2}u_z + \frac{1.75(1-\varepsilon_c)\rho_g}{\varepsilon_c^3 d_p}|u_z|u_z$$

$$-\frac{\partial p}{\partial r} = \frac{150\mu_g(1-\varepsilon_c)^2}{\varepsilon_c^3 d_p^2}u_r + \frac{1.75(1-\varepsilon_c)\rho_g}{\varepsilon_c^3 d_p}|u_r|u_r \tag{4.25}$$

where d_p is the diameter of the pellet (m), μ_g and ρ_g are the bulk gas mixture viscosity (Pa s) and density ($kg_{gas} \cdot m^{-3}$), respectively. The total pressure p (Pa) is given by:

$$p = C_t R T_g \tag{4.26}$$

where $C_t = \sum C_i$ is the total concentration in the gas phase ($mol_{gas} \cdot m^{-3}$), T_g is the gas temperature (K) and R is the ideal gas constant ($J \cdot mol^{-1} \cdot K^{-1}$).

The energy balance includes three phases (bulk gas phase, pellet, and column wall). The energy balance for gas phases in the reactor is given by:

$$\varepsilon_c C_t C_v \frac{\partial T_g}{\partial t} = -\left(-D_z \varepsilon_c \frac{\partial C_t}{\partial z} + u_z C_t\right)C_p \frac{\partial T_g}{\partial z} - \left(-D_r \varepsilon_c \frac{\partial C_t}{\partial r} + u_r C_t\right)C_p \frac{\partial T_g}{\partial r} + k_g \varepsilon_c \frac{\partial}{\partial z}\left(\frac{\partial T_g}{\partial z}\right)$$
$$+\frac{k_g \varepsilon_c}{r}\frac{\partial}{\partial r}\left(\frac{r\partial T_g}{\partial r}\right) + \varepsilon_c R T_g \frac{\partial C_t}{\partial t} - (1-\varepsilon_c)a_p h\left(T_g - T_p\right) - \frac{2h_w}{r_R}\left(T_g - T_w\right) \tag{4.27}$$

where C_v and C_p are the specific molar heat at constant volume and the specific molar heat at constant pressure of the gas mixture ($J \cdot mol^{-1} \cdot K^{-1}$), respectively. k_g is the thermal conductivity of the gas phase ($W \cdot m^{-1} \cdot K^{-1}$), while h is interstitial convection coefficient between the solid and gas phases ($W \cdot m^{-2} \cdot K^{-1}$), h_w is the heat transfer coefficient between the gas phase and the wall ($W \cdot m^{-2} \cdot K^{-1}$). r_R is the radius of the reactor (m) and T_w is the temperature of the wall (K).

On the other hand, the energy balance within the hybrid material pellet can be expressed by:

$$\begin{aligned}\left(\varepsilon_p C_v \bar{C}_{t,p} + \rho_p C_{pp} + \rho_p \bar{q}_{CO_2} C_{v,ads}\right)\frac{\partial T_p}{\partial t} &= k_p\left(1-\varepsilon_p\right)\left[\frac{\partial}{\partial z}\left(\frac{\partial T_p}{\partial z}\right)+\frac{\partial}{r\partial r}\left(\frac{r\partial T_p}{\partial r}\right)\right] \\ +a_p h\left(T_g - T_p\right)+\varepsilon_p RT_p\frac{\partial \bar{C}_{t,p}}{\partial t}+\rho_p&\left[\sum_{j=1}^{4}\bar{r}_j\left(-\Delta H_j\right)+\frac{\partial \bar{q}_{CO_2}}{\partial t}\left(-\Delta H_{ads}\right)\right]\end{aligned} \tag{4.28}$$

where $C_{v,ads}$ is the molar specific heat in the adsorbed phase at constant volume ($J \cdot mol^{-1} \cdot K^{-1}$), $\bar{C}_{t,p}$ is the average total gas concentration within the pellet ($mol \cdot m_{pellet}^{-3}$), C_{pp} is the pellet specific heat at constant pressure ($J \cdot kg^{-1} \cdot K^{-1}$), and ΔH_j is the reaction enthalpy of reaction j ($J \cdot mol^{-1}$). ΔH_{ads} is the heat of CO_2 adsorption on the pellet ($J \cdot mol^{-1}$).

Finally, the energy exchange of the reactor wall with the surroundings is described by the following equation:

$$\rho_w C_{pw}\frac{\partial T_w}{\partial t} = \frac{2r_R}{l_w\left(2r_R + l_w\right)}h_w\left(T_g - T_w\right) - \frac{2U\left(T_w - T_{furnace}\right)}{\left[\left(2r_R + l_w\right)\ln\left(\frac{r_R + l_w}{r_R}\right)\right]} \tag{4.29}$$

where ρ_w is the density of the column wall ($kg \cdot m^{-3}$), C_{pw} is the specific heat at constant pressure of the column wall ($J \cdot mol^{-1} \cdot K^{-1}$) and l_w is the thickness of the column wall (m). $T_{furnace}$ is temperature within the heating furnace (K) and U is the overall heat transfer coefficient ($W \cdot m^{-2} \cdot K^{-1}$) between the column wall and the external air in the furnace.

In addition, the detailed correlations of the properties of the gas phase, i.e., viscosity, gas thermal conductivity and molecular diffusion are calculated with the local conditions, while the axial and radial dispersion coefficients, mass and heat transfer coefficients are also related with the correlations shown in Table 4-9. The definitions of the symbols used can be found in the notation.

Table 4-9 Calculation of mass and heat transport parameters.

Axial and radial mass dispersion coefficients [76] can be calculated by:

$$\frac{\varepsilon_c D_z}{D_m}=\frac{\varepsilon_c}{\tau}+\frac{1}{2}Sc\,\mathrm{Re},\quad \frac{\varepsilon_c D_r}{D_m}=\frac{\varepsilon_c}{\tau}+\frac{1}{12}Sc\,\mathrm{Re},\quad \tau=8$$

Schmidt, Sherwood, Prandtl, Biot and Reynolds numbers are calculated as follows:

$$Sc=\frac{\mu_g}{\rho_g D_m},\ \mathrm{Re}=\frac{\rho_g u_z d_p}{\mu_g},\mathrm{Pr}=\frac{\mu_g C_{p,m}}{k_g},\mathrm{Bi}=\frac{k_f r_p}{5D_p\varepsilon_p},Sh=\frac{k_f d_p}{D_m}=2+1.1\mathrm{Re}^{0.6}\,Sc^{1/3}$$

Molar heat capacity [59] at constant pressure of species i is obtained by:

$$C_{p,i}=A+Bt+Ct^2+Dt^3+\frac{E}{t^2},t=\frac{T}{1000}$$

Molar heat capacity at constant pressure of the gas mixture is calculated as:

$$C_p=\sum_{i=1}^{n}y_i C_{p,i}$$

The mass heat capacity at constant pressure of species i is calculated as:

$$C_{p,m,i}=\frac{C_{p,i}}{M_i}$$

where M_i is the molecular weight of species i.

The mass heat capacity at constant pressure of the gas mixture is calculated as:

$$C_{p,m}=\frac{\sum_{i=1}^{n}y_i C_{p,i}}{\sum_{i=1}^{n}y_i M_i}$$

Viscosity [59] of the gas species i is calculated according to:

$$\mu_i=2.67\times10^{-6}\frac{\left(M_i T\right)^{0.5}}{\varepsilon_i\Omega_\mu},\quad \Omega_\mu=1.16\left(\frac{\varepsilon_i}{kT}\right)^{0.15}+0.52e^{\frac{-0.77kT}{\varepsilon_i}}+2.16e^{\frac{-2.44kT}{\varepsilon_i}}$$

where ε_i/k is the characteristic Lennard- Jones energy of species i.

The viscosity of the gas mixture is calculated with Wilke method [59]:

$$\mu_g = \sum_{i=1}^{n} \frac{y_i \mu_i}{\sum_{j=1}^{n} y_i \Phi_{ij}} \quad , \quad \Phi_{ij} = \left[8\left(1+\frac{M_i}{M_j} \right) \right]^{-0.5} \left[1+\sqrt{\frac{\mu_i}{\mu_j}} \left(\frac{M_i}{M_j} \right)^{-0.25} \right]^2$$

Thermal conductivity [59] of the gas species i is calculated according to:

$$k_i = \left(C_{p,m,i} + 1.25 \frac{R}{M_i} \right) \mu_i$$

The thermal conductivity of the gas mixture is calculate by:

$$k_g = \sum_{i=1}^{n} \frac{y_i k_i}{\sum_{j=1}^{n} y_i \Phi_{ij}}$$

The density of the gas mixture can be obtained from:

$$\rho_g = \frac{p}{RT} \left(\sum_{i=1}^{n} y_i M_i \right)$$

The molecular diffusivity [59] of the mixture gas is calculated follows:

$$D_m = \sum_{i=1}^{n} D_{m,i} y_i$$

The molecular diffusivity of the gas species i is calculated as follows:

$$D_{m,i} = \frac{1-y_i}{\sum_{j=1}^{n} \frac{y_j}{D_{ij}}}, D_{ij} = \frac{1.18809 \times 10^{-7}}{p \sigma_{ij}^2 \Omega_{ij}} \sqrt{T^3 \left(\frac{1}{M_i} + \frac{1}{M_j} \right)}, \quad \sigma_{ij} = \left(\sigma_i + \sigma_j \right) / 2$$

where σ_i is the characteristic Lennard-Jones length of species i. Ω_{ij} is calculated by:

$$\Omega_{ij} = 1.06 \left(\frac{\varepsilon_{ij}}{kT} \right)^{0.1561} + 0.19 e^{-0.476 \frac{kT}{\varepsilon_{ij}}} + 1.04 e^{-1.53 \frac{kT}{\varepsilon_{ij}}} + 1.76 e^{-3.89 \frac{kT}{\varepsilon_{ij}}}, \varepsilon_{ij} = \sqrt{\varepsilon_i \varepsilon_j}$$

Heat transfer coefficient between gas and wall h_w, and gas and solid h can be described as [58, 79, 80]:

$$h_w = 2.03 \left(\frac{k_g}{2 r_R} \right) \mathrm{Re}^{0.8} \exp\left(-\frac{6 d_p}{2 r_R} \right), \left(\mathrm{Re} = 7600 - 20 \right)$$

$$h_w = 6.15 \left(\frac{k_z^0}{2 r_R} \right), \left(\mathrm{Re} < 20 \right)$$

and $$h = \frac{k_g \left(2 + 1.1 \mathrm{Re}^{0.6} \mathrm{Pr}^{1/3} \right)}{d_p}$$

where k_z^0 in is defined as:

$$k_z^0 = k_g \left\{ \varepsilon_c + \left(1 - \varepsilon_c \right) / \left[0.139 \varepsilon_c - 0.0339 + \frac{2 k_g}{3 k_s} \right] \right\}$$

4.2.2.2 Numerical solution

The mathematical model consists of partial differential equations which are solved by gPROMS software (PSE Enterprise, London, UK). The discretization method for the spatial domain in the column is the orthogonal collocation with finite elements method with 200 and 10 intervals in the axial and radial direction, respectively, and the order of approximation is 2. The set of ordinary and algebraic equations obtained from discretization are integrated with the DASOLV solver, and a value of 10^{-5} for absolute tolerance. The modeling parameters used for the experimental and industrial scale reactor are listed in Table 4-10.

Table 4-10 Parameter of the reactors used in the experiments and simulations.

Parameter	Unit	Values	
		Experimental	Industrial
l_R	[m]	0.2	6
r_R	[m]	$1.65 \cdot 10^{-2}$	0.05
d_p	[m]	$4 \cdot 10^{-5}$	$2 \cdot 10^{-3}$
T_{inlet}	[K]	773	
$T_{furnace}$	[K]	773	
l_w	[m]	$1 \cdot 10^{-2}$	
U	[W m^{-2} K^{-1}]	200	
C_{pw}	[J kg^{-1} K^{-1}]	500	
ρ_w	[kg m^{-3}]	7750	
ρ_p	[kg m^{-3}]	1419	
ε_p	[ ]	0.21	
C_{pp}	[J kg^{-1} K^{-1}]	835	
R	[J K^{-1} mol^{-1}]	8.31	

4.2.2.3 Performance Assessment

To assess the performance of the overall process, the hydrogen purity [mol %] and the carbon monoxide content [ppm] during the reaction step are employed as follows:

$$H_2\ purity\left[mol\%\right]=\frac{\int_0^{t_{reaction}}\dot{n}_{H_2}dt}{\int_0^{t_{reaction}}\left(\dot{n}_{CO}+\dot{n}_{CO_2}+\dot{n}_{H_2}+\dot{n}_{CH_4}\right)dt}\times 100,$$
$$CO\ content\left[ppm\right]=\frac{\int_0^{t_{reaction}}\dot{n}_{CO}dt}{\int_0^{t_{reaction}}\left(\dot{n}_{CO}+\dot{n}_{CO_2}+\dot{n}_{H_2}+\dot{n}_{CH_4}\right)dt}\times 10^6 \quad (4.30)$$

where $\dot{n}_{H_2}$, $\dot{n}_{CO}$, $\dot{n}_{CO_2}$ and $\dot{n}_{CH_4}$ are the molar flow rate of the products in the outlet stream during the reaction step. While the net hydrogen yield [mol %] obtained in a cycle can be calculated by:

$$H_2\ yield\left[mol\%\right]=\frac{\int_0^{t_{reaction}}\dot{n}_{H_2}dt-\int_0^{t_{cycle}}\dot{n}_{H_2,0}dt}{6\int_0^{t_{reaction}}\dot{n}_{EtOH,0}dt}\times 100 \quad (4.31)$$

where $\dot{n}_{H_2,0}$ is the molar flow rate of hydrogen in the feed and $\dot{n}_{EtOH,0}$ represents the molar flow rate of the ethanol reactant during the reaction step. Finally, the net hydrogen productivity of the continuous SE-SRE process can be obtained from:

$$H_2\ productivity\left[mol\cdot kg^{-1}\cdot h^{-1}\right]=\frac{\int_0^{t_{reaction}}\dot{n}_{H_2}dt-\int_0^{t_{cycle}}\dot{n}_{H_2,0}dt}{m_{solid}\cdot t_{cycle}} \quad (4.32)$$

where m_{solid} is the weight of the hybrid material in a reactor and t_{cycle} is the time of a whole cycle.

The thermal efficiency of the hydrogen production process is evaluated by the following equation developed from a previous work [36]:

$$\eta_{SE-SRE}=\frac{n_{H_2}LHV_{H_2}}{n_{EtOH,0}LHV_{EtOH}+Q_{input}-Q_{recovered}} \quad (4.33)$$

where n_{H_2} is the molar amount of H_2 obtained from the outlet stream, $n_{EtOH,0}$ is the molar amount of ethanol used. LHV_{H2} (244 kJ·mol^{-1}) and LHV_{EtOH} (1330 kJ·mol^{-1}) are the lower heating value of hydrogen and ethanol. $Q_{recovered}$ is the energy recovered from the outlet steam-gas mixture by heat exchanger [81], and an average heat

recovery rate of 22 % was used in this study. Q_{input} is the energy input in the system, which is calculated from the enthalpy change due to reaction and adsorption:

$$Q_{input} = n_{mix,0}\Delta H_{latent} + \sum_i n_i H_i(T) - \sum_i n_{i,0} H_i(T) \quad (4.34)$$

where ΔH_{latent} is the latent energy of the inlet stream and $n_{mix,0}$ is the molar amount feed mixture that has been introduced into the reactor. $H_i(T)$ is the enthalpy of the compound i at temperature T. The enthalpy of the inlet and outlet stream depends on the enthalpy of each species i under operating conditions, the amount of each species fed into the column, and obtained from the outlet.

4.2.2.4 Experimental validation

Material: The catalyst and sorbent materials can be integrated with different methods for SERP [47]. Different catalyst-sorbent packing systems have been studied by Rawadieh and Gomes [22]; it was found that a well-mixed catalyst-sorbent configuration can produce hydrogen product with higher purity and lower carbon monoxide content compared to other configurations. However, due to the differences in pellet size, shape and density of the catalyst and sorbent materials, it is difficult to obtain an ideally well mixed catalyst-sorbent system in practice. To achieve an ideal dispersion, hybrid multifunctional materials consisting of sorbent, as support material, and active metals as catalytic phase have been developed in some recent studies [49, 50, 52, 82]. Promising SE-SRE reaction performance was found on the hybrid multifunctional material K-Ni-Cu-HTlc [53] that has been used in this work, where the active phase is the Ni-Cu alloy and the catalyst support K-promoted HTlc is the carbon dioxide sorbent.

The reaction scheme and rate expressions of SRE on the hybrid material can be found from Table 4-11. Where p_i is the pressure of the species i in the solid phase, $k_{ETD,}$ k_{ACD}, k_{SMR} and k_{WGS} are the reaction rate constants. Finally, $K_{ETD,}$ K_{ACD}, K_{SMR} and K_{WGS} are the equilibrium constants, which can be obtained from thermodynamic data. The denominator (DEN) is given by:

$$DEN = 1 + K^*_{EtOH} p_{EtOH} + K^*_{H_2O} p_{H_2O} + K^*_{CH_4} p_{CH_4} + K^*_{OH} p_{H_2O} p_{H_2}^{-0.5} + K^*_{CH_3} p_{CH_4} p_{H_2}^{-0.5} + K^*_{CO} p_{CO} + K^*_{H} p_{H_2}^{0.5} \quad (4.35)$$

where each K_i* represents the adsorption equilibrium constant of the adsorbed species.

Table 4-11 Reaction scheme of ethanol steam reforming.

Reactions	Rate expression
Ethanol dehydrogenation (ETD)	$r_{ETD} = \frac{k_{ETD} p_{C_2H_6O}}{DEN}\left(1 - \frac{1}{K_{ETD}} \frac{p_{C_2H_4O} p_{H_2}}{p_{C_2H_6O}}\right)$
Acetaldehyde decomposition (ACD)	$r_{ACD} = \frac{k_{ACD} p_{C_2H_4O}}{DEN}\left(1 - \frac{1}{K_{ACD}} \frac{p_{CO} p_{CH_4}}{p_{C_2H_4O}}\right)$
Steam methane reforming (SMR)	$r_{SMR} = \frac{k_{SMR} p_{H_2O} p_{CH_4}}{DEN^2}\left(1 - \frac{1}{K_{SMR}} \frac{p_{CO} p_{H_2}^3}{p_{H_2O} p_{CH_4}}\right)$
Water-gas-shift (WGS)	$r_{WGS} = \frac{k_{WGS} p_{H_2O} p_{CO}}{DEN^2}\left(1 - \frac{1}{K_{WGS}} \frac{p_{CO_2} p_{H_2}}{p_{H_2O} p_{CO}}\right)$

On the other hand, the carbon dioxide adsorption isotherm of the material is given by the Langmuir model:

$$q_{CO_2} = q_{\max} \frac{b_{CO_2} p_{CO_2}}{1 + b_{CO_2} p_{CO_2}}, b_{CO_2} = b_{CO_2,0} e^{\frac{-\Delta H_{ads}}{RT}} \quad (4.36)$$

The reaction and adsorption kinetic parameters used for the hybrid multifunctional material are calculated from the experimental data obtained from the work of Cunha et al. [53], which are given in Table 4-12.

Table 4-12 Parameters for the catalytic steam reforming of ethanol process and the CO_2 adsorption process over the hybrid material [53].

Kinetic Parameters		$k_{0,j}$ [mol·kg^{-1}·s^{-1}]	$E_{A,j}$ [kJ/mol]
$k_j(T) = k_{0j} \cdot e^{\frac{-E_{A,j}}{RT}}$	k_1	$1.61 \cdot 10^{1}$	29.1
	k_2	$1.13 \cdot 10^{1}$	22.2
	k_3	$1.27 \cdot 10^{7}$	116.9
	k_4	$8.32 \cdot 10^{4}$	40.0
Adsorption Equilibrium		$K_i^*{}_{(673.15)}$ [mol·kg^{-1}·s^{-1}]	ΔH_i [kJ/mol]
$K_i^*(T) = K_{i\,(673.15K)}^* \cdot e^{\frac{-\Delta H_i}{R}\left(\frac{1}{T}-\frac{1}{673.15}\right)}$	K_{EtOH}*	$9.83 \cdot 10^{0}$	-4.96
	K_{H2O}*	$1.32 \cdot 10^{-1}$	-56.8
	K_{CH4}*	$1.12 \cdot 10^{2}$	-66.8
	K_{OH}*	$1.73 \cdot 10^{-2}$	-53.5
	K_{CH3}*	$1.07 \cdot 10^{-3}$	-66.7
	K_H*	$7.35 \cdot 10^{-7}$	-27.1
	K_{CO}*	$1.48 \cdot 10^{-2}$	-79.5

Parameter	Unit	Values
q_{max}	mol kg^{-1}	1.21
b_{CO2}	Pa^{-1}	$2.11 \cdot 10^{-6}$
ΔH_{ads}	kJ mol^{-1}	-18.7
D_p	m^2 s^{-1}	$3.3 \cdot 10^{-7}$
k_{CO2}	s^{-1}	0.015

Experiments: According to the previous experiments carried out in an fixed-bed adsorptive reactor packed with 45.1 g of the hybrid material, numerical simulations are performed with the following conditions: T = 773 K, P = 101 kPa, $R_{S/C}$ = 5 and different feed flow rates. Comparisons of the product distribution as a function of reaction time from experiment and simulation are depicted in Figure 4-11. In addition, two constraints (dry basis) carbon monoxide content < 30 ppm and hydrogen purity > 99 mol % have been imposed to determine the prebreakthrough period.

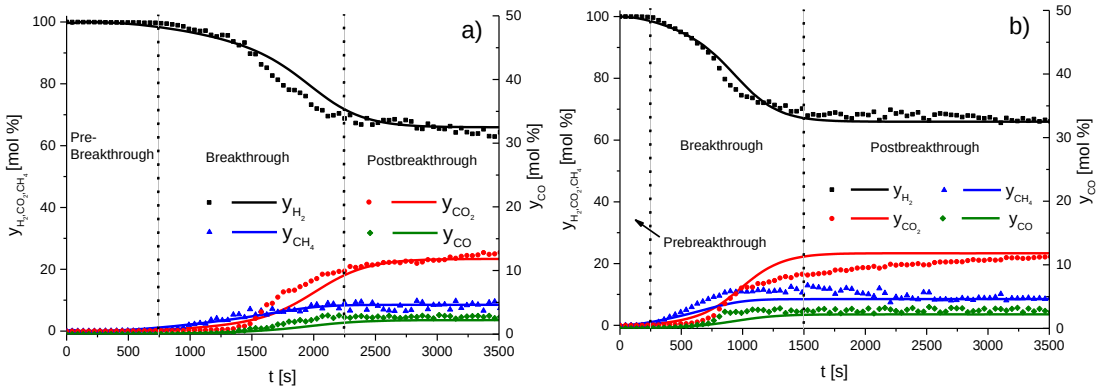

Figure 4-11 Product distributions as a function of time from the experimental reactor with $\dot{n}_0$ = $4 \cdot 10^{-5}$ mol·s^{-1} (a) and $\dot{n}_0$ = $8 \cdot 10^{-5}$ mol·s^{-1} (b). Operating conditions: T = 773 K, P = 101 kPa and $R_{S/C}$ = 5. Symbols correspond to experimental points and lines represent simulated results.

From both experimental and simulation results obtained in Figure 4-11, a prebreakthrough period can be found where high purity hydrogen product can be directly produced from the reactor for around 750 s. On the other hand, it can be found that the carbon dioxide breakthrough period happened between 750 and 2250 s after the start of reaction; the unconverted methane was the most abundant impurity during the prebreakthrough period. After material saturation with carbon dioxide, sorption enhancement became no longer effective and the postbreakthrough period began. The carbon dioxide molar fraction approached a steady value ~ 23 mol % after 2250 s, while both the molar fractions of methane and carbon monoxide also became stable during the post-breakthrough period. On the other hand, experimental and numerical tests performed with higher feed flow rate are shown in Figure 4-11b. A similar behavior can be found and the prebreakthrough period was much shorter than Figure 4-11a due to the higher feeding flow rate. The lines in the graph correspond to the simulated values at the outlet of the reactor, we can find that numerical simulation can successfully describe the experimental points, and the good agreement confirms the validity of the mathematical model proposed for SE-SRE process simulations. Therefore, further study will be carried out in the following section to investigate the SE-SRE dynamics in an industrial scale reactor packed with the hybrid material.

4.2.3 Reactor Dynamics

Since the radial variations in concentration, velocity and temperature within the 2D reactor have been considered in this work, the diameter of the reactor can be increased to the typical industrial conditions without compromising the degree of accuracy. The dynamic behavior of the SE-SRE reaction in a reactor with 6.0 m in length and 0.1 m in diameter has been investigated at 773 K, 304 kPa, a $R_{S/C}$ ratio of 4 and a molar flow rate of 0.05 mol·s^{-1} have been used in the feed. In addition, the porosity of the large reactor packed with the hybrid material can be obtained from the relationship between the radius of the reactor and the radius of the pallet [83]:

$$\varepsilon_c = 0.39 + \frac{1.74}{\left(\frac{r_R}{r_p} + 1.14\right)^2} \tag{4.37}$$

Other parameters of the industrial scale reactor can be found from Table 4-10.

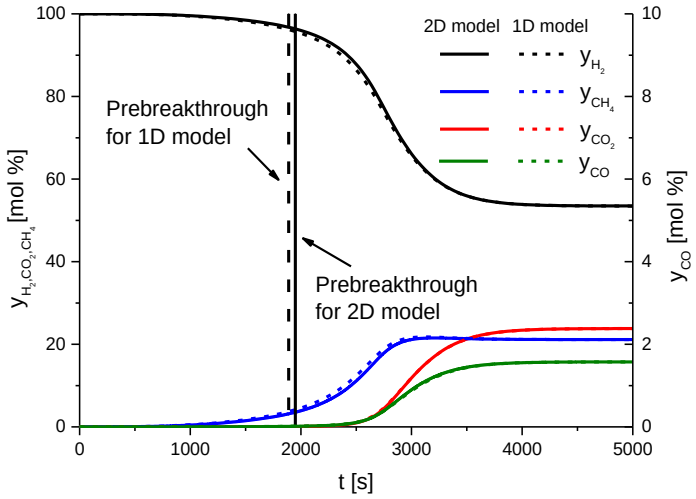

Figure 4-12 A comparison between the product distributions as a function of time obtained from the 1D and 2D model at 773 K, 304 kPa, $R_{S/C}$ = 4 and $\dot{n}_0$ = 0.05 mol·s^{-1}.

Figure 4-12a shows the gas effluent composition (dry basis) of the products as a function of time at the outlet of the reactor. A comparison between the results obtained from a 1D reactor model (without the radial variations) and that from a 2D reactor model has also been included. After the breakthrough period, where the carbon dioxide sorption enhancement became no longer effective and the reactants can only

be converted through the conventional reforming reaction, the distinction between the results obtained from two different models is very small (< 1 %) in this work. The results obtained during postbreakthrough period are in good agreement with the results reported by De Deken et al. [84], they found that the effects of radial variations can be neglected for the hydrogen production from typical industrial reformer.

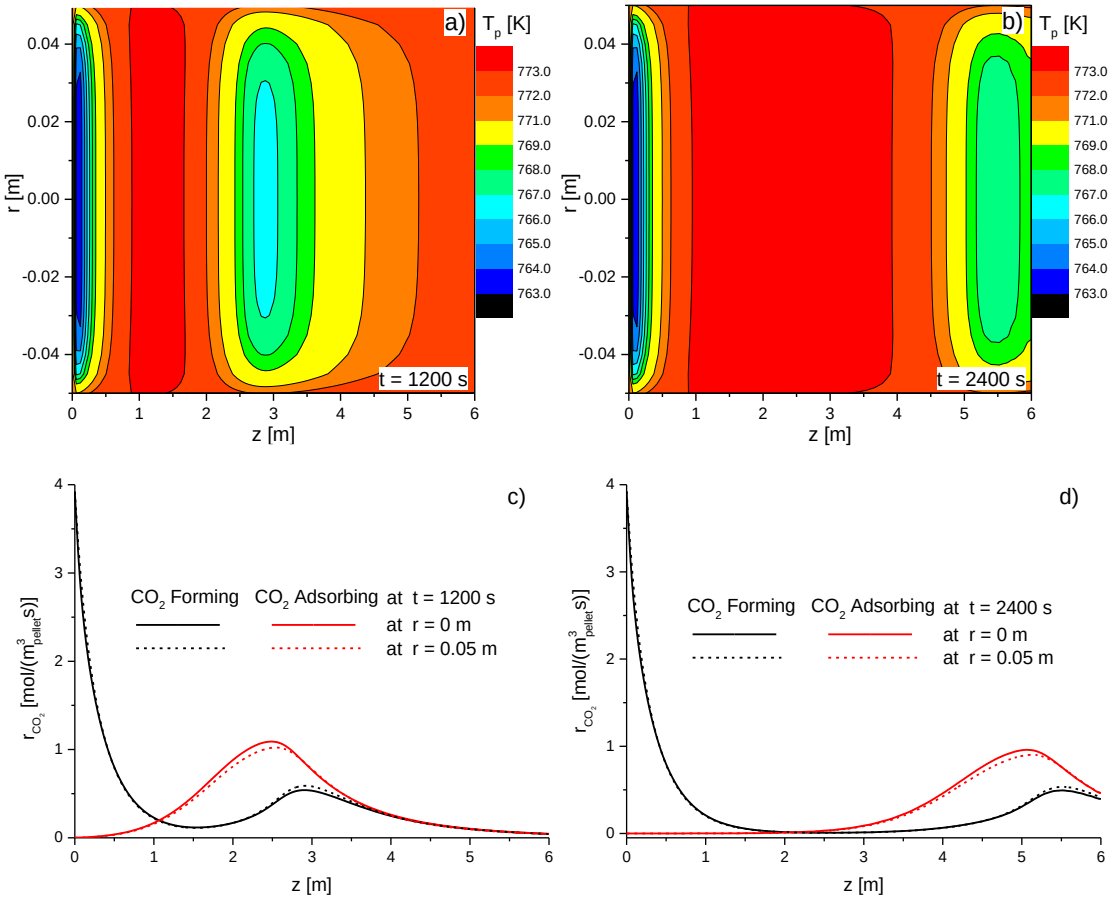

Figure 4-13 The temperature profiles of the pellet and the carbon dioxide production/adsorption rate in the reactor during the SE-SRE reaction at 773 K, 304 kPa, $R_{S/C}$ = 4 and $\dot{n}_0$ = 0.05 mol·s^{-1}.

However, a noticeable difference between the results from 1D and 2D model during the breakthrough period (SE-SRE reaction) can be found. The most abundant impurity in the product gas during the prebreakthrough period is also methane, which is similar to the results from the experiments (Figure 4-11). According to the calculation, hydrogen with purities higher 99 mol % with carbon monoxide content less than 30 ppm can be directly produced from the reactor for 1980 s with a 2D

model, while the length of prebreakthrough becomes 1920 s from the 1D model. The radial variation in temperature might be the reason for this difference, as shown in Figure 4-13.

The temperature profiles of the solid phase and in the reactor at 1200 s and 2400 s were given in Figure 4-13a and b, an oven temperature of 773 K is used to heat the reactor. A sharp temperature decrease can be found in the entrance region of the reactor, which is contributed to the highly endothermic SRE reaction. As a result, at the inlet part of the reactor (about 0 – 0.5 m from Figure 4-13c and d) the production rate of carbon dioxide is very high due to the high SRE reaction rate. After the inlet part of the reactor, a temperature wave front formation can be observed according to the results obtained at different times. It can be found that the temperature front is directly related with the carbon dioxide production rate front by comparing the left figures with the right ones, because the remaining reactants (ethanol) and intermediate products (methane and acetaldehyde) produced in the inlet part of the reactor can be then converted into carbon dioxide and hydrogen through the endothermic reforming reaction in this region, resulting in a carbon dioxide production rate front and a large temperature decrease. Afterwards, the produced carbon dioxide can be adsorbed in the following part of the reactor during the prebreakthrough period (t = 1200 s), resulting in a high purity hydrogen product at the outlet. However, after most of the sorbent in the reactor has been saturated with carbon dioxide, the adsorption rate of carbon dioxide cannot match the production rate (2400 s). The sorption enhancement becomes no longer effective, and a breakthrough of carbon dioxide can be found from the outlet stream after this time (Figure 4-12).

On the other hand, the effect of the radial variation in temperature can also be found from Figure 4-13. The production and adsorption rates of carbon dioxide are quite different at r = 0 m and r = 0.05 m due to the difference of temperature in the radial direction, and the temperature at the surface is always higher than at the center of the reactor, because the effects of temperature on the carbon dioxide production and adsorption are different. For example, the higher temperature favors the

production of carbon dioxide due to the endothermic reforming reaction. However, the adsorption of carbon dioxide on the sorbent is an exothermic process which can be suppressed by the higher temperature. In addition, a large temperature gradient between the surface and the center can be found and this gradient in the radial direction is nonlinear (Figure 4-13). Therefore, the use of an average temperature (without the radial direction, r) at each axial position for the numerical calculation may not be sufficiently accurate for the simulation of a SE-SRE process.

As a result, a noticeable difference in the lengths of prebreakthrough periods obtained from 1D (1920 s) and 2D model (1980 s) can be found, while the prebreakthrough period where desired product can be produced is of great importance in the design of a cyclic SE-SRE process. In a continuous cyclic process, the number of parallel columns is directly related with the time of reaction step (within the prebreakthrough period) and the time required preparing the reactor for the next cycle after reaction step. Therefore, the 2D reactor model will be employed in the following process design section to achieve a higher degree of accuracy.

4.2.4 Process Design

The simulation of a cyclic pressure swing process has been constructed. The schematic diagram of a seven steps cyclic configuration of the process is presented in Figure 4-14. Each cycle of the overall SE-SRE process can be carried out with seven steps:

- Reaction (cocurrently to feed). Sorption-enhanced reaction with reactants in the feed at high pressure (p_H);
- Rinse (counter-currently to feed). Rinse the column with steam (y_{H2O} = 100 % and $\dot{n}_{rinse}$ = 0.01 mol·s^{-1}) to remove the residual reactants and products within the gas phase at high pressure (p_H);
- Pressure Equalization (EQ, counter-currently to feed). This step is performed by connecting two reactors at different pressure levels into contact to save energy. The high pressure of the reactor can be reduced;

- Blowdown (BD, counter-currently to feed). After the pressure equalization step, the pressure of the column is reduced to atmospheric pressure (p_L);
- Regeneration (counter-currently to feed). Regenerating the carbon dioaixe sorbent by steam (y_{H2O} = 100 %) at low pressure (p_L);
- Received Pressure Equalization (REQ, cocurrently to feed). The high pressure stream from one reactor on the pressure equalization step is recycled to another reactor to increase pressure and reduce compression energy.
- Purge (counter-currently to feed). Purging the column with hydrogen and steam gas-mixture (y_{H2} = y_{H2O} = 50 % and $\dot{n}_{purge}$ = 0.01 mol·s^{-1}) with a pressure increase to high pressure (p_H) before the next cycle.

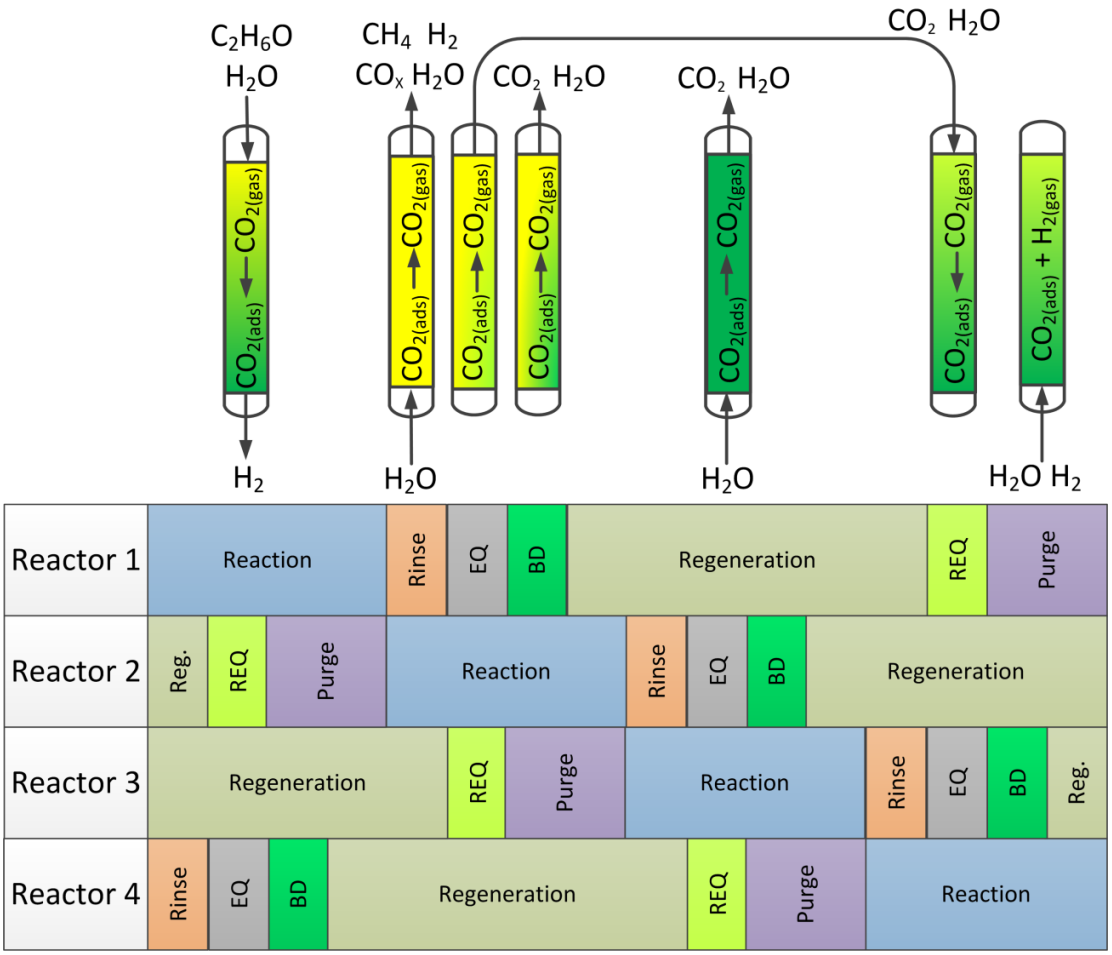

Figure 4-14 Four-reactor scheme and cyclic configurations employed SE-SRE process.

Table 4-13 Initial and boundary conditions for different steps.

Initial conditions				
$\bar{q}_{CO_2}(\bar{z},\bar{r})=0,\ \bar{C}_{p,i}(\bar{z},\bar{r})=0,\ y_{H_2}(\bar{z},\bar{r})=1,\ T_g(\bar{z},\bar{r})=T_p(\bar{z},\bar{r})=T_w(\bar{z},\bar{r})=T_{inlet}=T_{furnace}$				
Boundary conditions				
Steps	z = 0	z = l_R	r = 0	r = r_R
Reaction	$\frac{\varepsilon_c D_z}{u_z}\left.\frac{\partial y_i}{\partial z}\right\|_{z+} = y_i\|_{z-} - y_i\|_{z+}$	$\left.\frac{\partial y_i}{\partial z}\right\|_{z-} = 0$	$\left.\frac{\partial y_i}{\partial r}\right\|_{r+} = 0$	$\left.\frac{\partial y_i}{\partial r}\right\|_{r-} = 0$
	$u_z = \frac{RT_{inlet}}{p\pi r_R^2}\sum_i \dot{n}_{i,0}$	$\left.\frac{\partial T_g}{\partial z}\right\|_{z-} = 0$	$\left.\frac{\partial T_g}{\partial r}\right\|_{r+} = 0$	$\frac{k_g}{h_w}\left.\frac{\partial T_g}{\partial r}\right\|_{r-} = T_w\|_{r-} - T_g\|_{r-}$
	$\frac{k_g}{u_z}\left.\frac{\partial T_g}{\partial z}\right\|_{z+} = C_t C_p T_g\|_{z-} - C_t C_p T_g\|_{z+}$	$p_{z=l_R} = 304\ kPa$	$\left.\frac{\partial p}{\partial r}\right\|_{r+} = 0$	$\left.\frac{\partial p}{\partial r}\right\|_{r-} = 0$
Rinse	$\left.\frac{\partial y_i}{\partial z}\right\|_{z+} = 0$	$\frac{\varepsilon_c D_z}{u_z}\left.\frac{\partial y_i}{\partial z}\right\|_{z-} = y_i\|_{z+} - y_i\|_{z-}$	$\left.\frac{\partial y_i}{\partial r}\right\|_{r+} = 0$	$\left.\frac{\partial y_i}{\partial r}\right\|_{r-} = 0$
	$\left.\frac{\partial T_g}{\partial z}\right\|_{z+} = 0$	$u_z = -\frac{RT_{inlet}}{p\pi r_R^2}\sum_i \dot{n}_{i,0}$	$\left.\frac{\partial T_g}{\partial r}\right\|_{r+} = 0$	$\frac{k_g}{h_w}\left.\frac{\partial T_g}{\partial r}\right\|_{r-} = T_w\|_{r-} - T_g\|_{r-}$

	$p_{z=0} = 304\ kPa$	$\left.\frac{k_g}{u_z}\frac{\partial T_g}{\partial z}\right\|_{z-} = C_t C_p T_g\|_{z+} - C_t C_p T_g\|_{z-}$	$\left.\frac{\partial p}{\partial r}\right\|_{r+} = 0$	$\left.\frac{\partial p}{\partial r}\right\|_{r-} = 0$
EQ	$\left.\frac{\partial y_i}{\partial z}\right\|_{z+} = 0$	$\left.\frac{\partial y_i}{\partial z}\right\|_{z-} = 0$	$\left.\frac{\partial y_i}{\partial r}\right\|_{r+} = 0$	$\left.\frac{\partial y_i}{\partial r}\right\|_{r-} = 0$
	$\left.\frac{\partial T_g}{\partial z}\right\|_{z+} = 0$	$u_z = 0$	$\left.\frac{\partial T_g}{\partial r}\right\|_{r+} = 0$	$\left.\frac{k_g}{h_w}\frac{\partial T_g}{\partial r}\right\|_{r-} = T_w\|_{r-} - T_g\|_{r-}$
	$p_{z=0} = p'_{z=l_R}$	$\left.\frac{\partial T_g}{\partial z}\right\|_{z-} = 0$	$\left.\frac{\partial p}{\partial r}\right\|_{r+} = 0$	$\left.\frac{\partial p}{\partial r}\right\|_{r-} = 0$
BD	$\left.\frac{\partial y_i}{\partial z}\right\|_{z+} = 0$	$\left.\frac{\partial y_i}{\partial z}\right\|_{z-} = 0$	$\left.\frac{\partial y_i}{\partial r}\right\|_{r+} = 0$	$\left.\frac{\partial y_i}{\partial r}\right\|_{r-} = 0$
	$\left.\frac{\partial T_g}{\partial z}\right\|_{z+} = 0$	$u_z = 0$	$\left.\frac{\partial T_g}{\partial r}\right\|_{r+} = 0$	$\left.\frac{k_g}{h_w}\frac{\partial T_g}{\partial r}\right\|_{r-} = T_w\|_{r-} - T_g\|_{r-}$
	$p_{z=0} = 101\ kPa$	$\left.\frac{\partial T_g}{\partial z}\right\|_{z-} = 0$	$\left.\frac{\partial p}{\partial r}\right\|_{r+} = 0$	$\left.\frac{\partial p}{\partial r}\right\|_{r-} = 0$
Regeneration	$\left.\frac{\partial y_i}{\partial z}\right\|_{z+} = 0$	$\left.\frac{\varepsilon_c D_z}{u_z}\frac{\partial y_i}{\partial z}\right\|_{z-} = y_i\|_{z+} - y_i\|_{z-}$	$\left.\frac{\partial y_i}{\partial r}\right\|_{r+} = 0$	$\left.\frac{\partial y_i}{\partial r}\right\|_{r-} = 0$

	$\left.\frac{\partial T_g}{\partial z}\right\|_{z+} = 0$	$u_z = -\frac{RT_{inlet}}{p\pi r_R^2}\sum_i \dot{n}_{i,0}$	$\left.\frac{\partial T_g}{\partial r}\right\|_{r+} = 0$	$\left.\frac{k_g}{h_w}\frac{\partial T_g}{\partial r}\right\|_{r-} = T_w\|_{r-} - T_g\|_{r-}$
	$p_{z=0} = 101\,kPa$	$\left.\frac{k_g}{u_z}\frac{\partial T_g}{\partial z}\right\|_{z-} = C_t C_p T_g\|_{z+} - C_t C_p T_g\|_{z-}$	$\left.\frac{\partial p}{\partial r}\right\|_{r+} = 0$	$\left.\frac{\partial p}{\partial r}\right\|_{r-} = 0$
REQ	$\left.\frac{\varepsilon_c D_z}{u_z}\frac{\partial y_i}{\partial z}\right\|_{z+} = y_i\|_{z-} - y_i\|_{z+}$	$\left.\frac{\partial y_i}{\partial z}\right\|_{z-} = 0$	$\left.\frac{\partial y_i}{\partial r}\right\|_{r+} = 0$	$\left.\frac{\partial y_i}{\partial r}\right\|_{r-} = 0$
	$u_z = \frac{RT_{inlet}}{p\pi r_R^2}\sum_i \dot{n}_{i,0}$	$u_z = 0$	$\left.\frac{\partial T_g}{\partial r}\right\|_{r+} = 0$	$\left.\frac{k_g}{h_w}\frac{\partial T_g}{\partial r}\right\|_{r-} = T_w\|_{r-} - T_g\|_{r-}$
	$\left.\frac{k_g}{u_z}\frac{\partial T_g}{\partial z}\right\|_{z+} = C_t C_p T_g\|_{z-} - C_t C_p T_g\|_{z+}$	$\left.\frac{\partial T_g}{\partial z}\right\|_{z-} = 0$	$\left.\frac{\partial p}{\partial r}\right\|_{r+} = 0$	$\left.\frac{\partial p}{\partial r}\right\|_{r-} = 0$
Purge	$\left.\frac{\partial y_i}{\partial z}\right\|_{z+} = 0$	$\left.\frac{\varepsilon_c D_z}{u_z}\frac{\partial y_i}{\partial z}\right\|_{z-} = C_i\|_{z+} - C_i\|_{z-}$	$\left.\frac{\partial y_i}{\partial r}\right\|_{r+} = 0$	$\left.\frac{\partial y_i}{\partial r}\right\|_{r-} = 0$
	$u_z = 0$	$u_z = -\frac{RT_{inlet}}{p\pi r_R^2}\sum_i \dot{n}_{i,0}$	$\left.\frac{\partial T_g}{\partial r}\right\|_{r+} = 0$	$\left.\frac{k_g}{h_w}\frac{\partial T_g}{\partial r}\right\|_{r-} = T_w\|_{r-} - T_g\|_{r-}$
	$\left.\frac{\partial T_g}{\partial z}\right\|_{z+} = 0$	$\left.\frac{k_g}{u_z}\frac{\partial T_g}{\partial z}\right\|_{z-} = C_t C_p T_g\|_{z+} - C_t C_p T_g\|_{z-}$	$\left.\frac{\partial p}{\partial r}\right\|_{r+} = 0$	$\left.\frac{\partial p}{\partial r}\right\|_{r-} = 0$

The duration of each step is set taking into consideration the extension of the cycle to a process with four reactors, therefore, $t_{cycle} = 4 \times t_{reaction}$, $t_{reaction} = 4 \times t_{rinse} = 4 \times t_{EQ} = 4 \times t_{BD} = 4 \times t_{REQ} = 2 \times t_{purge} = \frac{2}{3} \times t_{regeneration}$. The high pressure ($p_H$) and low pressure ($p_L$) values of 304 kPa and 101 kPa for regeneration step have been employed, lower regeneration pressure has not been used because the use of a vacuum pump and sub-atmospheric steam can be cost intensive [21]. The detailed operating parameters of the cyclic SE-SRE process, the initial and boundary conditions for different steps are given in Table 4-13.

Table 4-14 Cyclic simulations with different parameters, product purity, yields, productivity and energy efficiency for SE-SRE process under CSS. Operating conditions: T = 773 K, p_H = 304 kPa, p_L = 101 kPa and $R_{S/C}$ = 4.

Run	$t_{reaction}$ [s]	$\dot{n}_{reaction}$ [mol·s^{-1}]	$\dot{n}_{regeneration}$ [mol·s^{-1}]	H_2 purity [mol %]	CO content [ppm]	H_2 yield [%]	H_2 productivity [mol·kg^{-1}·h^{-1}]	Thermal efficiency [kJ·kJ^{-1}]
1	250	0.05	0.05	99.61	11.28	82.71	0.61	0.60
2	500	0.05	0.05	99.42	16.86	82.69	0.60	0.59
3	750	0.05	0.05	99.10	25.75	81.64	0.59	0.59
4	1000	0.05	0.05	98.62	40.52	80.04	0.58	0.58
5	500	0.05	0.025	98.91	32.05	80.51	0.59	0.64
6	500	0.05	0.075	99.57	11.45	83.44	0.61	0.54
7	500	0.05	0.1	99.61	11.20	83.47	0.61	0.50
8	500	0.025	0.05	99.79	6.52	69.34	0.26	0.45
9	500	0.075	0.05	98.72	37.90	85.04	0.93	0.64
10	500	0.1	0.05	97.73	64.58	85.23	1.21	0.66
11	250	0.075	0.05	99.13	24.60	86.35	0.95	0.65

A $R_{S/C}$ ratio of 4 has been used in the feed, and the reactor has been filled with hydrogen before the test. The results in Table 4-14 are obtained under cyclic steady

state condition, a CSS was considered with equation(4.21). It can be found from runs 1–4 that hydrogen product with high purity and low carbon monoxide content can be obtained with a short cycle time (t_{cycle} = 4 × $t_{reaction}$ = 1000 s), and no significant difference is encountered in the performance parameters values obtained by using shorter cycle time. According to run 2 and 5–7, we can find that the use of a higher regeneration molar flow can increase the hydrogen purity and suppress the carbon monoxide content in the product, especially when the $\dot{n}_{regeneration}$ is increased from 0.025 mol·s^{-1} to 0.05 mol·s^{-1}, but the thermal efficiency decreases dramatically due to the excess latent heat required for the steam consumption during the regeneration step. On the other hand, the hydrogen productivity can be increased in a linear manner by the use of high feed molar flows (run 2 and 8-10), but a reduction in the product purity is observed. In addition, the improvement on the thermal efficiency becomes much less obvious when $\dot{n}_{reaction}$ is increased from 0.075 mol·s^{-1} to 0.1 mol·s^{-1}. As a result, operating parameters with a relatively high feeding flow rate ($\dot{n}_{reaction}$ = 0.075 mol·s^{-1}), a relatively small steam consumption ($\dot{n}_{regeneration}$ = 0.05 mol·s^{-1}) and a short cycle time (t_{cycle} = 4 × $t_{reaction}$ = 1000 s) have been used in the continuous cyclic operation process, as shown in run number 11.

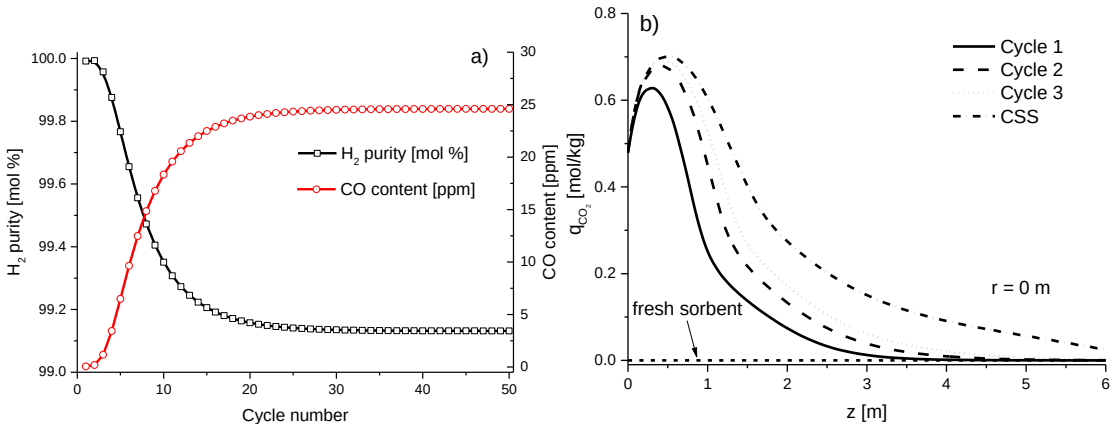

Figure 4-15 H_2 purity and CO content in the product as a function of cycle number during the cyclic operation (a), and CO_2 loading profiles on the sorbent at the end of feed step for different cycles (b). Operating conditions: 773 K, p_H = 304 kPa, p_L = 101 kPa, $R_{S/C}$ = 4, $\dot{n}_{reaction}$ = 0.075 mol·s^{-1}, $\dot{n}_{regeneration}$ = 0.05 mol·s^{-1}, $t_{reaction}$ = 250 s, t_{rinse} = t_{EQ} = t_{BD} = t_{REQ} = 62.5 s, t_{purge} = 125 s and $t_{regeneration}$ = 375 s .

With this operating schedule, we can find that the obtained hydrogen product has a purity higher than 99 mol % (dry basis) and a carbon monoxide content of 25 ppm, which can be directly used for hydrogen fuel cell applications [26]. From Figure 4-15a, we can find that the purity of hydrogen in the product for the first cycle is higher than that in the following cycles, since fresh sorbent has been used in the first cycle. After regeneration step in the following cycles, the recovered adsorption capacity of the sorbent decreases due to the residual carbon dioxide adsorbed on the sorbent (Figure 4-15b). As a result, with an increase in the cycle number, a decrease in SE-SRE reaction performance can be found due to the decay in the carbon dioxide adsorption capacity. The molar fractions of by-products such as methane and carbon dioxide at the outlet stream increases, which results in a lower hydrogen purity and higher carbon monoxide content, as shown in Figure 4-15a. After 45 cycles, cyclic steady state has been achieved and hydrogen-rich product (dry basis) with purity higher than 99 mol % and a carbon monoxide content of 25 ppm is obtained.

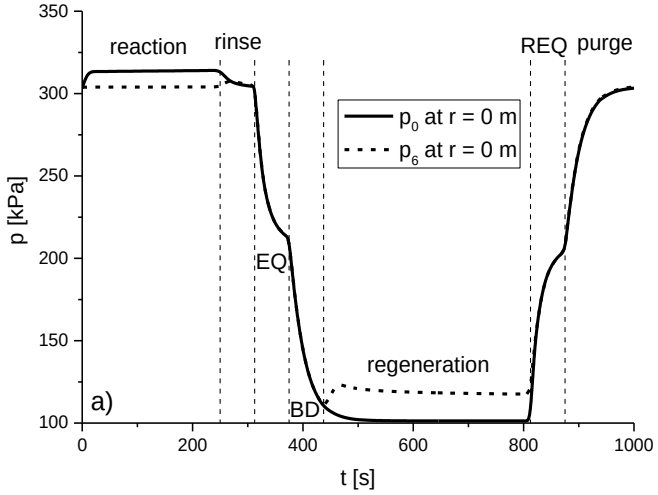

Figure 4-16 Pressure profiles at the top (z = 0 m, p_0) and bottom (z = 6 m, p_6) of the reactor during a cycle under CSS. Operating conditions: 773 K, p_H = 304 kPa, p_L = 101 kPa, $R_{S/C}$ = 4, $\dot{n}_{reaction}$ = 0.075 mol·s^{-1}, $\dot{n}_{regeneration}$ = 0.05 mol·s^{-1}, $t_{reaction}$ = 250 s, $t_{rinse} = t_{EQ} = t_{BD} = t_{REQ}$ = 62.5 s, t_{purge} = 125 s and $t_{regeneration}$ = 375 s .

On the other hand, Figure 4-16 shows the pressure at the top (z = 0 m, p_0), and bottom (z = 6 m, p_6) of the reactor during the process under CSS conditions at r = 0 m.

It can be found that the pressure at the bottom (p_0) of the reactor is higher than that (p_6) at the top during the reaction step, while during the regeneration step, the p_6 is higher than p_0 because of the pressure drop of the reactor caused by the relatively high gas superficial velocity.

Finally, a brief energy analysis has been carried out based on the results from reactor number 1 in a whole cycle under CSS conditions. Figure 4-17 shows the detailed energy variation during the process.

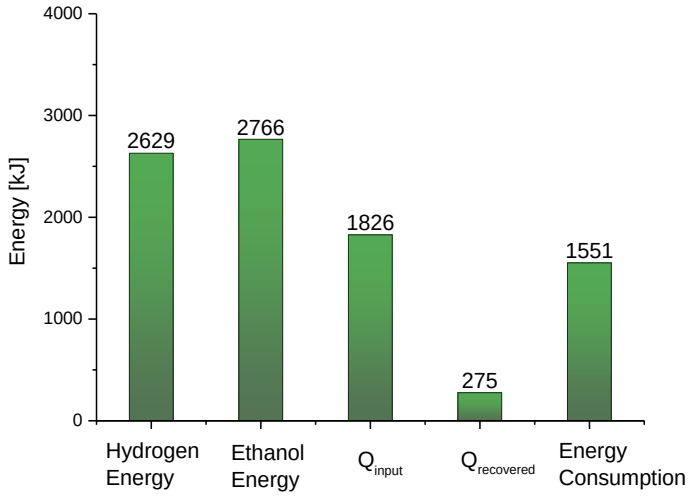

Figure 4-17 Energy changes in reactor number 1 in a whole cycle under CSS conditions during a continuous SE-SRE process for hydrogen production.

The hydrogen energy and ethanol energy are the lower heating values (LHV_{H2} = 244 kJ·mol^{-1}, LHV_{EtOH} =1330 kJ·mol^{-1}) of the net hydrogen produced (10.8 mol) and ethanol used (2.1 mol) in a cycle. Q_{input} is the energy consumed by the reaction/regeneration enthalpy change and the heating of feed stream, while $Q_{recovered}$ is the energy recovered from the outlet steam-gas mixture by heat exchanger, mainly due to the steam condensation [81]. Therefore, the net energy consumption (1551 kJ) during the process can be calculated from the difference between Q_{input} and $Q_{recovered}$. As a result, the cost of energy consumption for the hydrogen production can be estimated with an energy price of $ 4.5 per MMBtu (19/03/2014) [67], accordingly the energy cost is around $ 0.71 per kilogram of hydrogen that produced from SE-SRE process. On the other hand, we can find from the results that the ratio

between energy output (hydrogen energy) and energy input (energy consumption) in this process is around 1.7. In addition, around 8.4 kilograms of carbon dioxide can be captured per kilogram of hydrogen obtained, because carbon dioxide stream with high purity (> 99 mol %, dry basis) can be directly obtained during the regeneration step, which makes this hydrogen production process with low carbon emission more attractive.

4.2.5 Conclusion

A heterogeneous, two-dimensional (2D) adsorptive reactor model with two different scales for SE-SRE process has been developed and validated in this work with previous experimental data. According to the dynamic results obtained from an industrial scale reactor, the importance of a 2D reactor model has been demonstrated for the SE-SRE process. It is found that the radial variation in temperature has a noticeable effect on the performance of SE-SRE reaction in a large reactor during the prebreakthrough period, while the effect of radial variation is found to be negligible for conventional reforming reaction after the sorbent has been saturated. As a result, 2D adsorptive reactor model has been employed for the production of high purity hydrogen in a cyclic multi-bed SE-SRE operation process.

Four reactors have been used in the simulation of a pressure swing process with a seven steps cycle scheme to achieve a continuous hydrogen production operation. A parametric study has been carried out to improve the performance of cyclic operation, it is found under CSS condition, a continuous stream of hydrogen (dry basis) with purity higher than 99 mol % with a carbon monoxide content of 25 ppm can be produced by conducting SE-SRE in four parallel fixed-bed adsorptive reactors operated with a cycle time of 1000 s. A brief energy analysis shows that the ratio between energy output and input is around 1.8, and the estimated cost of energy is around $ 0.71 per kilogram of hydrogen produced in this process. In addition, more than 8 kilograms of carbon dioxide can be obtained during the regeneration step per kilogram of hydrogen produced in the cyclic operation.

Reference

[1] A.I. Lysikov, S.N. Trukhan, A.G. Okunev, *Int. J. Hydrogen Energy.* **2008**, *33 (12)*, 3061-3066.

[2] L. He, H. Berntsen, D. Chen, *J. Phys. Chem. A.* **2009**, *114 (11)*, 3834-3844.

[3] S. Gunduz, T. Dogu, *Ind. Eng. Chem. Res.* **2012**, *51 (26)*, 8796-8805.

[4] Y. Iwasaki, Y. Suzuki, T. Kitajima, M. Sakurai, H. Kameyama, *J. Chem. Eng. Jpn.* **2007**, *40 (2)*, 178-185.

[5] K. Essaki, T. Muramatsu, M. Kato, *Int. J. Hydrogen Energy.* **2008**, *33 (22)*, 6612-6618.

[6] A.F. Cunha, Y.-J. Wu, F.A. Díaz Alvarado, J.C. Santos, P.D. Vaidya, A.E. Rodrigues, *Can. J. Chem. Eng.* **2012**, *90 (6)*, 1514-1526.

[7] A.F. Cunha, Y.-J. Wu, J.C. Santos, A.E. Rodrigues, *Chem. Eng. Res. Des.* **2013**, *91 (3)*, 581-592.

[8] Y.-J. Wu, P. Li, J.-G. Yu, A.F. Cunha, A.E. Rodrigues, *Chem. Eng. J.* **2013**, *231* 36-48.

[9] Z.-s. Li, N.-s. Cai, J.-b. Yang, *Ind. Eng. Chem. Res.* **2006**, *45 (26)*, 8788-8793.

[10] W.E. Waldron, J.R. Hufton, S. Sircar, *AIChE J.* **2001**, *47 (6)*, 1477-1479.

[11] K. Duraiswamy, A. Chellappa, G. Smith, Y. Liu, M. Li, *Int. J. Hydrogen Energy.* **2010**, *35 (17)*, 8962-8969.

[12] M.H. Halabi, M.H.J.M. de Croon, J. van der Schaaf, P.D. Cobden, J.C. Schouten, *Int. J. Hydrogen Energy.* **2012**, *37 (6)*, 4987-4996.

[13] V.S. Derevschikov, A.I. Lysikov, A.G. Okunev, *Chem. Eng. Sci.* **2011**, *66 (13)*, 3030-3038.

[14] Z.-s. Li, N.-s. Cai, *Energy Fuels.* **2007**, *21 (5)*, 2909-2918.

[15] E.L.G. Oliveira, C.A. Grande, A.E. Rodrigues, *Chem. Eng. Sci.* **2011**, *66 (3)*, 342-354.

[16] K.B. Yi, D.P. Harrison, *Ind. Eng. Chem. Res.* **2005**, *44 (6)*, 1665-1669.

[17] G.-h. Xiu, P. Li, A. E. Rodrigues, *Chem. Eng. Sci.* **2002**, *57 (18)*, 3893-3908.

[18] G.-h. Xiu, J.L. Soares, P. Li, A.E. Rodrigues, *AIChE J.* **2002**, *48 (12)*, 2817-2832.

[19] G.-h. Xiu, P. Li, A.E. Rodrigues, *Chem. Eng. Sci.* **2003**, *58 (15)*, 3425-3437.

[20] G.H. Xiu, P. Li, A.E. Rodrigues, *Chem. Eng. Res. Des.* **2004**, *82 (2)*, 192-202.

[21] K.B. Lee, M.G. Beaver, H.S. Caram, S. Sircar, *Ind. Eng. Chem. Res.* **2007**, *46 (14)*, 5003-5014.

[22] S. Rawadieh, V.G. Gomes, *Int. J. Hydrogen Energy.* **2009**, *34 (1)*, 343-355.

[23] K.B. Lee, M.G. Beaver, H.S. Caram, S. Sircar, *Adsorption.* **2007**, *13 (3-4)*, 385-397.

[24] K.B. Lee, M.G. Beaver, H.S. Caram, S. Sircar, *Ind. Eng. Chem. Res.* **2008**, *47 (17)*, 6759-6764.

[25] H.M. Jang, K.B. Lee, H.S. Caram, S. Sircar, *Chem. Eng. Sci.* **2012**, *73* , 431-438.

[26] B. Rohland, V. Plzak, *J. Power Sources.* **1999**, *84 (2)*, 183-186.

[27] Y. Ding, E. Alpay, *Chem. Eng. Sci.* **2000**, *55 (17)*, 3461-3474.

[28] J. Xu, G.F. Froment, *AIChE J.* **1989**, *35 (1)*, 88-96.

[29] K.B. Lee, M.G. Beaver, H.S. Caram, S. Sircar, *AIChE J.* **2007**, *53 (11)*, 2824-2831.

[30] J.R. Hufton, S. Mayorga, S. Sircar, *AIChE J.* **1999**, *45 (2)*, 248-256.

[31] M.H. Halabi, M.H.J.M. de Croon, J. van der Schaaf, P.D. Cobden, J.C. Schouten, *Int. J. Hydrogen Energy.* **2012**, *37 (5)*, 4516-4525.

[32] E.L.G. Oliveira, C.A. Grande, A.E. Rodrigues, *Sep. Purif. Technol.* **2008**, *62 (1)*, 137-147.

[33] A. Haryanto, S. Fernando, N. Murali, S. Adhikari, *Energy Fuels.* **2005**, *19 (5)*, 2098-2106.

[34] P.D. Vaidya, A.E. Rodrigues, *Chem. Eng. J.* **2006**, *117 (1)*, 39-49.

[35] F. Auprêtre, C. Descorme, D. Duprez, *Catal. Comm.* **2002**, *3 (6)*, 263-267.

[36] Y.-J. Wu, J.C. Santos, P. Li, J.G. Yu, A.F. Cunha, A.E. Rodrigues, *Can. J. Chem. Eng.* **2014**, *92 (1)*, 116-130.

[37] M. Akiyama, Y. Oki, M. Nagai, *Catal. Today.* **2012**, *181 (1)*, 4-13.

[38] W. Liu, H. An, C. Qin, J. Yin, G. Wang, B. Feng, M. Xu, *Energy Fuels.* **2012**, *26 (5)*, 2751-2767.

[39] S. Choi, J.H. Drese, C.W. Jones, *ChemSusChem.* **2009**, *2 (9)*, 796-854.

[40] Z. Yong, V. Mata, A.E. Rodrigues, *Sep. Purif. Technol.* **2002**, *26 (2–3)*, 195-205.

[41] H.T.J. Reijers, S.E.A. Valster-Schiermeier, P.D. Cobden, R.W. van den Brink, *Ind. Eng. Chem. Res.* **2005**, *45 (8)*, 2522-2530.

[42] Z. Zhou, Y. Qi, M. Xie, Z. Cheng, W. Yuan, *Chem. Eng. Sci.* **2012**, *74* , 172-180.

[43] H.K. Rusten, E. Ochoa-Fernández, D. Chen, H.A. Jakobsen, *Ind. Eng. Chem. Res.* **2007**, *46 (13)*, 4435-4443.

[44] K.B. Lee, A. Verdooren, H.S. Caram, S. Sircar, *J. Colloid Interface Sci.* **2007**, *308 (1)*, 30-39.

[45] Y.-J. Wu, P. Li, J.G. Yu, A.F. Cunha, A.E. Rodrigues, *Chem. Eng. Technol.* **2013**, *36 (4)*, 567-574.

[46] S. Rawadieh, V.G. Gomes, *Int. J. Chem. React. Eng.* **2007**, *5 (1)*,

[47] Z.P. Lu, A.E. Rodrigues, *AIChE J.* **1994**, *40 (7)*, 1118-1137.

[48] N. Chanburanasiri, A.M. Ribeiro, A.E. Rodrigues, A. Arpornwichanop, N. Laosiripojana, P. Praserthdam, S. Assabumrungrat, *Ind. Eng. Chem. Res.* **2011**, *50 (24)*, 13662-13671.

[49] M.H. Halabi, M.H.J.M. de Croon, J. van der Schaaf, P.D. Cobden, J.C. Schouten, *Fuel.* **2012**, *99* , 154-164.

[50] H.Z. Feng, P.Q. Lan, S.F. Wu, *Int. J. Hydrogen Energy.* **2012**, *37 (19)*, 14161-14166.

[51] C.S. Martavaltzi, A.A. Lemonidou, *Chem. Eng. Sci.* **2010**, *65 (14)*, 4134-4140.

[52] J.-N. Kim, C.H. Ko, K.B. Yi, *Int. J. Hydrogen Energy.* **2013**, *38 (14)*, 6072-6078.

[53] A.F. Cunha, Y.-J. Wu, P. Li, J.-G. Yu, A.E. Rodrigues, *Ind. Eng. Chem. Res.* **2014**, *53 (10)*, 3842–3853.

[54] H.M. Jang, W.R. Kang, K.B. Lee, *Int. J. Hydrogen Energy.* **2013**, *38 (14)*, 6065-6071.

[55] L. He, J.M.S. Parra, E.A. Blekkan, D. Chen, *Energy Environ. Sci.* **2010**, *3 (8)*, 1046-1056.

[56] M.H. Halabi, M.H.J.M. de Croon, J. van der Schaaf, P.D. Cobden, J.C. Schouten,

Chem. Eng. J. **2011**, *168 (2)*, 872-882.

[57] N. Wakao, T. Funazkri, *Chem. Eng. Sci.* **1978**, *33 (10)*, 1375-1384.

[58] A.P. de Wasch, G.F. Froment, *Chem. Eng. Sci.* **1972**, *27 (3)*, 567-576.

[59] B.E. Poling, J.M. Prausnitz, J.P. O'Connell, *The properties of gases and liquids*, McGraw-Hill, New York, **2001**.

[60] F. Cavani, F. Trifirò, A. Vaccari, *Catal. Today.* **1991**, *11 (2)*, 173-301.

[61] J.P. Breen, R. Burch, H.M. Coleman, *Appl. Catal., B.* **2002**, *39 (1)*, 65-74.

[62] B. Banach, A. Machocki, P. Rybak, A. Denis, W. Grzegorczyk, W. Gac, *Catal. Today.* **2011**, *176 (1)*, 28-35.

[63] F. Díaz Alvarado, F. Gracia, *Chem. Eng. J.* **2010**, *165 (2)*, 649-657.

[64] Y.-J. Wu, F. Díaz Alvarado, J.C. Santos, F. Gracia, A.F. Cunha, A.E. Rodrigues, *Chem. Eng. Technol.* **2012**, *35 (5)*, 847–858.

[65] K. Vasudeva, N. Mitra, P. Umasankar, S.C. Dhingra, *Int. J. Hydrogen Energy.* **1996**, *21 (1)*, 13-18.

[66] P.D. Vaidya, A.E. Rodrigues, *Ind. Eng. Chem. Res.* **2006**, *45 (19)*, 6614-6618.

[67] EIA, Natural Gas Weekly Update in, http://www.eia.gov/naturalgas/weekly/, **2014**.

[68] TLV, http://www.tlv.com/global/TI/calculator/steam-unit-cost.html, **2013**.

[69] D. Gunn, *Chem. Eng. Sci.* **1987**, *42 (2)*, 363-373.

[70] H. Song, U.S. Ozkan, *Int. J. Hydrogen Energy.* **2010**, *35 (1)*, 127-134.

[71] J.R. Fernandez, J.C. Abanades, R. Murillo, *Chem. Eng. Sci.* **2012**, *84* , 1-11.

[72] N. Chanburanasiri, A.M. Ribeiro, A.E. Rodrigues, N. Laosiripojana, S. Assabumrungrat, *Energy Fuels.* **2013**, *27 (8)*, 4457-4470.

[73] I. Iliuta, H.R. Radfarnia, M.C. Iliuta, *AIChE J.* **2013**, *59 (6)*, 2105-2118.

[74] J.R. Rostrup-Nielsen, *Catalytic Steam Reforming*, in: J.R. Andersen, M. Boudart (Eds.) Catalysis: Science and Technology, Springer-Verlag, Berlin, **1984**.

[75] A.G. Dixon, *Can. J. Chem. Eng.* **2012**, *90 (3)*, 507-527.

[76] J.M.P.Q. Delgado, *Heat Mass Transfer.* **2006**, *42 (4)*, 279-310.

[77] J.R. Rostrup-Nielsen, J. Sehested, J.K. Nørskov, *Adv. Catal.* **2002**, *47* 65-139.

[78] H. Kvamsdal, H. Svendsen, O. Olsvik, T. Hertzberg, *Chem. Eng. Sci.* **1999**, *54 (13)*, 2697-2706.

[79] C.-H. Li, B.A. Finlayson, *Chem. Eng. Sci.* **1977**, *32 (9)*, 1055-1066.

[80] N. Wakao, S. Kaguei, T. Funazkri, *Chem. Eng. Sci.* **1979**, *34 (3)*, 325-336.

[81] K. Jeong, S. Sircar, H.S. Caram, *AIChE J.* **2012**, *58 (1)*, 312-321.

[82] M.A. Nahil, X. Wang, C. Wu, H. Yang, H. Chen, P.T. Williams, *RSC Adv.* **2013**, *3 (16)*, 5583-5590.

[83] F. Benyahia, K.E. O'Neill, *Part. Sci. Technol.* **2005**, *23*, 169-177.

[84] C. De Deken J, F. Devos E, F. Froment G, *Steam Reforming of Natural Gas: Intrinsic Kinetics, Diffusional Influences, and Reactor Design*, in: Chemical Reaction Engineering-Boston, ACS, **1982**.

5. Conclusions and Suggestions for Future Work

5.1 Conclusions

The main goal of this thesis is to produce high purity hydrogen by sorption-enhanced steam reforming of ethanol (SE-SRE) at intermediate temperatures. Hydrogen is considered as a promising energy carrier according to the concept of "hydrogen economy" [1]. However, nowadays hydrogen is mostly produced from fossil fuels by reforming technologies [2]. As alternative, ethanol that can be produced from renewable biomass resources becomes an ideal feedstock for hydrogen production [3, 4]. But products from SRE reaction always contains a large amount of carbon dioxide and other undesired by-products such as acetaldehyde, methane and carbon monoxide [5, 6]. Therefore, numerous separation and purification units are always required in a conventional high-purity hydrogen production process [7]. One promising alternative is the sorption-enhanced reaction process (SERP) [8]. The essence of SERP is the multifunctional reactor where reforming reaction and carbon dioxide removal by adsorption are integrated over a mixture of reforming catalyst and high temperature carbon dioxide sorbent. The hydrogen yield and purity are expected to be enhanced by shifting thermodynamic equilibrium of the SRE reaction towards product side through *in situ* carbon dioxide removal, resulting in a SE-SRE reaction process. The concept of SERP offers promising potential for cost saving compared with the conventional hydrogen production route [8, 9].

In order to produce high purity hydrogen from SE-SRE reaction, it is important to evaluate the performances of catalysts and sorbents for the sorption-enhanced reaction. Therefore, this study starts with the demonstration of sorption-enhanced reaction process on steam reforming of ethanol concept by the use of commercial materials in **chapter II**. A reactor with a multilayer pattern arrangement of Ni-based reforming catalyst (Octolyst 1001) and hydrotalcite-like material (PURAL MG30, HTlc) carbon dioxide sorbent has been employed. The effects of the operating conditions (temperature and feeding flow rates) on the performance of reaction have been studied. Hydrogen can be generated from SRE in the temperature range between 373 K and

873 K. A mechanism with ethanol dehydrogenation, acetaldehyde decomposition, methane steam reforming and water-gas-shift reactions has been proposed to explain the reaction pathways. Moreover, it is found that the hydrotalcite-like material acts as a relative good carbon dioxide sorbent at 673 K. The SERP concept has been verified for this system coupling the Octolyst 1001 catalyst with the MG30 hydrotalcite sorbent. High amounts of hydrogen with traces carbon monoxide (< 0.1 mol %) in the product gas stream can be obtained during the initial breakthrough periods.

On the other hand, thermodynamic analysis has been performed in **chapter II** with a Gibbs free energy minimization method to compare the conventional SRE process and SE-SRE with three most widely used high temperate carbon dioxide sorbents [10], CaO, Li_2ZrO_3 and HTlc. Initially, a noticeable difference has been found between the results based on real gas state and ideal gas state assumptions, therefore, it is recommended to employ real gas state for further thermodynamic calculations. From the thermodynamic study, we find that the use of a carbon dioxide sorbent can enhance the hydrogen yield and provide lower carbon monoxide content in the product gas at the same time. Besides, thermodynamic equilibrium analysis of SE-SRE indicates that HTlc has a better adsorption performance than other materials at lower temperatures. The results of the thermodynamic study shows that when adequate amount of sorbent has been used, the hydrogen yield can reach close to 6 mol hydrogen per mol ethanol converted, while the content of carbon monoxide in the product gas is less than 10 ppm at 773 K, atmospheric pressure and steam-to-carbon ($R_{S/C}$) molar ratio higher than 5. In addition, the use of further purification units would not be necessary for hydrogen fuel cell application. The results obtained from thermodynamic studies are also in a good agreement of data from previous experimental studies.

The kinetic study with the commercial nickel-based catalyst (Octolyst 1001) for SRE has also been included in **chapter II**. The kinetic behavior of SRE over the catalyst has been investigated from 473 K to 873 K with a $R_{S/C}$ of 5 in the feed. In the study, both the power rate law and Langmuir–Hinshelwood–Hougen–Watson (LHHW)

kinetic models that have been employed can successfully demonstrate the catalytic SRE process in a fixed-bed reactor among a large temperature range (473 K – 873 K). The energy of activation for SRE reaction is found as 31.8 $kJ \cdot mol^{-1}$, and the reaction order of the ethanol pressure obtained from the power rate law model is 1.52, which are in good agreement with other reports. The surface decomposition of methane is assumed as the rate determining step in the simplified LHHW model according to many previous studies. The values of the parameters for LHHW kinetic model indicate that the acetaldehyde decomposition reaction is much faster than the ethanol decomposition reaction, while the elementary reaction between θ_{CH3} and θ_{OH} is also a strong endothermic reaction similar as the steam methane reforming.

The catalyst and sorbent materials can be integrated with different methods for SERP. Various catalyst-sorbent packing systems have been studied by Rawadieh and Gomes [11], it is found that a well-mixed catalyst-sorbent configuration can produce hydrogen product with higher purity and lower carbon monoxide content compared to other configurations, which is in a good agreement with the results found by Lu and Rodrigues [12]. However, due to the differences in pellet size, shape and density of the catalyst and sorbent materials, it is difficult to obtain an ideally well mixed catalyst-sorbent system in practice. To achieve an ideal dispersion, hybrid multifunctional materials consisting of carbon dioxide sorbent, as support material, and active metals as catalytic phase have been developed in some recent studies [13-16]. Therefore, hybrid materials with Cu or Ni as active phase and HTlc as sorbent have been prepared and employed for SRE and SE-SRE studies in **chapter III**. Both the Cu- and Ni-HTlc materials show relatively good stability during the SRE and SE-SRE tests due to the unique layered structure. The hydrogen production through SRE was enhanced by carbon dioxide sorption over the Cu-HTlc material in the initial transient period, and high purity hydrogen over 90 mol % can be obtained. In addition, breakthrough tests have been performed with the Cu-HTlc material, and the material shows a carbon dioxide adsorption capacity from 0.11 to 0.18 $mol \cdot kg^{-1}$, which is similar as the pure hydrotalcites. On the other hand, both the reaction and adsorption kinetics of the Ni-HTlc material have been investigated and employed for

numerical simulation. The mathematical reactor model employed successfully predicts the SRE reaction and carbon dioxide adsorption process. Therefore, SERP with Ni-HTlc material has been simulated to investigate the effects of different reaction conditions. The reaction conditions where the material can achieve the highest possible enhancing performance are $R_{S/C}$ = 5, $m_{cat}/\dot{n}_{EtOH}$= 0.25 kg·h·mol^{-1} and 773 K. It is found that the hydrogen produced during the sorption-enhanced reaction period had an initially high purity (> 99 mol %). The concentration of hydrogen (dry basis) is kept higher than 95 mol % for the initial 500 s. Experimental SE-SRE tests have been carried out to confirm the simulated predictions which are in a good agreement. Besides, the catalytic stability at steady state conditions and cyclic operations for the Ni-HTlc material has also been investigated. It is found that the prepared material has good reaction and adsorption/desorption stability under the conditions employed, the composition and structure of the sample have been preserved.

Then, potassium promoted HTlc (K-HTlc) sorbent with potassium nitrate as the potassium precursor has been developed in **chapter III** to improve the carbon dioxide adsorption performance of pure HTlc material. The highest carbon dioxide adsorption capacity (1.13 mol·kg^{-1}) on the prepared material is obtained at 656 K with carbon dioxide partial pressure of 50 kPa at humid conditions. A mathematical model is developed and it satisfactorily simulates the adsorption and desorption processes. The stability of the material has also been tested with repeated adsorption/desorption cycles. It is found that both the carbon dioxide adsorption capacity and kinetics are not that much affected after ten cycles, and the adsorption capacity is found to decrease around 7 %. In addition, temperature swing (from 656 K to 708 K) regeneration operation has been performed, where a complete regeneration can be achieved within 60 min, which reduces to half the time required for regeneration under isothermal conditions. The K-HTlc material prepared is found to have very good thermal and cyclic stability, which makes it an attractive carbon dioxide sorbent for further SE-SRE study.

As a result, in the last section of **chapter III**, we extend the previous studies to develop a multi-functional material consisting of Cu-Ni alloy as active phase and K-HTlc sorbent material as the support. The prepared K-Ni-Cu-HTlc material has been studied for its catalytic properties for steam reforming of ethanol. It is found that Cu can preferentially catalyze ethanol dehydrogenation and water–gas shift reactions, while Ni is more suitable for acetaldehyde decomposition and steam reforming of methane. Additionally, Ni and Cu metals can form a $Ni_{0.5}Cu_{0.5}$ alloy with the advantage of ensemble formation. The formation of small ensembles of nickel and copper atoms on surface can avoid the interaction of adsorbed species, and the catalytic decomposition of methane and catalytic carbon monoxide decomposition can be avoided. On the other hand, promising carbon dioxide adsorption performance of the material can be obtained by the use of potassium promoter, and the adsorption capacity of K-Ni-Cu-HTlc material (0.83 $mol \cdot kg^{-1}$) is found to be much higher than that of the unprompted Ni-HTlc sample (0.26 $mol \cdot kg^{-1}$) at around 723 K with carbon dioxide partial pressure of 40 kPa. Finally, SE-SRE has been performed with the K-Ni-Cu-HTlc material in a fixed-bed reactor; high-purity hydrogen stream (99.8 mol % on dry basis) can be obtained during the prebreakthrough period at 773 K with $R_{S/C}$ = 5 in the feed.

With these promising materials for SE-SRE reaction, processes studies have been carried out in the following **chapter IV**. In addition, on the basis of the homogeneously packed column, the subsection-controlling strategy [17, 18] and a similar multi-section column concept [19] have been employed in the process study to improve the SE-SRE performance. It is found that by using different packing ratios of sorbent/catalyst in the reactor, the concentration of impurity can be decreased further in the produced gas, and additional degree of freedom can be obtained for flexible operation [19]. Therefore, a homogeneously packed column with two subsections for SE-SRE has been developed by simulation for high purity hydrogen production. Within the two subsections, two different volumetric ratios (1:2 and 1:4) between the Ni-HTlc and K-HTlc materials that were developed in the previous **chapter III** have been used. The effects of reaction conditions on the performance of SE-SRE reaction

have been investigated. It is found that a feasible operation window to produce carbon monoxide free (< 30 ppm) hydrogen gas cannot be achieved when $R_{S/C}$ is lower than 2 and the operation window is increasing with the $R_{S/C}$ rise. However, further increase $R_{S/C}$ from 5 to 10 causes a negative effect on the amount of hydrogen produced, and the overall thermal efficiency decreases in a linear manner due to the excess latent heat required for the feed stream [20]. Besides, higher amount of hydrogen produced during the SE-SRE reaction can be obtained when operation pressure increases from 101.3 kPa to 304.0 kPa. We find that the product gas with hydrogen purity above 99 mol % and carbon monoxide content of 30 ppm, which can be directly used in fuel cell applications, can be produced at 773 K, 304 kPa with $R_{S/C}$ = 5 in the feed.

On the other hand, a four-step pressure swing cyclic operation process has also been developed in **chapter IV** as follows: sorption-enhanced reaction with ethanol and steam in the feed at high pressure (304 kPa); the rinse of the column with steam to remove the residual products within the gas phase with a pressure decrease to atmospheric pressure (101 kPa); the regeneration of the carbon dioxide sorbent by steam at low pressure (101 kPa); and finally the purge of the column with hydrogen gas and steam with a pressure increase to 304 kPa before the next cycle. This cyclic SE-SRE operation process is predicted to have a great potential to produce fuel-cell-grade hydrogen with a high yield and thermal efficiency according to the results from calculation. The hydrogen productivity is around 0.51 $mol \cdot kg^{-1}h^{-1}$ and pure carbon dioxide (dry basis) can be obtained as a by-product during the regeneration step. The yields of hydrogen and carbon dioxide are 78.5 % and 75 %, respectively, which are much higher than the results from a conversional SRE process (hydrogen yield 38.3 % and carbon dioxide yield 51.0 %) under the same reaction conditions. The thermal efficiency of SE-SRE (0.45) is found to be much higher than the thermal efficiency of the SRE process (0.33). Besides, the cost of steam ($ 0.87 per kilogram of hydrogen) for the SE-SRE has also been calculated, which can be reduced even further by recycling the exhaust energy.

One-dimensional fixed-bed adsorptive reactors are the most widely used model for

SERP in previous researches [13, 17, 18, 21-27], where multifunctional reactors with small diameters have been employed. However, Rostrup-Nielsen [28] found that the radial temperature difference within a typical industrial reformer can be as large as 40 K, and the effect of energy transport in the radial direction might be significant when a large diameter reactor is used [29-33]. An accurate design of SE-SRE reactors requires an adequate description of the reaction/adsorption kinetics, momentum, heat and mass transfer processes. As a result, in the final section of **chapter IV**, a two-dimensional mathematical adsorptive reactor model has been developed, where K-Ni-Cu-HTlc material developed in the previous chapter is used for SE-SRE reaction. First, it is found that the product distribution from the numerical simulation matches well with experimental data obtained from a laboratory-scale fixed-bed adsorptive reactor. Afterwards, the diameter of the reactor has been increased to a typical industrial scale. We find in an adsorptive reactor with a diameter of 0.1 m, the radial variation in temperature has a noticeable effect on the performance of SE-SRE reaction in a large reactor during the prebreakthrough period, according to the comparison between the results obtained from a one-dimensional reactor model and that from a two-dimensional reactor model. However, the effect of radial variation is found to be negligible for conventional reforming reaction after the sorbent has been saturated with carbon dioxide. As a result, two-dimensional reactor model has been employed for the production of high purity of hydrogen in a cyclic multi-bed SE-SRE operation process.

Four adsorptive reactors, with two-dimensional mathematical model, have been used in the simulation of a pressure swing process with a seven-step cycle scheme to achieve a continuous hydrogen production operation can be found in **chapter IV**. A parametric study has been carried out to improve the cyclic process; it is found that under cyclic steady state condition, a continuous stream of hydrogen (dry basis) with purity higher than 99 mol % and carbon monoxide content less than 30 ppm can be produced by conducting SE-SRE in four parallel fixed-bed adsorptive reactors operated with a cycle time of 1000 s. Finally, a brief energy analysis shows that the ratio between energy output and input is around 1.7, and the estimated cost of energy

is around $ 0.71 per kilogram of hydrogen produced in this process. In addition, more than 8 kilograms of carbon dioxide can be obtained during the regeneration step per kilogram of hydrogen produced in the cyclic operation, which makes this low carbon emission hydrogen production process more attractive.

5.2 Suggestions for Future Work

The SE-SRE process is a very promising technology for high purity hydrogen production. The future work can be carried out with the commercialization of SE-SRE process as the ultimate goal. To achieve such a goal, future research efforts should focus on both the material and process developments.

On one hand, in order to reduce the possible pressure drop for the use in an industrial scale reactor, pellets of the hybrid material with a relatively large diameter should be prepared in the first place. The reaction/adsorption kinetic behaviors, time-on-stream performance and the cyclic stability of the pellets for SE-SRE have to be studied. Besides, the possible effects of impurities such as methanol and ethyl acetate in the bio-ethanol on the reaction performance have to be investigated. On the other hand, the mechanical strength of the hybrid material pellet is another important aspect for industrial applications. Therefore, it might be interesting to investigate the effects of depositing hybrid materials onto the Li-based ceramics, which is another widely used high temperate carbon dioxide sorbent, to improve the mechanical strengths and the adsorption capacity at the same time. In addition, molecular simulation by DFT calculations can be employed to guide rational catalyst-sorbent material design.

For the development of the process, a reforming reaction kinetic model including carbon deposit can be useful in the screening of potential operating conditions. In addition, the use of a rigorous thermodynamic property model for the fluid phase in the adsorptive reactor may improve the accuracy of simulation during the SE-SRE process, since ideal gas assumption has been used in the mathematical model. Besides, the effects of sorption-enhanced oxidative reaction and auto-thermal reforming on the

energy efficiency and hydrogen production performance can also be determined. Other possible applications of the SERP concept with glycerol, biomass, biogas and other renewable sources as the feedstock for hydrogen production can also be investigated in the future.

Finally, numerical study can be performed on the development of a detailed SE-SRE hydrogen production and usage system, which can provide fundamental answers that have not been readily solved in an industrial setting. To investigate the performance of the hydrogen fuel-cell power system with bioethanol feedstock, the whole system should be modeled. Therefore, future work may model the hydrogen production from SE-SRE process with hydrogen fuel cells together to obtain overall energy efficiency of the system, and economic analysis should also be performed.

References

[1] L. Barreto, A. Makihira, K. Riahi, *Int. J. Hydrogen Energy.* **2003**, *28 (3)*, 267-284.

[2] P. Ferreira‐Aparicio, M.J. Benito, J.L. Sanz, *Catal. Rev.: Sci. Eng.* **2005**, *47 (4)*, 491-588.

[3] A. Haryanto, S. Fernando, N. Murali, S. Adhikari, *Energy Fuels.* **2005**, *19 (5)*, 2098-2106.

[4] L.V. Mattos, G. Jacobs, B.H. Davis, F.B. Noronha, *Chem. Rev.* **2012**, *112 (7)*, 4094-4123.

[5] P.D. Vaidya, A.E. Rodrigues, *Chem. Eng. J.* **2006**, *117 (1)*, 39-49.

[6] A.F. Cunha, Y.-J. Wu, F.A. Díaz Alvarado, J.C. Santos, P.D. Vaidya, A.E. Rodrigues, *Can. J. Chem. Eng.* **2012**, *90 (6)*, 1514-1526.

[7] A.M. Ribeiro, C.A. Grande, F.V.S. Lopes, J.M. Loureiro, A.E. Rodrigues, *Chem. Eng. Sci.* **2008**, *63 (21)*, 5258-5273.

[8] D.P. Harrison, *Ind. Eng. Chem. Res.* **2008**, *47 (17)*, 6486-6501.

[9] J.R. Hufton, S. Mayorga, S. Sircar, *AIChE J.* **1999**, *45 (2)*, 248-256.

[10] S. Wang, S. Yan, X. Ma, J. Gong, *Energy Environ. Sci.* **2011**, *4 (10)*, 3805-3819.

[11] S. Rawadieh, V.G. Gomes, *Int. J. Hydrogen Energy.* **2009**, *34 (1)*, 343-355.

[12] Z.P. Lu, A.E. Rodrigues, *AIChE J.* **1994**, *40 (7)*, 1118-1137.

[13] M.H. Halabi, M.H.J.M. de Croon, J. van der Schaaf, P.D. Cobden, J.C. Schouten, *Fuel.* **2012**, *99*, 154-164.

[14] J.-N. Kim, C.H. Ko, K.B. Yi, *Int. J. Hydrogen Energy.* **2013**, *38 (14)*, 6072-6078.

[15] H.Z. Feng, P.Q. Lan, S.F. Wu, *Int. J. Hydrogen Energy.* **2012**, *37 (19)*, 14161-14166.

[16] M.A. Nahil, X. Wang, C. Wu, H. Yang, H. Chen, P.T. Williams, *RSC Adv.* **2013**, *3 (16)*, 5583-5590.

[17] G.-h. Xiu, P. Li, A.E. Rodrigues, *Chem. Eng. Sci.* **2003**, *58 (15)*, 3425-3437.

[18] G.H. Xiu, P. Li, A.E. Rodrigues, *Chem. Eng. Res. Des.* **2004**, *82 (2)*, 192-202.

[19] H.M. Jang, W.R. Kang, K.B. Lee, *Int. J. Hydrogen Energy.* **2013**, *38 (14)*, 6065-6071.

[20] L. He, J.M.S. Parra, E.A. Blekkan, D. Chen, *Energy Environ. Sci.* **2010**, *3 (8)*, 1046-1056.

[21] G.-h. Xiu, J.L. Soares, P. Li, A.E. Rodrigues, *AIChE J.* **2002**, *48 (12)*, 2817-2832.

[22] G.-h. Xiu, P. Li, A. E. Rodrigues, *Chem. Eng. Sci.* **2002**, *57 (18)*, 3893-3908.

[23] M.H. Halabi, M.H.J.M. de Croon, J. van der Schaaf, P.D. Cobden, J.C. Schouten, *Chem. Eng. J.* **2011**, *168 (2)*, 872-882.

[24] J.R. Fernandez, J.C. Abanades, R. Murillo, *Chem. Eng. Sci.* **2012**, *84*, 1-11.

[25] N. Chanburanasiri, A.M. Ribeiro, A.E. Rodrigues, N. Laosiripojana, S. Assabumrungrat, *Energy Fuels.* **2013**, *27 (8)*, 4457-4470.

[26] I. Iliuta, H.R. Radfarnia, M.C. Iliuta, *AIChE J.* **2013**, *59 (6)*, 2105-2118.

[27] E.L.G. Oliveira, C.A. Grande, A.E. Rodrigues, *Chem. Eng. Sci.* **2011**, *66 (3)*, 342-354.

[28] J.R. Rostrup-Nielsen, *Catalytic Steam Reforming*, in: J.R. Andersen, M. Boudart (Eds.) Catalysis: Science and Technology, Springer-Verlag, Berlin, **1984**.

[29] A.G. Dixon, *Can. J. Chem. Eng.* **2012**, *90 (3)*, 507-527.

[30] J.M.P.Q. Delgado, *Heat and Mass Transfer.* **2006**, *42 (4)*, 279-310.

[31] D. Gunn, *Chem. Eng. Sci.* **1987**, *42 (2)*, 363-373.

[32] J.R. Rostrup-Nielsen, J. Sehested, J.K. Nørskov, *Adv. Catal.* **2002**, *47* 65-139.

[33] H. Kvamsdal, H. Svendsen, O. Olsvik, T. Hertzberg, *Chem. Eng. Sci.* **1999**, *54 (13)*, 2697-2706.

Notation

a_{ji} number of j-type atoms in the species i,

a_p area-to-volume ratio of the material particle [m^{-1}]

ACD acetaldehyde decomposition

ATR auto thermal reforming

b_j number of j-type atoms

Bi Biot number

C_i concentration of component i in the gas phase [$mol \cdot m^{-3}$]

C_p specific molar heat at constant pressure [$J \cdot mol^{-1} \cdot K^{-1}$]

C_{ps} specific heat of the solid phase [$J \cdot kg^{-1} \cdot K^{-1}$]

C_{pw} specific heat of the column wall [$J \cdot kg^{-1} \cdot K^{-1}$]

$\bar{C}_{s,i}$ average concentration of compound i in the solid phase [$mol \cdot m^{-3}$]

CSS cyclic steady state

C_t total gas concentration [$mol \cdot m^{-3}$]

$\bar{C}_{t,s}$ total solid concentration [$mol \cdot m^{-3}$]

C_v specific molar heat at constant volume [$J \cdot mol^{-1} \cdot K^{-1}$]

$C_{v,ads}$ specific molar heat in the adsorbed phase at constant volume [$J \cdot mol^{-1} \cdot K^{-1}$]

CNT carbon nanotube

CPOX catalytic partial oxidation

d_p particle diameter [m]

$\bar{d}_{pore}$ average diameter of the pore [m]

DEN denominator

D_p sorbent pore diffusion coefficient [$m^2 \cdot s^{-1}$]

D_r radial dispersion coefficient [$m^2 \cdot s^{-1}$]

D_z axial dispersion coefficient [$m^2 \cdot s^{-1}$]

EQM equilibrium constants method

ETD ethanol decomposition

GFEM Gibbs free energy minimization

h	film heat transfer coefficient between the gas and the solid phase [$W \cdot m^{-2} \cdot K^{-1}$]
h_w	film heat transfer coefficient between the gas phase and the column wall [$W \cdot m^{-2} \cdot K^{-1}$]
HTlc	hydrotalcite like compound
k_0	pre-exponential factor
k_{CO2}	mass transfer coefficient of CO_2 [s^{-1}]
k_f	film mass transfer coefficient [$m \cdot s^{-1}$]
k_g	thermal conductivity of the gas mixture [$W \cdot m^{-2} \cdot K^{-1}$]
k_j	rate constant of reaction j [$mol \cdot kg^{-1} \cdot s^{-1}$]
K_i^*	adsorption equilibrium constant of component i [ ]
K_j	thermodynamic equilibrium constant of reaction j [ ]
K-HTlc	potassium promoted hydrotalcite
l_w	wall thickness [m]
LDH	layered double hydroxides
LDO	layered double oxides
LHV	lower heating value [$kJ \cdot mol^{-1}$]
LHHW	Langmuir–Hinshelwood–Hougen-Watson
IEO	international energy outlook
m_{cat}	weight of the catalyst material [kg]
m_{solid}	weight of the hybrid material [kg]
m_{sorb}	weight of the sorbent material [kg]
$\dot{n}_i$	molar flow rate of component i at outlet [$mol \cdot s^{-1}$]
$\dot{n}_{i,0}$	molar flow rate of component i in the feed [$mol \cdot s^{-1}$]
n_i	molar amount of component i obtained at outlet [mol]
$n_{i,0}$	molar amount of component i use in the feed [mol]
OECD	organization for economic cooperation and development
OSR	oxidative steam reforming
p	pressure [Pa]

p_{ci}	dimensionless critical pressure of component i
p_H	high pressure during the operation[Pa]
p_i	partial pressure of component i [Pa]
p_L	low pressure during the operation [Pa]
PEMFC	proton exchange membrane fuel cell
Pr	Prandtl number
PROX	partial oxidation
$\bar{q}_{CO2}$	average adsorbed carbon dioxide concentration in the particle [$mol \cdot kg^{-1}$]
$q_{CO2,eq}$	carbon dioxide concentration in the particle at the equilibrium state [$mol \cdot kg^{-1}$]
Q	energy exchange with the reactor [J]
r	radial direction [m]
r_j	reaction rate of reaction j [$mol \cdot kg^{-1} \cdot s^{-1}$]
r_R	radius of the reactor [m]
r_p	radius of the pellet [m]
R	gas constant [$J \cdot mol^{-1} \cdot K^{-1}$]
Re	Reynold number
RDS	rate determining step
RR	response reactions
$R_{S/C}$	steam-to-carbon molar ratio [$mol \cdot mol^{-1}$]
$R_{S/E}$	steam-to-ethanol molar ratio [$mol \cdot mol^{-1}$]
Sc	Schmidt number
S_{H2}	hydrogen selectivity [%]
SERP	sorption-enhanced reaction process
SE-SRE	sorption-enhanced steam reforming of ethanol
SE-SMR	sorption-enhanced steam methane reforming
SE-WGS	sorption-enhanced water-gas-shift
SMR	steam methane reforming
SRE	steam reforming of ethanol

t	time [s]
T_{ci}	dimensionless critical temperature of component i
T_g	temperature of the gas phase [K]
T_s	temperature of the solid phase [K]
T_w	wall temperature [K]
$T_{furnace}$	temperature in the furnace [K]
u	superficial velocity [$m \cdot s^{-1}$]
U	global external heat transfer coefficient [$W \cdot m^{-2} \cdot K^{-1}$]
$\dot{V}_0$	volume flow rate of the reactants [$m^3 \cdot s^{-1}$]
V_R	reactor volume [m^3]
WGS	water-gas-shift
X_{EtOH}	ethanol conversion [%]
X_{H2O}	water conversion [%]
Y_{H2}	hydrogen yield [%]
z	axial direction [m]

Greek Letters

α	volume fraction of active phase in the particle [ ]
ε_c	porosity of the column [ ]
ε_p	porosity of the pellet [ ]
ΔG_{fi}^{0}	Gibbs free energy of formation for species i [$J \cdot mol^{-1}$]
ΔH_{ads}	adsorption enthalpy of CO_2 [$J \cdot mol^{-1}$]
ΔH_j	enthalpy of reaction j [$J \cdot mol^{-1}$]
$\eta_{SE\text{-}SRE}$	thermal efficiency of SE-SRE process [$kJ \cdot kJ^{-1}$]
λ_j	Lagrangian multipliers
μ_i	chemical potential of species i
μ_g	gas viscosity [Pa·s]
ρ_b	bulk density of the catalyst [$kg \cdot m^{-3}$]
ρ_g	gas density [$kg \cdot m^{-3}$]
ρ_p	pellet density [$kg \cdot m^{-3}$]
ρ_s	density of the solid [$kg \cdot m^{-3}$]
ρ_w	column wall density [$kg \cdot m^{-3}$]
τ	space time [s]
$\upsilon_{j,i}$	stoichiometric number of component i in reaction j [ ]
$\hat{\phi}_i$	fugacity coefficient of component i
ω_i	acentric factor of component i